The use of Envisat ASAR Global Monitoring Mode data to map rapid broad-scale flood events

JAMES COOK UNIVERSITY
AUSTRALIA

Damien O'Grady

School of Earth and Environmental Sciences

James Cook University

Thesis submitted in partial fulfilment of the requirements for the award of

Doctor of Philosophy

November 2012

Statement on the contribution of others

Nature of assistance	**Contribution**	**Name**
Intellectual support	Editorial assistance	**Dr. Marc Leblanc** (supervisor) **Prof. David Gillieson** (co-supervisor)
Finacial support	Grant	ARC partial funding under Discovery grant **DP110103364**
Data collection	Permission	**Viv Sinnamon** Kowanyama Aboriginal Land & Natural Resources Management Office (KALNRMO)
	Rangers	**Anzac Frank** (KALNRMO) **Phillip Mango** (KALNRMO) **Raven Greenwool** (KALNRMO)

Acknowledgements

I would like to express my gratitude to my supervisors, Dr. Marc Leblanc and Prof. David Gillieson, for their wisdom, knowledge, support and for their confidence in my work.

Thanks go also the Australian Research Council, who partially funded this research under Discovery grant DP110103364, and to the European Space Agency, for the provision of radar data through project number C1P.5908.

I am grateful also to Viv Sinnamon of the Kowanyama Aboriginal Land and Natural Resources Management Office for his cooperation, and in particular rangers Anzac Frank, Phillip Mango and Raven Greenwool for their help with the data loggers.

Above all, thank you Flora and Ryan, for being just wacko enough to let me do this.

Abstract

This thesis seeks to enhance our ability to map the extent of large floods in near real time using coarse resolution C-band radar remote sensing. The microwave part of the electromagnetic spectrum has a great advantage over visible and infrared light in its ability to penetrate cloud cover, and as radar is an active system, it does not rely on daylight hours for reflected solar radiation. The European Space Agency's Advanced Synthetic Aperture Radar aboard the Envisat satellite, operating in Global Monitoring Mode (GM), is targeted for particular consideration due to its high temporal frequency, comprehensive coverage and ease of acquisition. Challenges are identified which relate both to the use of radar generally, and also in particular to GM data, in the demarcation of water and land, as well as to the practical business of data processing.

These challenges relate to the way that water is identified, which can be by a low signal where specular surface reflection away from the sensor occurs, or by a high signal where multiple interactions occur between the water surface and emergent structures such as vegetation. Thresholds must make the distinction between the two cases, and as such, some prior knowledge of land cover is needed in the segmentation process. With such coarse data as GM, mixed pixels comprising both high and low water signals are often encountered, which result in a mid-range pixel value that masks the presence of water. The thresholding process is further complicated by the relationship of the signal returned to the sensor with incidence angle, which varies between about 14–44° with GM data. Under some wind conditions, waves of a particular pitch and orientation on the surface of open water cause resonance effects, returning a very high signal - sometimes

even a gain - to the sensor. In particular circumstances, where flood waters flow through arid land, the low signal returned from open water due to specular reflection cannot be distinguished from the low signal returned from desert due to attenuation and absorption. In literature surrounding research in this field, results from observations of radar response in wetlands and flooded grasslands are mixed, pointing to the importance for further work in this area. In Australia, the need for a better understanding of the expected backscatter response from inundated areas in tropical savanna, which covers one third of its landmass, is clear.

The computational framework was set up for the efficient download, registration and orthorectification of GM data using scripting and open source software. Full advantage was made of the parallel processing capabilities of James Cook University's High Performance Computing network, scripts were tailored to GM data's characteristics and test results proved the method appropriate for the high volume processing required by the large GM dataset. This capability was used to carry out regression on a pixel-wise basis across a year's worth of GM data, categorised by seasonal rainfall periods, in order to normalise backscatter values with respect to incidence angle. Correlation of the resulting characteristics with surface parameters, such as regolith, vegetation and soil type were observed. The potential confusion between absorption in dry, homogeneous soils, and specular reflection on surface water was predicted. It was observed that the degree of change of backscatter with incidence angle on open water appeared independent of the presence of Bragg Resonance, despite absolute values being at opposite ends of the scale, depending on whether resonance did, or did not, occur.

A major flood event in Pakistan was successfully mapped and made available in near-real time for the disaster relief effort. An image differencing technique allowed the successful separation of low backscatter response from open water with that from the immediately surrounding desert. GM data were found to fill a gap in the period where the flood was obscured to visible and infrared sensors, during the crucial first week of the event. Definition of the extremities of the flood were tackled with a spatial threshold using a region-growing algorithm, and the radiometric backscatter threshold was established using an incremental convergence technique, employing multiple κ-statistic calculations with contemporaneous MODIS SWIR data. Both the stability of the radar threshold, and the instability of the MODIS SWIR reflectance threshold, were highlighted.

The backscatter responses to two large flood events in the tropical savanna of northern Australia were investigated, showing markedly different results. One flood, in the floodplain of Queensland's Flinders River, involved total inundation of tussock grasslands over an area of 9000 km^2, allowing accurate classification using GM data ($\kappa = 0.7$), with predictable dihedral scattering returns as the flood receded and the emergent tussock grasses caused multiple interactions between the radar signal and the surface water. Inundated areas covered by emergent vegetation in the other flood, in Cape York's Staaten River floodplain, were almost completely indistinguishable from the surrounding wet vegetation. Data from water height loggers established in the neighbouring Mitchell floodplain over a dry/wet season period provided an insight into the interaction of these particular vegetation conditions under flood. Results concurred with the work of others, that backscatter response is a complex combination of effects depending on relative water height, vegetation spacial density, biomass, and verticality, or enmeshment, of super-surface grasses.

The need for further work is discussed, together with spin-off opportunities, in the context of current and planned alternative C-band satellite data sources. The planned contribution of C-band data, along with contemporary visible/infrared products in the upscaling of current and ongoing JCU research into greenhouse gas emissions in the Mary River in the Northern Territory is outlined, together with the possible use of C-band radar to gauge fuel moisture content and fire potential, in the light of our findings in the tropical savanna. The potential use of GM data to explore correlation between *Gravity Recovery and Climate Experminent* (GRACE) data and surface water and soil moisture over time is discussed.

Contents

List of Figures

List of Tables

List of Perl Scripts

Nomenclature

Greek Symbols

α Local incidence angle

β^0 Radar brightness coefficient

ϕ Off-Nadir angle

γ Range-independent (ground-range projected) backscatter coefficient

κ Kappa Statistic

Λ Look angle

λ Wavelength

Ω Angle subtending the target and the satellite, at the centre of the ellipsoid

ω Angle subtending the *apparent* target and the satellite, at the centre of the ellipsoid

σ Radar cross-section (m^2)

σ^0, σ^0_n Normalised radar backscatter coefficient

σ^0_α Radar backscatter coefficient at incidence angle α

θ Incidence angle (context-specific)

Other Symbols

CH_4 Methane

CO_2 Carbon Dioxide

NO_2 Nitrogen Dioxide

det Determinant of a matrix

G^2_{ele} Two-way antenna elevation pattern gain

HH Co-polarised Horizontally

HV Cross-polarised, H on transmission, V on reception

K Absolute calibration constant

S Slant range

S' Nominal zero-Doppler slant range

$\hat{\mathbf{v}}$ Unit vector (vector of length 1)

$\mathbf{v_1} \times \mathbf{v_2}$ Cross product of two vectors

VH Cross-polarised, V on transmission, H on reception

VV Co-polarised Vertically

Acronyms

AEP Antenna Elevation Pattern

ANN Artificial Neural Network

ASAR Advanced Synthetic Aperture Radar

SAR Synthetic Aperture Radar

dB Decibels

DEM Digital Elevation Model

DN Digital Number - raster image pixel value

ENL Equivalent Number of Looks

ESA European Space Agency

GDAL Geospatial Data Abstraction Library

GIS Geographic Information Systems

GLCM Grey Level Co-occurrence Matrix

GM Envisat ASAR Global Monitoring Mode

GRD Gross Rock Descriptor

HPC High Performance Computer

JCU James Cook University

LS Lacustrine Sediment

PNN Probabilistic Neural Network

REGEX Regular Expressions

SRT Slant Range Time

SWIR Short-wave Infrared

TS Tropical Savanna

VIR Visual / Infra-red

Introduction

The primary objective of the research described in this thesis is to enhance our ability to map the extents of large floods.

In recent decades, our dependence on empirical data for such a task has given way to rapidly developing satellite imaging technology, which has enabled us to successfully map flood inundation to a fine degree of accuracy, and has contributed greatly to the study of flood dynamics and to our efforts in disaster relief and prevention.

0.1 Relevance and Importance

Flooding amounts to nearly 50% of natural disasters, and accounts for over 70% of all lives affected by natural disasters (Kugler *et al.*, 2007). Justification for research into the understanding of floods covers a broad area of science. In order to understand the hydrology of large river systems, it is vital that the dynamics of inundation patterns are better understood (Frappart *et al.*, 2005). Wetlands receive increasing attention as indicators of changing biodiversity. Powell *et al.* (2008) tell us that *"Recent research into water requirements for wetland systems shows that duration, frequency, depth, timing and extent of flooding are the most important influences on ecological communities"*, and that *"Modelling these systems is hampered by a lack of data and inappropriate model structures"*. Signatories to the Ramsar Convention are encouraged to set up national wetland inventories in order to advise government on policy and management strategies, yet a review has discovered gaps in coverage of such inventories and problems with the associated information management systems; Rosenqvist *et al.* (2007) point out that The Asian Wetland Inventory and *Convention Resolution VIII.6* specifically highlight remote sensing as a key tool in rectifying this situation.

Environmental degradation is an increasing concern in respect of river catchments. Some changes in land use and management practices cause increases in surface run-off which, in turn, can have a major effect on the volume and rate of discharge of water. This can cause erosion and large-scale changes to fluvial behaviour patterns as well as increasing the potential for increased phosphates to be carried downstream (Bonn & Dixon, 2005). Henderson & Lewis (2008) point out that mangroves are considered “the world’s most productive ecosystem based on net productivity”, and that over 54% of the world’s mangroves have disappeared over the last few decades. The characteristics of the annual inundation pulse in the Amazon are, according to Rosenqvist *et al.* (2002), the “dominant environmental factor affecting aquatic biota on the floodplain” .

Rosenqvist *et al.* (2002) bring up another issue which is widely discussed, and that is the quantities of methane which are produced in flooded areas. This amounts to some forty times the quantity produced by wet soils (Arnell, 2002). Wetlands also play a part in the accrual of heavy metals in surface waters (Baghdadi *et al.*, 2001). Methane is produced during the anaerobic decomposition of biota, and thus is particularly prevalent during the inundation of terrestrial vegetation (Noernberg *et al.*, 1999), and therefore an understanding of flood patterns against vegetation maps will become an increasingly important tool to assist in the modelling of greenhouse gas emissions (Rosenqvist *et al.*, 2002).

Under certain environmental conditions, perhaps the best satellite instruments to use for the separation of water from land are “passive” instruments (relying on reflected solar energy or on thermal emissions, for example) that operate at wavelengths between the visible and infrared ranges of the electromagnetic spectrum, due to the fact that radiation through much of the infrared spectrum is absorbed by water.

There are, however, inherent limitations to the use of passive sensors. The reliance on the relative position of the sun halves the data acquisition period (on average, depending on latitude and season), rendering us blind to night-time flood activity. Perhaps more significantly, radiation at these wavelengths is absorbed, reflected or attenuated by atmospheric water vapour to such an extent that the surface flooding is hidden from the satellite sensors by cloud cover, commonly present at most flood events.

The research described in this thesis, therefore, singles out the use of active sensors operating in the microwave range ($\lambda \approx$ 1mm – 1m). Such instruments analyse reflected radiation originating from their own source, and therefore are not reliant on the sun. In addition, atmospheric effects on microwave radiation at certain wavebands (such as C-band, studied here), are negligible by comparison to those which effect the light used by passive sensors.

0.2 Challenges and opportunities

The use of radar data, specifically, to map flooding, is well researched and reported. Although the advantages over passive sensors, as described above, have been confirmed and put to good use, much of the published material on the subject comprises conspicuously large sections documenting the limitations of radar data for the purpose, and for good reason. These limitations stem from major differences between microwave and optical data, and the methods used to acquire images:

1. Optical data is two-dimensional, the physical position of receipt of data on the "retina" of the instrument is analogous to the relative position on the earth's surface from which the energy was reflected.

   Radar data is one-dimensional, the position of the reflector having to be calculated using a variety of geometric and temporal parameters. Terrain affects radar imagery differently to optical imagery, and requires different processing. Terrain also causes *radiometric*, as well as geometric distortion of values, and in some cases causes total masking, which must be taken into account.

2. Microwave sensors operate in narrow wavebands, and the radiation is therefore subject to summation interference effects to which all coherent radiation is susceptible, causing a "salt and pepper" effect on the resultant image, known as *speckle*.

3. Regular textural patterns at certain orientations, such as small wind-induced waves on the surface of water, cause additive effects due to resonance, which result in an amplified signal, the value of which lies at the opposite end of the scale to what we would expect from water.

4. Received values have a relationship with the angle of the transmitted radiation incident to the surface of the reflector. This angle must therefore be known, and the relationship understood. The relationship itself depends on the nature of the reflector (in terms of scale, structure and dielectrics), which compounds the complexity of requirements at the processing stage.

5. Where structures such as vegetation or buildings emerge through flood water, multiple reflections can cause a deceptively high signal response, which falls into the range of values expected from wet soil, making it difficult to accurately define the boundaries of a flood.

6. The radar backscatter response to open water is usually characterised by a low value, due to specular reflection away from the sensor by the surface of the water. Errors in classification are contributed to by other smooth surfaces causing a similar reflection, or by extremely dry, homogeneous surfaces such as desert sand, which present a low radar value due to attenuation and absorption of the incident radiation.

As stated, the above are factors which limit the use of radar data to map flooding, and most have been well documented. What is lacking, however, is a measure of the precise extent to which these factors may be mitigated, and beyond which the use of radar data to map flooding is precluded.

Mapping relatively small floods (such as in urban areas) to a fine detail requires relatively high spatial-resolution data. Data at such a resolution is usually confined to a temporal frequency of one per orbit cycle (usually just over a calendar month). Thus for a fast flood event, there is an element of luck in employing such data, and even when timing is favourable, unless the flood is extraordinarily slow in progression, its dynamics may only be interpreted from one or two instances in time.

Mapping floods that occur on a large scale, spanning tens or hundreds of kilometres, however, may make use of coarse resolution data such as that made available by the European Space Agency (ESA) from their Advanced Synthetic Aperture Radar (ASAR) instrument aboard the Envisat satellite, when operating in Global Monitoring Mode (GM). Much higher temporal frequency is achieved, as this instrument records data across a swath over 400 km in width, which overlaps considerably (depending on the latitude) with each consecutive orbit cycle.

Analysing the response of GM data to large flood events gives us the opportunity to fill the gap in research - to define the constraints governing the use of such data for the important task of understanding large and rapid flood events. At the same time, the massive dataset of GM output affords us the ability to understand the relationship of incidence angle with different surface reflectors, and allows us to investigate how this, and the other effects which compromise the accuracy of flood maps, may be mitigated.

0.3 Objectives

The ultimate objective is, therefore, to record an optimum method to monitor and map large flood events quickly, to a reasonable degree of accuracy, and to understand the environmental and geophysical conditions to which such a method is limited. This objective is approached by seeking to address the following questions:

- How can the large dataset be managed, the incidence angle and other geospatial data be extracted and the imagery preprocessed in a fast, efficient way, and in such a manner as to maintain complete control and transparency for all calculations performed in the process?
- What is the relationship between incidence angle and radar backscatter for different surface properties? Can knowledge of this relationship be used to enhance our ability to delineate flooded regions? If necessary, how can incidence-angle effects be most accurately mitigated?

- How can ambiguities in radar backscatter due to absorption, under particular environmental conditions, be reduced? How can the most accurate thresholds be established in floods whose scale, timing and geographical constraints forestall the acquisition of empirical data? Answering such a question may be critical for disaster response efforts.

- How do existing vegetation and rapidly-growing aquatic vegetation affect radar response in flooded regions? To what extent can these effects be mitigated or taken advantage of? To what degree do these effects preclude the use of GM and other radar data under certain environmental conditions?

0.4 Thesis structure

This thesis records research and analysis that was carried out in order to answer these questions. Following the introductory sections which cover theory and related research, the questions are tackled systematically in independent chapters. The major successive chapters are structured as comprehensive stand-alone papers, for submission to research journals. Two of the articles are under review, and one has been published. The format and content of the articles are altered here only to provide continuity and to avoid undue repetition of common but necessary theoretical explanations which will appear independently in the individual submissions.

0.4.1 Thesis flow diagram

Figure 1 shows a schematic outline of the structure of this thesis. The diagram shows the overall flow of the work, the broad reasons for paths taken, the direct and indirect outcomes of the research and brief summary of work that is proposed to follow on from it. Colours are coded roughly as follows:

Black	Sections, chapters of the thesis
Red	Gaps, questions, obstacles
Blue	Solutions
Green	Outcomes, direct or indirect

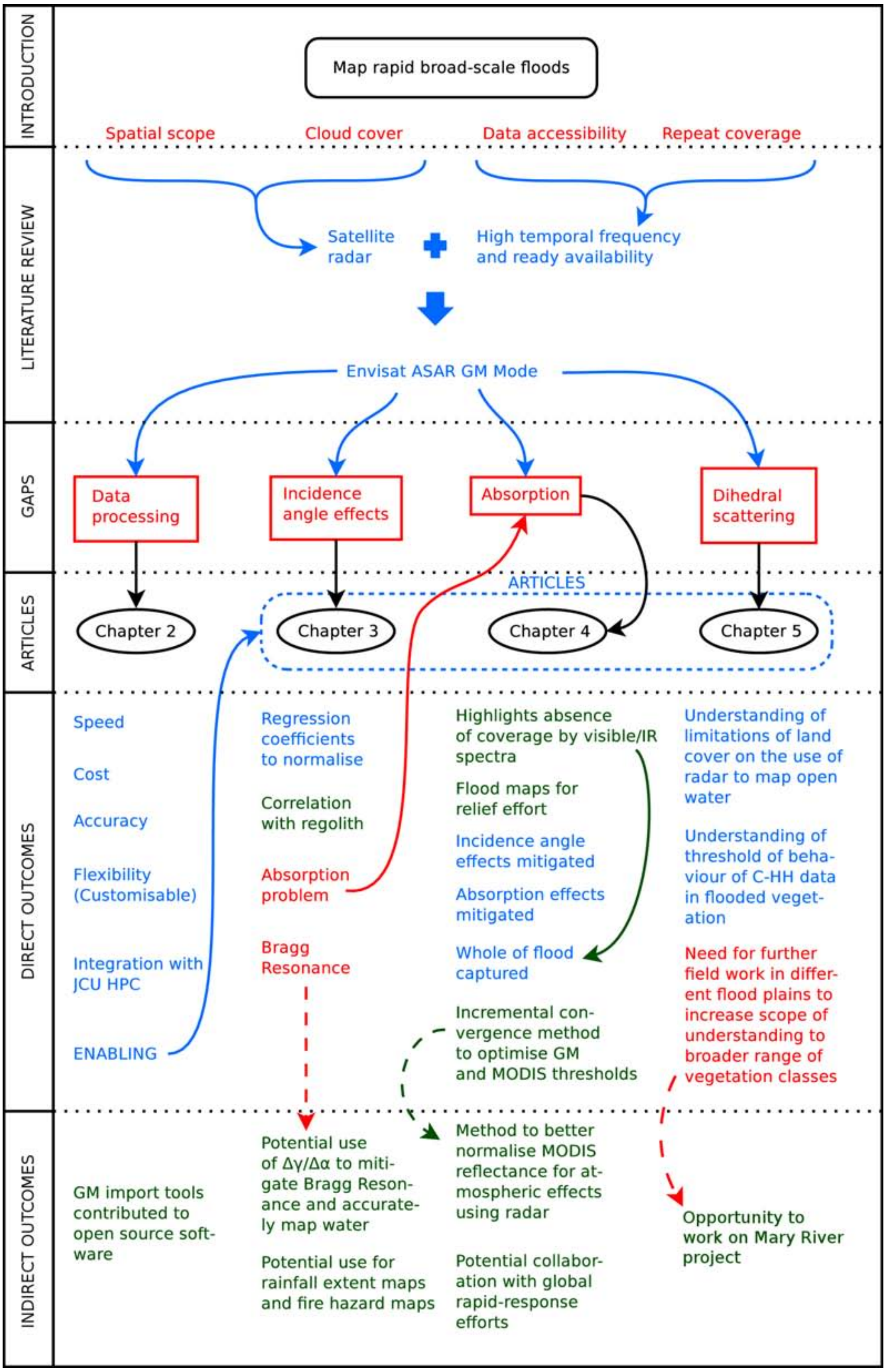

Figure 1: Flow diagram outlining structure of thesis

Headings in the left margin refer to relevance within the thesis. In the diagram, what is shown in the *Introduction* and *Literature Review* sections are summaries of the major challenges and the logic that leads on to the decided focus of research, whereas these actual chapters in the thesis cover much more detail which need not be shown schematically here. The *Gaps* section of the diagram results from the concluding part of the literature review, and represents the focus of the work to follow. From this point of the diagram onwards, items are arranged in a matrix, with horizontal groupings separating articles from direct and indirect outcomes, and with vertical columns grouping problems, solutions and outcomes under the *article*, and therefore *chapter*, in which they arise. The findings listed in these groups all form a part in the *Conclusion* section of the thesis, which is not explicitly labelled in the diagram.

A *Chapter context* diagram is shown at the beginning of each chapter to explain the relevance of the chapter in the context of the whole thesis, and to prevent the reader from becoming lost. These are based on the Thesis Flow Diagram above (Figure 1). The connectivity diagrams are milestones, or place markers, and therefore do not appear in the List of Figures.

0.4.2 Chapter flow

The chapters appear as follows:

- The front matter of the thesis includes the contents, lists of figures and tables and a list of the nomenclature (symbols and acronyms) used throughout.

- Following the introductory chapter, a literature review presents an explanation of the theory behind the use of radar remote sensing in the mapping of floods, in the context of research literature to date. Here we discuss the parameters that play a part in the processing of radar data for this purpose, and the challenges that they present.

- The method of managing the data, extracting the parameters and performing the geo-referencing and orthorectification, using object-oriented scripting and parallel processing over a distributed network, is detailed. This is a necessary precursor to all the work that follows. Methods to address the questions discussed in this introduction, and arising from the literature review, form the basis of the following chapters, each of which represents a journal submission:

- The effects of incidence angle on radar backscatter, given different surface characteristics, such as regolith, vegetation and soil types, is investigated. In particular, the separability of water in comparison to those parameters is measured. The relationship of incidence angle with backscatter is established by carrying out regression for each pixel over time, making full use of the high temporal frequency of GM data available. The work results in a means to normalise radiometrically across a wide swath with respect to incidence angle, which is essential to be able to apply a threshold to the pixel values to determine the presence of flooding. Two problems are highlighted as a result of this chapter. One is a phenomenon known as Bragg Resonance, for which a potential solution is discussed. Another is a problem with ambiguity in backscatter values which could represent water, due to absorption in dry sand. A solution to this problem is tackled in the following chapter.
- Is this problem with ambiguity due to absorption likely to present a real problem? How might a solution be found? A case study is performed, mapping the rapidly developing extents of a major flood event in Pakistan in 2010. This study was initiated as the result of a request by a UNESCO team, who were about to fly to the region as part of the relief effort, lacking maps detailing the extent of the flooding. Methods to mitigate incidence angle effects and sand absorption ambiguities are successfully carried out, and a method to non-empirically optimise thresholding is detailed.
- Having successfully established the suitability of complementing remote sensing data from the optical / infra-red spectra with GM data to map floods in an arid / semi-arid environment with a low-height vegetation matrix, the applicability of this method to a northern Aus-

tralian environment is investigated. This addresses the fourth major challenge highlighted in the *gaps* section of the literature review, related to *dihedral scattering*. An investigation into the limitations presented by vegetation on the use of radar remote sensing to delineate water is carried out, by studying two major floods in the north of Queensland, which took place in catchments with different vegetation matrices. This chapter highlights the need for more detailed research, which is outlined in the subsequent chapter. Backscatter observations are compared to fieldwork data, with interesting results.

- The following chapter outlines the proposed next step, to take the benefits arising from the research carried out for this thesis and pave the way for its application to the broader environment. The suggested work builds on research that has been commenced and is ongoing by a team from JCU's Hydrology department, who are taking measurements in the field in a bid to estimate fluctuations in greenhouse gas emissions in a flood plain in the Northern Territory. The research described in this proposal would serve to provide the existing team with the remote sensing function required to upscale their own results to the wider floodplain, whilst at the same time using its spatially detailed data to work towards a better inversion model for the interpretation of radar data to map flooding. The potential use of C-band radar to investigate fire fuel conditions, given findings from the previous chapter, is outlined.

- A conclusion summarises the results of the thesis, discusses shortfalls and summarises the avenues of future research that arise from it.

- The appendix contains the program code developed to pre-process the data, as discussed in Chapter 2, and that used in the regression analysis discussed in Chapter 3. It also lists the data used in some of the chapters.

Chapter 1

The Theory & feasibility of mapping surface water with satellite radar data - a literature review

Chapter context

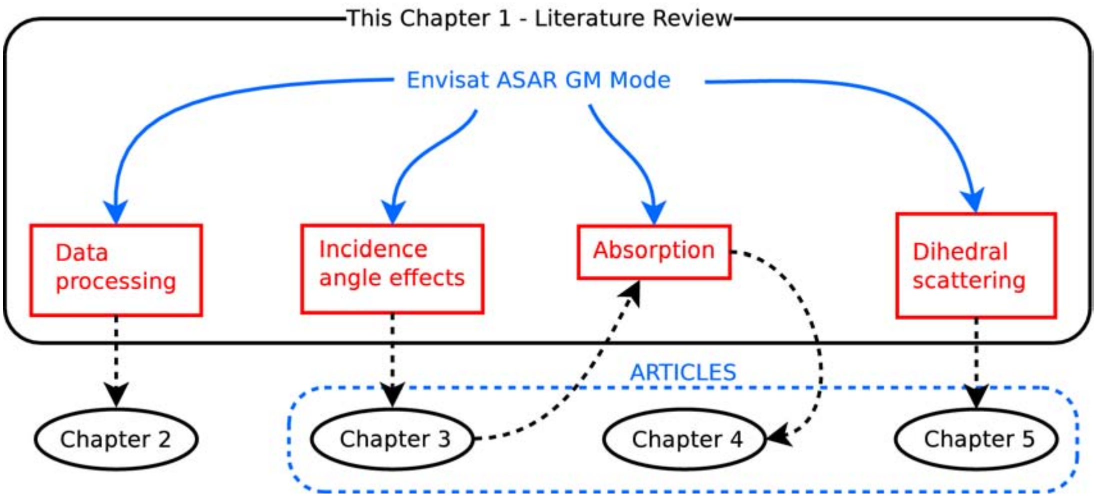

Abstract

A review of the mapping of water extents, using radar data, is made, briefly outlining the theory behind the field, as well as the many challenges faced, including speckle, spatial resolution, variance with incidence angle, temporal frequency and ambiguity in interpretation. With regards to opportunities presented by the large time series of data available, four broad areas are identified that contain gaps in existing literature: The practical methodology behind the registration and orthorectification of a very large data set; the relationship of backscatter response with incidence angle specific to pixel-scale regions; the separation of water with dry soil, which share low backscatter values due to absorption; the separation of high backscatter response from dihedral scattering with that from wet soil.

1.1 Introduction

This review aims to study the use of radar remote sensing to map the extents of water inundation over time. Of particular interest is the feasibility of using Envisat *Advanced Synthetic Aperture Radar* (ASAR) *Global Monitoring* Mode (GM) data as a source for this task, complimented with data from other ASAR modes and from other active and passive sensors. The detailed specifics of GM data will be discussed later in section 1.2.3. Briefly, ASAR provides radar backscatter measurements in the C-band ($\lambda = 5.6cm$) in a 35 day repeat cycle orbit, with data being provided in a variety of modes with different specifications (ESA, 2007a). For certain modes, temporal frequency is greatly increased using ASAR's ability to steer its beam to different elevation angles. A consequence of this is that spatial resolution is compromised, and a greater complexity associated with data coming from a variety of incidence angles is introduced. GM is one such mode, having the lowest spatial resolution and highest temporal frequency of all of the ASAR modes. A graphic representation of the temporal frequency of GM data available covering the Australian continent is shown in figure 1.1.

GM data has a swath width of 405km, a pixel size of 500m and a spatial resolution of 1km. Such a spatial resolution would seem to constrain the value of GM data to broad-scale views of radar-distinguishable features that cover areas

Figure 1.1: Map showing the frequency of ASAR GM mode coverage acquired for the Australian mainland for the first 128 days of 2009

greater than a few square kilometers. The European Space Agency (ESA) originally envisaged GM data's greatest value being in the monitoring of Antarctic ice sheets, with ASAR's Image Mode Precision (IMP) mode targeted for flood monitoring, having 30m spatial resolution and a 5 day repeat coverage available on request (ESA, 2007a). However, in the past some frustration has been expressed over the tendency for the data request and acquisition process (generally) to cause peak flood events to be missed (Oberstadler *et al.*, 1997; Sanyal & Lu, 2004). Additionally, it will be shown that the potential for detailed and extensive time series analysis afforded by the high temporal frequency and ready availability of GM data allows us, to some extent, to overcome issues of low spatial resolution, providing us with the means for the effective distinction and mapping of inundated areas not envisaged previously, enabling also the mapping of flood durations and patterns. Broadly, this review seeks to explore the extents (and therefore the limitations) of using GM data for this purpose.

1.2 Theoretical context

1.2.1 Radar remote sensing

This section is intended to serve as a theoretical introduction to radar remote sensing for the mapping of water extents.

1.2.1.1 Modulation

The first step to analysing any image data is to understand what the values associated with each pixel represent. The two parameters considered in respect of coherent electromagnetic radiation are *amplitude* and *phase*.

The phase difference between two radar signals is used in interferometry to provide a very accurate elevation value in, for example, SRTM DEM data (Lillesand & Kiefer, 2004). The value of each pixel in a DEM image represents this elevation. Phase information is included with some data products (Single Look Complex, for example) usually in the form of two files comprising the real and complex conjugates.

The value dealt with in this analysis is the *Digital Number* (DN), which is the pixel value of the GM data and is related to *radar brightness* β^0 by the equation

$$DN^2 = K \cdot \beta^0 = K \cdot \frac{\sigma^0}{\sin(\alpha)} \tag{1.1}$$

where σ^0 is the radar backscatter coefficient, α the local incidence angle and K the absolute calibration constant (ESA, 2004). The significance of σ^0 will be dealt with in detail in section 1.4.1.5.

Whilst the radar brightness β^0 is a measure of amplitude and is analogous to the brightness value from an optical sensor, there is a fundamental difference, and this is to do with the way that a return signal's spatial attributes are determined. Most electromagnetic sensors, such as a camera, are *directional*, in that the part of the sensor in which the signal is received depends on the spatial position of the area from which the signal was reflected. In this respect, the received signals form a two-dimensional analogy of the area under observation. With a radar sensor carried on an aeroplane or a satellite, only the spatial dimension along the azimuth, or flight path, is controlled. The returning signal is one-dimensional, and the spatial dimension perpendicular to the azimuth (the *range* dimension), is determined by calculating the time it takes for the signal to get back to the sensor. This leads to a problem which is fundamental to understanding radar images: a single signal can return to the sensor at the same time from two different positions along the swath. This is demonstrated in Figure 1.2, taken from Delio Tortosa's website *Geoforum* (Tortosa, 2008). In this case, C and D are are in separate locations along the swath, but are combined in the return signal (represented by C'D'), as they are the same distance from the sensor. This phenomenon, tending to shorten the apparent displacement between two points, is known as *foreshortening*.

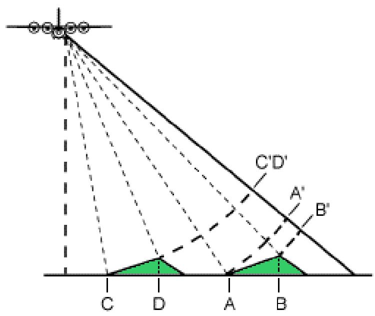

Figure 1.2: Relief displacement and foreshortening (Tortosa, 2008)

From the transformation of AB to A'B', it can be seen that an identical physical structure can be represented differently, depending on where it lies along the swath.

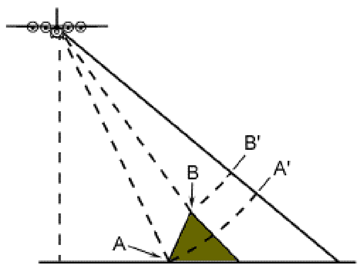

Figure 1.3: Layover (Tortosa, 2008)

Figure 1.3 shows another symptom of the radar imaging process, known as *layover*, where the relative positions of A and B are actually reversed in the output image.

Knowing the relative heights of such features gives us the ability to calculate the distortion effects, and to some extent make corrections to the data. Different levels of processing offered by distributors of radar data take such effects into account.

Another limiting factor which can be seen from Figure 1.4 is *radar shadow*. It can be seen that objects over a certain height at a certain incidence angle will obscure adjacent areas below that incidence angle. These radar shadows can be "filled in" by combining two sets of data covering the exact same area, but taken from opposing sides. Such image pairs from, for example ALOS PALSAR, are available in one file. Another way to mitigate this problem to some extent is by choosing a smaller incidence angle, but this has effects on resolution and attenuation, as will be seen.

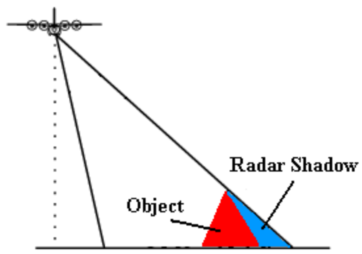

Figure 1.4: Radar Shadow (Tortosa, 2008)

1.2.1.2 Backscattering and Attenuation

The strength of a returned radar signal depends on a variety of response parameters, including physical structure, surface properties, electrical characteristics and attenuation. Figure 1.5 shows how different surfaces will produce different responses. Specular surface reflection will produce very little backscatter towards the sensor. 'Rough' surfaces cause varying degrees of backscattered signal, largely determined by the *Rayleigh Criterion*. Lillesand & Kiefer (2004) cite a preferred *modified Rayleigh Criterion*, which determines a surface to be **rough** when

$$h_{rms} > \frac{\lambda}{4.4 \times \cos \alpha} \tag{1.2}$$

and **smooth** when

$$h_{rms} < \frac{\lambda}{25 \times \cos \alpha} \tag{1.3}$$

where h_{rms} is the rms surface height variation, λ is the wavelength and α is the local angle of incidence (Lillesand & Kiefer, 2004). The summary shown in Table 1.1 gives an idea of how this relates to X and L-band at, for example, $\alpha = 45°$. There are alternative definitions—for example for the *Fraunhoffer* criterion for smoothness, replace 25 with 32 in equation 1.3.

Root-Mean-Square Surface Height Variation (cm)	X Band ($\lambda = 3.2cm$)	L Band ($\lambda = 23.5cm$)
0.05	Smooth	Smooth
0.10	Smooth	Smooth
0.5	Intermediate	Smooth
1.5	Rough	Intermediate
10.0	Rough	Rough

Table 1.1: Synthetic Aperture Radar Roughness at a Local Incident Angle of 45° (Lillesand & Kiefer, 2004)

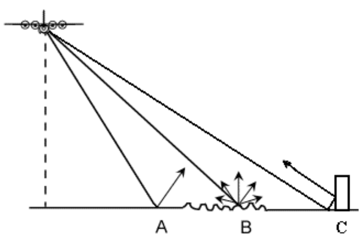

Figure 1.5: Radar reflection from various surfaces: (A) specular reflector, (B) diffuse reflector, (C) corner reflector. (Tortosa, 2008)

Attenuation of radar radiation through a medium is largely a function of the medium's *complex dielectric constant*. For our purposes, it is sufficient to know that water has a dielectric constant over ten times that of most dry minerals (Lillesand & Kiefer, 2004, p671).

Microwave radiation is refracted through media with higher dielectric constants in much the same way as optical light through optically denser media. It is slowed down, its path is refracted towards the normal (thus usually made shorter) and its wavelength is actually increased according to

$$\lambda = \lambda_0 \sqrt{\epsilon_0 \epsilon_a} \tag{1.4}$$

where λ_0 and ϵ_0 are the wavelength and permittivity through free space, and ϵ_a is the average dielectric constant through the penetrated medium (Schaber, 1999).

Radar response specifically to water will be dealt with in section 1.2.1.9.

1.2.1.3 Noise

Noise appears on radar images mainly in the form of speckle, and this is largely due to constructive and destructive interference of incident and reflected radiation. It therefore stands to reason that cross-polarised data (where the incident and reflected light are polarised in orthogonal planes) will be less subject to this form of interference. This and other forms of speckle are mitigated by processing *multilook* images, where multiple images of the same area are added, and in which such noise is averaged out (Lillesand & Kiefer, 2004). Despeckling filters, both spatial and temporal, will be looked at in relation to GM data in section 1.3.1.

1.2.1.4 Radar Wavebands

Radar wavelengths are grouped into ranges, or wavebands, identified by a single letter. Table 1.2 shows all of the common wavebands and their wavelengths and frequencies. Currently only L, C and X-bands are available from active sensors aboard satellites.

A more detailed look at response characteristics of the wavebands is taken in Section 1.2.1.9.

Band Designation	Wavelength λ (cm)	Frequency $\nu = c\lambda^{-1}$ [MHz (10^6 cycles sec^{-1})]
K_a	0.75–1.1	40,000–26,500
K	1.1–1.67	26,500–18,000
K_u	1.67–2.4	18,000–12,500
X	2.4–3.75	12,500–8,000
C	3.75–7.5	8,000–4,000
S	7.5–15	4,000–2,000
L	15–30	2,000–1,000
P	30–100	1,000–300

Table 1.2: Radar band designations (Lillesand & Kiefer, 2004)

1.2.1.5 Polarisation

Emitted radiation may be polarised either horizontally (H) or vertically (V). The received signal may be similarly polarised. There are, therefore, four possible polarisation configurations — HH, HV, VH, VV. Reflection by different materials at certain incidence angles and at certain wavelengths has a polarising effect, and the use of polarisation therefore has a filtering effect, which can either be beneficial or detrimental. Lillesand & Kiefer (2004) note that due to the complex nature of the relationship between polarity and the parameters at play, it is difficult to know whether using cross-polarised or co-polarised radiation is going to be best for a particular application until they are tried.

1.2.1.6 Local incidence angle

The local incidence angle α is the angle between the radiation vector and the normal of the object surface. Whilst the look angle (or *angle of elevation*), which is the angle between the sensor direction and the nadir, is known, the local incidence angle is usually not, and unfortunately it is this latter parameter which has a direct bearing on how incident radiation will be scattered. It has complex effects. An increased angle gives us worse layover, foreshortening and shadow, as discussed in Section 1.2.1.1. However, according to Equation 1.2, a given surface's 'roughness' will increase with an increased incidence angle (and therefore *look angle*), as found by Robinson *et al.* (2006) (Section 1.2.1.1 above refers). It will also be seen later that greater angles of incidence allow structural characteristics to have an enhanced effect on backscatter, which is particularly important in the investigation of biomass (section 1.2.2.3 refers).

Schaber *et al.* (1997) tell us that a reduced incidence angle results in less speckle for co-polarised images, whereas not much difference is observed with cross-polarised images.

It should also be noted that increasing the incidence angle improves the range resolution, according to the following equation, adapted from Lillesand & Kiefer (2004):

$$R_r = \frac{c\tau}{2\sin\alpha} \tag{1.5}$$

where τ is the pulse duration (discussed next).

1.2.1.7 Pulse Frequency

Radiation is emitted from radar sensors in bursts, or pulses, of energy at a given frequency. Two object points very close together may return pulses which *overlap*, or merge, making the two points indistinguishable. Therefore, a shorter pulse duration (i.e. a higher pulse frequency) serves to improve range resolution. This may not seem important for our purposes, as range resolution is always quoted with available data products, but it serves to illustrate that increasing the look angle will also improve range resolution.

1.2.1.8 Resolution

Having discussed the range resolution (perpendicular to the azimuth), there remains the azimuth, or line-of-flight, resolution. Synthetic Aperture Radar (SAR) devices use a very wide broadcast angle, which would normally result in a very poor azimuth resolution. However, spatial position of an object parallel to the azimuth is finely resolved by measuring the frequency of the return signal, which is increased ahead, and reduced behind, the position of the sensor (due to the Doppler effect). Thus the azimuth resolution depends on the smallest discernible difference in frequency that can be detected by the sensor. Effectively, it seems that with most data products, the azimuth and range resolutions are coordinated towards a similar figure.

1.2.1.9 Radar Response to Water

Open water, in the absence of resonance effects, or roughness due to weather causing waves, has a relatively smooth surface which causes radar radiation to be reflected away from the sensor, resulting in a low return signal (Henderson & Lewis, 2008).

Schaber *et al.* (1997) describe a phenomenon which is akin to Bragg Resonance in optics, where regularly spaced scatterers can cause resonant amplification of a signal, even if the scatterers and their distances apart are tiny with respect to larger undulations on which they are superimposed, and that this signal can *"dominate"* the response in the case of satellite sensors. Resonance conditions take the form

$$\frac{2\Lambda}{\lambda \sin\theta} = n \qquad n = 1, 2, 3 \cdots \tag{1.6}$$

where Λ is the spatial wavelength, θ the incidence angle and n any integer. This is relevant where any regularly-spaced deposits are found. The phenomenon allows for the possibility of tiny ripples caused by a breeze on the surface of still water to produce a high backscatter signal, where we would expect specular reflection to cause a low signal. In a large body of water, these *capillary* waves (on a scale of centimetres) are combined with the gravity waves (which occur on the scale of metres) to form a range of waveforms called the *wave spectrum* (Woodhouse, 2006).

Given that wind gives this structural component to water, and that the orientation of the ripples vary, it follows that the resultant backscatter is also a function of the relationship between the horizontal *azimuth* look angle and the orientation of the waves. The resultant backscatter coefficient σ^0 can be represented by the idealised function

$$\sigma^0 = A + B\cos(\phi - \phi_R) + C\cos^2(\phi - \phi_R) \tag{1.7}$$

where ϕ is the azimuth look angle, ϕ_R the orientation of the waves with respect to the same reference, A is the mean backscatter, B the upwind/downwind variation and C the asymmetry of the ripples (Ulaby *et al.*, 1982; Woodhouse, 2006).

1.2.1.10 Hydrological features and parameters

In the absence of water, hydrological features can be determined mainly by their structural characteristics. In a single, uncalibrated image, a feature can be determined if it contrasts with its surroundings. In the case of radar imaging, this contrast is likely to be due either to dielectric or scalar/roughness inhomogeneities between the feature and its surroundings. If a structure such as a drainage channel is significant enough in scale, it may have edges facing the radar sensor which appear very bright, with dark bands behind them due to layover, foreshortening and shadow effects as discussed in Section 1.2.1.1.

Vining & Wiseman (2006) record that relict *meander scars* appear as low-return "radar dark" arcs in Radarsat data, which is attributed purely to different textural qualities. This is corroborated by Schaber *et al.* (1997), who point out that non-calcified small-gravel alluvium is specular, and hence radar-dark. Schaber *et al.* (1997, p344) tell us that co-polarised data are more sensitive to surface roughness on the scale of the particular band's wavelength, whereas cross-polarised data may be more sensitive to geometry or texture.

Surface infiltration capacity is a parameter in flood prediction, and surface moisture an indicator of saturation. In fact, soil moisture, surface roughness and incidence angle together combine to produce large variations in backscatter (Pathe *et al.*, 2009). Surface roughness in itself is an important parameter in flood prediction, as it controls the speed of surface run-off (Bonn & Dixon, 2005).

1.2.2 Contemporary radar research

Henderson & Lewis (2008) carried out a review of the use of radar remote sensing in the detection of wetland ecosystems, consolidating prior reviews and updating the contemporary status of such research. This serves as an excellent source of information.

In his review of the past and potential use of Synthetic Aperture Radar (SAR), Gens (2007) gives us a statistical comparison of the volume of journal publications on the use of SAR, against their subject, which is reproduced in figure 1.6.

As mentioned previously, there are many examples of the use of radar remote sensing to map flooding. Some examples are the assessing of the extents of flooded

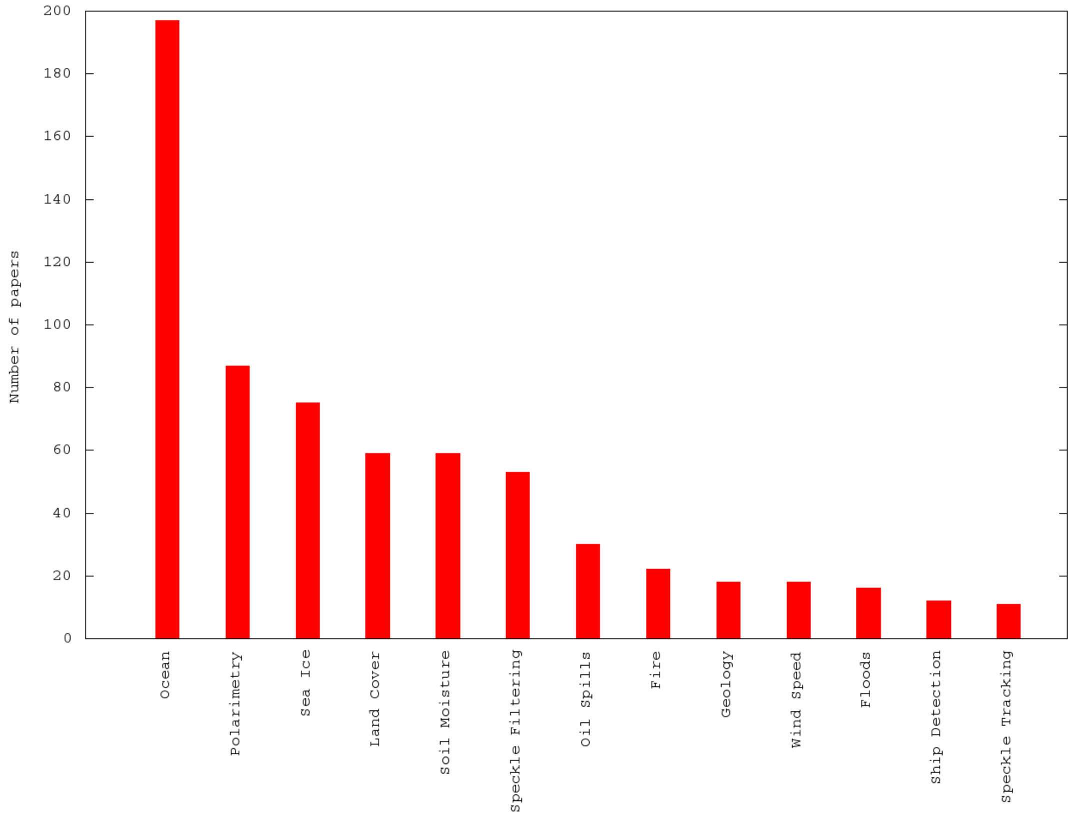

Figure 1.6: Journal papers published on SAR techniques and applications between 1985 and 2006 (reproduced from Gens (2007))

paddies by Waisurasingha *et al.* (2007), the mapping of the 1997 flooding of the Red River by Wilson & Rashid (2005), and the mapping of flood extents and surface roughness (for flood prediction) by Bonn & Dixon (2005). Parmuchi *et al.* (2002) map wetlands using multi-temporal data with a decision tree classifier, and Töyrä & Pietroniro (2005) examine the relationship between flood duration and vegetation patterns. All of these examples use RADARSAT data. Rosenqvist *et al.* (2002) use a time series of JERS imagery to model flood extents in the Amazon.

Research using radar remote sensing can be classified according to the attributes of the data which effect the scope of detection capabilities: wavelength, polarisation, incidence angle, modulation and the use of complimentary data. These attributes are considered in the following sections.

1.2.2.1 Wavelength

It has been seen that certain parameters which effect backscattering by a responder are a function of wavelength — refraction (equation 1.4), Bragg resonance (equation 1.6) and roughness (equation 1.2), for example. These dependencies conspire to dictate that structural scale of responders effect backscatter from radiation of different wavelengths, differently. It therefore follows that the choice of waveband when considering the use of radar remote sensing depends on the predominant structure of the object under investigation, or that of its environment. When attempting to map the extents of flood inundation in a river catchment, it is the aquatic, riparian and terrestrial vegetation which must be considered in addition to physical structure and orientation, as it is these which interact with the incident radiation and scatter it.

What soon becomes clear when reviewing research in this field is that when a vegetated area becomes flooded, one cannot consider the expected response of the water and that of the vegetation separately, as their effect is synergistic. As we have seen, water, when smooth, is a specular reflector. Vegetation, depending on its type, size and structure, and on the wavelength of the radiation, is a volume backscatterer and will therefore tend to return a higher signal to the sensor. During inundation, therefore, in cases where such vegetation is totally submerged, the net effect is a drop in backscatter to some degree. During partial submersion, however, radiation which is scattered by the vegetation towards the water (which under dry conditions would most likely be absorbed by the soil or substructure) undergoes specular reflection from the surface of the water and enters back into the volume scatterer. This process is often called "double-bounce" (Parmuchi *et al.*, 2002), or "dihedral scattering" (Rosenqvist *et al.*, 2002). This will be discussed further in section 1.3.4.

Generally, C-band is considered most suitable for the study of smaller-structured vegetation components (Noernberg *et al.*, 1999)—leaf-off low biomass conditions of deciduous trees, for example (Henderson & Lewis, 2008), aquatic plants (Henderson & Lewis, 2008) and wetlands dominated by herbaceous vegetation (Parmuchi *et al.*, 2002). It is also to be expected that growth of a plant will see its relative scattering effects on C-band and L-band, for example, change. Pope *et al.* (1997) found that a rise in water levels in a marsh following burning show no increase in backscatter in L-band, but a 6 dB increase in C-band response , presumably from dihedral reflection. In fact, Pope *et al.* (1997) go on to say that an increase in C-band backscatter can sometimes correspond with a *decrease* in that of L-band.

For reasons of scale, it is not surprising that C-band is more sensitive to ripples on water surfaces (Hostache *et al.*, 2009a), and we would expect L-band to better respond to slightly larger wavelets. Of course, for the purposes of this study, it is not the observation of such waves that concerns us, so much as their elimination, as their presence only serves to make water bodies less distinguishable from the surrounding environment.

It may generally be considered that longer wavebands, such as L-band, produce a higher response in forested areas, and C-band in areas of shorter, sparser vegetation (e.g. Henderson & Lewis (2008)). Multiple wavebands would obviously be the optimal acquisition. On an encouraging note for the use of the C-band GM data, many consider C-band to be the most sensitive to flooding. Pope *et al.* (1997), whose data included phase information (section 1.2.1.1 refers), found that in a comparison of C and L-band co-polarised and cross-polarised configurations (amplitude modulated) and C and L-band phase modulated data, the most sensitive to flooding was C-band phase difference. Perhaps unfortunately for GM data users, the same study found that C-band HH data was the *worst* for detecting some flooded marshes, but that, once again, this was very much dependent on the size and structure of the vegetation—*Cattail* and *Sawgrass* marshes, in the Yucatan Peninsula, showed a significant increase in C-HH backscatter when flooded.

1.2.2.2 Polarisation

As discussed previously, it is difficult to predict the best cross-polarised or copolarised configuration for a particular purpose until they have been tried and tested on the particular area under investigation. This notwithstanding, Henderson & Lewis (2008) tells us of parallels drawn by Ramsey (1998) *"between the interaction of radar parameters (especially polarization) with vertically oriented* *flooded trees at L-band and vertically oriented stalks of flooded herbaceous vegetation at shorter wavelengths."*. Interestingly, Ramsey (1998) found that variation in attenuation of C-band signal with incidence angle was not dependent on polarisation, whereas this was not the case at L-band (Henderson & Lewis, 2008).

Noernberg *et al.* (1999) show us that like-polarised signals (HH and VV) give us clear separation of open water with various vegetation types in the area of -25dB to -31dB, but with cross-polarised signals, the water response may be confused with that of dead trees. This is perhaps intuitive, in that both water and tree trunks present a dominant structure which is orthogonal to one of the two axes of polarisation.

In their evaluation of the suitability of C-band SAR data for the mapping of wetlands, Baghdadi *et al.* (2001) classified 3 images at various polarisations as a function of incidence angle, reporting accuracies of 74%, 76% and 59% for HH, HV/VH and VV respectively (based on error methods which will be discussed in section 1.4.4).

Bourgeau-Chavez *et al.* (2001) found HH polarisation to be better than VV for the discrimination of wetland while mapping riparian ecosystems in Virginia using C and L-band data.

1.2.2.3 Incidence angle

The theoretical contribution of the local incidence angle to radar backscatter was briefly discussed in section 1.2.1.6. A more detailed look at this relationship will be taken when considering the proposed preprocessing of GM data. In terms of contemporary research, the consideration depends, once again, largely on the use to which the data is put.

There is general consensus that, where canopy needs to be penetrated in order to experience the maximum dihedral scattering to discriminate flooded from non-flooded woodland or forest, a low angle of incidence is best (Bourgeau-Chavez *et al.*, 2001; Henderson & Lewis, 2008; Ramsey, 1998; Sanyal & Lu, 2004; Töyrä & Pietroniro, 2005; Töyrä *et al.*, 2001). This, as Ramsey (1998) points out, is due to the increased signal/canopy interaction at higher incidence angles. Later in this review, when considering the preprocessing of GM data, the issue over the possible normalisation of pixel values in terms of incidence angle will arise. Given the potential for dihedral scattering and other interactions that vary with incidence angle (and with the structural nature of the scatterer) that are discussed here, it is reasonable to suggest that no such normalisation is possible without a precise knowledge of the underlying structure and orientation. Given how quickly vegetation can change, especially in the tropics, this may never be practicably achievable in the scale at which this review wishes to look. Section 1.4.1.5 deals with this issue.

If, indeed, a lower angle of incidence increases dihedral scatter in flooded forests, then it follows that a ratio between data from a higher incidence angle and that from a lower angle will be an excellent indicator of flooding in wooded environments. As discussed, with smooth open water, the predominant response results from specular reflection away from the sensor. For this reason, Kandus *et al.* (2001) recommend large incidence angles to discriminate the interface between land and water (Henderson & Lewis (2008),Kandus *et al.* (2001)). A ratio, therefore, of high incidence angle with low would seem a good method for distinguishing open water. In fact, such a combination was found to have significantly higher accuracy when classifying open water, as compared to the use of single images by Töyrä & Pietroniro (2005).

1.2.2.4 Modulation

Potentially, any of the parameters mentioned in sections 1.2.1.1 and 1.2.1.2 which effect the scattering of incident radar radiation on a subject may be used in detection. The Rayleigh and Fraunhoffer criteria were discussed, which govern the property *roughness*. As part of their research into flood forecasting by estimating surface run-off risk, Bonn & Dixon (2005) make use of this relationship to attempt to measure surface roughness using Radarsat data. Incidentally, with reference to the previous section, Bonn & Dixon (2005) find that greater incidence angles provide greater radiometric resolution in terms of surface roughness.

Due to the fact that water tends to reflect most of the incident signal away from the sensor, a simple threshold is the most common method used to classify water in the research studied (Abhyankar *et al.* (2007); Baldassarre *et al.* (2009)

and Hostache *et al.* (2009a) are examples). There are variations on this theme—Chandran *et al.* (2006), for example, use a threshold on the variance of an 11×11 moving window to discriminate flooded areas. Shifting in phase in HH and VV polarisations at C and L-bands may be used do discriminate flooded from non-flooded forests (Henderson & Lewis, 2008).

Grings *et al.* (2009) use electromagnetic models of structural and dielectric properties of soil and vegetation to predict backscatter response of marshland locations and to extract water level estimates, with some success, particularly when using interferometric techniques. Frappart *et al.* (2005) also use radar altimetry to gauge heights and estimate water storage volumes in the Negro basin in South America.

1.2.2.5 Ancillary data

Having established that there are a variety of parameters at play affecting how an object or area scatters or absorbs radar radiation, the inversion of the signal response necessarily involves having a qualitative and quantitative understanding of properties which cannot be extracted from the radar data. These may include the following:

Terrain and elevation: Governed by both the requirement for orthorectification and by the dependence of backscatter on local incidence angle. A Digital Elevation Model (DEM) is an essential component of the orthorectification process (section 1.4.1.3 refers). Further, any corrections due to local incidence angle or height calculation will necessarily require an accurate DEM. Waisurasingha *et al.* (2007), for example, use a DEM (unidentified) and Radarsat-derived flood extents to estimate flood depth to a high degree of accuracy. Usually an exceptional level of height accuracy is required of a DEM to derive water levels, such as that attainable using LIDAR (Töyrä & Pietroniro, 2005).

Soil moisture: The dielectric properties of water changing the signal response significantly, and a valuable tool in flood prediction, as discussed.

Regolith: The dielectric properties of the surface material having a direct result on the signal attenuation.

Soil types: As regolith, but in addition may play a part in soil infiltration capacity and flood propensity estimates.

Meteorological data: For covariant analyses of flood-related events.

In situ hydrological data: Data collected in the field is an essential requirement for calibrating and verifying the results derived from remote sensing.

Other: Many other satellite data products were used in the literature researched to verify derived results or to play an integral part in class segmentation. Zhou *et al.* (2000) use multi-temporal NOAA AVHRR and Radarsat data to monitor flooding in China. Landsat data was used by Bartsch *et al.* (2008) to compare inundation mapped with GM data. Seiler *et al.* (2009) use ASTER data to compare texture analysis methods with ASAR. Töyrä & Pietroniro (2005) use multi-temporal SPOT and Radarsat data over a five year period to accurately map wetland variations. In the latter paper, the importance of spatio-temporal databases built up over time, with the understanding of relationships between vegetation patterns and flood dynamics over an entire delta, are stressed.

1.2.3 Envisat ASAR Global Monitoring mode

ENVISAT ASAR's Global Monitoring mode uses ScanSAR technology, incorporating *beam steering*, to cover wide swaths with varying look angles (ESA, 2007a), and has the potential to operate continuously, making it unique amongst SAR instruments aboard satellites (Pathe *et al.*, 2009). The resulting product has an excellent temporal coverage (figure 1.1 refers), at the expense of the spatial resolution at around 1km, and a significant noise component to the signal (Sabel *et al.*, 2008). Figure 1.7 shows the swath configurations against their look angles. Table 1.3 shows the specifications for GM data.

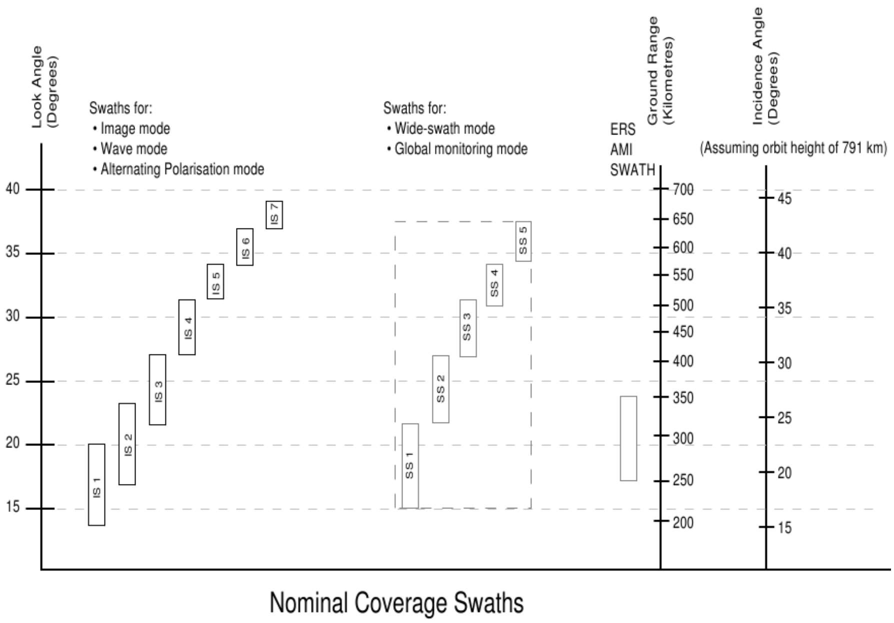

Figure 1.7: ASAR swath designations (ESA, 2007b)

Table 1.3: ASAR Global Monitoring Mode Image product summary, taken directly from ESA's ASAR Product Specifications (ESA, 2007b). Note that *ENL* refers to *Equivalent Number of Looks*(ESA, 2007a)

PRODUCT NAME	ASAR Global Monitoring Mode Image
DESCRIPTION	ASAR product generated from data collected when the instrument is in global monitoring mode. It is a multi-look coarse resolution image.
APPLICATIONS	It is for users wishing to perform applications-oriented analysis of large scale phenomena, where high resolution is not needed.
COVERAGE	Up to 400 km across track by up to 40000 km along track.
THROUGHPUT	1 product per orbit
PRODUCT SIZE	Stripline Max: 139 MB (80000 MDSRs $\times$ (850 samples $\times$ 2 bytes/sample + 17 bytes header)). Extracted Scene Max: 1.40 MB (800 MDSRs).

Continued on next page...

Table 1.3: ASAR Global Monitoring Mode Image product summary (contd.)

	Totals include all aux. data.
GEOMETRIC SAMPLING	pixel spacing 500 m by 500 m
GEOMETRIC RESOLUTION	approximately 1000 in ground range by 1000 m in azimuth
GEOMETRIC ACCURACY	absolute location accuracy: 1000m + orbit data error
RADIOMETRIC RESOLUTION	Product ENL > 15 (TBC); Rad. resolution = $10 \log(1 + \frac{1}{\sqrt{ENL}})$
AUXILIARY DATA INCLUDED	Orbit State Vectors, Time correlation parameters, Main Processing Parameters ADS, Doppler Centroid ADS, Chirp ADS, Antenna Elevation, Pattern ADS, Geolocation Grid ADS, PQS ADS.
ALGORITHMS USED	data decompression; raw data correction; replica construction and power estimation; calibration pulse processing; antenna elevation gain function calculation; noise power estimation; image formation (SPECAN); geolocation.
NOTES	Produced systematically from the GM Level 0 product. The product covers a continuous area along the imaging swath. User extracts child product of region of interest, subject to minimum scene size

The ASAR instrument operates at a wavelength of 5.6cm (C-band), potentially with HH or VV polarisation. All GM data covering the Australian mainland acquired to date has used HH polarisation.

1.3 Methodological challenges with radar data

1.3.1 Speckle

As with all measurement processes using coherent radiation (e.g. Pathe *et al.* (2009)), GM data suffers noise in the form of *speckle*, resulting from additive and subtractive interference processes. Although the worst of this is removed by averaging over 7–9 equivalent numbers of looks (ENL) (ESA, 2007a), further filtering is generally required. There are many tried and tested spatial filters used to mitigate the effects of speckle, possibly the most popular of which is the Lee Adaptive filter (Henderson & Lewis, 2008).

Essentially all spatial filters are identifying a pixel as speckle by some criterion based on its variation from its neighbourhood. They are then adjusting the value of this pixel, again, according to some function of the values of the neighbourhood. This function may simply be an average—though the median is often used (Bourgeau-Chavez *et al.*, 2001), as this ensures that the value used belongs to the domain of actual values received.

1.3.2 Temporal resolution

The importance of adequate temporal frequency of data in respect of the monitoring of inundation dynamics has been touched upon in the introduction and elsewhere. Oberstadler *et al.* (1997) express frustration at the time taken to access data when a flood event has occurred, a sentiment agreed with by Sanyal & Lu (2004). Rosenqvist *et al.* (2002) consider adequate time series of data to be the "prime factor" governing the reliability and accuracy of flood models. Limitations of single frequency images are identified by Parmuchi *et al.* (2002), who also anticipate the emergence of greater availability of multi-temporal data and some of its possibilities.

When considering a particular region over a period of time, for which multi-temporal data of high frequency is available, there exists the opportunity to establish parameters which are very specific to each square kilometre of the region by analysing data taken at varying incidence angles and at various times under different environmental conditions.

1.3.3 Spatial resolution

Most applications of radar remote sensing would benefit from data with as high a spatial resolution as possible, but this must be played off against constraints in terms of data transfer practicality, storage and processing time. Increasingly, data storage and processing time become less of an issue. This review is concerned with the use of GM data, which has a nominal spatial resolution of 1km. The constraint that this imposes is fairly straightforward, but the consequences may be more complex. Certainly, the ability to derive details about the environment within a pixel is reduced, thus increasing the requirement for more auxiliary data against which to analyse the radar signal.

The obvious limitation of coarse resolution data is the minimum scale at which classes can be distinguished. With multi-temporal data, this can be mitigated to a limited extent for structures that are stable over a long period, which can be discriminated by temporal averaging at a finer resolution—an example of this may be seen in figure 1.8, which shows a mean of many GM images over Cape York at a resolution of 16" ($\approx 500m$).

However, for the purposes of analysis, the minimum size for a homogeneous class such as a river channel to be discernible will be a function of pixel size and the contrast between the backscatter value of the interfacing classes we wish to separate. The following section will have some bearing on the minimum discernible features.

1.3.4 Ambiguity of response

Simplistically, if water presents itself with a low backscatter value, and dry land with a high value then a mid-range value will tell us we have some of both within a pixel, and the actual value may give us an indication of the proportion of each. Further to this, if we know the terrain precisely, we may know the pattern adopted by the rising stage of water and in theory could even predict the extents within the pixel. Unfortunately we are not looking at a region that is made up of water and dry homogeneous land.

During a flood, in fact, the high moisture content of the surrounding soil will result in an increased backscatter (e.g. Pope *et al.* (1997)). The flooded area itself

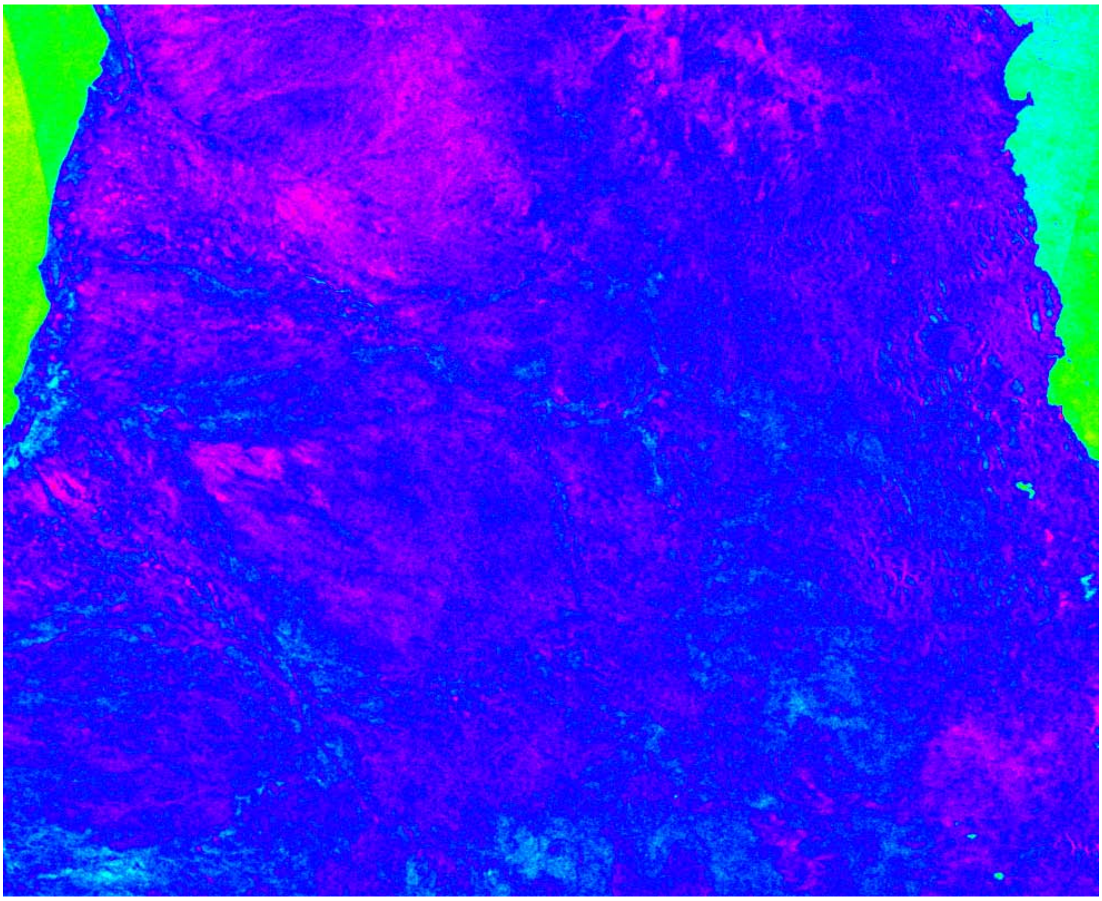

Figure 1.8: Southern Cape York Peninsula: Mean of 12 GM images in 2009

may also be returning an almost lossless signal due to dihedral scattering from the interaction of water with emergent vegetation, as discussed in section 1.2.2.1. Some researchers approach the complexity introduced by vegetation by masking it out (Bonn & Dixon, 2005). However, many wetlands and floodplains are covered with aquatic vegetation, which renders this approach counter-productive.

Therefore, having detailed vegetation mapping which takes into account the type and structure of the vegetation, allowing us to predict its response, and its corresponding contribution to the received signal, is important. There are various ways to do this. Bracaglia *et al.* (1995) develop an electromagnetic model for the analysis of crops using radiative transfer theory and matrix doubling. Grings *et al.* (2009) adapt this model for a technique to monitor flooded marshes, using cylinders and discs to model different species. The role of vegetation is not a static one, as it is dynamic in both spatial extent and in size, and the emergence of vegetation and differential leaf geometry in different seasons can lead to a different (and, in fact, opposite) response (Bartsch *et al.*, 2009).

Data in known conditions, together with empirical data, may allow us to establish a baseline with which to analyse backscatter during periods of inundation, enabling the pixel values to be inverted and to derive a measure of the extent of inundation. Knowing the degree of effects such as dihedral scattering is important. There seems to be a minimum scale of vegetation for which the phenomenon occurs—Pope *et al.* (1997) tell us that during their study of marshes, this effect was only observed with C-band HH data in tall marshes with less than one third spatial coverage. Henderson & Lewis (2008) tell us of the interaction between specular reflection, volume scattering and dihedral scattering, and that the ratio between them changes as the water level varies. Martinez *et al.* (2001) observe peaks in backscatter from regrowth interaction with water in marshland. Bartsch *et al.* (2009) find that inundated areas with emergent vegetation are difficult to distinguish from areas of soil with a high moisture content.

The effect of wind on water has been discussed. Parmuchi *et al.* (2002) observe large variations in water response even with low wind conditions, whereas Wilson & Rashid (2005) experience near perfect (specular) reflection from water in the absence of wind. The fact that wind does effect the ability to distinguish water is a problem discussed by various researchers (Hostache *et al.*, 2009a; Sanyal & Lu, 2004; Töyrä *et al.*, 2001). Mitigation of this problem can, apparently, only come by recording wind conditions (and direction—equation 1.7 on page 21 refers) against all data. Additionally, we may consider our choice of incidence angle from the available data during times of strong wind conditions. Töyrä & Pietroniro (2005) point out that higher incidence angles provide data that is less subject to this effect. A good visual example of the effects of certain wind conditions on the radar response from water can be seen in Figure 3.11, later in Chapter 3.

Of course, having discussed only those ambiguities which are peculiar to radar data, we must also consider the simple fact that many different responders produce a similar brightness value or DN value for any single-band electromagnetic sensor.

It is felt that the uncertainties inherent in this evaluation of radar data should form an integral part of the segmentation analysis when seeking the demarcation of water. Binary decisions early in the process propagate and magnify errors through to the final output. This project seeks to improve accuracy over single-image thresholds, by effectively adding data channels using displacements in respect of *time* and of *incidence angle*.

Multi-temporal data lends itself well to classification based on decision tree analysis, examples of which will be dealt with in section 1.4.2. Such an approach allows for a series of logical steps, each of which may involve different evaluation techniques.

1.3.5 Local incidence angle

ESA's *ASAR Product Handbook* identifies the potential of high incidence angles and HH polarisation to map flooding, but concedes that *"Combined use of images acquired with different incidence angles poses a new set of challenges"* (ESA, 2007a).

The theoretical relationship between backscatter and local angle of incidence was covered in section 1.4.1.5. The main consideration is, in fact, that the local incidence angle is not known, and when dealing with pixel sizes of 500m, the aggregate contribution of all of the structural orientations within a pixel would be too complex to calculate, even with an accurate DEM, as the effects of radar shadow, foreshortening, layover (section 1.2.1.1 refers) and corner reflection etc. would vary in relation to each other with the changing look angle.

GM data gives us the time series capability that allows us to establish the relationship between local incidence angle and relative backscatter by observation. An example of this process using GM data is given to us by Sabel *et al.* (2008) in their investigation into the detection of surface soil moisture in Australia. In this case, the full time series was used to fit a function to the incidence angle and then the data was normalised to an angle of 30°. This was modelled on a linear fit, as described by Pathe *et al.* (2009), who demonstrated the relationship between backscatter and local incidence angle determined using a scatterometer in the Grasslands of Oklahoma—their plot is reproduced in figure 1.9. The two vertical lines in the plot highlight the region used in GM data, and demonstrate the suitability of a linear approximation under these conditions (Pathe *et al.*, 2009).

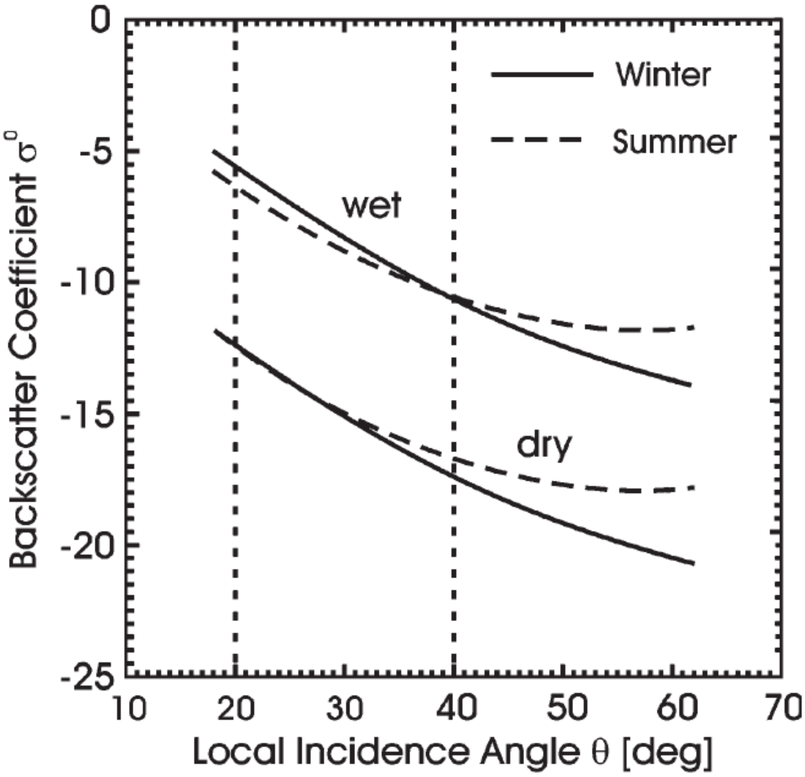

Figure 1.9: Dry and wet backscatter reference curves for winter conditions with minimum vegetation cover and summer with maximum vegetation cover (Pathe *et al.*, 2009).

There is an approximate 50% split between data taken from an ascending orbit and from a descending orbit. Backscatter values from an area taken from the same look angle but opposing directions may, where structural components of the backscatter are significant, bear little relationship to each other. However, the flat nature inherent in floodplains and open water make orbit direction less consequential for these cases.

The varied incidence angles used in GM data provide an opportunity to better distinguish water from land. Ahmed (2006), for example, uses local incidence angle as part of the classification process, and Töyrä & Pietroniro (2005) describe the use of the low incidence angle Radarsat S1 data with the high incidence angle S7 data to obtain a *"significant increase"* in the classification of open water.

Certainly the experimentation with images having a close temporal proximity but having different incidence angles is worthy of pursuit.

1.3.6 Data acquisition

One of the strengths of GM data is the fact that it is generated systematically and made available over the Internet very easily. The process requires a *Category-1 fast registration* with the European Space Agency through its *Earth Observation Principal Investigator Portal* (ESA, 2009a). Data is downloaded directly from one of two processing stations, at Kiruna in Sweden (ascending orbits) and at the ESA Centre for Earth Observation (ESRIN), at Frascati in Italy (descending orbits). Other satellite data is available from ESA and other space agencies through the submission of project proposals.

In order to make full use of the abundance of GM data available globally, it will be necessary to consider the software and hardware required to download and process a high volume of such data.

1.4 Data analysis

1.4.1 Preprocessing

1.4.1.1 Despeckling

The occurrence and cause of speckle have been discussed in section 1.3.1. When confronting its mitigation there are several options to consider. Firstly is the type of filter. In the broadest terms, and in respect specifically of GM data, averaging or sampling can take place spatially or temporally. For each of these there are then many choices of method. Whether applying a single filter, or a combination of filters, there is also sequence and staging to consider.

There are some good reasons to consider despeckling measures prior to the georectification process. The grid axes of the raw data bear a direct relationship to the azimuth direction and therefore the planar axes parallel and orthogonal to the incidence angle. If any terrain corrections due to orientation are to be taken into account, then maintaining this relationship would be a distinct advantage.

Despeckling would necessarily need to take place prior to such corrections. Also, as speckle is largely the result of interference due to the coherence of the electromagnetic waves (Pathe *et al.*, 2009), analysis using, for example, wavelets (Amirmazlaghani *et al.*, 2009) would benefit from knowledge of the emission angles. Finally, applying despeckling measures prior to the interpolation process necessary for georectification would avoid "contaminating" any neighbouring pixels with the erroneous speckle value. Practically speaking, only spatial filters may be applied prior to georectification, as the latter process is what ties the temporal snapshots together.

Notwithstanding such arguments in favour of despeckling prior to georectification, there is also a strong reason to leave this process until after orthorectification. This is due to the fact that, as will be seen later in Section 2.2.2, terrain effects (foreshortening, for example) can cause backscatter values from several locations to be added to a single pixel, where the terrain causes the *slant range* distances to differ less than a critical amount, depending on the resolution. For example, using GM data, taking a central look angle of 30°, and assuming a satellite height of 800km, a difference in elevation of adjacent pixels of around 300m would cause the entire value of a pixel to be added to that of its neighbour. Lesser elevation differences incur value transfers to lesser degrees, but they occur nonetheless. Speckle filters seek to "iron out" contrasting pixel values such as would be created by this effect. Thus, if orthorectification, which reverses the terrain effect described, were carried out after despeckling, then we could end up with artificially low, or even negative, pixel values as a result.

Choice of spatial filter can be done in a testing phase. There is much information available on other comparisons of filters for different purposes, from which to draw. Henderson & Lewis (2008), for example, describe a test involving 18 spatial despeckling filters which found that the Lee Sigma filter, with three iterations of different window sizes, increased the accuracy of brackish marsh detection from 79% to 95%.

It is envisaged that the processing required to combat other distorting effects will involve raster algebra with more than one data file. This, in itself, must have an averaging effect which can only serve to diminish outlying values. Also, a strong contender as a despeckling approach, as we are intending ultimately to produce a binary determination of whether a pixel does or does not represent flood waters, would be a post-classification clustering algorithm, which accounts for texture rather than individual value; alternatively, a simple modal filter would be appropriate.

1.4.1.2 Georeferencing

The geolocation of GM data makes use of the *Geolocation Grid* which is included within Annotation Data Set Record (ADSR) of the binary data file. This grid includes the incidence angle and a geodetic latitude and longitude for a number of data points throughout the image. These data points occur at a nominal distance of 40km in azimuth, and at 11 locations across the swath, the spacing of which depends on the incidence angle (ESA, 2007a). Typical root-mean-square (RMS) errors, in the third-order polynomial fit used in the georeferencing process during this research, were calculated at around 0.16 pixels ($\approx 80m$). The corresponding incidence angles, which are the calculated incidence angles with respect to the WGS84 ellipsoid (ESA, 2004), are required for further processing.

1.4.1.3 Orthorectification

Orthorectification serves to minimise the geometric distortions in an image caused by terrain. Methods specific to ScanSAR images are documented (Low & Mauser, 2003). The fact that the terrain under investigation (flood plains) is usually flat means that relative distortion and therefore displacement will be minimum. Bartsch *et al.* (2009) orthorectify GM data over flat terrain using GTOPO30 data. Open source software, the *NEXT ESA SAR Toolbox*, which is being developed on ESA's behalf (Array S. C. Inc., 2009), will orthorectify GM data (amongst many others), and will download SRTM3 DEM data automatically in the process. The software also includes speckle filtering and many analysis tools.

In the case where it is intended to download and pre-process all GM data systematically, benefits of an alternative means to orthorectify must be considered. In order for data to be registered, as will be discussed in the next section, bespoke scripts are used to extract header information from the data files. Querying the data files in this way using an abstraction layer from the Geospatial Data

Abstraction Library (GDAL)[1], gives us all the information we need to carry out the orthorectification ourselves, giving us control over the whole process. Using open-source programming languages such as Perl[2] or C++[3], could allow us to run our scripts on the university's High Performance Computer (HPC), allowing us to take advantage of high-speed parallel processing capabilities. To this end, the scripts will need to be written with multi-threading in mind.

1.4.1.4 Database registration

The binary GM data files contain a header in text format. From this header, much salient details of the file can be extracted prior to any further processing, and fed through to a database. This data includes corner coordinates which allow the image outlines to be mapped without any georectification (which were used, for example, for the production of figure 1.1 on page 13), and this, together with other information, allow the efficient selection of data for further analysis prior to full processing. The data file may then be temporally co-registered with other data such as wind, rainfall and other remotely sensed data to build an environmental context for analysis.

1.4.1.5 Sigma-nought versus beta-nought

Most satellite radar data comes with DN values which are a function of radar brightness β. Conversion of GM data to β involves squaring the DN and dividing by a calibration constant. Most analysis of radar data converts the raw DN values to the coefficient of backscatter, σ^0, which involves further multiplication by the sine of the local incidence angle of the transmitted signal to the surface reflecting it. This common approach is questioned (and answered) by Raney *et al.* (1994) in their article entitled "Plea for radar brightness", and by others (David *et al.*, 1998). By way of clarification, it is first necessary to examine exactly what the GM data pixel values (DN) represent.

The ASAR sensor on board the satellite is able to measure, in raw terms, power. Knowing the angle from which the power is received and the distance it

[1]http://www.gdal.org
[2]http://www.perl.org
[3]http://www.cplusplus.com

has travelled, the system uses an algorithm to estimate the incidence angle (based on the WGS84 ellipsoid) and attribute this power to an area, giving a measure of power per unit area (called, in most fields, *intensity*, though this term has some ambiguity, as shall be seen). Knowing the dimensions of the receiving antenna and (approximately) the relative displacements of the satellite and the scatterer, allows the determination of the solid angle over which the backscattered radiation is received, giving a measure of the power per unit area (of the backscatterer) per unit solid angle (or steradian). This, in radar terms, is also sometimes called intensity (Woodhouse, 2006), but from here on shall be called *brightness*, which has units $Wm^{-2}sr^{-1}$.

As mentioned, most articles using radar remote sensing for some sort of classification refer to backscatter values in terms of the *normalised radar backscatter coefficient*, σ^0, usually converted to decibels. This is due to the fact that, in order to describe the backscatter response of a feature, a quantity which is independent of the sensor is sought. σ^0 is derived from the *radar cross-section*, σ, where

$$\sigma = \frac{I_{received}}{I_{incident}} \cdot 4\pi R^2 \tag{1.8}$$

where, I is the intensity in the classical sense of power per unit area (Woodhouse, 2006). σ has units m^2. However, as a greater incidence angle θ causes the power to be spread over a larger area, σ is dependent on θ. This gives rise to σ^0, which is the radar cross-section per unit ground area, or

$$\sigma^0 = \frac{\sigma}{A} \tag{1.9}$$

(Woodhouse, 2006). This makes σ^0 dimensionless. ESA's ASAR calibration guidelines (ESA, 2004) tell us that DN, β^0 and σ^0 are related by

$$DN^2 = C \cdot \beta^0 = K \cdot \frac{\sigma^0}{\sin\alpha} \tag{1.10}$$

where C is some constant and K is known as the *absolute calibration constant.* K is described as being

> "...processor and product type dependent, and might change be-

tween different beams for the same product type" (ESA, 2004).

For the GM data in this study, it has been found that K has had the same value throughout (2.19×10^7), although the preprocessing script has been designed to extract the value from each individual file during every calibration.

For a volume scatterer, as α increases, the incident power is distributed over a larger area (Woodhouse, 2006), making σ^0 a function of $\cos\alpha$. To take this into account, it therefore may become more convenient to talk in terms of γ (or the *range independent backscatter coefficient* (Shimada, 2010a)), such that

$$\gamma = \frac{\sigma^0}{\cos\alpha} \tag{1.11}$$

However, it must be understood (and indeed it is pointed out in the guidelines (ESA, 2004)) that α is the *local* incidence angle, which is not usually known. In fact, the derivations of γ and σ^0 above assume *volume scatterers* and a flattish, smooth surface (based on the WGS84 ellipsoid). Water, being largely a specular reflector as discussed, and wet surfaces, are more greatly effected by varying incidence angle, as shall be seen. Also, as pointed out by Raney *et al.* (1994) and David *et al.* (1998), the actual incidence angle is not one angle, but rather a complex quality made up of all of the orientations of structural components within a pixel. This is especially true when considering what was discussed in section 1.3.5, that scatterers will respond differently in an ascending orbit and a descending one due to irregular structural orientation (effectively making the real incidence angles different, where the nominal ones are the same).

Therefore the DN (or perhaps β^0, simply reversing the output scaling operation (Parmuchi *et al.*, 2002)), should be taken on its own merits, and processed according to the intention of the analysis, rather than being automatically converted to an erroneous σ^0.

In fact, the effects of incidence angle are greater than the gamma conversion in equation 1.11 accounts for. This fact is illustrated in figure 1.10.

Baghdadi *et al.* (2001), in their evaluation of C-band SAR data for mapping

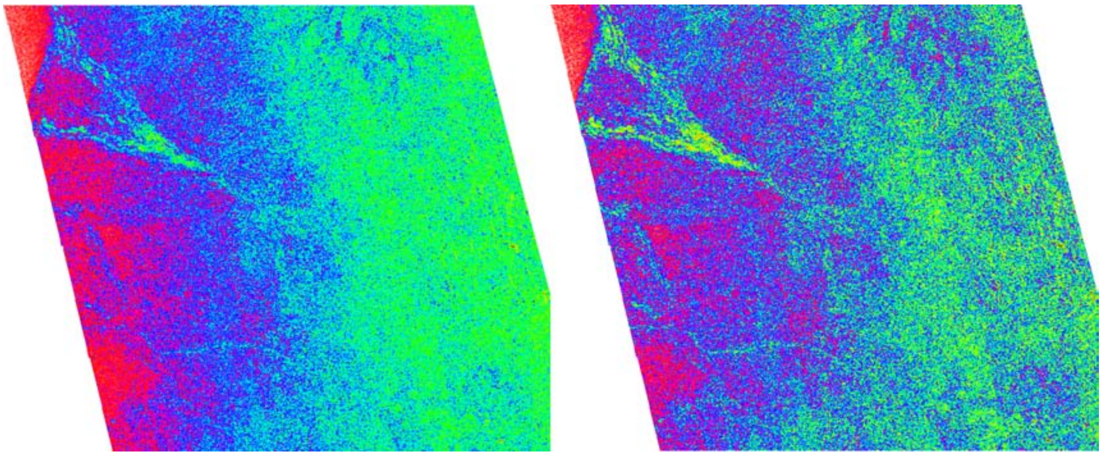

Figure 1.10: Two GM data images of the Mitchell catchment using GM data. The first has undergone a conversion to σ^0 using equation 1.10, and the second to γ using equation 1.11. It is clear that the effects of the geodetic "local" incidence angles have not yet been fully factored out, as viewed by the tendency for higher values (seen here in red) on one side of the swath.

wetlands, normalise σ^0 using a function $F(\alpha)$ where

$$\sigma_n^0 = \frac{\sigma_\alpha^0}{F(\alpha)} \tag{1.12}$$

where $F(\alpha)$ is the mean angular dependence for a given date and given polarisation. This is shown as a cosine function, which for HH typically $\approx \cos^{2.5}\alpha$. Baghdadi *et al.* (2001) derive this function by assuming the relationship

$$\sigma_\alpha^0 \approx \sigma_n^0 \cos^\psi \alpha \tag{1.13}$$

(adapted from Ulaby *et al.* (1982)), where ψ is the slope of the linear fit of σ^0(dB) against $10\log(\cos\alpha)$ (Baghdadi *et al.*, 2001).

Pathe *et al.* (2009) model radar backscatter as a function of incidence angle, soil moisture and time, where

$$\sigma^0(\theta, t) = \sigma_{dry}^0(30) + \beta(\theta - 30) + Sm_s(t) \tag{1.14}$$

where m_s is the relative soil moisture content and $S(t)$ the sensitivity of the radar backscatter to relative soil moisture changes at time t. Note that Pathe *et al.* (2009) assume a linear change with respect to incidence angle θ, which varies only between 20° and 40°. Sensitivity S for each 30' tile is estimated as

$$S = \sigma^0_{wet}(30) - \sigma^0_{dry}(30) \tag{1.15}$$

Wet and dry references are established through time series analysis.

The research following this review will seek to fit a function similar to that in equation 1.13 to observed values in the time series. As a single region is being examined, it is felt that rather then attempting to fit one parameter across the (heterogeneous) area, parameters specific to subregions of a few pixels can be mapped and applied more discriminatingly.

Further, much analysis will be on the basis of change detection, in which case the operative values are relative to a subregion or pixel, and normalising becomes unnecessary. Here even using the linear DN values are an option, eliminating some steps in the preprocessing of data, an approach adopted by, for example, Rosenqvist *et al.* (2002) when modelling inundation patterns in the Amazon, and as advocated by Raney *et al.* (1994) and David *et al.* (1998).

1.4.2 Classification

Radar images, with essentially a single band, do not allow the same comparison of signatures of different responders at different wavelengths possible with optical and multi-spectral images. However, there are other comparisons which may be made in the same way by choosing different modes of image as channels in place of wave bands. The ASAR product Alternating Polarisation (AP) modes, for example, offer two images taken at the same time, being one of the following combinations: HH–VV, HH–HV, VV–VH (ESA, 2009c). There are techniques to classify single radar images. The most simple of these in the discrimination of water from land is a threshold. Abhyankar *et al.* (2007), for example, recommend a simple threshold of -15dB for this purpose, but point out the problems already discussed, where the presence of waves on the water causes an increase in backscatter value. Hostache *et al.* (2009a) take a less deterministic, more probabilistic approach by classifying in terms of likelihood of values representing flooding. A minimum threshold is established by choosing the lowest backscatter value found in the definite non-flooded regions. Below this threshold, it is assumed that values represent flooding. A maximum threshold is then established by selecting the highest values observed in the non-flooded water bodies (lakes, permanent river channels, etc.). Values above this threshold are assumed to represent non-flooded areas. Values between the thresholds are then classified as *potentially flooded* (Parmuchi *et al.*, 2002). Outliers would need to be taken into consideration with this approach, and in the case of strong winds, for example, it might be possible for most of the flooded areas to fall only within the "potentially flooded" classification, making the exercise of limited use.

A common method for classifying single radar images is to take into account textural relationships between pixels. The Grey Level Co-occurrence Matrix model (GLCM), for example, is a two-dimensional histogram of grey levels for a pair of pixels which are separated by a fixed spatial relationship (Antoniol *et al.*, 2005). Various different textural measures are calculated from this histogram, and depend on the choice of window size and pixel displacement. These include *entropy*, a measure of the similarity of values within the local window, *correlation*, a measure of linear dependency of values of neighbouring pixels, and *angular second moment*, a measure of local homogeneity (Antoniol *et al.*, 2005).

Seiler *et al.* (2009) use variance and entropy from an ASAR Image Mode product, together with a Normalised Difference Vegetation Index (NDVI) and Normalised Difference Water Index (NDWI) using ASTER data, to good effect, in deriving eight classes around a flood plain. The improvements found by introducing textural components to the segmentation process are reproduced in figure 1.11.

Töyrä & Pietroniro (2005) note that their GLCM texture analysis increased the accuracy of their classification from 22% with a single Landsat image to 74%, based on a Kappa coefficient (κ) test (section 1.4.4 refers). Arzandeh & Wang (2002) use outputs from a GLCM analysis as channels for the supervised classification of a single Radarsat image. An interesting comparison of the use of different window sizes and the resulting accuracy was carried out (see figure 1.12). Whilst many categories such as swamps and forests seem to be more accurately identified with larger window sizes, water remains with a reasonably constant (and high) level of accuracy, which seems to benefit from smaller window sizes (Arzandeh & Wang, 2002).

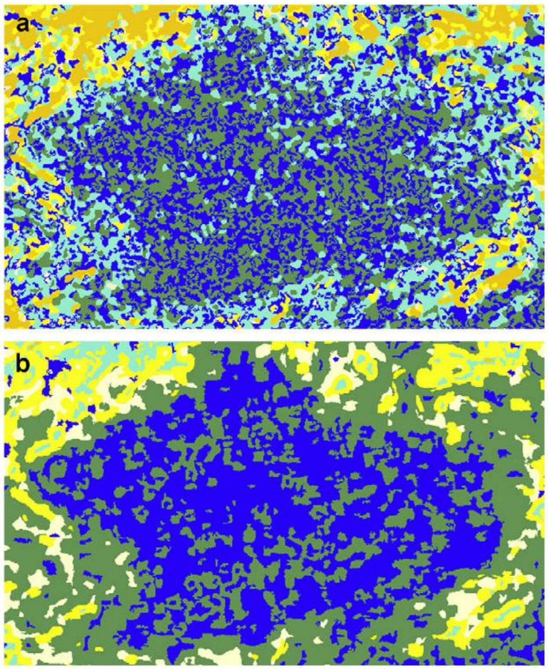

Figure 1.11: Detail of ASAR scene (a) and composite image of ASAR, Variance, Entropy (b) (Seiler *et al.*, 2009).

One classification method which exploits the use of a spectral class model known as a Gaussian mixture distribution is the Sequential Maximum A Posteriori (SMAP) method. The model works by segmenting the image at various scales or resolutions and using the course scale segmentations to guide the finer scale segmentations (Bouman & Shapiro, 2004), and is available with some remote sensing software such as GRASS (GRASS Development Team, 2009).

Grandi *et al.* (2009) use wavelet variance analysis to derive textural signatures from radar data, and in particular use the Fischer Criterion (Grandi *et al.*, 2009) to demonstrate the feasibility of such a tool as a supervised classifier. Among the five methods described by Baldassarre *et al.* (2009) is an active contour model, which uses a region growing algorithm to minimise an energy function which seeks to encircle as many "good" pixels as possible.

The segmentation processes discussed are pertinent to a single radar image. With the benefit of a high frequency time series, classification methods can take into account backscatter responses of an area over a range of environmental conditions and incidence angles, giving a more complex choice of signatures to analyse.

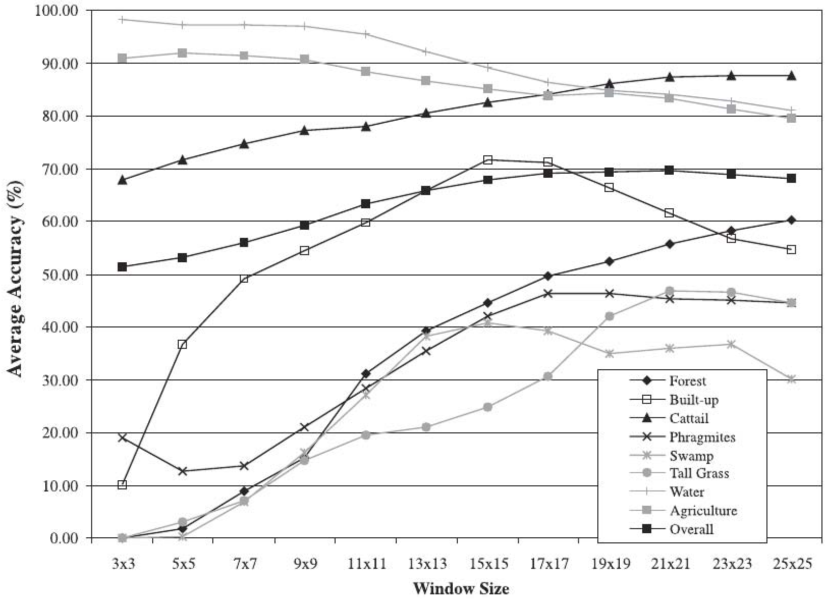

Figure 1.12: Influence of window size on the average overall accuracy of the classification results of texture features for different land cover types (Arzandeh & Wang, 2002)

This offers a much greater potential for accurate classification of a single image, as well as behavioural classification of the whole series. A number of approaches to dealing with this complexity present themselves in the available literature, two of which are Artificial Neural Networking (ANN) (Ahmed, 2006; Quan *et al.*, 2008) and Decision Tree Analysis (DTA) (Baghdadi *et al.*, 2001; Parmuchi *et al.*, 2002). In some cases both approaches are adopted, either together, or for comparison (Zhou *et al.*, 2000).

A good example of a decision tree based on individual thresholds in a hierarchical step-wise process, is reproduced in figure 1.13. It is conceivable that certain decisions may be made, not only on the basis of a cross-image threshold, but also on some pre-classification process, that effectively allows a different threshold for a different geographical location. Also, the threshold can be made dependent on incidence angle, and orbit direction. Any analysis method can be contained within such a decision tree, including an index, for example, such as that combining the response to high and low incidence angles, as used by Töyrä & Pietroniro (2005) and discussed in section 1.3.5. Also discussed in this section was the likely difference between two backscatter signals representing the same

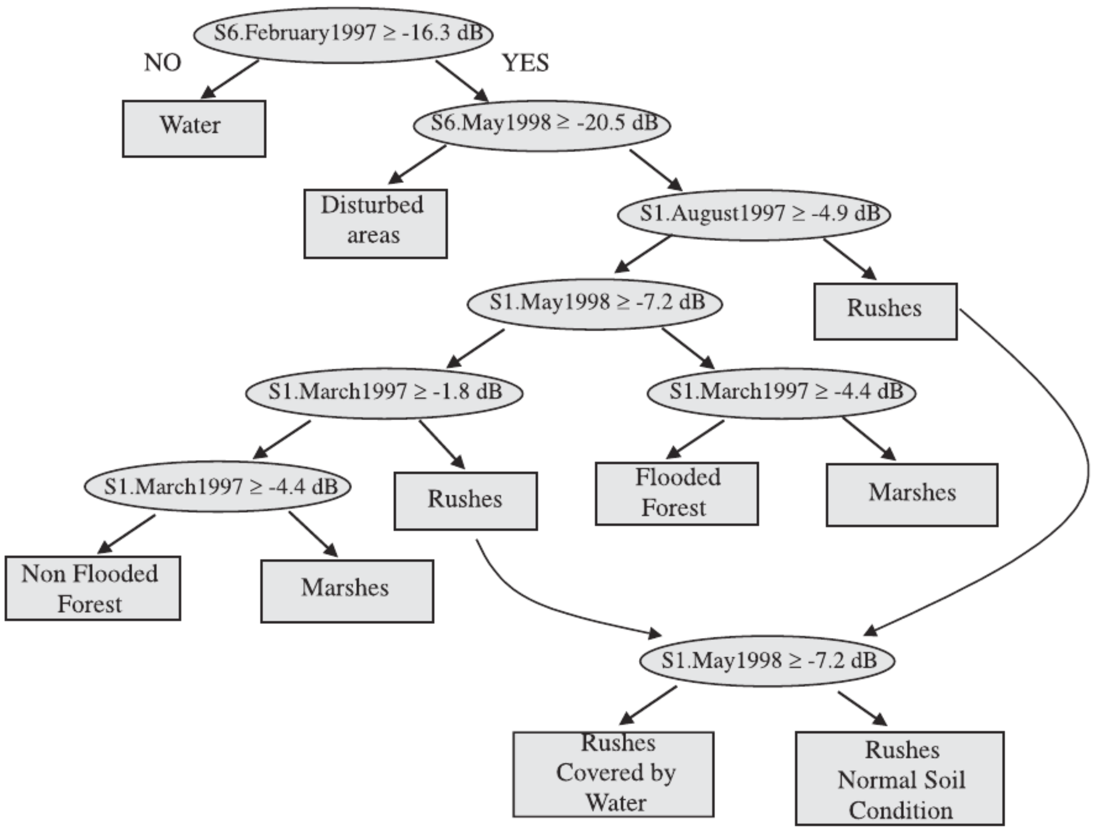

Figure 1.13: Decision tree design from multi-temporal RADARSAT SAR images (Parmuchi *et al.*, 2002)

area with the same angle of incidence, but with opposing orbit directions, due to structural asymmetry. One responder that is structurally closest to the ellipsoid estimation, and thus would suffer less from this effect, is water.

Ahmed (2006) provides a comparison of accuracies for a *K nearest neighbour* analysis and that of an artificial neural network (ANN) in the classification of land cover, including water. Overall it is determined that the ANN provides the most robust results, with water being well distinguishable using both techniques. Interestingly, temporal comparisons are made only with like incidence angles.

Bourgeau-Chavez *et al.* (2001) describes a semi-automatic hierarchical classification process that uses a cost reduction algorithm to produce an optimal model for classification of, in this case, SIR-C data, in which an accuracy of $\approx 90\%$ is measured for the open water classification.

Oberstadler *et al.* (1997) use the Evidence-Based Interpretation of Satellite images (EBIS) algorithm to perform a supervised classification of water and non-water classes. The classifier is based on the "Dempster–Shafer theory", assigning a pixel to a class based on the relative probability of the value belonging to that class, the probabilities being established for all values in the initial training (or *parametric*) stage, using a multinomial distribution model. The conclusions which were relevant to flood mapping emphasised the fact that the resolution of the ERS-1 data was too coarse for the purpose of flood mapping in Germany, and that temporal frequency was insufficient.

Noernberg *et al.* (1999) use coefficients of variation for different polarisation configurations to discriminate classes, and find open water easily distinguishable in all cases—this is, however, using C-band to a resolution of 6m.

Quan *et al.* (2008) combine Probabilistic Neural Network (PNN) with Multi-scale Auto Regressive (MAR) models to extract multi-scale features of SAR images. The MAR is used to train the PNN. Interestingly, the MAR is a borrowed time-series analysis technique, used here for spatial analysis of the same image. The scale recursion device used in this algorithm seems akin to the SMAP model discussed above. This combination of techniques is interesting, as the scaling method can identify and account for speckle; the method appears to produce particularly good results from homogeneous areas returning heterogeneous values (see figure 1.14).

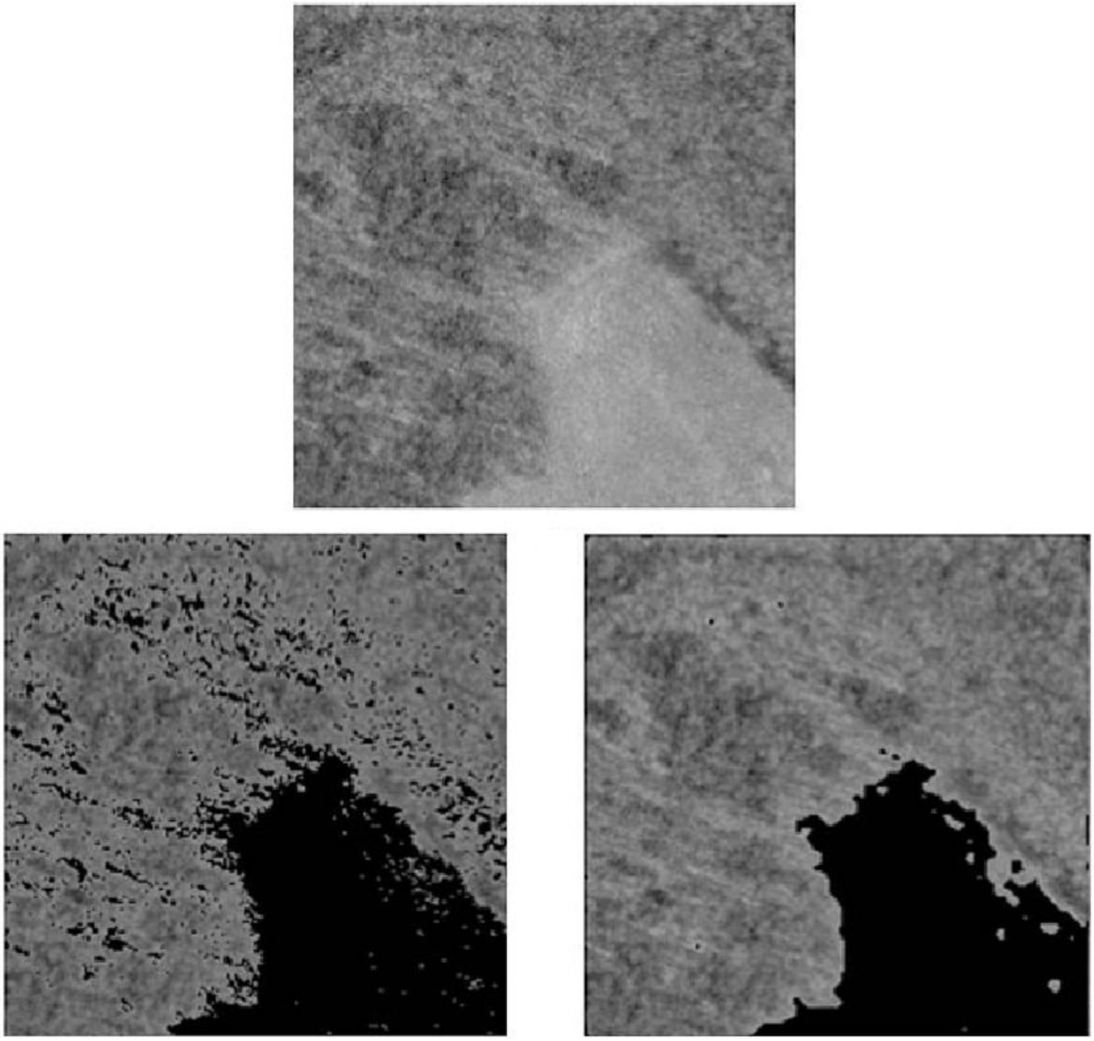

Figure 1.14: (Top) Original SAR image, (left) Segmented image obtained using PNN algorithm and (right) Segmented image obtained using MAR and PNN (Quan *et al.*, 2008)

Parmuchi *et al.* (2002) conclude their research with two findings which fit well with the aims and methodology of the research proposed in this review:

> *"(1) the need for multi-temporal SAR data acquired under different environmental conditions for mapping wetlands, and (2) the advantages and flexibility of physically based reasoning classifiers for synthetic aperture radar (SAR) data classification."* (Parmuchi *et al.*, 2002)

1.4.3 Output

Figure 1.15 shows a basic schematic representation of the processing and output of GM data proposed. The normalisation function $F(DN, K, r, \alpha)$ represents the function derived from the time series data describing the relationship between orbit direction, computed local incidence angle α and the backscatter, together with the reversal of the scaling operation at the sensor, being a function of α and the absolute calibration constant K, as discussed in section 1.4.1.5. Final output might be, for example, single flood extent maps, relative soil moisture maps, or flood duration maps (Rosenqvist *et al.*, 2002). An important compliment to such data will be a measure of their accuracy.

1.4.4 Analysis of accuracy

Each stage of processing changes values or assigns categories based on assumptions, and the magnitude of error of each stage should be considered independently.

The GM data itself is understood to have a radiometric accuracy of 1.2dB (Pathe *et al.*, 2009; Sabel *et al.*, 2008). As stated previously, georectification and orthorectification are expected to contribute low spatial errors in the case of GM data in flood plains (see sections 1.4.1.2 and 1.4.1.3).

For automated classification processes involving training areas, pixels within the training areas may be randomly assigned to either training or testing, following classification (Bourgeau-Chavez *et al.*, 2001). A common method of analysis against a known accurate classification is the use of error matrices, where differ-

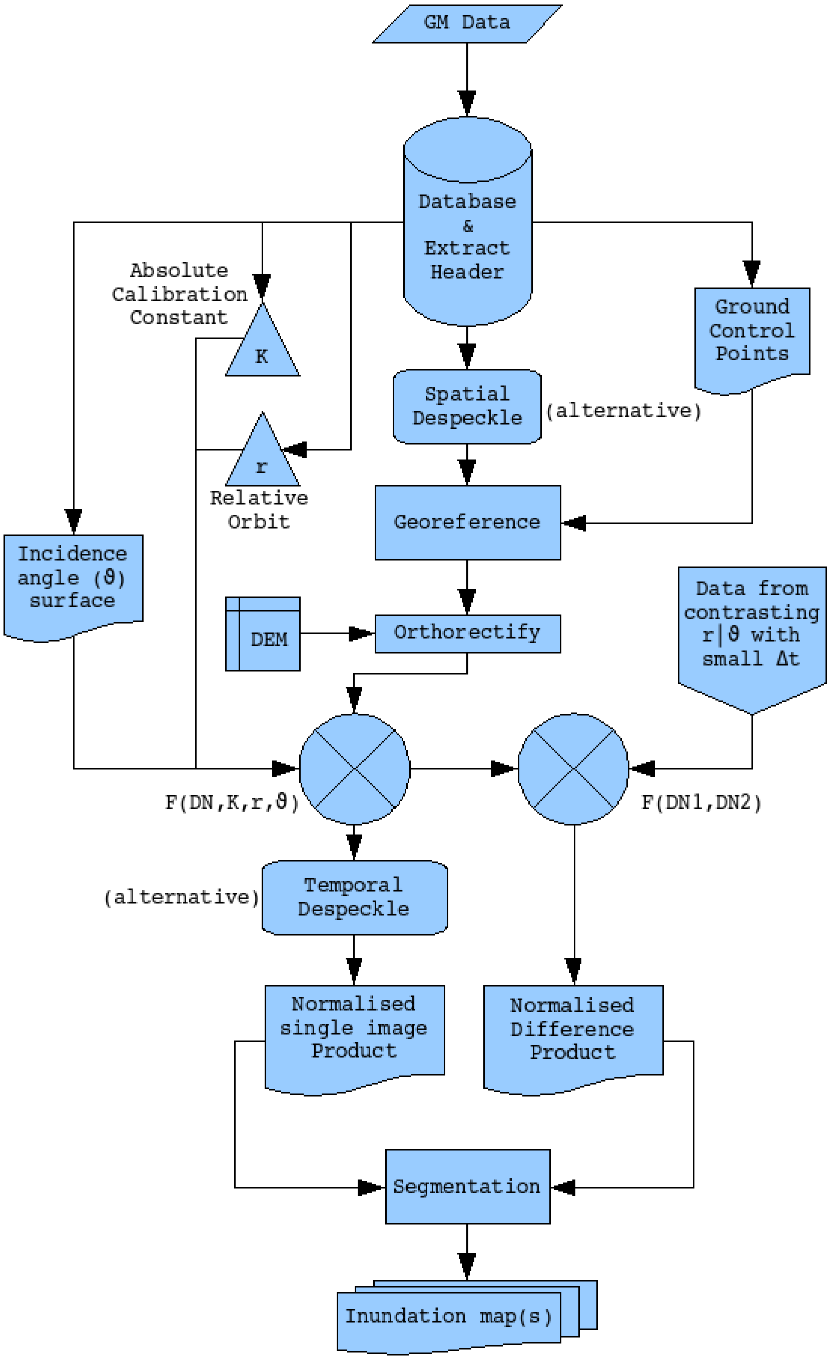

Figure 1.15: Flow diagram outlining one possible processing sequence using methods discussed

ences are quantified by the kappa coefficient κ (Ahmed, 2006; Arzandeh & Wang, 2002; Töyrä *et al.*, 2001; Waisurasingha *et al.*, 2007), simplified by the estimation $\hat{\kappa}$ as follows (Campbell, 2007):

$$\hat{\kappa} = \frac{\text{observed} - \text{expected}}{1 - \text{expected}} \tag{1.16}$$

As this represents a sample, some researchers go on to test the statistical significance of the results using a z-test (Waisurasingha *et al.*, 2007). In the case of the mapping of inundation (a binary decision), accuracy can be stated in overall terms, or separately in respect of errors of omission (ϵ_o) and commission(ϵ_c) (Rosenqvist *et al.*, 2002).

1.5 Gaps in existing research

Computing power to manage multi-temporal time series analysis

Much research has been done on river systems using radar remote sensing (Bonn & Dixon, 2005; Chandran *et al.*, 2006; Frappart *et al.*, 2005; Waisurasingha *et al.*, 2007; Wilson & Rashid, 2005). However, *multi-temporal* analysis has been confined to a handful of images, perhaps taken in different seasons. Where data needs to be ordered in advance, it is often done post facto, and it is highly unlikely that a pre-flood image will be obtained unless the flood itself is highly predictable. GM data affords us the opportunity to analyse data from a high-frequency time series with near-global coverage, from which data may be drawn hours after a flood event.

The challenges which face any attempt to separate flood water from unflooded areas, as described, are amplified when dealing with such a large dataset, particularly in terms of computing constraints. Ever-increasing advances in data storage capacity and processing speed make the task of managing the computation required to pre-process and analyse GM data feasible. It is, however, a necessary prerequisite for such analysis to set up a robust, automated system that can download, register and pre-process GM data to suit the needs of this research, and that can, preferably, make full use of the HPC distributed network available to researchers at James Cook University. This involves choices of software and languages which are sympathetic to the HPC server environment, with which tasks may be multi-threaded and assigned to some of several hundred processing nodes. Apart from the orthorectification and geolocation operations as described, consideration must be given to our ability to customise the process, to drive the system towards different types of output, depending on the operation being performed. In certain instances, for example, it may not be necessary for the processing of a single data file to result in an individual image output, where the information gleaned from the data is merely required to contribute to an aggregate. In such cases, there exists the opportunity to save on input/output procedures and on memory, making the overall calculation process more efficient. It seems clear that the research to follow would benefit from (and, indeed, may prove to be conditional upon) a bespoke pre-processing set-up which concedes control of each part of the process for the sake of flexibility.

Pixel-specific normalisation for incidence angle

The broad-brush standard for "normalising" for incidence angle effects which are commonly adopted, have been discussed. The limitations in relying on differential measurements across a swath to apply linear corrections to the radiometric value of a pixel include the potential loss of differences due to flooding. The large time series available with GM data allows us to test for localised parameters against previously described models, to use in normalising for incidence angle. This involves calculations for local incidence angle based on a DEM and on satellite coordinates extracted from the data file, and on regression analysis of backscatter against local incidence angle (or functions of these) over the time series. Such calculations therefore build upon the ground-work done in setting up the computational system described above.

The resultant measure of the behaviour of a target area with respect to incidence angle can be correlated with various environmental parameters such as ground cover, regolith and soil types in order to determine the drivers behind particular radar signatures.

Limitations in the use of radar remote sensing due to land cover

Usually, the ground in the region surrounding flood waters has been saturated, by surface flow, by direct rainfall or by flood waters themselves where the level has dropped. For this reason, the backscatter values seen in these areas are usually very high, as characterised by wet soil, contrasting well with the expected low return values from open water. As discussed in Section 1.3.4, a similar high backscatter response is received from areas where vertical structures, such as tree trunks or dense grasses, protrude through the surface of the water, causing dihedral backscattering. For a particular radar data product, at its spatial frequency, wavelength and at a particular incidence angle, there must be environmental conditions such that, as flooding progresses over a certain proportion of a pixel, there will never be sufficient open water to drop the aggregate pixel value significantly enough to detect flooding. This means that there are land cover conditions for which, for example, C-band radar data with 500m pixels could not be used to monitor flooding under (almost) any circumstances. Given the overall objective of this thesis, an understanding of these conditions, in respect of GM data needs to be achieved.

Ambiguity of low backscatter response due to absorption

It may be for the same reason as described above, i.e. that flood waters are usually surrounded by wet soil, that ways to overcome ambiguity due to radar attenuation and absorption by dry soil or sand have not been investigated to any significant degree. The perception of the problem may not have any prominence in the field, as it may not be expected to be a problem at all. However, in a country such as Australia, where we see how heavy rainfall in Queensland causes surface flows between two deserts to flood the Eyre basin in South Australia, hundreds of kilometres away, we can perhaps see this phenomenon more clearly as a potential problem. This is, of course, a potential issue for all rivers running through arid regions, and the question as to whether the advantages brought by radar remote sensing to the mapping of floods can be applied to these cases, in light of this problem, deserves investigation.

1.6 Conclusion

The mapping of inundation using GM data seems, given certain constraints, feasible. The difficulties faced by this task are worth attempting to overcome, due to the benefits that GM data can offer. Indeed, GM data may provide the only means of monitoring large scale inundation and recession which occur very quickly, in hydrological systems which need, increasingly, to be understood. The challenges are complex. Firstly, given the coarse spatial resolution of GM data, its use is limited to large flood plains with continuous coverage of a few square kilometres at least. In fact, it is the large, flat, quickly-changing flood plains that benefit most from the use of GM data, due to difficult timely access to gather data from the ground. Secondly, it is important that the effects on radar response of parameters such as local terrain, vegetation, soil moisture and incidence angle are understood, so as to be able to interpret the radar data to a known and sufficient degree of accuracy. It is envisaged that the opportunity to compare signal responses from an area using two or more incidence angles in very close temporal proximity will allow the segmentation of water to a degree not possible from a single angle. Also, there are opportunities to take advantage of the high temporal frequency of GM data to explore different segmentation methods beyond simple thresholding of single radar images. More specifically, the following questions arise from this review:

1.6.1 Research questions

1. How does radar backscatter vary with incidence angle for different surface conditions? How does this affect the segmentation of open water?

2. Under what vegetation conditions (vegetation type, size, density, orientation) does multihedral backscatter distort the radar signal so as to make flood water indistinguishable from its surroundings?

3. How can we separate dry soil/sand from floods through arid regions? How significant is this problem?

4. How can the processing of such a large dataset be managed? How can we

automate the download, registration and orthorectification of a high volume of GM data files to allow efficient analysis?

These questions represent the primary thrust of what is to follow. If we can answer them to some degree of success, then the contribution of this thesis will be the demonstration that GM data, and its foreseen successors, can be counted as valuable tools with which to map large floods, crucially within a time-frame in which immediate action may be taken to assist the many people whose lives may be affected. Any contribution to such a cause, however small, must surely be significant.

Chapter 2

Practical high volume preprocessing of Envisat ASAR Global Monitoring Mode data over a distributed network

Chapter context

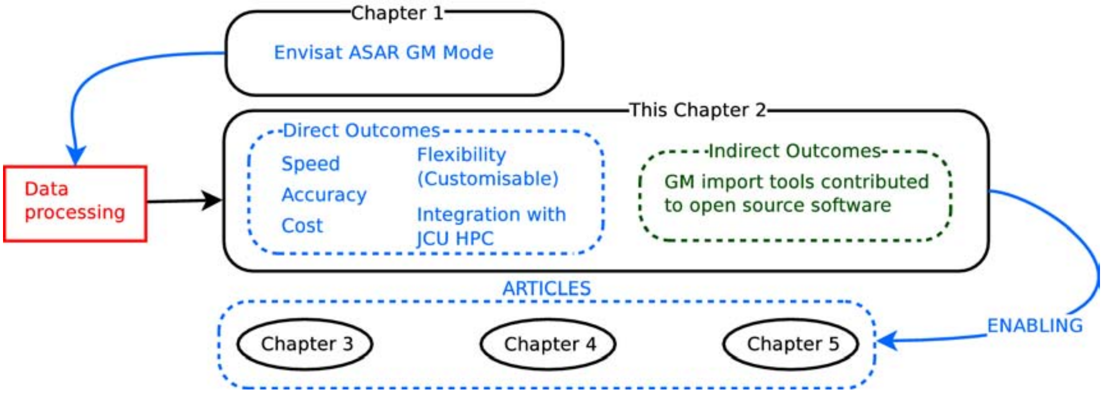

Abstract

A means to pre-process a large volume of Envisat ASAR Global Monitoring Mode (GM) radar data, using open source software and abstraction layers, is described. The preprocessing includes orthorectification, in which case the Digital Elevation Model (DEM) is projected into the local frame of reference of the data file and header parameters are extracted, to calculate the local incidence angle and to make along-swath adjustments against terrain displacement effects.

The objective is to develop a practical method to pre-process GM data using the tools available on James Cook University's High Performance Computing facility. The method allows for control throughout the whole preprocessing stage, so that adjustments can be made early on to eliminate unnecessary calculations in cases where, for example, parameters may be factored out, to avoid undue overhead. Spatial accuracy tests well against alternative software. Tools to extract and interpolate tie-point coordinates, incidence angles and slant-range times into Grass ASCII data files from GM data files will be made available for contribution to the GRASS GIS development community.

2.1 Introduction

From the inception of Geographic Information Systems several decades ago, advances in GIS and remote sensing instrumentation and methodologies have run concurrently with increasing computation and data storage capabilities required to take advantage of the expanding field. Satellite radar data has been widely recognised as having an important role in the application of remote sensing, due largely to its independence from solar radiation and for its abilities to penetrate cloud cover (Alsdorf *et al.*, 2007; Badji & Dautrebande, 1997; Leblanc *et al.*, 2011). Within the Radar field, ScanSAR technology has allowed increased temporal frequency of radar coverage, enabling its use to track rapid events such as floods, where the use of other data is precluded by the presence of cloud (Baup *et al.*, 2007), and has provided temporally denser time series data sets, increasing the scope of methods available for, for example, temporal speckle filters (Ciuc *et al.*, 2001; Trouvé *et al.*, 2003), and change detection (Colesanti & Wasowski, 2006; Quegan *et al.*, 2000).

This increase in data volume requires increased computing capacity to meet preprocessing requirements. Radar data, for example, commonly requires georectification, terrain correction and usually some form of recoding or normalisation, together with some form of spatial filtering to reduce effects such as speckle. Prior to the recent demise of Envisat (see Section 6.2.1 towards the end of this thesis), GM data was made available in near real-time for download to parties with at least a Category-1 fast-track agreement with ESA. The data was available quickly because it was preprocessed at the sensor, before being transmitted down to one of two ground stations in Europe. This was made possible by keeping file sizes and processing requirements low, by using a coarse resolution (pixel size: 500m, spatial resolution: 1km) (ESA, 2007b). The main use to which GM data was perceived to be put was the monitoring of large-scale changes in polar ice extents, with ice and open water having readily distinguishable backscatter characteristics (Zink *et al.*, 2001), but the frequency of coverage of GM data (see Table 2.1) extend the possibilities to other variables such as soil moisture (Pathe *et al.*, 2009) and flood extents (O'Grady *et al.*, 2011).

Latitude (+/-)	0°	45°	60°	70°
Frequency	5	7	11	16

Table 2.1: Average revisit frequency capability per 35-day orbit cycle as a function of latitude, for descending orbit path only (ESA, 2007a)

There are a couple of software tools available to preprocess GM data, such as *NEST* (Next ESA SAR Toolbox) and *BEAM* (Basic ERS & Envisat (A) ATSR and Meris Toolbox) as made available for download by ESA via their website[1]. Partly in recognition of the access and computing requirements for the near real-time processing of large data sets, ESA has developed a web-accessible grid environment called Earth Observation Grid Processing On Demand (G-POD), which gives fast access to data and computing resources and allows verification of algorithms (Cossu *et al.*, 2009). However, as our analysis requires a greater control over the georectification and terrain correction process, and as a high volume of data is required to be transferred, it was considered beneficial to write bespoke

[1] https://earth.esa.int/web/guest/pi-community/toolboxes

code to handle the process (e.g. Rees & Steel (2001)). This chapter outlines a practical method of preprocessing large volumes of GM data, employing parallel processing over James Cook University's (JCU) high performance network using open-source software and part procedural, part object-oriented code.

2.2 Theory

2.2.1 Theoretical basis

The adopted algorithms adjust for range shifts and ignore azimuth shifts. The consequences of this are tested against the results of tools provided by ESA, using data files covering areas of mixed topography. The algorithms adjust for cross-track displacement caused by the fact that the process used by the ASAR sensor to geo-locate the source of a backscatter value assumes that the source lies on the surface of the WGS84 ellipsoid, without taking into account its height above the datum. The algorithm therefore requires an elevation for each pixel, and for this purpose, a SRTM 250m DEM (Jarvis *et al.*, 2008) is resampled to the 500m pixel spacing of the GM data. In the raw GM data file, the position of a pixel within a row corresponds to its position across the ground range swath. For this reason, the processing is done in the local x-y grid of the raw data prior to rectification to geographical coordinates. In order to convert the raw GM data values into backscatter values, the *local incidence angle* α is required, which in turn requires the *(nominal) incidence angle* θ and the local orientation of the target pixel with respect to the incident radar beam. This latter parameter is established using the DEM values adjacent to the target pixel.

2.2.2 Orthorectification

2.2.2.1 Establishing the displacement error

This algorithm works within the frame of reference of the raw data, whose rows and columns lie parallel to the swath and azimuth respectively. Consider Figure 2.1, where R represents the distance of the sensor from the centre of the WGS84 ellipsoid, r is the radius of the ellipsoid at the target coordinates, h is height

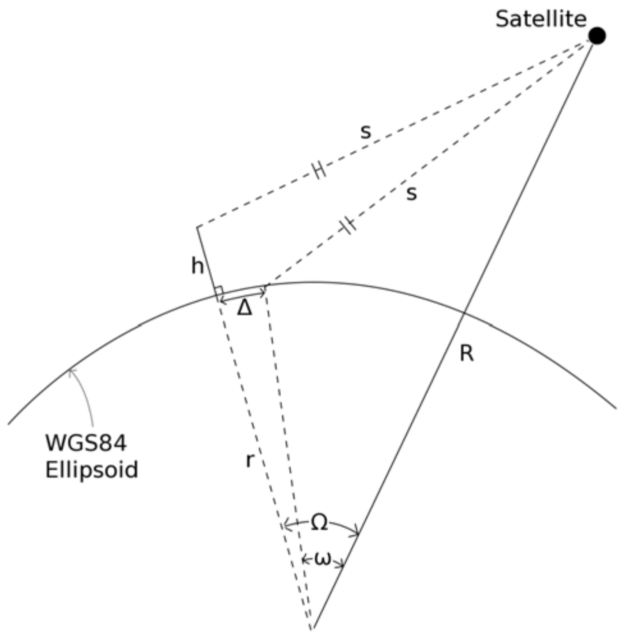

Figure 2.1: Geometry used in the calculations for orthorectification

above WGS84 of the target, (i.e. the DEM value) and s is the slant range, or the direct distance from the target to the sensor.

The target pixel is positioned in the data according to its distance along the ground-range swath as calculated using the slant range s. This calculation assumes a target positioned precisely on the WGS84 ellipsoid. Where the target has height h, it can be seen that the calculated distance has a displacement Δ closer to the nadir than the actual target position. In Figure 2.1, two triangles can be seen for which the length of all of the sides are known. From this, we can calculate angles Ω and ω, which in turn gives us the displacement arc Δ.

$$\Delta = r(\Omega - \omega) \tag{2.1}$$

where Ω and ω are in radians. This assumes that r is constant over the displacement Δ, despite the ellipsoidal, rather than spherical model. This is perfectly acceptable, as the difference would only amount to a few millimetres over an entire pixel width (e.g. Rees & Steel (2001)). Angles Ω and ω are calculated as follows.

According to the cosine rule, in any euclidean triangle,

$$a^2 = b^2 + c^2 - 2bc\cos A$$

where A is the angle subtended by the side of length a, and b and c are the lengths of the other two sides.

Rearranging gives us

$$A = \cos^{-1}\left(\frac{b^2 + c^2 - a^2}{2bc}\right)$$

If we equate A with Ω, then

$$\Omega = \cos^{-1}\left(\frac{(r+h)^2 + R^2 - s^2}{2R(r+h)}\right) \tag{2.2}$$

and similarly for ω

$$\omega = \cos^{-1}\left(\frac{r^2 + R^2 - s^2}{2Rr}\right) \tag{2.3}$$

Equations 2.2 and 2.3 may then be substituted into Equation 2.1 to obtain the displacement Δ.

2.2.2.2 Redistribution of cell value

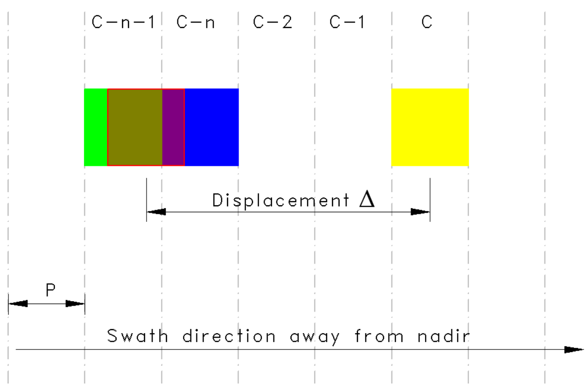

Figure 2.2: Orthorectification value reassignment

Consider the cell (the yellow cell in Figure 2.2) in column (or *range address*) C

of our desired terrain-corrected final image, whose terrain correction displacement is Δ. Due to the difference in height between the datum ellipsoid and the target, the value from this cell has been wrongly assigned, partly to the cell at $C - n$, and the remainder to the cell at $C - n - 1$. Let η be the number of cells within displacement Δ, where

$$\eta = \frac{\Delta}{P} \quad \text{and} \quad n = \lfloor \eta \rfloor \tag{2.4}$$

We cannot simply reassign the values from the cells in columns $C - n$ and $C - n - 1$, as their overall brightness value may be the sum of contributions of values from more than one cell experiencing foreshortening or layover. It is therefore necessary first to establish how many contributions to each cell value were made, and then to determine what proportion of the overall value was contributed by the target cell. We cannot determine the precise contribution from various locations along the swath to an aggregated value. The best we can do is to give equal weight to each contribution, effectively redistributing a contribution average to each correct location. In practice, this requires a two-pass algorithm. Let K_i be the total number of cells contributing to the final value of the cell in column i. Then, given Equation 2.4:

$$\begin{aligned} K_{C-n} &\leftarrow K_{C-n} + 1 - \eta + n \\ K_{C-n-1} &\leftarrow K_{C-n-1} + \eta - n \end{aligned}$$

The second pass of the algorithm may then assign a new value V_i to the cell in column i, such that

$$V_C = (\eta - n) \cdot \frac{U_{C-n-1}}{K_{C-n-1}} + (1 - \eta + n) \cdot \frac{U_{C-n}}{K_{C-n}} \tag{2.5}$$

where U_i is the original value of the cell in column i.

If desired, we can record the K values and output a raster to give a measure of the degree of foreshortening encountered. Whether *layover* has occurred is trivial, as it is simply a matter of the relative value of the displacement Δ of a cell with respect to that of its neighbours. What is of far greater importance is that no contributions are allocated to cells from which no backscatter has reached the sensor due to radar shadow.

2.2.2.3 Establishing Radar Shadow

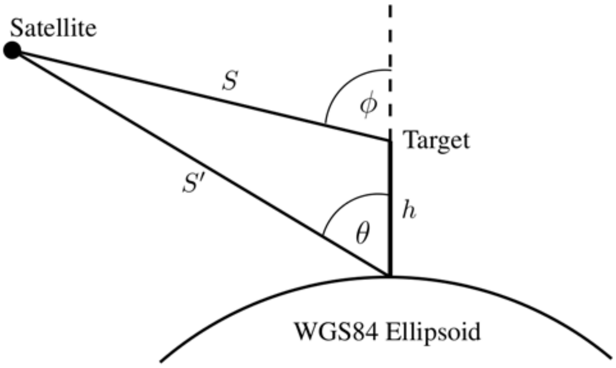

Figure 2.3: Satellite–Target geometry, showing Slant Range S, Nominal Zero-Doppler Slant Range S', Incidence Angle θ and Off-nadir Angle ϕ

With reference to the diagram in Figure 2.3, if θ is the incidence angle of the target at the WGS84 ellipsoid, then ϕ is the incidence angle at the target height, or the *Off-nadir angle*, being the angle between the zero-Doppler slant range S and the normal to the ellipsoid at the target pixel, in the plane containing the sensor, the target and the ellipsoid center. Let ϕ_i be the Off-nadir angle for a cell with range address i, where i is zero closest to the nadir. If there exists a range address j closer to the nadir for which $\phi_j > \phi_i$, then i is obscured by j and is therefore in shadow:

$$\text{Shadow} \quad = \quad \{i \quad | \quad \exists j \quad \ni \quad (i > j) \quad \wedge \quad (\phi_i < \phi_j)\} \tag{2.6}$$

2.2.3 Local incidence angle

Figure 2.4 shows the signing convention used here. The X and Z axes lie in the plane containing the sensor, target and swath. The Y axis comes out of the page. Λ and θ are the *Look angle* and *Incidence angle* respectively. $\hat{\mathbf{n}}$ is the unit vector normal to the target surface, and $\hat{\mathbf{r}}$ of incident radiation returning to the

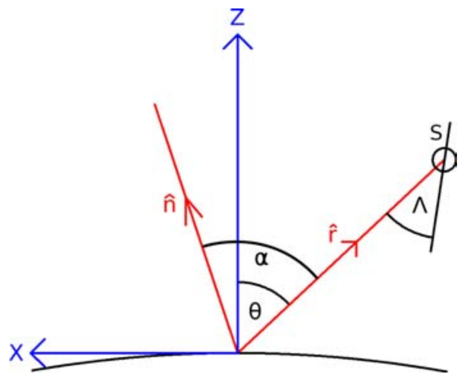

Figure 2.4: Signing convention for the following calculations. The X axis lies on the plane containing the satellite and the target, and is tangential to the WGS84 ellipsoid. Λ, θ and α are the *look angle*, *incidence angle* and *local incidence angle* respectively. The direction of $\hat{\mathbf{n}}$ is dependent on topography, and is arbitrary in this diagram.

sensor. Using this convention, the X and Z components of $\hat{\mathbf{r}}$ are $-\sin\theta$ and $\cos\theta$ respectively:

$$\hat{\mathbf{r}} = \begin{pmatrix} -\sin\theta \\ 0 \\ \cos\theta \end{pmatrix} \tag{2.7}$$

We are interested in finding the *local* incidence angle α, which is the angle between $\underline{\hat{n}}$ and $\underline{\hat{r}}$.

$$\text{Let } \hat{\mathbf{n}} = \begin{pmatrix} A \\ B \\ C \end{pmatrix}$$

We know that $\mathbf{a} \cdot \mathbf{b} = ab\cos\alpha$ where α is the angle between vectors $\mathbf{a}$ and $\mathbf{b}$.

$$\begin{aligned} \Rightarrow \hat{\mathbf{n}} \cdot \hat{\mathbf{r}} &= \begin{pmatrix} -\sin\theta \\ 0 \\ \cos\theta \end{pmatrix} \cdot \begin{pmatrix} A \\ B \\ C \end{pmatrix} \\ &= C\cos\theta - A\sin\theta \end{aligned}$$

$\Rightarrow$ Local Incidence Angle

$$\alpha = \cos^{-1}(C\cos\theta - A\sin\theta) \tag{2.8}$$

as $\hat{\mathbf{n}}$ and $\hat{\mathbf{r}}$ are both of unit length.

2.2.3.1 To establish normal vector

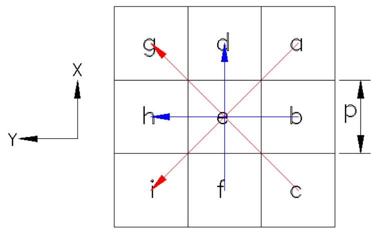

Figure 2.5: DEM Grid surrounding target pixel of height e

The vector $\mathbf{n}$ can be established from the cross product of two vectors contained in the target surface. Figure 2.5 represents the target pixel in the centre, with DEM height e, where the X axis from our local frame of reference described in Figure 2.4 points upwards, with the origin at the centre of the target pixel at height e. Thus a vector $\mathbf{v_1}$ from the origin to the top-right pixel would be

$$\mathbf{v_1} = \begin{pmatrix} p \\ -p \\ a-e \end{pmatrix}$$

where p is the pixel spacing, and a vector $\mathbf{v_2}$ from the origin to the bottom-left pixel would be

$$\mathbf{v_2} = \begin{pmatrix} -p \\ p \\ i-e \end{pmatrix}$$

A diagonal vector $\mathbf{d_1}$ from the bottom-left to the top-right pixel would therefore be

$$\mathbf{d_1} = v_2 - v_1 = \begin{pmatrix} 2p \\ -2p \\ a-i \end{pmatrix}$$

Similarly, another diagonal vector

$$\mathbf{d_2} = \begin{pmatrix} 2p \\ 2p \\ g-c \end{pmatrix}$$

We can derive a vector normal to the plane containing vectors $\mathbf{d_1}$ and $\mathbf{d_2}$ by calculating their cross-product using the determinant of the formal matrix

$$\begin{aligned} \mathbf{d_1} \times \mathbf{d_2} &= \det \begin{bmatrix} \mathbf{i} & \mathbf{j} & \mathbf{k} \\ 2p & -2p & (a-i) \\ 2p & 2p & (g-c) \end{bmatrix} \\ &= \mathbf{i}(-2p(a-i) - 2p(g-c)) \\ &- \mathbf{j}(2p(g-c) - 2p(a-i)) \\ &+ \mathbf{k}(4p^2 + 4p^2) \end{aligned}$$

giving us the normal vector

$$\mathbf{n_1} = \begin{pmatrix} 2p(i-a+c-g) \\ 2p(a-i-g+c) \\ 8p^2 \end{pmatrix} \tag{2.9}$$

Similarly two other vectors contained with the target plane are

$$\mathbf{d_3} = \begin{pmatrix} p \\ 0 \\ d-e \end{pmatrix} - \begin{pmatrix} -p \\ 0 \\ f-e \end{pmatrix} = \begin{pmatrix} 2p \\ 0 \\ d-f \end{pmatrix}$$

and

$$\mathbf{d_4} = \begin{pmatrix} 0 \\ p \\ h \end{pmatrix} - \begin{pmatrix} 0 \\ -p \\ b \end{pmatrix} = \begin{pmatrix} 0 \\ 2p \\ h-b \end{pmatrix}$$

whose cross product

$$\mathbf{d_3} \times \mathbf{d_4} = \det \begin{bmatrix} \mathbf{i} & \mathbf{j} & \mathbf{k} \\ 2p & 0 & (d-f) \\ 0 & 2p & (h-b) \end{bmatrix}$$

giving us another "normal" vector

$$\mathbf{n_2} = \begin{pmatrix} 2p(f-d) \\ 2p(b-h) \\ 4p^2 \end{pmatrix} \tag{2.10}$$

Of course, neither of the vectors in equations 2.9 nor 2.10 represent the true normal to the target plane (which only really exists as a mathematical concept), but they are approximations to the normal based on the surrounding terrain. It seems reasonable that our best approximation of the normal could be taken as the bisector of these two vectors, found by averaging $\mathbf{n_1}$ and $\mathbf{n_2}$ to give us

$$\mathbf{n} = \begin{pmatrix} p(i-a+c-g+f-d) \\ p(a-i-g+c+b-h) \\ 6p^2 \end{pmatrix}$$

To obtain the unit vector we divide $\mathbf{n}$ by its length

$$\hat{\mathbf{n}} = \frac{1}{|\mathbf{n}|} \begin{pmatrix} p(i-a+c-g+f-d) \\ p(a-i-g+c+b-h) \\ 6p^2 \end{pmatrix} \tag{2.11}$$

where

$$|\mathbf{n}| = \sqrt{\begin{array}{l} p^2(i-a+c-g+f-d)^2 + 36p^4 \\ +p^2(a-i-g+c+b-h)^2 \end{array}}$$

$$= p \cdot \sqrt{\begin{array}{l} (i-a+c-g+f)^2 + 36p^2 \\ +(a-i-g+c+b-h)^2 \end{array}}$$

2.2.3.2 Final algorithm

This gives us the final algorithm for the local incidence angle α. We recall from equation 2.8 that

$$\alpha = \cos^{-1}(C\cos\theta - A\sin\theta)$$

Into this we can now substitute the X and Z components of equation 2.11, such that

$$A = \frac{S}{\sqrt{S^2 + 36p^2 + T^2}}$$

and

$$\begin{aligned} C &= \frac{6p}{\sqrt{S^2 + 36p^2 + T^2}} \\ T &= a-i-g+c+b-h \\ S &= i-a+c-g+f-d \end{aligned}$$

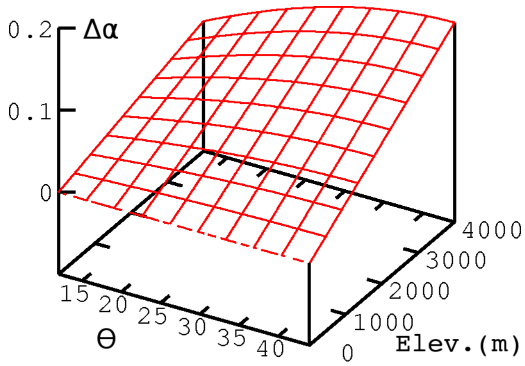

Figure 2.6: Errors ($\Delta\alpha$) in local incidence angle (degrees) as a consequence of adopting the use of the incidence angle θ provided in the GM data without adjusting for DEM height, over the full range of incidence angles θ.

Thus α is fairly easily calculated from DEM values, the pixel spacing p and θ, which is the angle of incidence with respect to the WGS84 ellipsoid. These angles are provided within the raw data files for sample tie points along each swath line. Keeping the calculations in the frame of reference of the raw data (ie prior to georectification) allows us to derive such values for all intermediate pixels by interpolation, along with the slant range times which are used in the orthorectification process, described in Section 2.2.2.

2.2.3.3 Methodological errors

There is an error caused by the use of the nominal incidence angle θ, as opposed to the off-nadir angle ϕ (see Figure 2.3), to arrive at the vector $\hat{\mathbf{r}}$ representing incident radiation in Equation 2.7. This error is plotted in Figure 2.6. In extreme cases, for example where $\theta = 44°$ and with an elevation of 4000m, the this error would amount to less than 0.2°. This is considered negligible for our purposes.

The SPECAN algorithm used by the ASAR sensor in GM mode corrects for antenna elevation gain using functions derived from the periodic calibration data (ESA, 2007a). The correction is updated when a new periodic calibration cycle occurs according to continually shifting relationship between the sensor location and the datum ellipsoid. The error in incidence angle described above has a consequence on the output data, as the Antenna Elevation Pattern (EAP) is

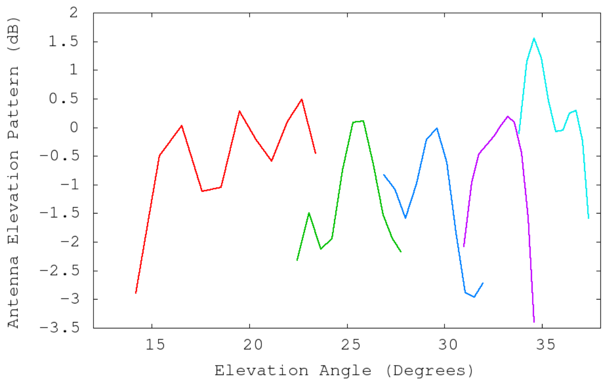

Figure 2.7: Antenna elevation pattern against Elevation angle, for each of the five predetermined overlapping antenna beams operated in the ScanSAR modes, extracted from a GM data file centred over Australia.

indirectly dependent upon the incidence angle. A typical relationship between the elevation angle and the EAP is shown in Figure 2.7.

The relationship between the ground-projected backscatter γ before and after orthorectification, the incidence angle θ and the off-nadir angle ϕ is as follows:

$$\gamma_{ORTH} = \gamma_{SRT}\left(\frac{G^2_{ele}(\theta)}{G^2_{ele}(\phi)}\right)$$

where G^2_{ele} is the two-way antenna elevation pattern gain (Shimada, 2010b). Thus when converting to decibels, this gives us

$$\Delta\gamma \text{ (dB)} = \Delta G^2_{ele} \text{ (dB)}$$

The greatest rate of change of G^2_{ele} with respect to elevation angle observed was below -6 dB degree^{-1}. This would result in an extreme case (4000m target height above datum, 44° look angle) in a difference of 1.2 dB to the final γ figure. Whilst this amount is significant, it is within the stated radiometric accuracy of GM data (1.54–1.74 dB, ESA (2007a)), and in most cases the error would be considerably less, and it is not accounted for in this procedure.

2.3 Method

2.3.1 Choice of software and programming languages

The decision to use the *Geographic Resources And Support System* (GRASS) GIS package to manage raster files in a prototype image preprocessing module is not a difficult one to make (GRASS Development Team, 2009). GRASS adheres to the *Unix Philosophy* (Kernighan & Pike, 1984), ensuring that its modules can be combined into shell scripts or can be easily incorporated into other modules. It is open source, meaning that its source code is readily available, and that any work done to build functionality that is not currently available, such as is intended by this research, may contribute source code in turn that is then available to the wider community, and in this way GRASS, which has been around for nearly three decades, maintains currency in the ever-broadening field of GIS. GRASS can be used in a multi-user environment (Neteler & Mitasova, 2008), lending itself to be set up for parallel tasks, and it is able to handle large data sets with low memory load (Huang *et al.*, 2011; Jasiewicz, 2010).

Although GRASS is written in C++[1], Perl[2] was used for the prototype for a variety of reasons. Perl is known for its strength as a rapid prototyping language, being high level and having lazy memory management. It is compiled just-in-time, rather than being interpreted, and allows pre-execution syntax and sanity checks. Perhaps the three most valuable benefits of Perl are its ready availability on almost all Unix servers, important when considering the use of High Power Computing (HPC), its ability to run inside the GRASS shell environment, and its powerful REGEX engine. This latter virtue is of particular importance in handling output streamed from GRASS and from auxiliary software to extract header information from binary data files, and allows rapid data exchange between arrays and data stored in text files, buffering output to reduce expensive system calls.

[1] http://www.cplusplus.com
[2] http://www.perl.org

2.3.2 Structure

The code was organised in a hybrid procedural/object-oriented manner. It was designed so that the task of preprocessing a large number of data files could be split among multiple nodes in an HPC. For each node, a unique GRASS environment is set up, including the automated output of a GRASS batch script, the setting of the GRASS_BATCH_JOB variable and the creation of a unique MAPSET within which to work, to avoid any locking conflicts. Each node is set to run a procedural batch script, the arguments of which include a target output directory and the allocated file input list. This script then calls GRASS commands and initiates Perl object instances, ultimately to output a GeoTIFF file, containing a minimum of two bands, representing the orthorectified DN values and the local incidence angles. A radar-shadow mask and a representation of layover/foreshortening can easily be produced (as these are calculated), but in this first instance this explicit output is avoided, to reduce I/O system calls and free up memory. Radar shadow is manifest in the output image in the form of null values.

Figure 2.8 shows the salient features of the principle classes used. The pivotal class is GrassAscii, which comprises the attributes and methods necessary to write to and read from an ASCII raster file compatible with GRASS GIS. Classes Alpha and Ortho are themselves child classes of GrassAscii, Alpha containing the method by which to calculate local incidence angles, and Ortho the method to perform the terrain correction. The GM class represents the raw data file, and comprises the methods required to extract the Annotation Data Set Records (ADSR) within the GM file and to interpolate the Slant Range Times (SRT), Latitudes and Incidence angles. These, together with the DN values and the recoded DEM, are exported as GrassAscii objects.

Figure 2.9 shows the operation flow and exchange of data between the *process_gm* procedure and the various modules. Operations on the left side are carried out in geographical lat-long coordinates, while those on the right occur within the x–y grid local to the raw data file. Data exchanges via ASCII grid files are shown in yellow.

Algorithm 1 shows pseudo-code demonstrating the orthorectification proce-

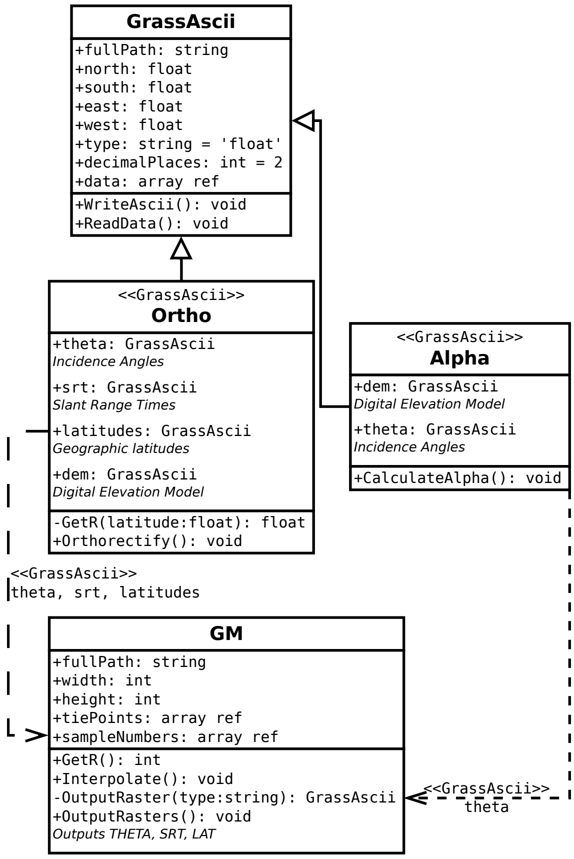

Figure 2.8: Class outline used

dure carried out by the Ortho class. For each row (each azimuth address) in the Digital Number (DN) array, two passes are made through the pixels, effectively travelling across the radar swath in the direction away from the nadir. The first pass (lines 5–19) determines the off-nadir angle ϕ. If there has been a previous value of ϕ higher than the current value on the same swath, the pixel is marked as *shadow*; otherwise, the misplaced contribution value of the current pixel, based on its SRT and incidence angle, is added to the relevant address in the CONTRIBUTIONS array. In the second pass (lines 20–24), now knowing the total number of contributions that were aggregated to produce the pixel values in the raw data, these values are then redistributed according to the displacement Δ recorded in the first pass.

The function **RedistributeDNValue** in line 22 then apportions values in accordance with Equation 2.5 and as shown in Figure 2.2 in Section 2.2.2.2, as

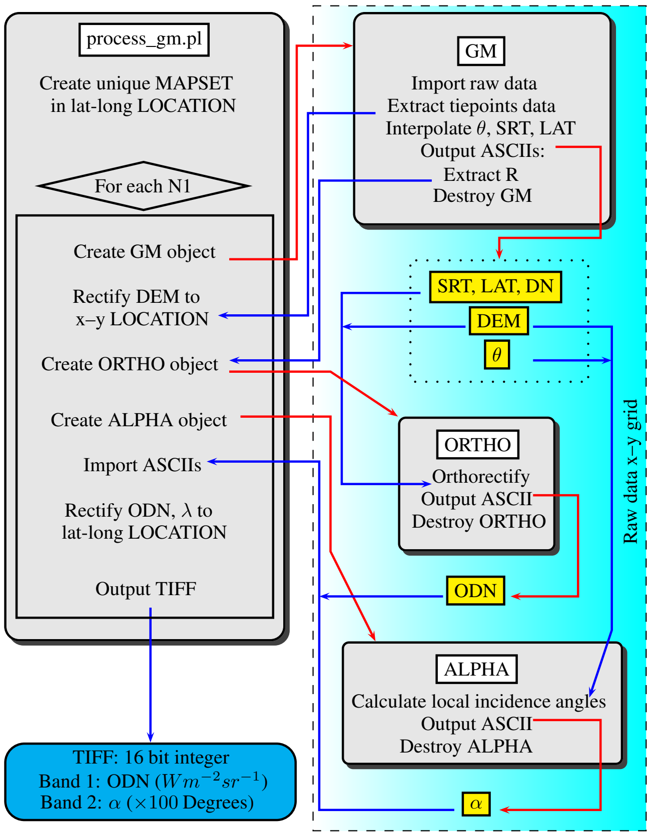

Figure 2.9: Flowchart showing preprocessing carried out by one node running process_gm.pl

follows:

$$
\begin{aligned}
&\mathrm{ODN}[c] \\
\leftarrow\ & \left[(\Delta - \lfloor\Delta\rfloor) \cdot \frac{\mathrm{DN}[c - \lfloor\Delta\rfloor - 1]}{\mathrm{CONTRIBUTIONS}[c - \lfloor\Delta\rfloor - 1]}\right] \\
+\ & \left[(1 - \Delta + \lfloor\Delta\rfloor) \cdot \frac{\mathrm{DN}[c - \lfloor\Delta\rfloor]}{\mathrm{CONTRIBUTIONS}[c - \lfloor\Delta\rfloor]}\right]
\end{aligned}
$$

where c is the current pixel range address. Pseudo-code representing the interpolation method provided in the GM class is shown in Algorithm 2. The algorithm interpolates firstly between tie-points across the swath to produce a full raster row (lines 3–7), and then interpolates down the columns for each pixel

Algorithm 1 Orthorectify()

```
1: Fetch into arrays (DEM, DN, LAT, SRT, THETA)
2: for each row in DN do
3:    Zero-fill arrays (SHADOW, CONTRIBUTIONS, DELTA)
4:    φ_max ← 0 # Max Off-nadir angle so far
5:    for each pixel in row do
6:       s ← Calc Slant Range Distance (SRT)
7:       φ ← Calc Off-nadir Angle (s, THETA, DEM)
8:       if φ_max > φ then
9:          SHADOW ← true
10:      else
11:         φ_max ← φ
12:         r ← Calc Radius At Latitude (LAT)
13:         Ω ← Calc Omega (r, DEM, R, s)
14:         ω ← Calc Little Omega (r, R, s)
15:         Δ ← Calc Delta (r, Ω, ω)
16:         Add contribution (CONTRIBUTIONS)
17:         Update Arrays (DELTA, SHADOW)
18:      end if
19:   end for
20:   for each pixel in row do
21:      if  NOT SHADOW then
22:         RedistributeDNValue (DELTA, DN, ODN, CONTRIBUTIONS)
23:      end if
24:   end for # Next Pixel
25: end for # Next Row
```

between the current raster row and that corresponding to the previous tie-point row (lines 8–10).

2.3.3 Parameters

The GM binary data contains within it a data set pertaining to a series of tie points, numbering precisely eleven across the swath (approximately 37 km apart) the number of rows in the azimuth direction depending on the length of the frame strip, which varies. For each tie point is given geodetic latitudes and longitudes, allowing ground control points to be derived. These, together with SRT, incidence angles and 2-way antenna elevation gains are extracted from the ADSR by calling

Algorithm 2 Interpolate()

```
for each Pointfile Row do
    RasterRow ← Get Corresponding Raster Row (PointfileRow)
    for each Tiepoint in PointfileRow do
        lastTPval ← Get Tiepoint Value (This)
        nextTPval ← Get Tiepoint Value (Next)
        lastTPcol ← Get Raster Column of Tiepoint (This)
        nextTPcol ← Get Raster Column of Tiepoint (Next)
        for each col ← raster column between lastTPcol and nextTPcol do
            Pixelvalue ← lastTPval + ( (nextTPval - lastTPval) × (col - lastTPcol) / (nextTPcol - lastTPcol) )
        end for # Next col
    end for # Next Tiepoint
end for # Next Pointfile Row
```

the command line tool Pds2Ascii, provided within EnviView by ESA (ESA, 2010).

Parameter	Function	Dataset	Field
Absolute Calibration Constant K	Conversion to σ^0	2	calibration_factors
Orbit State Vectors X,Y,Z	Calculation of $R_{satellite}$	2	orbit_state_vectors
Tie Points	Lat, Long, SRT, θ	7	*_line_tie_points
AEP	EAP, Λ	6	elevation_pattern.*

Table 2.2: Parameters extracted from GM data file using Pds2Ascii

Table 2.2 shows the parameters extracted from the GM data file, together with the particular data set and field in which they are contained. Data set 2 refers to the Main Processing Parameters ADS, 6 is the MDS1 Antenna Elevation Pattern ADS and 7 is the Geolocation Grid ADS. $R_{satellite}$ is the distance of the satellite from the center of the WGS84 ellipsoid, used in Equations 2.2 and 2.3 in Section 2.2.2.1. The radius r (ellipsoid radius at target location) used in the same equations is calculated as follows (e.g. Groten (2004)):

$$r_\Theta = a(1 - f \sin^2 \Theta)$$

where a = Equatorial Radius = 6378137m (WGS84)

f = flattening = $(a - c)/a$

c = polar radius = 6356752.3m

Θ = Geocentric Latitude

The Geocentric Latitude Θ relates to the Geographic Latitude Φ by

$$\tan\Theta = (1 - f)^2 \tan\Phi$$

2.3.4 Multi-node network distribution

The key benefit of having control over the scripts which manage the preprocessing of a large number of GM data files is the ease with which the task can be split and allocated to a High Power Computing network (HPC). The HPC used in this instance managed multiple nodes on a Portable Batch System (PBS[1]). The perl script which manages the distribution of work to the HPC may be found in Appendix A, Listing 6. The essence of the workings of the script is described in Algorithm 3 below.

The script looks for all GM data files under the current directory and separates them into batches, creating a directory for each batch and symbolic links within each to those folders. Each batch will then be processed concurrently. Two batch scripts are then created by the main script for each batch - one being the instructions for Grass GIS, the other being the PBS batch script. The latter is submitted to the HPC server. The start of each PBS script sets the GRASS_BATCH_JOB variable to point to the individual Grass batch script, and starts a new instance of GRASS GIS, creating a unique temporary MAPSET within which to work.

2.4 Results and discussion

The decision to develop a bespoke method for the preprocessing of GM data was based on the need to have control over the process, partly due to the sheer numbers of data files to be managed, but partly also to allow for interruption to parts of the process where appropriate - to allow for deviation from the usual methods under certain circumstances. Examples of this would be the case of work done using image differencing techniques involving data taken from the same orbit track, where certain incidence angle multipliers may be factored out

[1] http://www.OpenPbs.org/

Algorithm 3 PBS algorithm

for each Batch **do**
  Create Batch Directory
  Link allocated GM files to Batch Directory
end for # *Next Batch*
for each Batch Directory **do**
  Write to ThisGrassBatch "process_gm.pl ThisGrassBatch ThisDirectory"
  Make ThisGrassBatch executable
  Write to ThisPBSBatch"Load Grass"
  Write to ThisPBSBatch "Set GRASS_BATCH_JOB = ThisGrassBatch"
  Write to ThiSPBSBatch "Start Grass using MAPSET name MThisDirectory"
  Make ThisPBSBatch executable
  Submit ThisPBSBatch to PBS Server
end for # *Next Batch Directory*

of the calculations early in the processing (O'Grady *et al.*, 2011), and in the case of regression calculation applied over hundreds of images, where the individual results of image processing are not kept, but rather, following preprocessing, their pixel-wise contribution to running sums used in the final calculations is aggregated (in the case of linear regression, for example, aggregate images would store Σx, Σx^2, Σxy, Σy^2, $\Sigma x^2 y^2$ and n).

Adequacy of the methods described here, in terms of fitness for purpose, accuracy and speed are an issue. Once adequate accuracy is established, fitness for purpose is gleaned from the use of the methods, the worth of their results and the ability for the process to be run in a reasonable time. In this regard, the speed requirement for the purposes of our research was actually a binary condition of fitness for purpose. Using the HPC in the manner described, hundreds of GM data files were able to be processed in a matter of minutes. Having the data-download and preprocessing of the (typically) 70 or so daily images being automated remotely overnight by the cron (time-based scheduler) daemon, this fact meant an easy tick for the speed criterion. Speed benchmarking tests were not carried out for this reason.

Accuracy was tested by comparing outputs from our process with that for the same data files processed by what is perhaps the most suitable contender -

the well resolved *NEST* (Next ESA SAR Toolbox) package developed by Array Systems Computing [1] and made available online through ESA's website [2].

The tests were confined to the range of latitudes and elevations for which our methods were to be used in Australia. A number of bodies of open water were chosen around the region at various heights above sea level. Transects were sampled across the centre of the water bodies in azimuth and range directions. The resultant values from three images were overlain against each other in plot outputs; MODIS Band 6 (SWIR $\lambda \approx 1620$ nm), radar backscatter (σ^0) from our preprocessed data and that from the data processed using NEST. The MODIS plot shows us a good indication of the spatial demarcation between land and water for comparison with the responses from the two separately derived radar images. The differences observed, in terms of pixels, are tabulated and can be seen in Table 2.3. Accuracy for both of the radar images was worse in the azimuth direction, with displacement averaging at 2.56 pixels for NEST and 2.33 for our method. In the range direction, average displacement for NEST was 1.63, against our 1.31. The apparent greater accuracy in the azimuth direction using out method comes as somewhat of a surprise, due to the fact that our calculations work solely in the range direction, but it is considered likely that the results would be reversed in more extreme terrain, which would be outside the scope of our research with this method.

Figure 2.10 shows some of the output of the analysis as it appeared graphically. The conclusion was that our method produced a level of spatial and radiometric accuracy that was certainly comparable with a very worthy third-party alternative.

[1] http://www.array.ca/
[2] http://nest.array.ca/web/nest

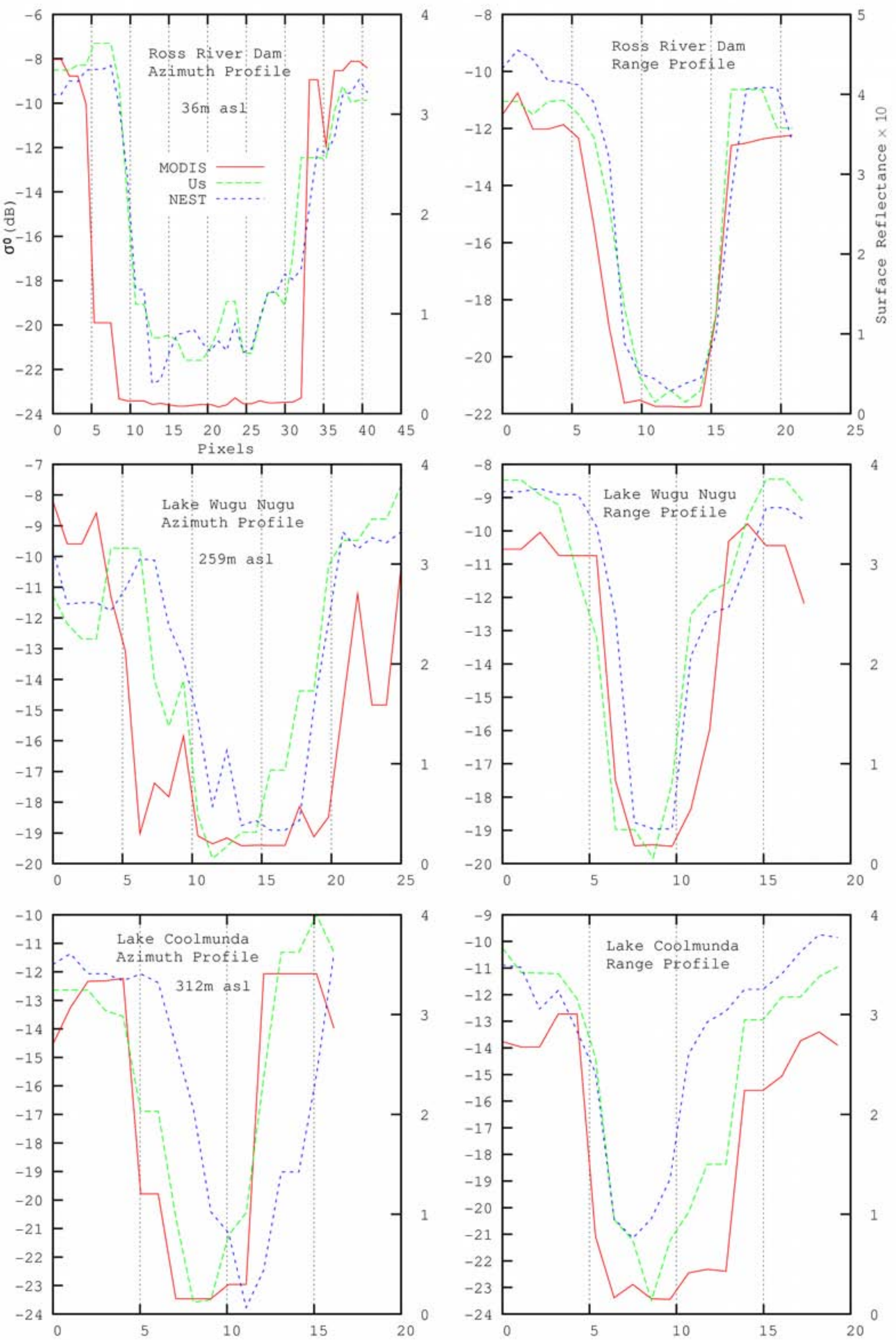

Figure 2.10: Transect value profiles in Azimuth (left) and Range (right) directions across three bodies of water in Australia. The red profile corresponds to MODIS Terra or Aqua Reflectance in thousands (scale on the right of the plots), the green corresponds to σ^0 output using our algorithm, and the blue using NEST software, both scaled in dB on the left axes.

	Azimuth			Range		
Ref	Our diff from MODIS	NEST diff from MODIS	Our diff from NEST	Our diff from MODIS	NEST diff from MODIS	Our diff from NEST
1	1	2	3	1	2	1
2	2	2	0	2	2	0
5	2	1.5	0.5	2	1	1
6	3	2.5	0.5	1	1	0
7	6	5	1	-	-	-
8	1.5	3.5	2	1.5	2.5	1
9	1.5	1.5	1	1	1.5	0.5
10	0	3	3	1	2.5	1.5
11	4	2	2	1	0.5	0.5
MEAN	2.33	2.56	1.44	1.31	1.63	0.69

Table 2.3: Spatial displacement ("diff") in pixels between edges of sampled water bodies as identified in outputs from our described process, ESA's NEST software and MODIS Band 5. Values were obtained by comparing profiles for transects across the water bodies in the azimuth and range directions. Water thresholds were chosen as $\sigma_0 = -16$dB for the radar data, against a reflectance of 0.2 for MODIS Band 5.

2.5 Conclusion

Preprocessing of GM data was performed using GDAL functions, GRASS raster manipulation techniques and Perl scripting, allowing control and transparency over the whole procedure, and allowing a very high volume of data to be processed quickly on JCU's HPC. The accuracy of the process was tested to the extent that enabled us to determine the method's fitness for purpose. Throughout its subsequent use, many "one-off" comparisons were possible with occasional data processed by ESA's NEST software, and in this way the ongoing satisfactory performance of the method described above was further verified.

The philosophy of collaboration, transparency and sharing which enables the development of tools that are so valuable to the GIS and remote sensing community, such as GDAL and GRASS, as well as the hugely important and ubiquitous tools such as Perl and C++, ties in very well with the philosophy of collaborative research in the scientific field. Whilst many of these tools pre-date much of the commercially-developed software available, the open source model is becoming increasingly prominent, and we envisage it playing a vital role in meeting the increasing needs of emerging technologies in remote sensing.

Chapter 3

Relationship of incidence angle with satellite radar backscatter for different surface conditions

Chapter context

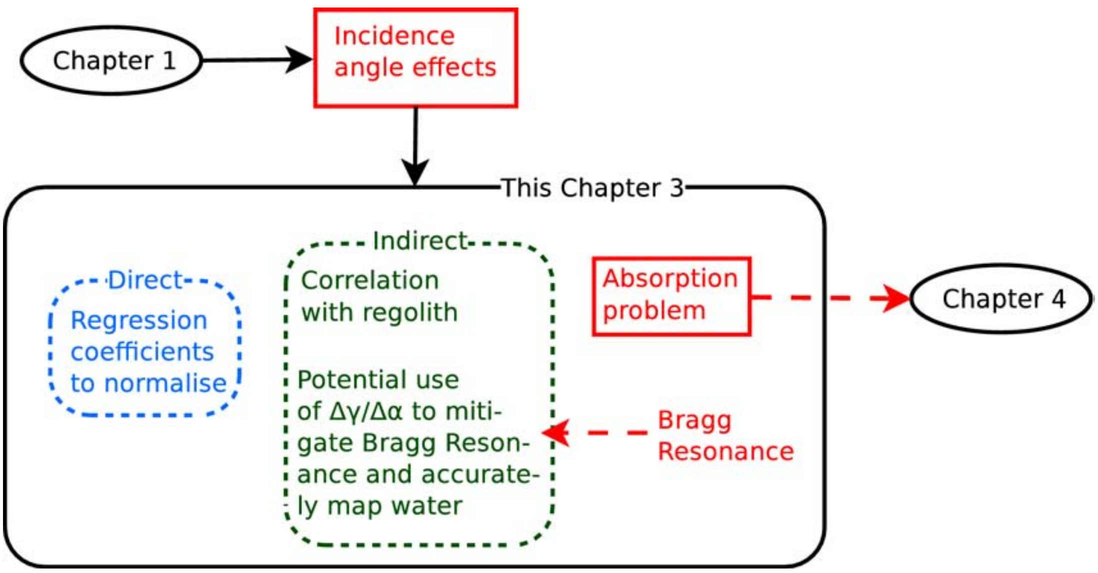

Abstract

This chapter aims to exploit the use of multiple angles of incidence, and the high temporal frequency of Envisat's *Advanced Synthetic Aperture Radar* (ASAR) *Global Monitoring* Mode data to observe the relationship between the radar backscatter response from different land surfaces with varied angles of incidence. The primary objective is to establish a parameter surface for a region against a model relating the variation in backscatter with incidence angle, in order that backscatter values across the swath in a GM image can be normalised. Backscatter response characteristics to varied incidence angles are examined against various surface categories using pixel-level regression across a large time series, with regolith displaying the strongest correlation. The potential use of the slope of the linear model approximating the relationship of incidence angle with backscatter, to directly map open water accurately, is observed, with the method's possible reduction of Bragg Resonance effects in C-HH data being apparent.

3.1 Introduction

Much research has been carried out to investigate the value of satellite radar data in the classification of ground surface properties (Bindlish *et al.*, 2009; Bonn & Dixon, 2005; Chandran *et al.*, 2006; Frappart *et al.*, 2005; Waisurasingha *et al.*, 2007; Wilson & Rashid, 2005). Where data taken from differing look angles is used for comparison or change detection, the elimination of the effects of differing incidence angle by *normalisation* to some common angle is usually attempted alongside despeckling, as a necessary part of preprocessing.

However, change in backscatter with respect to incidence angle is a function of the structural and dielectric properties of the target surface, being sensitive, therefore, to differences in regolith, soil types, vegetation and land use, for example. As these are the very parameters by which researchers mean to classify the surface, it is important that normalisation functions applied in the preprocessing stage are specific to these properties, in order that changes in backscatter observed at a particular location can be confidently attributed to an environmental change, rather than to a difference in the incidence angles used to obtain the respective values.

The high frequency of coverage provided by Envisat ASAR's *Global Monitoring Mode* (GM) products affords us a time series across multiple incidence angles that gives us sufficient data to carry out regression, across the time series, for all locations, in order to derive a relationship of backscatter with incidence angle specific to the ground conditions in each location.

3.2 Theoretical Context

Recapping a little from Section 1.4.1.5, GM data, as made available by the European Space Agency (ESA), comprises digital numbers (DN) which are related to the local incidence angle α by

$$DN^2 = K \cdot \beta^0 = K \cdot \frac{\sigma^0}{\sin(\alpha)} \tag{3.1}$$

where σ^0 is the radar backscatter coefficient and K the absolute calibration constant (ESA, 2004). For a volume scatterer being comprised of random scatterers of varying sizes and orientations, we expect

$$\gamma_\alpha = \frac{\sigma^0_\alpha}{\cos \alpha} \tag{3.2}$$

where γ_α is the *range independent* backscatter coefficient at incident angle α (Shimada, 2010a).

3.2.1 Local incidence angle

The quantity of GM data available affords us the opportunity to directly investigate the relationship between the incidence angle and σ^0 or γ, as derived from equations 3.1 and 3.2.

Recalling the assumption by Baghdadi *et al.* (2001) that

$$\sigma^0_\alpha \approx \sigma^0_n \cos^\Psi \alpha \tag{3.3}$$

(adapted from Ulaby *et al.* (1982)), where Ψ is the slope of the linear fit of σ^0(dB) against $10\log(\cos\alpha)$ (Baghdadi *et al.*, 2001).

From Equations 3.2 and 3.3 we can say

$$\gamma_\alpha \approx \sigma^0_n \cos^\psi \alpha \tag{3.4}$$

where $\psi = \Psi - 1$.

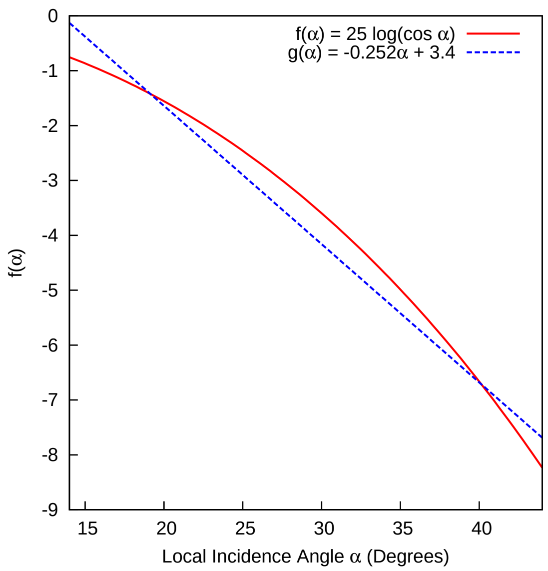

Figure 3.1: Function $f(x) = \cos^\psi \alpha$ for $\psi = 2.5$ and $\psi = 10$ within the range of incidence angles α relevant to GM data

Some researchers have assumed a near linear relationship between σ^0 and α (e.g. Pathe *et al.* (2009)), in cases where incidence angles are confined to a narrow range. Based on equation 3.4, typical values of ψ were found to be between 2.5 over land and 10+ over water. Figure 3.1 shows that a linear approximation of these powers of cosine within the range of incidence angles found in GM data (15°–44°) would be reasonable, especially in the context of the 1.2 dB radiometric resolution of GM data (Pathe *et al.*, 2009; Sabel *et al.*, 2008).

3.2.2 Physical models

Simple physical models class radar scatterers as surface scatterers, volume scatterers and heterogeneous combinations of the two. The backscatter of surface scatterers depends on the dielectric properties of the surface for scattering strength, and on the surface roughness for the distribution of scatter with respect to incidence angle. With volume scatterers, dielectric discontinuities and heterogeneous densities dictate scattering strength, with the dependence on incidence angle being governed by boundary surface roughness, average dielectric constant and structural scale within the medium (Ulaby *et al.*, 1982).

The effects on backscatter of a variety of different types of surface must be considered, especially where pixels are 0.5km in size. The response of bare soil is governed mainly by surface roughness and soil moisture content, with volume scattering contributing in the case of extremely dry soil. Studies have found that for bare soil at a given angle of incidence, radar backscatter (in decibels) has a near-linear relationship with the soil moisture content / moisture capacity ratio (Ulaby *et al.*, 1982). Where the soil is covered by vegetation, the relationship between the structural dimensions of the components of the vegetation and the wavelength of radar signal, together with the extent of cover, add to the response characteristics of the soil. C-band radar is more sensitive to smaller-structured vegetation components (Noernberg *et al.*, 1999), such as grasses and herbaceous vegetation (Parmuchi *et al.*, 2002) and aquatic plants (Henderson & Lewis, 2008).

3.3 Methodology

3.3.1 Data

GM data were downloaded systematically from ESA's *Earthnet Online* Portal through a Category 1 Fast Registration agreement (ESA, 2009b). This data comprised all GM acquisitions for the year 2009 between latitudes 10° S and 29° S and from longitude 140° E to 155° E.

MODIS data were downloaded via NASA's GSFC web portal (NASA, 2011). A comprehensive list of data used may be found in Appendix B.

3.3.2 Procedure

For each GM data file, a raster surface representing local incidence angles was created with 18" pixel spacing, using satellite geo-location parameters, digital elevation models and tie-point data provided within the data header files.

Firstly, DN values were converted to backscatter according to equation 3.1, to obtain σ^0_α, and orthorectified. An investigation was carried out assuming the relationship described in equation 3.4. This equation may be written

$$\gamma_\alpha(dB) \approx \psi \cdot 10\log(\cos\alpha) + \sigma^0_n(dB) \tag{3.5}$$

the slope of γ_α, as a function of $10\log(\cos\alpha)$, being ψ. Regression was carried out for each pixel over the time series for each quarter of 2009.

To analyse the variance of γ_{30} and $\Delta\gamma/\Delta\alpha$ for different physical parameters, 20,000 point sites were randomly chosen within a region of Queensland. For each of the points, values of the following parameters were extracted from the ancillary data:

1. Dominant vegetation species
2. Vegetation growth form
3. Soil type
4. Geology
5. Lithology
6. MODIS Band 6 ($\lambda \approx 1.6\mu m$)

The value of ψ derived for the whole of 2009 over Queensland compared reasonably well with those of Baghdadi *et al.* (2001) for horizontally co-polarised C-band data over different land covers. Coefficient of Determination R^2 showed a poor fit over land, averaging 0.1, but averaged around 0.8 over the sea, where values of ψ were typically above 10.

Further regression was carried out on the same dataset based on the relationship described for σ^0:

$$\bar{\sigma}^0_\alpha = \bar{\sigma}^0_0 e^{-\alpha/\alpha_0} \tag{3.6}$$

by Ulaby *et al.* (1982) after Moore & Fung (1979), who found the e-folding angle α_0 to be 5.35° for HH polarised 13.9 GHz Skylab scatterometer data over the sea (Ulaby *et al.*, 1982). In our case a comparable e-folding angle over sea was found to have a mean of 5.1°, with a standard deviation of 0.6°. The same regression resulted in an average e-folding angle over land of 48.5°. However analysis of the R^2 showed goodness-of-fit to be confined once again to open water.

The second round of analysis was based on the assumption that, given the narrow range of incidence angles from which the GM data was derived (15°– 44°), and the radiometric resolution of 1.2 dB (see Figure 3.1), the range independent backscatter coefficient γ could be normalised with respect to α based on a linear function whose slope and intercept were derived for each pixel over the time series.

Due to the great influence of surface wetness and soil moisture on backscatter values, and considering the seasonal variation in rainfall over Queensland, regression was carried out over each of the quarters of 2009 separately.

3.4 Results and discussion

3.4.1 Relationship of backscatter with incidence angle

Figure 3.2 shows the range independent backscatter coefficient γ_{30}, calculated by feeding 30° into the linear best-fit function for each pixel, over each quarter. Figure 3.3 shows the slope of the same function, $\Delta\gamma/\Delta\alpha$. It can be seen that γ_{30} and $\Delta\gamma/\Delta\alpha$ show quite different features over the surface of northern Queensland. It is also apparent that the significant difference seen between the γ_{30} values in the first (wettest) quarter and the other drier quarters are not matched with quite such a difference in the values of $\Delta\gamma/\Delta\alpha$. This is to be expected, as while wet soil and vegetation return a higher backscatter value than their dry equivalent, they remain diffuse reflectors.

Figure 3.4 shows a comparison of the γ_{30} and $\Delta\gamma/\Delta\alpha$ values for the third

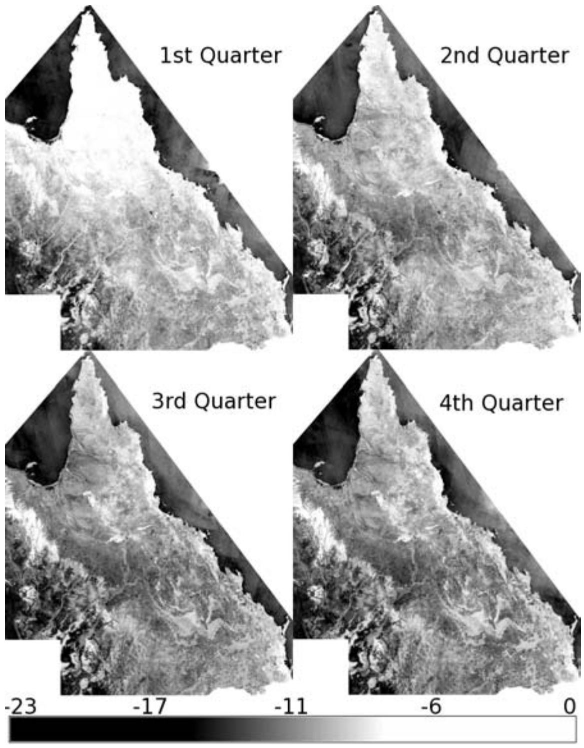

Figure 3.2: Range independent backscatter coefficient γ_{30} (dB), calculated from the linear best-fit function at 30°, for each quarter of 2009. High backscatter values caused by the wet season in the tropical far north of Queensland dominate the whole of Cape York Peninsula in the first quarter.

quarter of 2009. The greater separability between terrestrial values and those of the sea in the $\Delta\gamma/\Delta\alpha$ image over the γ_{30} image are clear. Additionally, the γ_{30} image shows bright areas of increased value in the sea along the east coast. These are the result of wind effects due to *Bragg resonance* on the surface of the water (Schaber *et al.*, 1997). The prevalence of these effects is confirmed by their presence in this image despite the fact that, rather than being instantaneous, the image is a composite modelled on some 40 data files. It is significant that these effects are not seen, at least to the same degree, in the $\Delta\gamma/\Delta\alpha$ image.

The difference in separability of land and water between γ_{30} and $\Delta\gamma/\Delta\alpha$ can be seen by comparing Figures 3.5 and 3.6. The density plot in the former shows that the separation of land from water would be problematic, whereas the latter shows us that, given sufficient data surrounding a flood event by which to establish $\Delta\gamma/\Delta\alpha$, the separability between water and land is greatly increased. The con-

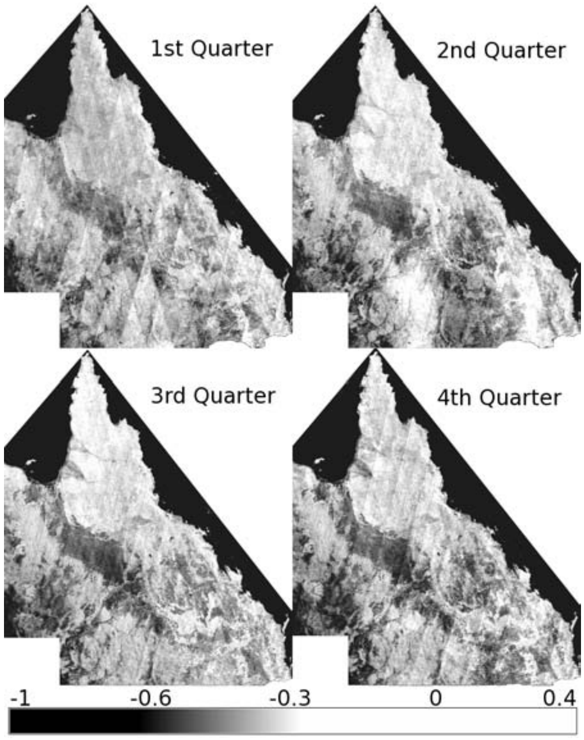

Figure 3.3: Slope $\Delta\gamma/\Delta\alpha$ (dB per degree) from linear regression for each quarter of 2009

sequence of this is that, given a sufficient temporal data frequency, $\Delta\gamma/\Delta\alpha$ may give us a means to accurately separate open water from land, despite the presence of Bragg resonance effects.

3.4.2 Variation with land surface properties

In the categorical analysis to determine, if applicable, the driving factor behind $\Delta\gamma/\Delta\alpha$ characteristics in terms of surface conditions, separability between categorical groups was examined both between each group pair, and over each categorical group as a whole. In the latter case, the singular values (SV), which give the ratio of the between- and within-group standard deviations on the linear discriminant variables, were calculated (the SV is the square root of the canonical F-statistic), with the results shown in Table 3.1.

The results of Table 3.1 tell us that the factors *regolith* and *dominant vegetation species* in Queensland have demarcations which fall closer into line with the variation of both γ_{30} and $\Delta\gamma/\Delta\alpha$, in comparison with the other classifiers.

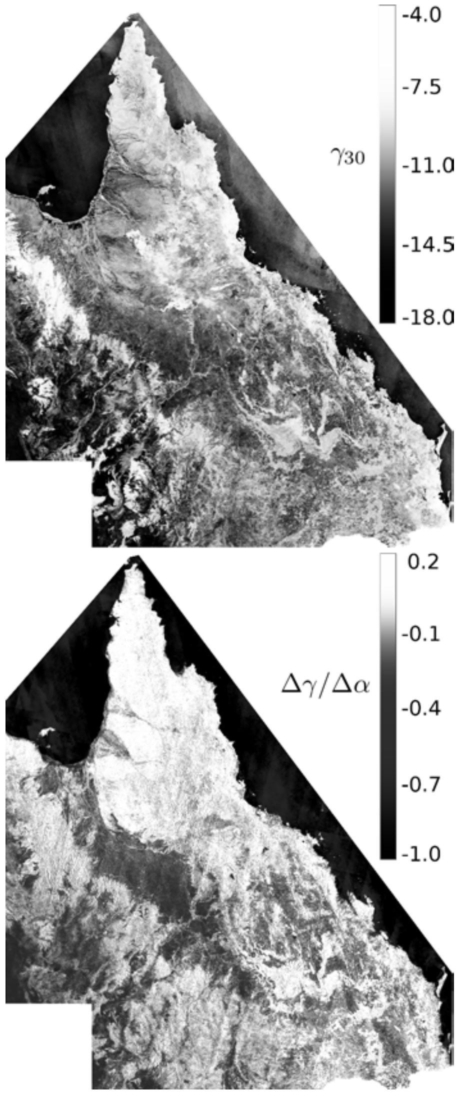

Figure 3.4: Comparison of γ_{30} (above) and $\Delta\gamma/\Delta\alpha$ (below) for the third quarter of 2009

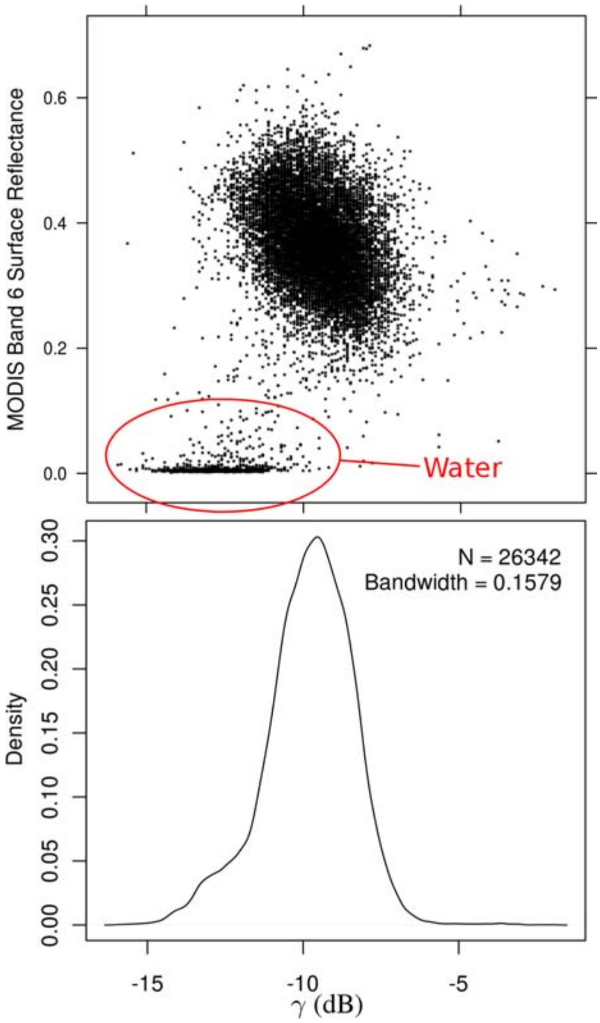

Figure 3.5: (Top) Scatter plot showing MODIS Band 6 reflectance against γ_{30}, which clearly separates water from land, and (bottom) the corresponding density plot of γ_{30} values, demonstrating their separability (or lack thereof)

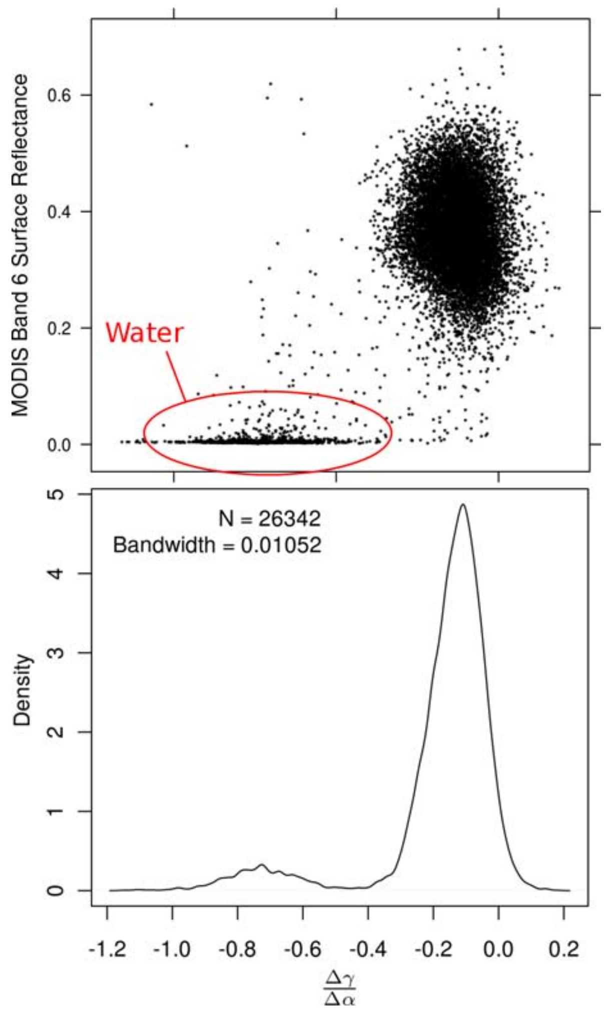

Figure 3.6: (Top) Scatter plot showing MODIS Band 6 reflectance against $\Delta\gamma/\Delta\alpha$, which clearly separates water from land, and (bottom) the corresponding density plot of $\Delta\gamma/\Delta\alpha$ values, demonstrating their separability

Classifier	SV	
	γ_{30}	$\Delta\gamma/\Delta\alpha$
Soil type	18.99	66.24
Gross rock Descriptor	19.08	48.24
Growth form	23.79	79.27
Dominant species	29.64	109.08
Regolith	30.07	109.14

Table 3.1: Singular values indicating categorical separability among land cover classifiers, using γ_{30} and $\Delta\gamma/\Delta\alpha$

From Figures 3.7 and 3.8 it can be seen that there is some spatial correlation between regolith and species. The clue as to which factor influences backscatter lies with the SV result for the classifier *growth form*, which groups the γ_{30} values according to the following forms:

- Hummock Grasses
- Low shrubs $<$ 2 metres
- Low trees $<$ 10 metres
- Medium trees 10–30 metres
- Other herbaceous plants
- Tall Shrubs $>$ 2 metres
- Tall trees $>$ 30 metres
- Tussocky or tufted grasses

If the relatively high separability of vegetation classes using γ_{30} were due to the structural properties of the vegetation itself, we might expect to see a similar SV value for growth form as we see for vegetation (the *Dominant Species* classifier), but this is not the case. This suggests that, of the classifiers studied, regolith has the highest correlation between incidence angle and backscatter.

Figure 3.9 shows us dominant vegetation species, displaying standard deviation (boxes), 25% and 75% percentiles (outer tics) and median values (central tics) of γ_{30} and $\Delta\gamma/\Delta\alpha$ for each class. From the γ_{30} plot on the left, it is clear that the characteristically low γ_{30} values of water are shared by some vegetation classes, particularly *Chenopodiaceae* (Saltbush and Bluebush), *Astrebla* (Mitchell Grass) and *Acacia*. The plot on the right, showing $\Delta\gamma/\Delta\alpha$ values against the

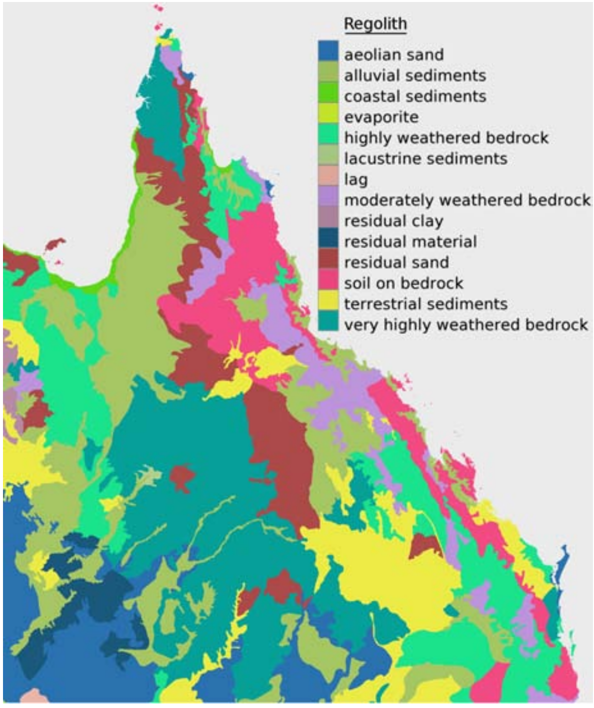

Figure 3.7: Map showing regolith of Queensland (source Geoscience Australia)

same vegetation species, separates water from everything else due to its relatively high change in backscatter with respect to incidence angle.

The mean and standard deviations for γ_{30} and $\Delta\gamma/\Delta\alpha$ against regolith classes are shown in Table 3.2. Figure 3.10 shows the corresponding box plots. In the γ_{30} plot on the left of Figure 3.10, the backscatter values for water have the biggest overlap with classes representing *aeolian sand* and *residual material*. As can be seen from the regolith class map in Figure 3.7, these classes occupy the dry interior in the south-west of Queensland, and the low backscatter represents absorption and attenuation of the signal. Perhaps the only specular reflectors other than water represented here are *lacustrine sediments*. All of these classes become clearly separable from water in the $\Delta\gamma/\Delta\alpha$ plot.

If we return once again to the vegetation species which are less easily separable from water in terms of their γ_{30} values (i.e. *Chenopodiaceae* , *Astrebla* and *Acacia*), and look at their distribution over the region (Figure 3.8), we find that they are, to a large extent, confined to those areas of the western interior where absorption dominates the nature of backscatter response.

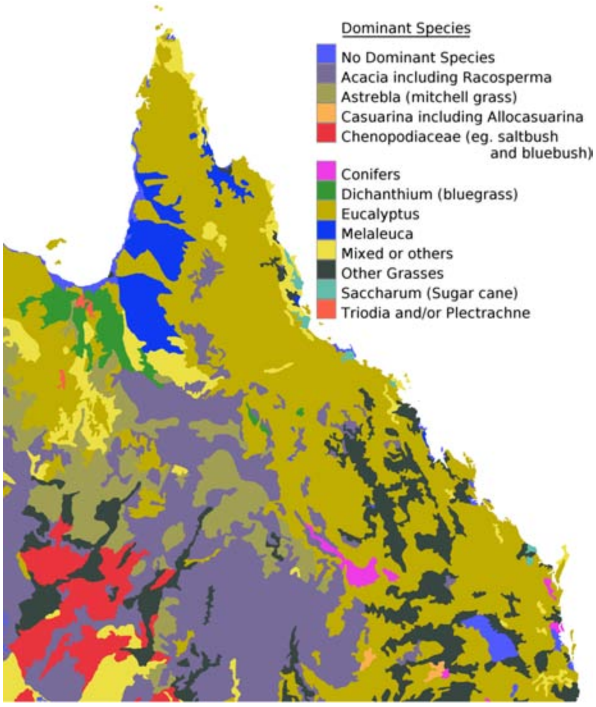

Figure 3.8: Map showing dominant vegetation species of Queensland (source Geoscience Australia)

3.5 Conclusion

We have established the slope for a linear model describing the location-specific variation of backscatter with incidence angle, by which we may normalise backscatter values to mitigate the effects of the variance of incidence angle across a swath. This is an important precursor to the appliance of a threshold in the classification of water.

Surface soil moisture and Bragg resonance have less of an effect on the change of backscatter with respect to incidence angle than on absolute backscatter values, providing a possible means to mitigate their hindering of land-water segmentation. The potential for the use of multiple images, at multiple incidence angles, to observe a quasi-instantaneous rate of change of backscatter with incidence angle in order to determine the presence of water with a greater degree of confidence is apparent. The potential use of such a method may be considered in the event of future C-Band ASAR missions providing sufficiently frequent coverage. This is

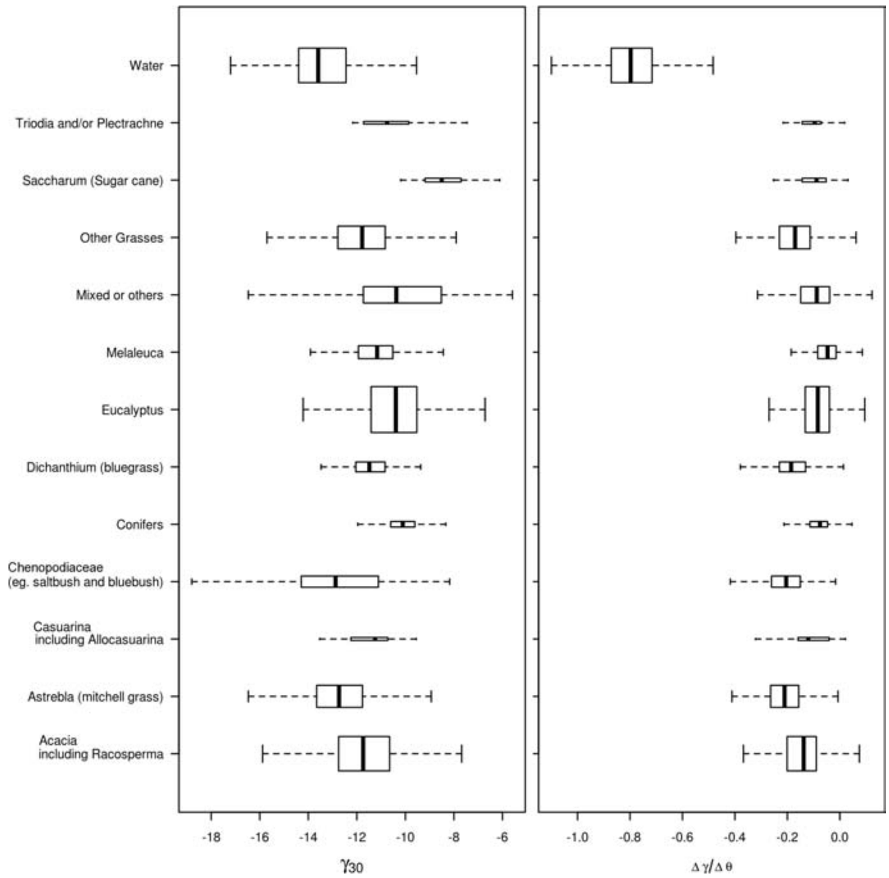

Figure 3.9: Box plots showing median, 25% and 75% percentiles (tics) for values of ground range projected backscatter γ (dB, left) and $\Delta\gamma/\Delta\alpha$ (right) against dominant vegetation species, based on 20,000 randomly-selected sites in Queensland. Box widths are proportional to number of sites within each category

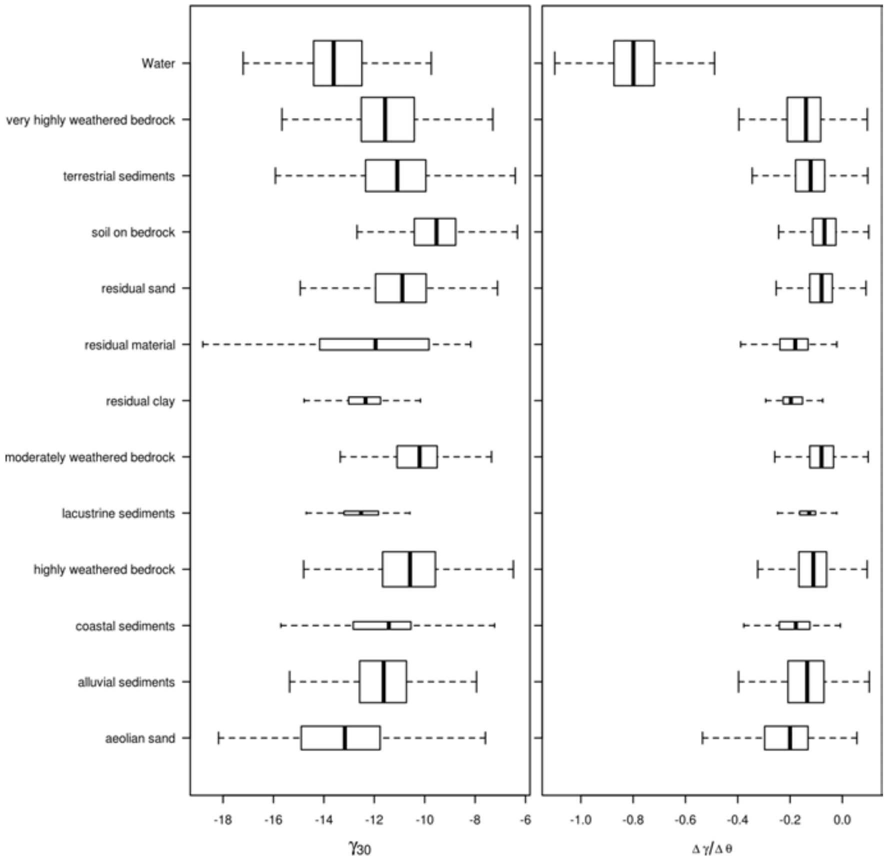

Figure 3.10: Box plot showing ground range projected backscatter γ (dB, left) and $\Delta\gamma/\Delta\alpha$ (right) against lithology classes, based on 20,000 randomly-selected sites in Queensland.

REGOLITH	γ_{30} MEAN	γ_{30} STD	$\Delta\gamma/\Delta\alpha$ MEAN	$\Delta\gamma/\Delta\alpha$ STD
Aeolian sand	**-13.19**	**1.98**	**-0.21**	**0.11**
Alluvial sediments	-11.73	1.58	-0.14	0.09
Coastal sediments	-11.69	1.97	-0.18	0.08
Highly weathered bedrock	-10.60	1.75	-0.11	0.07
Lacustrine sediments	-12.43	1.10	-0.13	0.05
Moderately weathered bedrock	-10.30	1.13	-0.08	0.07
Residual clay	-12.24	1.14	-0.18	0.05
Residual material	**-12.12**	**2.30**	**-0.18**	**0.07**
Residual sand	-10.93	1.38	-0.08	0.07
Soil on bedrock	-9.54	1.28	-0.07	0.07
Terrestrial sediments	-11.20	1.79	-0.12	0.08
Very highly weathered bedrock	-11.45	1.49	-0.14	0.08
Water	**-13.47**	**1.38**	**-0.78**	**0.13**

Table 3.2: Mean and standard deviation γ_{30} and $\Delta\gamma/\Delta\alpha$, for regolith classes

especially the case if, as seen, the high backscatter observed as a result of Bragg Resonance varies to a similar degree as would be observed from water where the phenomenon were not present. This would provide a possible means to eliminate an effect which is a significant barrier to the broad use of C-HH radar for the classification of water (Figure 3.11 demonstrates the results of Bragg Resonance well).

From the above analysis, we may conclude as follows:

1. For GM signals, the underlying regolith is the most important contributor to the level of backscatter under dry conditions.

2. Where there are sufficient contemporary GM images of a water body at varied incidence angles, the rate of change of backscatter with incidence angle may provide a far clearer means to map the water extents than a single threshold on backscatter alone.

3. Where absolute backscatter values are to be used as a threshold in the detection of water, absorption in very dry soils and specular reflection on lacustrine sediments are potential sources of commission errors.

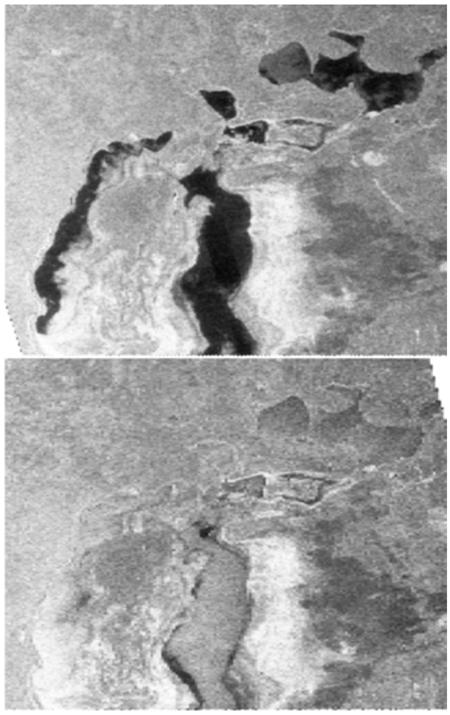

Figure 3.11: GM images of the Aral Sea on 18 June (above) and 21 June 2010 (below). The contrast is all but eliminated by what can only be the effects of Bragg Resonance due to particular wind conditions on 21 June.

Chapter 4

Use of ENVISAT ASAR Global Monitoring Mode to complement optical data in the mapping of rapid broad-scale flooding: case study of the 2010 Indus flood

Chapter context

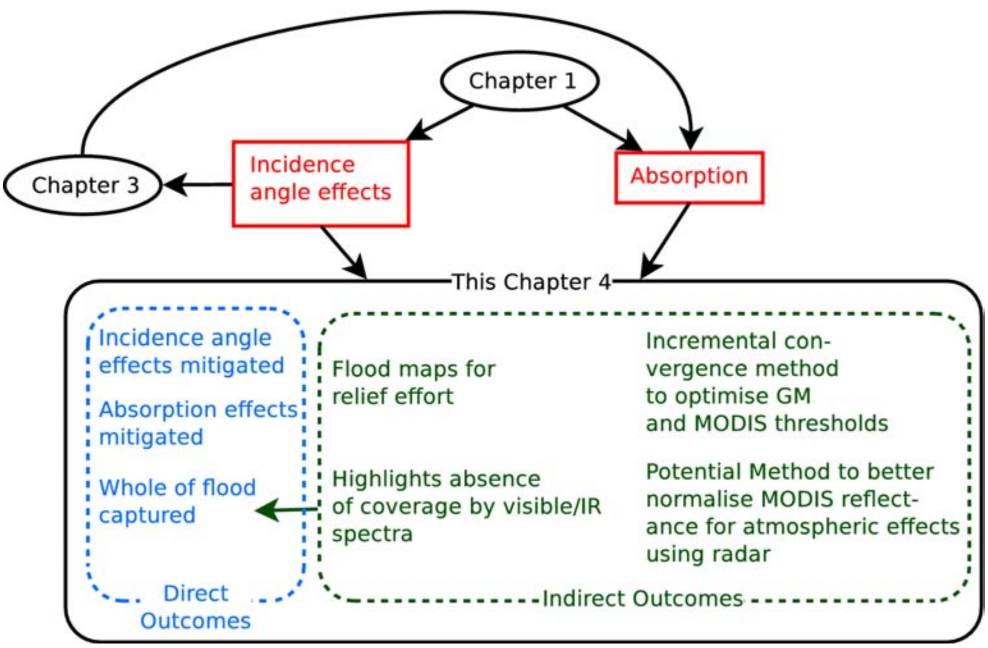

Abstract

Envisat ASAR Global Monitoring Mode (GM) data were used to produce maps of the extent of the 2010 flooding in Pakistan which were made available to the rapid response effort within 24 hours of acquisition. The high temporal frequency and independence of the data from cloud-free skies makes GM data a viable tool for mapping flood waters during those periods where optical satellite data is unavailable, which may be crucial to rapid response disaster planning. Image differencing techniques were used, with pre-flood baseline image backscatter values being deducted from target values to eliminate regions with a permanent flood-like radar response due to volume scattering and attenuation, and to highlight the low response caused by specular reflection by open flood water. The effect of local incidence angle on the received signal was mitigated by ensuring that the deducted image was acquired from the same orbit track as the target image. Poor separability of the water class with land in areas beyond the river channels was tackled using a region-growing algorithm which sought threshold-conformance from seed pixels at the center of the river channels. The resultant mapped extents were tested against MODIS SWIR data where available, with encouraging results.

4.1 Introduction

4.1.1 Pakistan floods

Over the 2010 monsoon season, Pakistan saw extensive flooding of the Indus river and its tributaries, which affected over 20 million people, damaging over 2 million hectares of crop land and causing the loss of 1,985 lives (NDMA, 2011). Heavy rainfall in the northern regions of the Khyber Pakhtunhwa, reaching 280 mm on 29 July, damaged major irrigation headworks on the Swat River at Munda, which were built to a discharge capacity of 4.5 Mls^{-1} and which were damaged by the peak discharge of 8.5 Mls^{-1}. Further rainfall in Gilgit and Jammu and Kashmir and further south in Balochistan, contributed further to the huge body of water which flooded irrigation channels and agricultural land covering tens of thousands of square kilometers. The UN Food and Agricultural Organization estimate losses of wheat stocks at around 450,000 tonnes (Fair, 2011). The Damage Needs Assessment conducted by the World Bank estimated that the recovery from the floods would cost between \$8.7 and \$10.9 billion (WBG, 2011).

To facilitate the international relief effort in such crises, maps are made available in near real time by facilities such as NASA's *MODIS Rapid Response System*, which makes use of the Moderate Resolution Imaging Spectroradiometer (MODIS) on board NASA's Aqua and Terra satellites. Such instruments are, however, limited by the cloud cover that is often present for some time after such flood events. It is largely for this reason that, in recent years, satellite-borne radar instruments have attracted much research into their viability as a means to map flooding, due to their ability to penetrate cloud cover and to their independence from the relative position of the sun (Rosenqvist *et al.*, 2007; Waisurasingha *et al.*, 2007; Wilson & Rashid, 2005).

The classification of water with satellite radar data is problematic and error-prone, particularly when some of the main environmental factors affecting the result, such as wind speed and direction and soil moisture, are unknown. The clear advantage of the independence from cloud cover may result in the availability of radar data where more reliable optical data is not available. Revisit time is an important feature of remotely sensed data used for disaster management. The COSMO-SkyMed constellation [1] comprises a cluster of four X-band SAR sensors on the same orbit path which are capable of a revisit time of less than 12 hours. Most radar sensors such as the *Advanced Synthetic Aperture Radar* (ASAR) aboard the European Space Agency's (ESA) Envisat satellite, and the *Phased Array type L-band Synthetic Aperture Radar* (PALSAR) on the Japanese Aerospace Exploration Agency's (JAXA) ALOS satellite[2] have repeat orbit cycles of more than a month, but are able to provide a higher repeat coverage thanks to operation modes which overlap regions at different incidence angles on adjacent orbits. Here we take a closer look at data from the ASAR sensor operating in Global Monitoring (GM) mode, which is systematically acquired when data in other configurations is not required. GM data is made available in near real-time

[1] http://www.cosmo-skymed.it/

[2] both of which satellites have unfortunately become defunct recently

for download to parties with at least a Category-1 fast-track agreement with ESA. The data is available quickly because it is preprocessed at the sensor, before being transmitted down to one of two ground stations in Europe. This is made possible by keeping file sizes and processing requirements low, by using a coarse resolution (pixel size is 500m, spatial resolution is 1km). Such a coarse resolution over the full range of incidence angles ($12°$ to $44°$) may prohibit the data's viability as an alternative means to map flooding, but we believe that its temporal frequency and ready availability give the data potential advantages that warrant further investigation. The following questions emerge:

- Is the frequency of GM coverage such that it can provide an alternative source of data to map flooding when cloud cover prohibits the use of optical data?
- Can effects due to factors such as incidence angle be eliminated?
- Will the radiometric uncertainty of signals received from partially and totally inundated areas and non-flooded areas allow the classification of flooding to a level of accuracy sufficient to produce useful maps, given the coarse resolution of GM data?

4.2 Study Area

The flood plain of the Indus River occupies nearly half of Pakistan's area. Bounded by the Karakoram, Hindu Kush and Pamir mountain ranges to the north and the Balochistan Plateau to the west, the Indus and its tributaries flow southwards from the northern ranges to the Arabian Sea more than 1000km to the south (see Figure 4.1).

Having left the ranges, the river falls only a few hundred metres across this distance. Outside of the major cities of Lahore in the north and Karachi in the south, much of Pakistan's population lives close to the Indus and Chenab rivers, farming wheat, cotton, rice and other crops to sustain its population of some 170 million. The 2010 monsoon season saw higher than usual rainfall (Figure 4.2 refers), contributing to floods which started affecting populated areas in the north

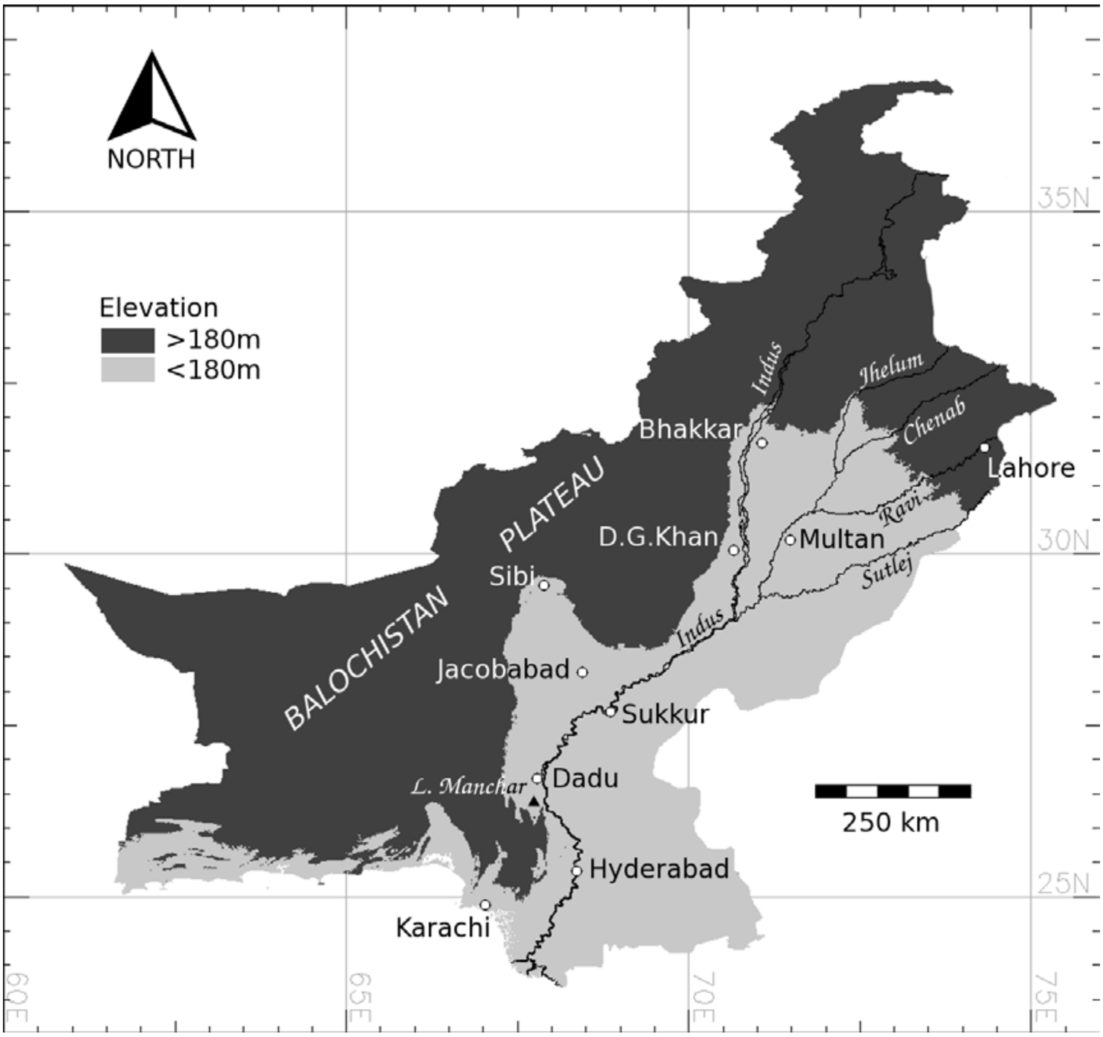

Figure 4.1: Pakistan and the Indus-Chenab flood plain

in July and progressed southwards throughout the following months, remaining in some areas throughout October and beyond.

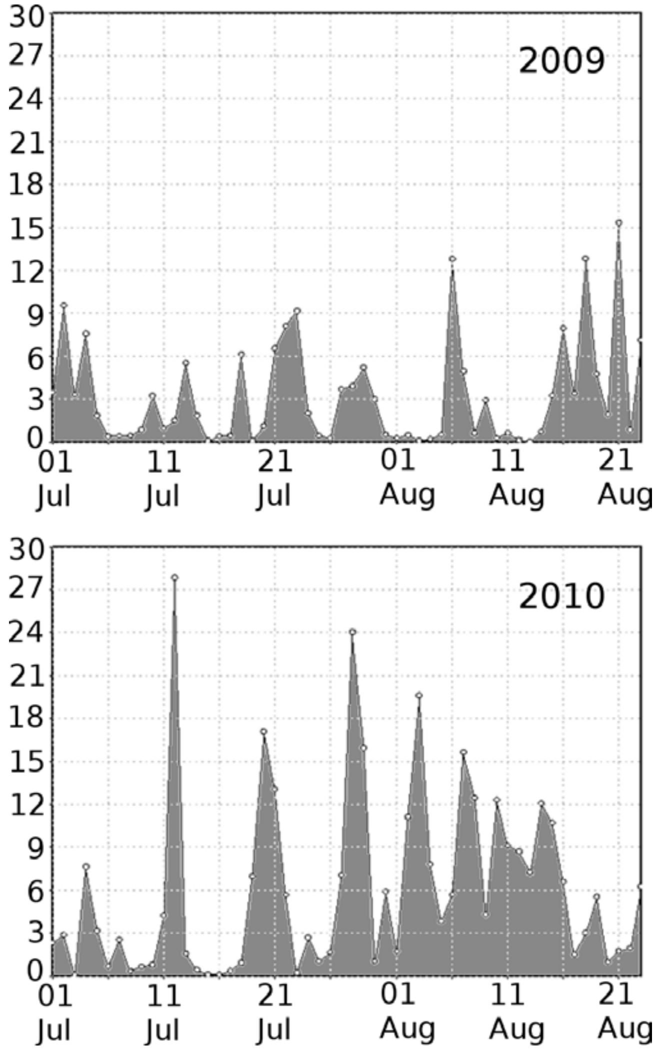

Figure 4.2: Daily rainfall (mm) across the Pakistan region (Lat.28N–35N, Long.70E–74E) in July/August 2009 (above) and 2010 (below). Reproduced from GESDISC (2011).

4.3 Theoretical Basis

Fundamental choices of radar data rest on wavelength, polarisation configuration, spatial and temporal frequency. Radar signals will interact with their target in a manner dictated by structural, textural and dielectric properties of the target surface. Structural and textural properties are matters of scale, and must be considered in relation to the wavelength of the radar signal. When considering the detection of flood water, we are interested in the radar response from water itself, from the surrounding land cover and, where partial inundation occurs, a combination of the two. The radar response from each of these three categories is a complex combination of effects. In the case of vegetation, C-band radar (wavelength λ = 3.75–7.5 cm) will tend to interact with small branches and leaves, and L-band (λ = 15–30cm) with larger branches and trunks, each in a scale of order comparable to their own wavelength. Where partial inundation occurs, the radar signal may interact multiple times between the emergent structure (vegetation or buildings, for example), in a phenomenon known as dihedral scattering (or "double-bounce"), resulting in a very high return signal. The extent of this occurrence is dependent, therefore, on the relative scale of the emergent structure with respect to the wavelength of the signal. Where open water is found, if the surface is smooth, much of the radar signal is reflected away from the sensor, resulting in a low backscatter response. The extent of the return signal in this case has a sinusoidal relationship with the angle that the radar is incident to the surface of the water. However, where there are regular waves on the surface of the water, Bragg resonance can result in a very high return signal (e.g. Schaber *et al.* (1997)). The degree to which this occurs depends once again upon the relationship between the scale of the wave and the wavelength of the radar signal. C-band radar is sensitive mainly to small capillary waves and L-band to larger "chop", as might be expected. The alignment of the waves with respect to the direction of the incident radar wave is also important here. The effect is greatest when the incident signal is orthogonal to the alignment of the wave (or parallel to the wind direction), and may not occur at all when the radar signal and the wave direction are parallel (Liebe *et al.*, 2009).Finally, the strength of the radar signal returned to the sensor is reduced by an increasing incidence angle (Monsiváis *et al.*, 2006).

Whilst simple geometry allows us to calculate the theoretical degree of this effect, its precise value is the combination of various target characteristics averaged over a pixel-space, and is therefore not readily known for a given time. The change in radar signal for a given degree increase in incidence angle is greater for a specular reflector such as smooth water, than for a diffuse or volume scatterer such as bare soil or vegetation. The particular environment encountered in Pakistan presents a further complication in the detection of flood waters using radar data. Desert areas which remain dry during the flood event absorb and attenuate microwave radiation (Robinson *et al.*, 2006; Schaber *et al.*, 1997), returning a low signal which encroaches into the range of that expected by open water. The difference with the desert response is its relative permanency, and so by deducting values from a GM image taken from the same orbit track prior to the flood, we are able to discern the water from the desert. Digital Numbers (DN) in ASAR detected products correspond to brightness amplitude. The radar backscatter coefficient σ^0 may be calculated from the DN values by:

$$\sigma^0 = \frac{\mathrm{DN}^2}{K} \cdot \sin\alpha \qquad (4.1)$$

where K is the absolute calibration constant (ESA, 2004). However, the received backscatter is further dependent on α by some function F which is peculiar to the target environmental conditions (Baghdadi *et al.*, 2001; Ulaby *et al.*, 1982) such that

$$\sigma_0^0 = \sigma_\alpha^0 \cdot F(\alpha) \qquad (4.2)$$

Given a reasonably close temporal separation of images, and in the absence of flooding, the environmental conditions, and therefore the nature of F, are similar for a given pixel in the target image to the corresponding pixel in the *dry* baseline offset.

Converting to decibels and deducting the base backscatter values σ_b^0 from the target values σ_t^0 gives

$$\Delta\sigma^0 = 10\left[\log(\sigma_t^0) + \log(F(\alpha)) - \log(\sigma_b^0) - \log(F(\alpha))\right] \tag{4.3}$$

Substituting 4.1 into 4.3 gives

$$\Delta\sigma^0 = 20 \cdot \log\left(\frac{DN_1}{DN_0}\right) \tag{4.4}$$

This assumes that the difference in α between the two images is negligible. This difference between local incidence angles for the image pairs was found to have a mean value of -0.02°, with a standard deviation across the region of interest of 0.08°. Taking an extreme case of MEAN $- 3 \times$ STDDEV gives a difference of -0.26°, which would result in an error in the final difference image of 0.02 dB at 44° and 0.07 dB at 15°. Given the radiometric uncertainty in the GM data of 1.54–1.74 dB (ESA, 2007a), such differences may be disregarded for our purposes.

4.3.1 Expected values

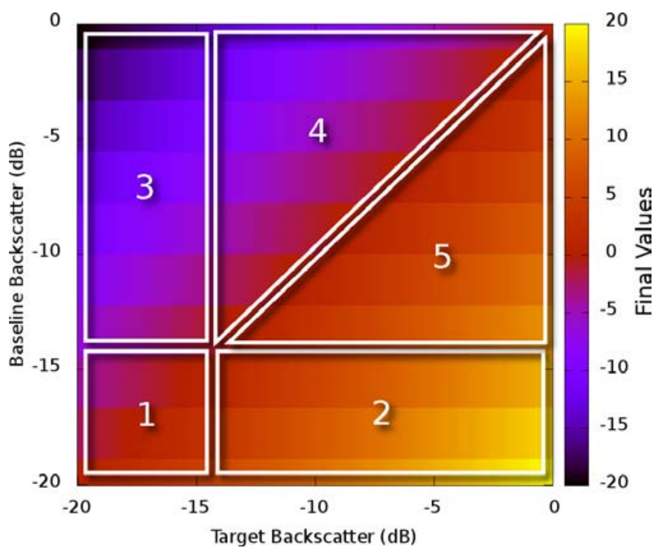

Figure 4.3: Key map to describe range of $\Delta\sigma^0$ values derived from image differencing process

The range of values encountered in the resultant $\Delta\sigma^0$ image are represented graphically in Fig. 4.3, and may be categorised as follows:

1. Areas with values common to both the target and the baseline image are shown in red (values close to zero), and include permanent water and desert, shown in Box 1, together with all other unchanged values between Boxes 4 and 5.

2. Would occur where water were present in the baseline image and not in the target image (which is unexpected). Such values are far more likely to represent the surface of desert or very dry radar-dark soils becoming wet, which greatly increases backscatter (Robinson *et al.*, 2006). These values can also represent the occurrence of Bragg Resonance due to wind effects on permanent water (Schaber *et al.*, 1997).

3. Flooding. Mid-high values in the baseline image have become mid-low.

4. These have values below the threshold which may therefore be rightly or wrongly classified as flood water. It is with the intent to capture such errors that the region-growing algorithm, making spacial association relevant to the classification decision process, is adopted here.

5. Mid-high baseline values which undergo a small-large increase in backscatter values between the baseline and target images. Again, this can represent a dry surface becoming wet, but could also encompass open flood waters where conditions are right for wind-induced Bragg resonance to return a high backscatter signal.

In the image differencing process, permanent water bodies, which are common to the baseline and target images, are removed. However, where water bodies are permanent and semi-permanent, their extents are easily mapped and overlain if required. We are interested here in mapping inundation outside of the current river coarse. The filling-in of permanent water after the flood classification and prior to testing would increase accuracy, but the results here are left as they are, with such limitations remaining exposed. Part of the reason for this is that the flood dynamics of the Pakistani rivers are complex, punctuated by sudden effects such as the breaching of the many levees which regulate their flow, and we therefore prefer in this instance to make no assumptions as to any possible deviations to the normal channel flow.

4.4 Method

4.4.1 Data acquisition

Data was acquired systematically via download from ESA's Kiruna and ESRIN ground stations, made available in a two-week moving window through the Category 1 Fast Track Registration agreement.

4.4.2 Coverage

Area and frequency of cover of the region of interest was compared with MODIS Aqua and Terra data. In order to test comparative coverage, a mask was created by buffering the Indus river by 50km. For each day of August, the sum of pixels covered by GM data for that day were recorded along with the number of cloud-free pixels contained within the MODIS Terra and Aqua images, as a percentage of the total pixels for the masked region.

4.4.3 Image Preprocessing

Incidence angles (θ), slant-range times (SRT) and geographical coordinates are provided within the raw GM data file, corresponding to tie points that form a grid with a spacing of 80–85 pixels across the image. Interpolation of θ and SRT was carried out first across the swath, and then the azimuth direction, to obtain values for each pixel. Terrain correction was also carried out in the frame of reference of the raw data file, due to the fact that columns and rows run parallel to the azimuth and swath respectively, making the geometry involved in the calculation much simpler. For this purpose, SRTM 7.5 arc-second Digital Elevation Model (DEM) data (Jarvis *et al.*, 2008; Reuter *et al.*, 2007) were projected into the local x–y coordinate system. The incidence angles θ and the DEM were then used to calculate local incidence angles (α) for each pixel. Both the orthorectified Digital Number (DN) and α surfaces were then transformed to geographic coordinates by third order polynomial transformation.

4.4.4 Image Differencing

For each target image acquired over the study area, a matching image from the same orbit track was chosen as a baseline, being the latest available image covering all of the azimuth extent of the target and occurring prior to the commencement of the flood event. Details of the data used are shown in Table 4.1. The raw data files were registered in a database, at which time tie point data, including coordinates, incidence angles and slant-range times were extracted.

Table 4.1: GM Data used in this study. The *Baseline Cycle* refers to the orbit cycle corresponding to the deducted baseline data

	Date	Orbit Cycle	Orbit Track	Baseline Cycle
1	2010-04-01	88	134	-
2	2010-04-17	88	363	-
3	2010-05-13	89	234	-
4	2010-05-16	89	277	-
5	2010-05-26	89	420	-
6	2010-06-01	90	5	-
7	2010-06-06	90	84	-
8	2010-06-07	90	91	-
9	2010-06-12	90	170	-
10	2010-06-15	90	213	-
11	2010-06-17	90	234	89
12	2010-06-19	90	270	-
13	2010-06-20	90	277	89
14	2010-06-22	90	313	-
15	2010-06-23	90	320	-
16	2010-06-28	90	399	-
17	2010-07-01	90	442	-
18	2010-07-03	90	463	-
19	2010-07-04	90	485	-
20	2010-07-05	90	499	-
21	2010-07-09	91	48	-
22	2010-07-11	91	84	90
23	2010-07-12	91	91	90
24	2010-07-15	91	134	88
25	2010-07-17	91	170	90

Continued on next page

Table 4.1: GM Data used in this study (Contd.)

	Date	Orbit Cycle	Orbit Track	Baseline Cycle
26	2010-07-22	91	234	89
27	2010-07-24	91	270	90
28	2010-07-25	91	277	89
29	2010-07-27	91	313	90
30	2010-07-28	91	320	90
31	2010-07-31	91	363	88
32	2010-08-02	91	399	90
33	2010-08-04	91	420	89
34	2010-08-05	91	442	90
35	2010-08-07	91	463	90
36	2010-08-08	91	485	90
37	2010-08-09	91	499	90
38	2010-08-10	92	5	90
39	2010-08-13	92	48	91
40	2010-08-15	92	84	90
41	2010-08-16	92	91	90
42	2010-08-19	92	134	88
43	2010-08-21	92	170	90
44	2010-08-24	92	213	90
45	2010-08-26	92	234	89
46	2010-08-28	92	270	90
47	2010-08-29	92	277	89
48	2010-08-31	92	313	90
49	2010-09-01	92	320	90
50	2010-09-04	92	363	88
51	2010-09-06	92	399	90
52	2010-09-08	92	420	89
53	2010-09-09	92	442	90
54	2010-09-11	92	463	90
55	2010-09-12	92	485	90
56	2010-09-13	92	499	90
57	2010-09-14	93	5	90
58	2010-09-17	93	48	91
59	2010-09-20	93	91	90
60	2010-09-25	93	170	90

Continued on next page

Table 4.1: GM Data used in this study (Contd.)

	Date	Orbit Cycle	Orbit Track	Baseline Cycle
61	2010-09-28	93	213	90
62	2010-10-05	93	313	90
63	2010-10-06	93	320	90
64	2010-10-09	93	363	88
65	2010-10-14	93	442	90
66	2010-10-17	93	485	90

4.4.5 Baseline datasets from MODIS

MODIS data were chosen from the results of the cloud-cover study described in Section 4.4.2, for three dates, with which to establish GM data classification thresholds and by which to gauge the accuracy of the classification process.

4.4.6 Thresholding and Classification

In order to obtain a binary map of the inundated regions, a region-growing function provided as part of the GRASS GIS package (GRASS Development Team, 2009) was used. The *r.lake* function is primarily intended to fill a lake to a target water level from a given start point, or seed. This starting point can be a set of coordinates, or a raster map in which the seed points are represented by non-null values. The function will grow a region, starting at the seed points, until a specified water level is reached, as determined by a given DEM. In our case, the seed was a rasterised line-type shape file of Pakistan's river channels, the "DEM" was the $\Delta\sigma^0$ image, and the "water level" was set to the various thresholds tested. This method allows the use of a threshold value that is well inside the standard deviation of values for non-flooded areas, with the provision that the selected pixels are adjacent to other selected pixels as grown from the river channels. In order to try to mitigate errors of commission on the outskirts of the selected regions, a 3×3 modal neighbourhood filter was then applied to the binary classification.

MODIS band 6 data, representing Short Wave Infra-Red (SWIR) radiation (λ

= 1628–1652 nm), were used to map flooding and to establish thresholds to use with the radar images. Light in this short-wave infra-red waveband is absorbed by all but the most turbid water, and is therefore often used to map water (e.g. Dheeravath *et al.* (2010); Ordoyne & Friedl (2008)). Whilst MODIS reflectance bands provided by USGS attempt to achieve surface reflectance values, it is the case that attenuators such as thin cloud, that vary from image to image, preclude the use of a single absolute threshold applied to MODIS data in order to establish the benchmark. Fig. 4.4 shows the density plot of MODIS Band 6 reflectance values over the flooded region from two images, taken two days apart. There is a clear full-range displacement of reflectance values of 0.03–0.05.

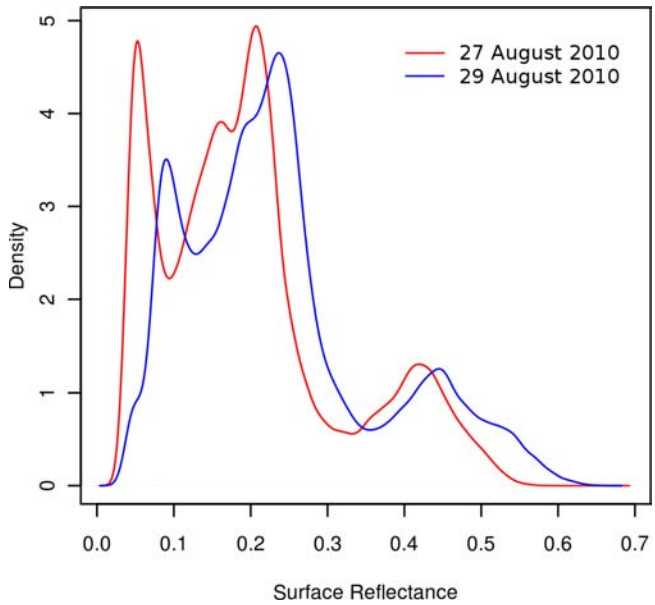

Figure 4.4: Density plot of MODIS Band 6 reflectance values over the flooded region on 27 and 29 August 2010. The peaks at reflectance values of 0.05 and 0.1 represent water, as is seen later in the kappa analyses.

To account for this uncertainty, a bivariate sensitivity analysis was carried out, matching conformance of a range of radar backscatter thresholds in the radar images against a range of thresholds in the contemporaneous MODIS images. A peak in cross-correlation outside of the extreme threshold values (which would classify the whole image as flooded or non-flooded) would only likely represent common optimal flooded/non-flooded thresholds, as beyond the low signal response to water common to SWIR and radar data, the characteristic responses of each of the wavebands are largely independent. In order to gauge the performance of classifications under varied thresholds, it is insufficient to simply determine the percentage of coincidence of allocated classes, as this gives a distorted result. If, for example, a flooded area comprises 5% of the region under study, then a classification omitting all the flooding would, with such a method of assessment, be 95% correct. For this reason, Cohen's kappa statistic is often used as a "coefficient of agreement" between two classification processes (Cohen, 1960; Foody, 2006; Hunt *et al.*, 2010; Tolpekin & Stein, 2009). The kappa statistic κ is calculated as

$$\kappa = \frac{p_0 - p_c}{1 - p_c}$$

where p_0 is the proportion of pixels in which agreement is observed and p_c is the theoretical proportion expected by chance selection (Cohen, 1960). It is the latter parameter which is perceived in certain instances to be problematic, as the observed proportion of allocation to each class is used as a basis to calculate random expectation (in effect, assuming that the decision process will always allocate the correct proportion of pixels to each class, whether the specific allocations are correct or not). This is not considered an issue in our case. Firstly, the assumption of proportion is observed to be approximately correct. Secondly, we are, while in pursuit of an optimal threshold, seeking a relative measure of classification accuracy rather than an absolute one.

Where good clear MODIS data were available during the flood event, κ was calculated for a matrix of classifications made with SWIR reflectance upper thresholds ranging between 0.05 and 0.25, and GM (difference image) $\Delta\sigma^0$ upper thresholds ranging between -10 and 0 dB. From this, the optimal backscatter thresholds could be observed, together with their sensitivity and inter-image variability. A comparison was made using the single target GM image, with a ground-range projected backscatter (γ) upper threshold range between -20 and 0 dB. A threshold to be used where MODIS data were unavailable was decided in this way, and its suitability assessed on a further series of κ analyses on another date for which MODIS data were available.

4.5 Results

4.5.1 Coverage

During the 98 days between 11 July and 17 October 2010, the average repeat coverage period by GM data over the region studied was around 9 days (see Figure 4.5). Though this would be insufficient for a complete time series of the flood dynamics, it can feasibly serve to fill the gaps in information gained from optical sensors such as MODIS caused by the presence of cloud cover. Figure 4.6 shows a comparison of percentage of the full flood extent captured independently by MODIS Terra, MODIS Aqua and GM data, for each day of August 2010. Cloud cover limited the use of MODIS data through the first week of August, during the build-up of flood waters north of Sukkur, whilst there were sufficient GM data to build a picture of the flood extents at this time. Much of the rain that caused the floods in Pakistan fell on the ranges to the north, and as such, there were significant periods free of cloud further down stream where most of the catastrophic flooding occurred, and so in this respect, as a "dry flood", this event enjoyed better coverage than most similar events with optical data, and in many other flood events, it may be reasonably assumed that the difference in availability of data could be far greater.

4.5.2 Image Differencing

It can be seen from the probability density functions shown in Figure 4.7 that attempts to map flooding using a simple threshold would result in large errors of commission and omission, due to the range of overlap of values. In the non-flooded areas, as we have chosen a region close to the known flooding, the slight rise in average backscatter value may be due in part to increased surface soil moisture (Pathe *et al.*, 2009) in the vicinity of the flood and possibly from dihedral scattering from vegetation emergent from flood waters at the boundary of the flooded class regions (Hess *et al.*, 2003). In addition to native vegetation close to the main river channel, wheat, cotton, onion, sunflower, rice, pulses and dates are all grown in the region (Ashraf & Majeed, 2006). The large standard deviation of $\Delta\sigma^0$ values in the non-flooded regions can be explained by a couple of factors.

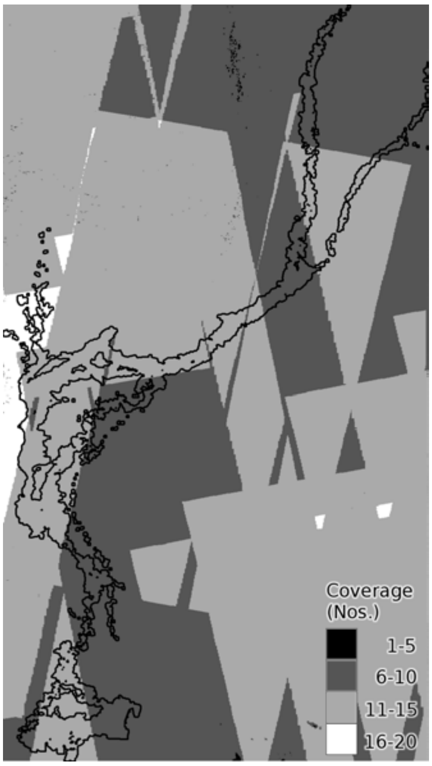

Figure 4.5: Count of frequency of cover by GM data over the 98 day study period. The black outlines represents the maximum flood extent

Firstly the propensity of radar data to contain noise, most of which is speckle. This is characterised by high and low valued pixels whose values represent interference arising from the use of a coherent electromagnetic radiation source, rather than having anything to do with the target. Speckle can lead to sharp differences in values between any two radar images. Secondly, variations in the immediate recent rainfall history can cause large differences in backscatter value. Not only moist soil, but also wet vegetation tends to give a high backscatter response at C-band (e.g. Ulaby *et al.* (1982)). A drop in radar value in non-flooded areas can be seen where smooth specular reflecting alluvial sediments, for example, dry out. Low backscatter also occurs where the signal is absorbed / attenuated by very dry sand (Robinson *et al.*, 2006; Schaber *et al.*, 1997), though such a fall from relatively wet to very dry conditions necessary to produce a low $\Delta\sigma^0$ value are unlikely to have occurred so close to the main channel.

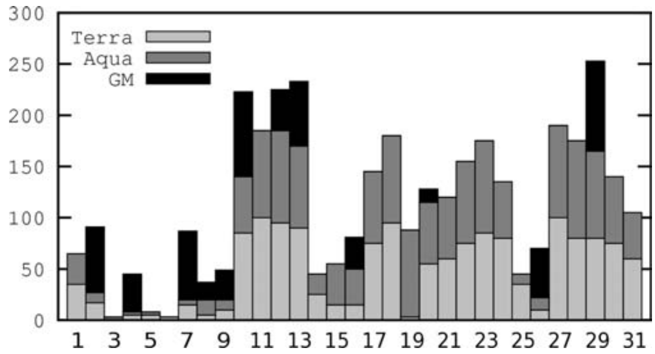

Figure 4.6: Percentage of full flood extent covered on each day of August 2010 by MODIS Terra, MODIS Aqua and GM data

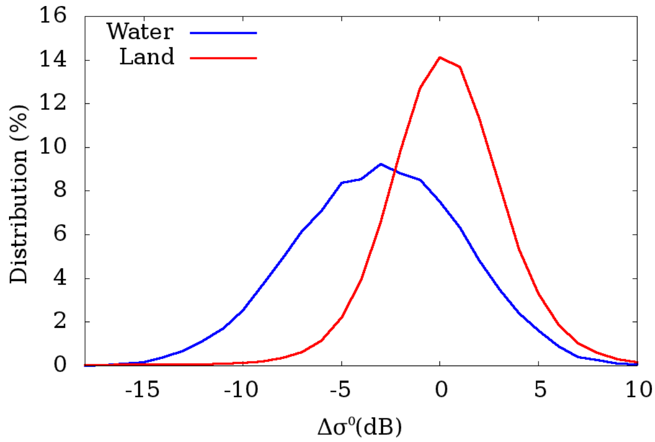

Figure 4.7: Probability density functions for $\Delta\sigma^0$ for water and land over the flooded region on 29 August 2010, as determined by classification using MODIS SWIR Reflectance Threshold of 0.13

The distribution of $\Delta\sigma^0$ values in the flooded region is perhaps best explained in terms of what may be observed in Figure 4.8. The images centre on the segment of the Indus river running between Sukkur and Dadu, where its course changes from a south-west to a south-east direction. The image on the left shows radar backscatter values acquired on 20 August 2010. The image on the right shows the same values, with those of a previous cycle deducted. The regions labelled D and F represent sections of the river characterised by a large flood channel superimposed with the meandering and anabranching main Indus channel (see Figure 4.9). At the time of acquisition, this large channel was completely flooded, and appears as radar dark in the first image. However, due to the fact that alluvial sediment can also act as a specular reflector in the same way as water, much of the D region is punctuated with mid-range value pixels in the difference image, and region F is all but indistinguishable from non-flooded land. The large area at A with low backscatter values in the first image shows that part of the lowlands which protrudes into the Sulaiman mountains of Balochistan, comprising mainly the districts of Bolan and Sibi. This region is normally dry, with an annual rainfall of 200–250 mm. The low backscatter is considered to be the result of attenuation and absorption of the signal, rather than of specular reflection. The low backscatter values are clearly offset in the difference image, leaving only those low values representing the rivers that run west below A and then south towards Lake Manchar below B. Similarly, the dark region in the first image at C is at the western edge of the Thar Desert. The bright strip running north-south immediately to the right of C shows the relatively high backscatter from the vegetation bordering the Nara Canal and its irrigated hinterland. As with A, the response of both the irrigated strip and the desert are common to the consecutive orbit cycles, and hence do not appear in the difference image.

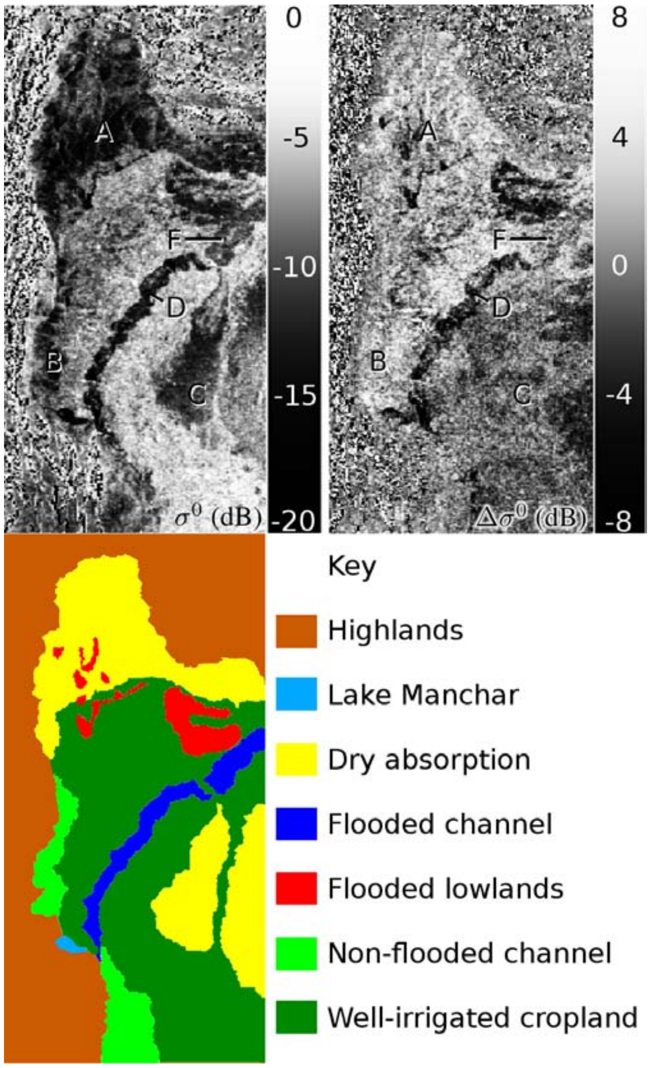

Figure 4.8: The region between Jacobabad and Nawabshah in mid August 2010. The image on the left shows backscatter values in decibels. Smooth open water is commonly represented by values of around -16dB or below. The image on the right shows the same data, with the values from the previous cycle along the same orbit track having been deducted. A better understanding of the true extent of flooding can be discerned by a difference of around -4dB in this image.

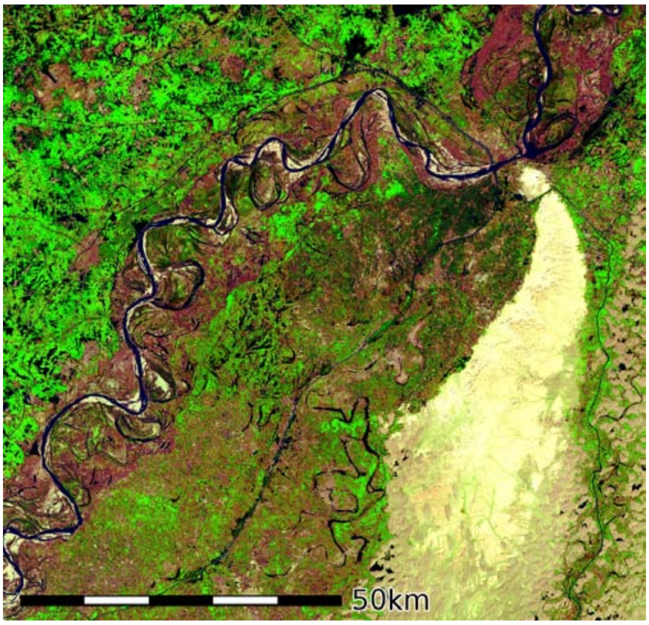

Figure 4.9: Landsat composite colour image of the Indus and its floodplain southwest of Sukkur. The Nara canal is seen running north–south to the right of the image

4.5.3 Thresholding and Classification

A comparison of value profiles of $\Delta\sigma^0$ and MODIS Band 6 across a section of the flooded Indus, as at 10 August 2010, is shown in Figure 4.10. It can be seen that, at this scale, the choice of threshold of Band 6 to classify water is not particularly sensitive between around 0.2 and 0.15 units, where the profile crosses the flooded area, with relatively few pixels taking intermediate values. There is little doubt that where SWIR reflectance values fall close to zero on all legs, there is open water. In these areas along legs 1, 2 and 3, the corresponding $\Delta\sigma^0$ values fall below -2 dB, corresponding to a fall in backscatter values caused by increased specular reflection, due to the increased presence of water. Along legs 4 and 5, however, there are large fluctuations of $\Delta\sigma^0$ values. This is mainly due to the fact that, as mentioned before, the alluvial sediment can also act as a specular reflector in the same way as water, thus the dry baseline low pixel values are offset from the target image, producing mid-range difference values. Areas where a slight rise in SWIR reflectance coincides with a sharp rise in $\Delta\sigma^0$ (such as at 40km and 120km on the x-axis) are believed to represent partial inundation with emergent vegetation, the high $\Delta\sigma^0$ values being the result of dihedral scatter.

These profiles demonstrate the volatility of $\Delta\sigma^0$ values, especially in those areas that show a low backscatter response under non-flooded conditions, as discussed above. It was found that the choice of a simple $\Delta\sigma^0$ threshold to suit conditions in the main river channel would result in many regions mapped incorrectly as flooding in areas well away from the river channels. For this reason it was decided to make contiguousness with other flooded pixels adjacent to the river channels a condition of the flood class, in addition to the satisfaction of the $\Delta\sigma^0$ threshold. Therefore flooded regions were mapped by growing contiguous areas that satisfied the threshold criterion from pixels at the centre of the river channel outwards, using the technique described in Section 4.4.6.

4.5.3.1 Bivariate sensitivity analysis to determine threshold

κ statistic values calculated in the sensitivity analysis described in section 4.4.6 are shown in Figs. 4.11, 4.12 and 4.13. It can be seen that, while the optimal SWIR reflectance threshold varies between the dates, the optimal $\Delta\sigma^0$ threshold

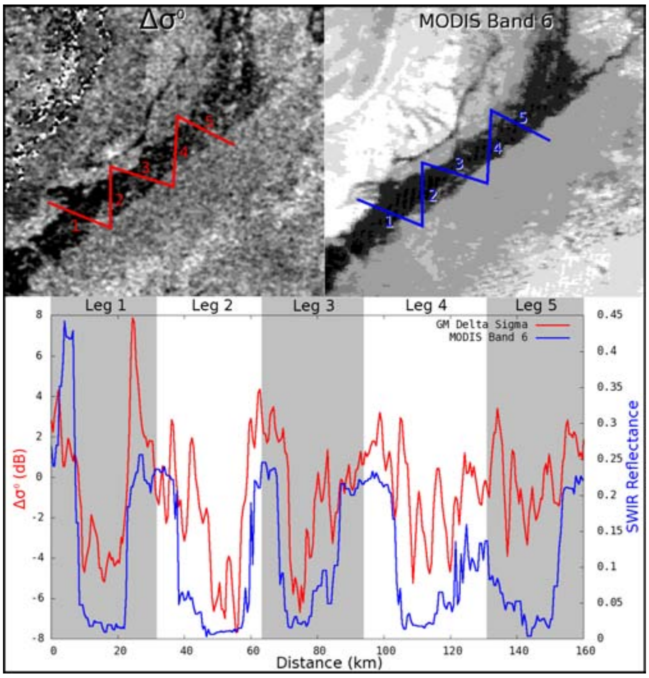

Figure 4.10: Comparison of value profiles of $\Delta\sigma^0$ (top-left image, red profile) and MODIS Band 6 (1628–1652 nm) (top-right image, blue profile) from a section of the flooded Indus on 10 August 2010

of around -2dB is common to the three instances. The reasons for the differences in the MODIS thresholds was discussed in section 4.4.6 and the difference between the optimal reflectance thresholds of 0.07 and 0.11 on 27 and 29 August respectively are manifest in the shift in distribution of values between the two MODIS images that was shown in Fig. 4.4.

Fig. 4.14 shows flood extent estimates from MODIS (top), the single contemporaneous GM image (centre) and the GM Difference image (bottom), each using thresholds optimized from the process described above.

With the single image in the centre, there are two processes resulting in the low backscatter response. To the north-west of the dashed line, the low response is dominated by specular reflection from the surface of flood waters. To the south-east of the dashed line, the low backscatter response is caused by absorption in desert sands. The wrongly classified desert area is eliminated in the third image, as this low response from the desert areas is common to both the target image

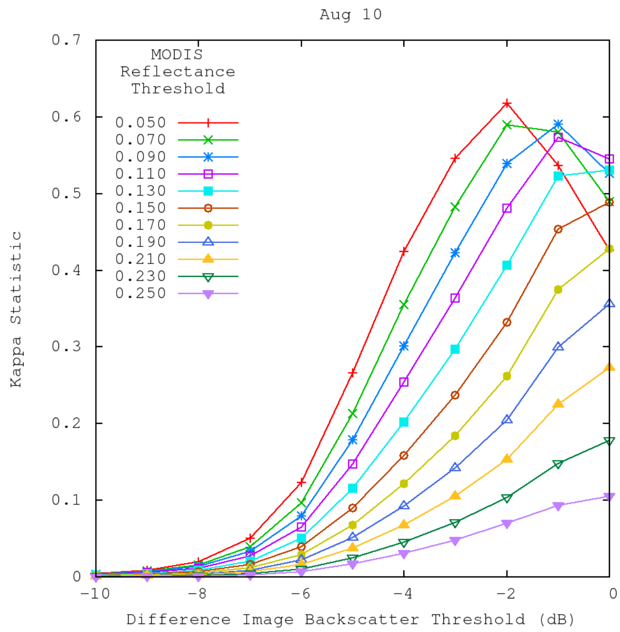

Figure 4.11: κ statistic calculated for individual classifications of flooding on August 10, 2010, based upon $\Delta\sigma^0$ thresholds ranging from -10 to 0 dB. The series represents corresponding MODIS Band 6 reflectance thresholds used in the reference image, ranging from 0.05 to 0.25

and its baseline partner, and is therefore subtracted out.

When comparing the MODIS (top) image with the Difference image (bottom), it can be seen that whilst the boundaries of the flood are well defined, areas of permanent water or radar-dark flood plain regions are also eliminated. In the central image derived from the single GM data set, such areas which do fall within the flooded region are more completely defined. With a priori knowledge of terrain and environmental conditions, one can mask out desert areas and achieve a more accurate classification using the single image. Masking must be very precise, however, as some absorption areas can lie extremely close to the flooded region, as can be seen from the area encircled in red in the middle image. Assuming sufficient information is available within the time frame allowed, the higher accuracy which may be achieved by such masking is demonstrated in Fig. 4.15, where a κ value of 0.7 is achieved. Note that the precedence of MODIS SWIR thresholds matches that seen in Fig. 4.12, as expected.

Where a fast indicator of the extent of flooding through otherwise dry land is urgently required, we propose that the image differencing technique offers a

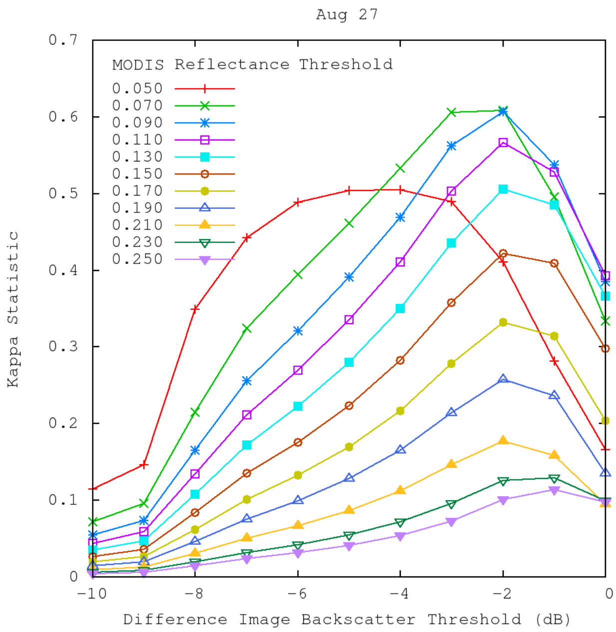

Figure 4.12: κ statistic calculated for individual classifications of flooding on August 27, 2010, based upon $\Delta\sigma^0$ thresholds ranging from -10 to 0 dB. The series represents corresponding MODIS Band 6 reflectance thresholds used in the reference image, ranging from 0.05 to 0.25

reasonably stable means to identify those extents between periods where optical data are unavailable, enabling a broad scale view of the flood dynamics with a better temporal resolution than could otherwise be achieved.

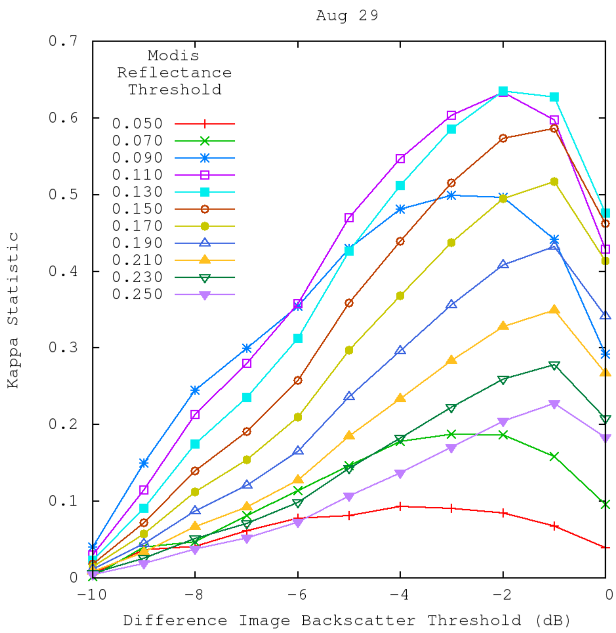

Figure 4.13: κ statistic calculated for individual classifications of flooding on August 29, 2010, based upon $\Delta\sigma^0$ thresholds ranging from -10 to 0 dB. The series represents corresponding MODIS Band 6 reflectance thresholds used in the reference image, ranging from 0.05 to 0.25

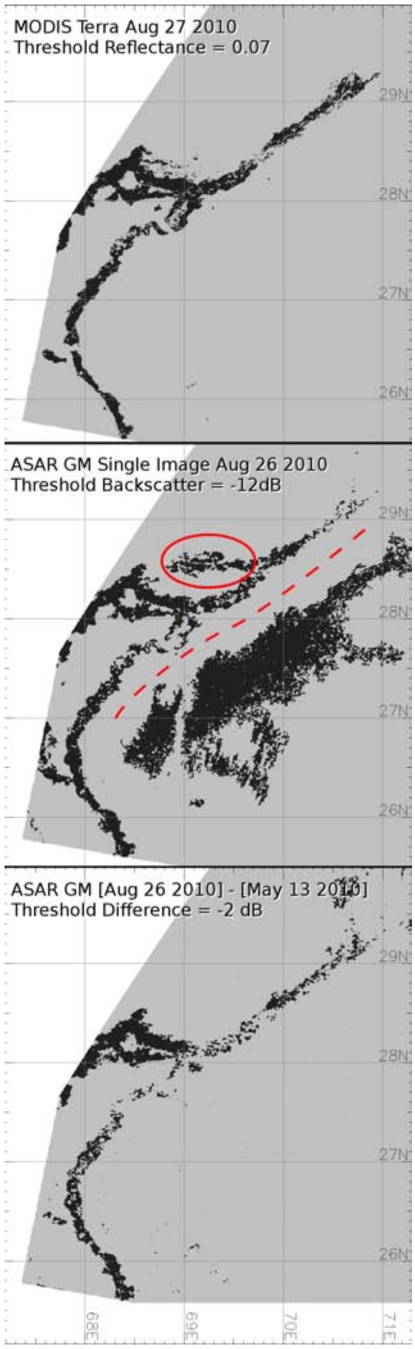

Figure 4.14: Flood extent estimates from MODIS (top, $\kappa = 1$), the single contemporaneous GM image (centre, $\kappa = 0.3$) and the GM Difference image (bottom, $\kappa = 0.6$), using optimised thresholds.

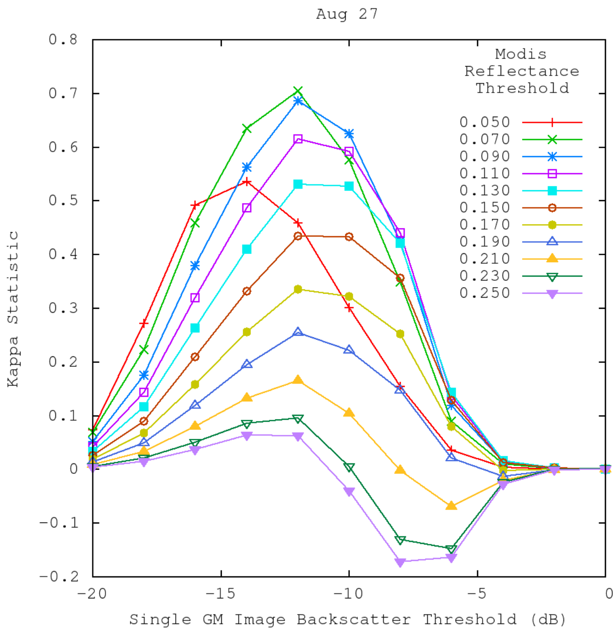

Figure 4.15: κ statistic calculated for individual classifications of flooding on August 27, 2010, based upon γ thresholds ranging from -20 to 0 dB, following precise masking of radar-dark dry land established from the image differencing process. The series represents corresponding MODIS Band 6 reflectance thresholds used in the reference image, ranging from 0.05 to 0.25

4.5.4 Inundation Dynamics

Figure 4.16 shows instances from the resultant time series of binary flood maps. The first two images show the build up of the upper reaches of the Indus. By August 7, the Chenab has flooded and the main flood has reached Kashmore. The image at August 12 shows the situation following the breaching of a bund at Thori in Kashmore. By August 20 the flood has reached the Hyderabad district. The August 29 image shows the results of two significant breaches, one at Sukkur, allowing the flood to split and inundate the Jacobabad region to the north of the Indus, and another at Sarjani to the south, where part of a dyke collapsed on August 26. This resulted in the extensive flooding in the south which is evident on September 11. The final two images, set three weeks apart, show the flooded region covering over 7,000 km^2 between Jacobabad and the Manchar Lake in Dadu, which remained for many weeks. Beyond 20 October 2010, there followed a period in which the Envisat satellite underwent a scheduled program change, during which time GM data was unavailable.

Figure 4.17 shows the duration of flooding over the full extents, up to 17 October 2010, as derived from the GM data. Many regions remained inundated for several weeks, the greatest duration being observed in the area around Jacobabad described above. The greatest flood duration shown at 97 days represents the enlarged Lake Manchar to the southwest of this region.

An idea of the propagation speed of flood waves can be gained from Figure 4.18, which shows the distance along the Indus river channel of the head of the main flood, and the receding tail end. The initial advance covered some 500km in 5 days (about 4 km per hour), with the flood reaching the southern extents towards the end of the first week in September. The greatest length of flooding occurs where the recession curve is flattest at around 21 August. The recession rate is seen to increase at the end of August, following the bund breaches at Sukkur and Sarjani, flattening off once more in early September, when the front of the flooding is seen to retreat back to localised areas.

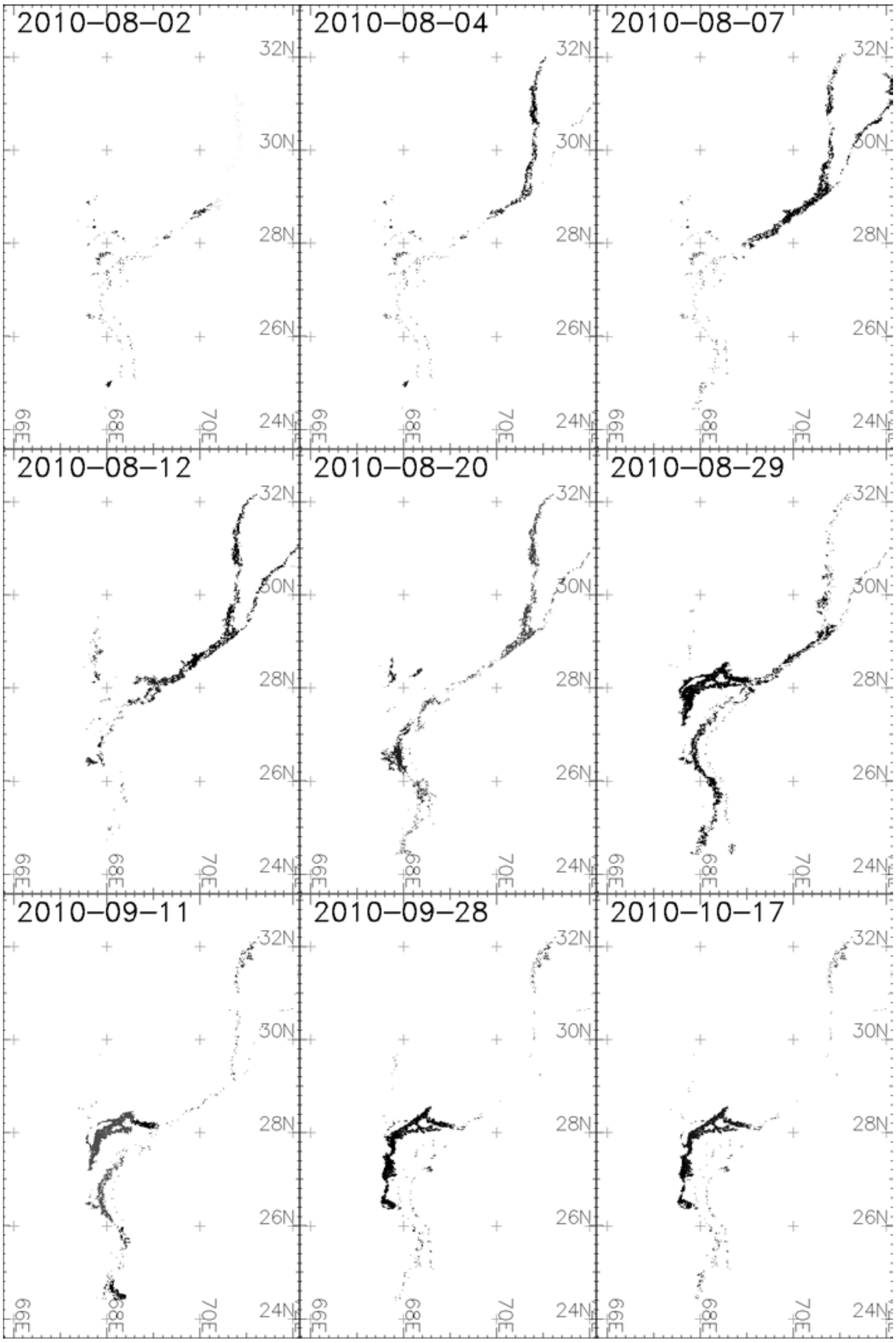

Figure 4.16: Selected instances from the time series showing the build-up of flooding and much of its recession. Flooding is still evident in the third week of October 2010, at which time data temporarily ceased to be available, due to ESA's scheduled preparations for Envisat's project extension program.

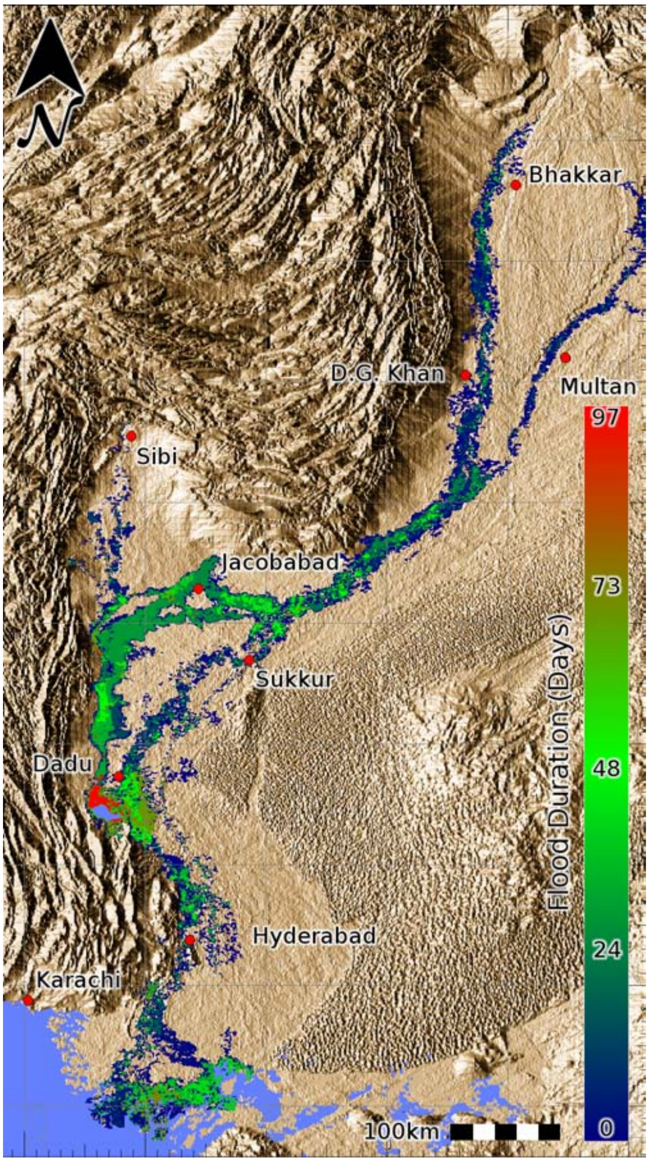

Figure 4.17: Map showing the extent and duration of inundation surrounding the Indus and Chenab rivers as derived from satellite radar data acquired between July and October 2010.

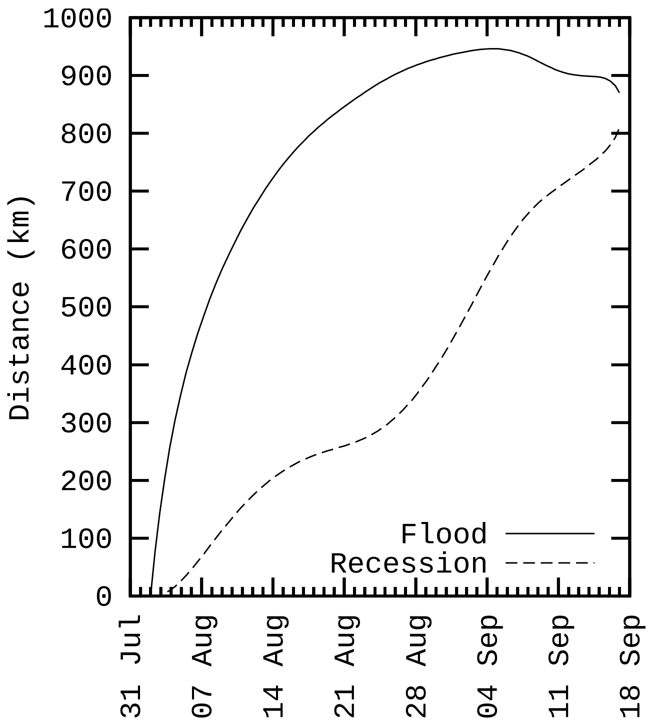

Figure 4.18: Distance of the flood head and tail along the Indus channel from the foot of the northern ranges at 71° N, 32° S

Figure 4.19 shows the flooded area over the time series, derived from the combination of GM and MODIS data. The lower curve shows only the flooding around the main Indus Channel. The upper curve shows the total area, including the near-static flooding between Jacobabad and Dadu, which remained well into October 2010.

4.5.5 Accuracy

A measure of the classification accuracy of this method was known throughout from the κ statistic values used to ascertain the optimal thresholds to use. The consequence of fixing a $\Delta\sigma^0$ threshold of -2 dB based on the κ tests done on 10 and 27 August was further tested on the classification done for 29 August, the results of which are tabulated in Table 4.2 and shown graphically in Figure 4.20. The κ statistics over the full range of MODIS Band 6 reflectance values and $\Delta\sigma^0$ values were also seen in Fig. 4.13.

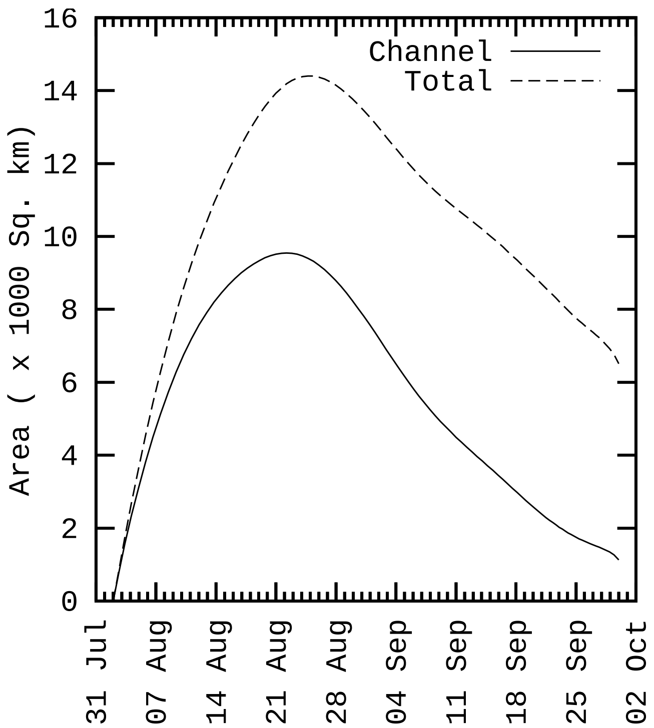

Figure 4.19: Area of inundation over time, of the Indus Channel and the total flood.

The following factors are considered to be the main contributors to inaccuracy:

- As discussed in Section 4.5.2, much of the flooded region covers the immediate flood plain which ordinarily contains large meanders, anabranching and ox bow lakes. Low backscatter returns from these semi-permanent water bodies contribute to to a lower value in a larger area of the baseline image when averaged to a pixel size of 500m. This is offset from similar values in the target image, resulting in mid-range values, incorrectly interpreted as land.

- Semi-submerged vegetation can cause high backscatter values due to multihedral scattering as discussed, which, again, when averaged with low values from open water may return a mid-range value.

- Wind conditions may be such that Bragg Scattering occurs, causing relatively high return values. Determination of the extent of this effect would

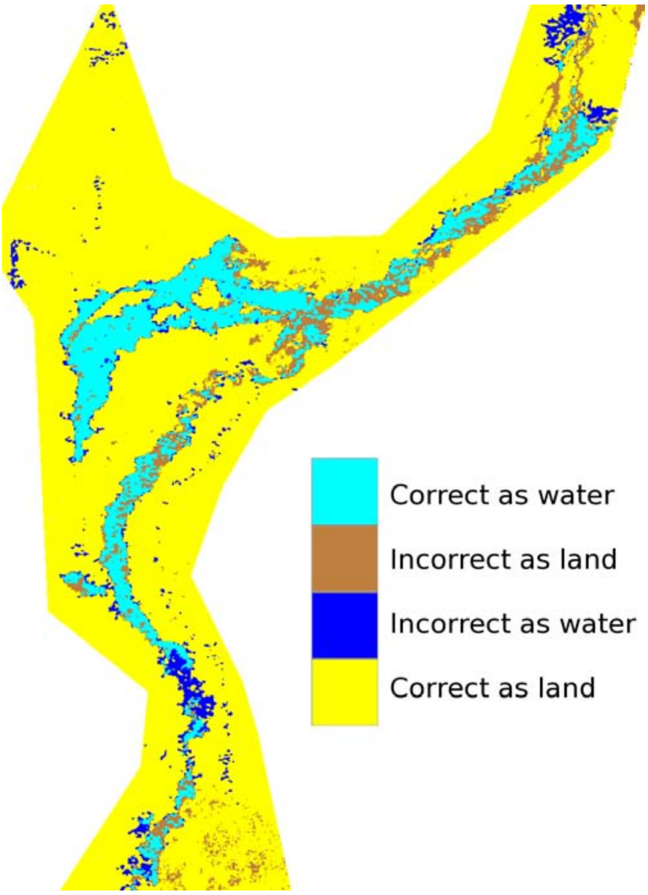

Figure 4.20: Comparison of the $\Delta\sigma^0$-derived flood map on from 29 August 2010 against MODIS flood classification.

require detailed wind speed and direction data, which were not available for this period.

4.6 Discussion

4.6.1 Natural disaster response

For regions which face a high risk of flooding that may be ever increasing (Schiermeier, 2011), mitigating the impact of flooding can fall within two broad categories: planning and organisation based on predicted scenarios, and reactive response during and after an event. Action under the first of these requires an

Table 4.2: Error matrix and κ statistic for the flood map on 29 August 2010 when compared with MODIS flood classification.

	Category	MODIS Flooded	MODIS Non-Flooded	Row Sum
Δ	Flooded	34761	10464	45225
σ^0	Non-Flooded	18662	228902	247564
	Col Sum	53423	239366	292789

Cats	% Commission	% Omission	Est. κ
Flooded	23.1	34.9	0.71
Non-Flooded	7.5	4.4	0.59

κ	κ Variance
0.65	0.000004

Obs Correct	Total Obs	% Observed Correct
263663	292789	90.1

understanding of processes which govern the magnitude and extent of possible floods. Such an understanding cannot rely exclusively on historical data where land use and climate are changing, but must instead require predictive modelling.

Remote sensing has played an increasingly important role in this process in recent years. The establishment of parameters in hydrological models have called upon, for example, leaf area index calculations or on surface water extents using data from optical sensors such as Landsat Thermal Mapper (Chen *et al.*, 2004; Milzow *et al.*, 2009a; Stisen *et al.*, 2008) and have increasingly incorporated soil moisture values gained from Envisat ASAR in such modelling (Decharme *et al.*, 2009; Liu *et al.*, 2010; Saux-Picart *et al.*, 2009). Radar-derived DEM's have been assessed and used in hydrological modelling widely (e.g. Ludwig & Schneider (2006)). More directly, hydraulic processes involved in flooding have been modelled to estimate flood magnitudes (Conesa-Garcia *et al.*, 2010; Hostache *et al.*, 2009b) and to develop flood inundation models (Schumann *et al.*, 2007). Coupled models using SAR data have been employed in the last few years to useful effect. Montanari *et al.* (2009) investigate the usefulness of SAR data to gauge flood extents and stage heights in deriving soil saturation values. Milzow *et al.*

(2009b) seek to verify hydrological models by comparing simulated flood patterns with flood maps derived using AVHRR and ASAR data. Pauwels *et al.* (2009) calculate soil hydraulic conductivity values through a combination of SAR-based moisture maps and land surface modelling.

Predictive modelling has significant limitations in certain instances. An example of this can be observed in the case of the floods in Pakistan. There are limitations to ascertaining water volumes for the modelling process in large areas of very low gradient, necessitating a spatially and radiometrically high resolution DEM (Sanyal & Lu, 2004). Further to this, the use of levees on a large and small scale is widespread throughout the floodplain, many of which are built "privately" and therefore remain unmapped [1]. In this case, therefore, the importance of flood mapping based on observation, increases. So too does the significance of data availability, speed of acquisition, spatial coverage and temporal resolution.

4.6.2 Use and limitations of the GM data for flood mapping

The swath width of GM data is ∼405 km and permits a synoptic assessment of large flood events at the basin scale. Capturing the onset of a flooding event as early as possible is critical for emergency response. ENVISAT ASAR GM was one of the few sensors capable of capturing the full extent of the flooding in Pakistan during the first week and a half (e.g. MODIS data were unavailable from 2 to 9 August 2010 due to high cloud cover). ENVISAT ASAR GM acquisition is not systematic but will depend on other modes being switched off. Hence the coverage of a particular region can be variable. Across Asia, we found from September 2009 to May 2011 an average of 2–3 weekly observations at a single location. Over the same period there were no GM data acquired over New Zealand and 8 per week in parts of North America. Average frequency of land coverage per week by GM data over this 600 day period is shown in Figure 4.21. The temporal distribution is not evenly spread. South-east Asia, for example, received virtually no coverage for the first four months of the study period.

[1] see http://tribune.com.pk/story/219602/private-dykes-on-public-land-may-lead-to-another-bout-of-floods/, for example

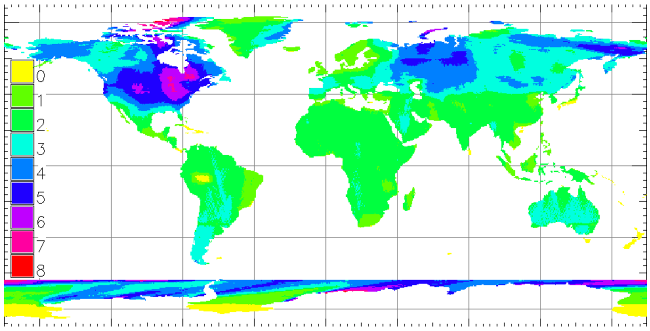

Figure 4.21: Average frequency of terrestrial coverage per week by GM data between September 2009 and May 2011

In Pakistan, we found the coverage of the ENVISAT ASAR Global Mode data was adequate to capture the dynamics of the propagation of the 2010 flood across the entire Indus Basin (Figs. 4.5 and 4.6). However, a lower acquisition frequency from 17 August 2010 onwards only allows for partial coverage of the recession of the flood.

A major limitation of the ASAR GM mapping technique used here is that inundated area with emergent vegetation can be confused with land area of high soil moisture. Wind-induced waves can also generate a roughening of the water surface which increases the scattering of the radar signal due to Bragg resonance; a phenomenon that is more pronounced in C than L-band over inland water bodies (Alpers, 1985; Alsdorf *et al.*, 2007). Finally, partial flooding inside a pixel can be a common feature at this scale (spatial resolution of ∼1 km) especially along braided channels and will result in mixed pixels composed of land, water and flooded vegetation, which can return a wide range of signals.

The original mapping presented here was carried out in response to a request for a timely indication of the extent of flooding by a UN emergency response team when the event was in full throw, when expediency and simplicity competed with sophistication of technique as priorities. The methods lend themselves to seek greater accuracy by further analysis, building on thresholding and region-growing techniques by, for example, Galland *et al.* (2009); Matgen *et al.* (2011); Yu & Clausi (2007) and Silveira & Heleno (2009). Other successful segmentation methods for SAR images involving texture and shape (van der Werff & van der Meer, 2007), active contours (Ben Ayed *et al.*, 2005; Chakraborty *et al.*, 2009;

Fu *et al.*, 2008) and multi-objective algorithms (Collins & Kopp, 2008) may be suitable. However, it is felt that the basic premise of same-track image differencing (to mitigate incidence-angle effects and ambiguous low-backscatter response due to absorption), coupled with a robust region-growing segmentation technique (e.g. Matgen *et al.* (2011)) to account for the small inter-modal range in the probability density functions of flooded and non-flooded areas, is well suited to map flooding in arid regions using SAR data.

4.6.3 A complement to other mapping techniques

Optical sensors, such as Landsat TM and MODIS, can easily detect open water using the strong absorption of solar energy by water in the near and middle infra-red. Shallow depths and turbid waters, are better detected at greater wavelengths ($> 1\mu$m; short-wave infra-red) where the illumination of the suspended materials or of the shallow bottom of a water column is considerably reduced (Bukata, 2005; Li *et al.*, 2003). However during storm events the use of optical data can be severely limited by cloud cover. Radar imaging is less affected by cloud cover and can penetrate vegetation at a depth which depends on the wavelength used and the structure (density and height) of the vegetation (Alsdorf *et al.*, 2007; Hess *et al.*, 2003; Martinez & Le Toan, 2007; Rosenqvist *et al.*, 2007). The use of L band data from the JERS and ALOS PALSAR sensors for flood monitoring is mainly restricted by acquisition times and limited archives, rather than by weather or vegetation condition. ALOS PALSAR data in the wide swath mode are particularly attractive to cover large regions, but unfortunately the system failed in April 2011 and this resource is therefore no longer available for data beyond that time[1]. Passive microwave data (e.g. SSM/I and ISCCP) are helpful for delineating inundated areas (e.g., Hamilton *et al.* (2002); Sippel *et al.* (1998)), in particular when used in conjunction with other sensors to limit confounding factors such as atmospheric condition and vegetation (Prigent *et al.*, 2007), but their use in natural disaster response is limited by their low spatial resolution (tens of km). The geosynchronous weather satellites (e.g. Meteosat II, GOES, GMS) may often be able to bypass clouds with their high temporal resolution allowing

[1] http://www.palsar.ersdac.or.jp/e/

for the mapping of open water at ~1km spatial resolution. In the specific case of flooding events occurring in semi-arid and arid regions, such as the Pakistan flood studied here, water under flooded vegetation can also be mapped using composite data from the thermal bands of these weather satellites (Leblanc *et al.*, 2003, 2011).

Amongst the most promising potential developments in remote sensing of surface water is the future Surface Water and Ocean Topography (SWOT) mission. It is currently planned to be launched in 2020 and will provide significant improvements in our abilities to map inundated areas from space [1]. Using wide-swath altimetry technology, SWOT will provide temporal and spatial variations in water volumes stored in rivers, lakes, and wetlands at unprecedented resolution (Biancamaria *et al.*, 2010). SWOT will generate a global 3D mapping of all terrestrial water bodies whose surface area exceeds 250 m^2 and rivers whose width exceeds 100 m (Biancamaria *et al.*, 2010). The principal instrument of SWOT will be a K_a-band Radar Interferometer (KaRIN), which will provide heights and co-registered all-weather imagery of water over 2 swaths, each 60 km wide, with an expected precision of 1 cm/km for water slopes, and absolute height level precision of 10 cm/km^2. ESA will also be extending and improving C-band SAR capabilities with the launch of the Sentinel-1 system, expected in 2013. This pair of satellites is planned to provide data with a spatial resolution of 20 m, with a revisit time of between 1 and 3 days for Europe and Canada [2].

4.6.4 Other applications of GM data

Space borne technologies are increasingly found to be a key source of information for wetlands conservation and management, as many of the World's wetlands have insufficient on-ground data in part due to their size, number and limited accessibility (Jones *et al.*, 2009). Even at such a time when technological advancement in data processing, storage and communication enables ever higher spatial resolutions from airborne and satellite sensors, the use of coarser resolution data still has a very firm place in the remote sensing field where broad-scale monitoring

[1] http://swot.jpl.nasa.gov/mission/
[2] http://www.esa.int/esaLP/SEMBRS4KXMF_LPgmes_0.html

is required, such as the monitoring of algal blooms (Ahn & Shanmugam, 2006), assessing risks of fire (A. & R., 2008; Chéret & Denux, 2007) or drought (Rojas *et al.*, 2011), the development of land surface models (Jarlan *et al.*, 2005), the assessment of animal stocking rates (Hunt & Miyake, 2006) and the mapping of shorelines (M.-Muslim *et al.*, 2007). The perceived role of GM data was primarily in the monitoring of sea ice (ESA, 2007b), to which field it has indeed contributed (e.g. Quincey & Luckman (2009)). However, its coverage and availability have already been identified as useful advantages in other areas, and have been put to good use, particularly in the areas of relative soil moisture (Bartsch *et al.*, 2008, 2009), surface soil wetness (Pathe *et al.*, 2009; Scipal *et al.*, 2005) and in wetness dynamics (Scipal *et al.*, 2005). The implication of GM data's sensitivity to surface wetness has recently led to the interesting extension to its potential use in the monitoring of freeze-thaw cycles in permafrost regions (Park *et al.*, 2011).

The need for coarse scale inundation mapping has been identified and acted upon, resulting in, for example, the 25 km resolution surface water product described by Schroeder *et al.* (2010) which tests favourably against finer resolution products, and the 0.25° global inundation map produced by Prigent *et al.* (2007).

This study aims to contribute to this latter group at a resolution that falls between those global-oriented scales and the finer river-channel-scale resolutions that can be achieved with other sensor-mode configurations such as JERS, ALOS PALSAR or ASAR in its finer modes. It is felt that ENVISAT ASAR GM data could be used to monitor inundation patterns over large wetlands in complement to estimates from other sensors (e.g. Sakamoto *et al.* (2007)).

4.7 Conclusions

It is clear that during periods of cloud cover, in which optical satellite data with which to map a flood event are not available, GM data may be available to varying degrees that cover the region of interest. Much of the rain (and the cloud) that affected the flooding in Pakistan occurred in the mountains away from the flood plain, and so it is fair to say that the relative availability of GM data with optical data may be greater in flood events closer to the precipitation source, making the use of GM data of greater value.

Ambiguity resulting from low backscatter values from non-flooded areas have been shown to have been reduced greatly by the image differencing process, as these low backscatter values are reasonably consistent between orbit cycles. A greater challenge is presented by the ambiguities in origin of data values, where effects such as dihedral scattering, Bragg resonance and speckle can raise and lower pixel values and prohibit the accurate classification of water. Where the objective is to ascertain the extent of flooding in near real time, there is little that can be done about Bragg resonance unless precise wind conditions are known, other than to hope that temporal frequency of data is sufficient to allow us to understand where this effect may have occurred and to rectify it in an updated image. The effects of speckle can be reduced with filtering. Dihedral scattering can, to some extent, be managed by acceptance that only open water is being mapped, or by further analysis using textural measures. Where, for example, dihedral scattering is dominant in a pixel, we expect the $\Delta\sigma^0$ value to be high, and would expect such areas of partial inundation to surround areas of total inundation. Further analysis could therefore encompass such regions into the flooded class and improve the overall accuracy. The coarse spatial resolution of GM data compounds all of the above problems, where adjacent regions of low and high backscatter values return an averaged mid-range value.

It has been shown, however, that a reasonable level of overall accuracy can be achieved using GM data which allows an understanding of the dynamics and broad-scale extents of a large flood during periods when there are no other means by which to judge these parameters. In the interests of flood mitigation planning, where thousands of lives are at stake, we feel that the potential use of GM data for this purpose is significant.

Chapter 5

Effects of vegetation on mapping of floods using satellite radar data

Chapter context

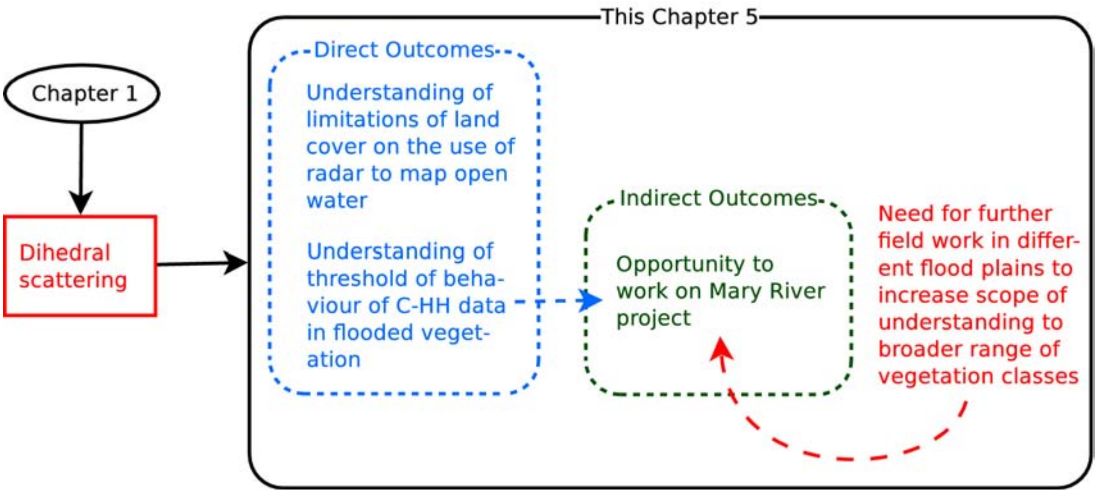

Abstract

The viability of mapping the extents of flooding in two rivers in northern Queensland, Australia, using Envisat ASAR Global Monitoring Mode (GM) data, is examined, through observations of a major flood in each. In the Flinders River event, the flooding, which covered over 9,000 square kilometres, can clearly be distinguished, from low backscatter values in the case of total inundation, to high backscatter where partial inundation occurs. The Staaten flood event demonstrates neither of these characteristics. The resulting classification of the Flinders flood achieves a kappa statistic of 0.7, with the region of lowest accuracy being topographically distinct, and more similar to that of the Staaten region. Water height loggers were set up in the lower Mitchell flood plain, neighbouring the Staaten, and the GM data response monitored throughout a year, during a quarter of which time the vegetation was partially inundated. It was found that extensive flooding under local conditions resulted in a barely perceptible drop in backscatter values, due to the mixing of high and low values, confining the use of GM data for the monitoring of floods to regions with particular surface conditions.

5.1 Introduction

The use of radar as a consistent and reliable tool for the mapping of floods has been shown to be complicated, and requires an understanding of when to expect, under particular environmental conditions, a low backscatter response due to specular reflection on the surface of water, and a high backscatter response due to dihedral scattering (double-bounce) (e.g. Bartsch *et al.* (2008); Costa & Telmer (2006); Grings *et al.* (2009); Kasischke *et al.* (2003)). To further complicate the process, open water can exhibit Bragg Resonance, where coherent additive effects return very bright signals from targets with regular textural qualities, such as waves on the surface of the water (Alsdorf *et al.*, 2007; Liebe *et al.*, 2009; O'Grady *et al.*, 2011; Schaber *et al.*, 1997), or furrows in a ploughed field in a particular orientation (Bonn & Dixon, 2005; Sanyal & Lu, 2004). While such limiting phenomena can occur in any environment under study, there are some ground-cover characteristics which render a region particularly prone to ambiguous radar signals, and therefore preclude the use of radar of particular specifications for the mapping of flood extents. It is useful to understand what some of these conditions may be in the context of a particular data product, to avoid abortive work and erroneous inundation maps. Here we look at two large floods in near-neighbouring catchments in the Gulf Plains of north-west Queensland, observing a major difference in our ability to map their extents using GM radar data, and examine the likely reasons. From this, it may be possible to determine those areas that are off-limits to the use of GM data for flood mapping, and also help in our understanding of the particular radar characteristics of grasslands and tropical savanna.

5.2 Study Area and Flood Events

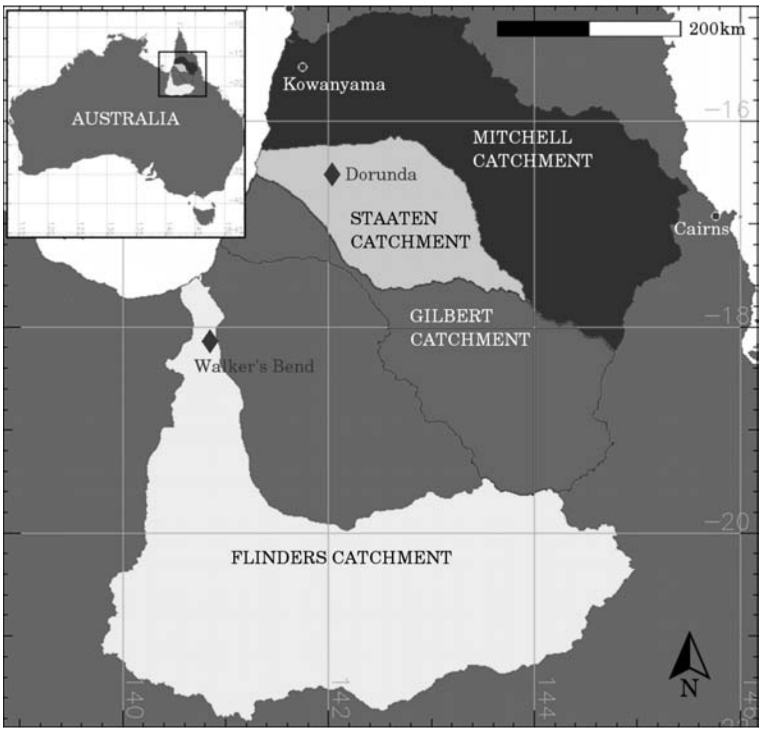

Figure 5.1: Catchments under study in Northern Queensland, Australia

5.2.1 Flinders

The Flinders Basin occupies an area of nearly 110,000 square kilometres of the northern Queensland Gulf Plains bioregion, draining into the Gulf of Carpentaria. The lower floodplain is dominated by grasslands, in particular Dichanthium, or Bluegrass. Tussock grasses such as these occur in clay soils through which water does not readily penetrate, resulting in either water logging or an absence of moisture, depending on rainfall (Spessa *et al.*, 2005). Such conditions are not favourable to trees, and this region is therefore dominated by open grassland plains. In February 2009, a period of sustained rainfall resulted in the flooding of the lower basin, the inundated area covering over 9,000 square kilometres. Figure 5.2 shows the rainfall average for the whole basin, leading up to the flood event. The largest extent of the flood occurred following the final large rainfall peak in mid-February. At this time the gauge height at Walkers Bend, situated downstream of the largest flooded area, was on the decline from its peak at 15m (Fig. 5.2). Following 15 February, the gauge height increased as the upstream flood evacuated.

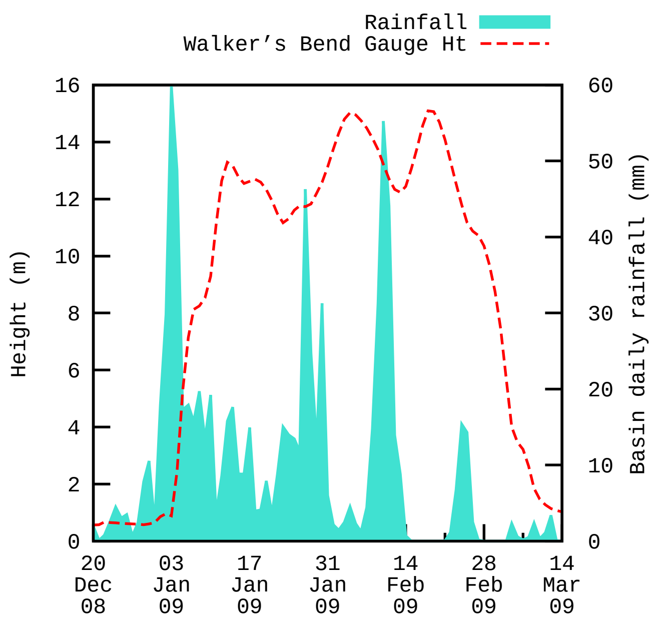

Figure 5.2: Flinders basin rainfall (blue) and river height (red) at Walker's Bend gauging station on the Flinders river in early 2009

Figure 5.3 shows a MODIS Band 6 reflectance image (left) of the flooded region on 15 February 2009, in which the low values representing absorption of the short-wave infra-red radiation by water appear as dark. The image on the right shows GM data acquired on the same day, with radar backscatter values ranging from close to zero dB (bright) to -25 dB (dark), the latter representing the specular reflection of the radar signal on open water. It is clear that the main body of flood water in the centre of the images has been captured in the GM data, along with the coastal wetlands of the Southern Gulf Aggregation to the north-west of the images. However, the fan of laden tributaries running into the Norman River to the east of the MODIS image is less clearly defined in the GM data. The bright patch in the GM image to the west of the gulf coast is attributed to Bragg Resonance.

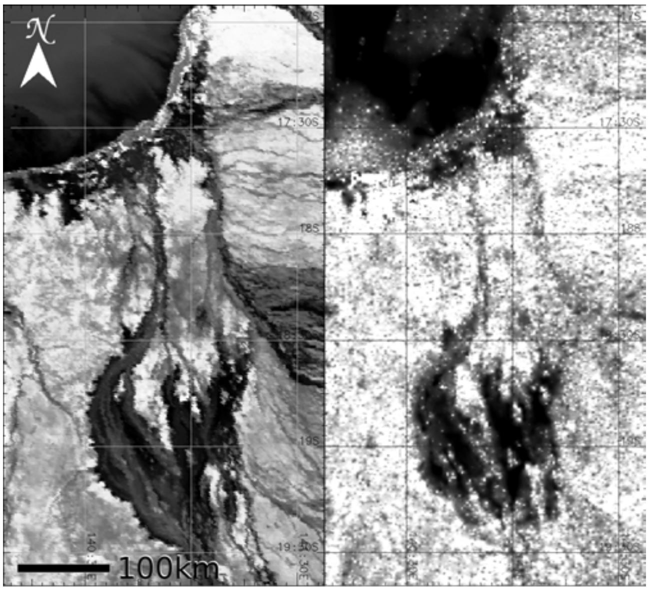

Figure 5.3: ASAR GM image of flooding in the Flinders catchment on 15 Feb 2009 (left), compared with an image derived from MODIS Band 6 reflectance values from the same date (right)

5.2.2 Staaten

Covering an area of 25,572 square kilometres, the Staaten Basin ranges from the Bulleringa National Park in central Cape York to the west coast of the cape, narrowing as it reaches the Gulf of Carpentaria. The basin comprises ephemeral riverine channels in an alluvial plain dissected with many streams, oxbow lakes and *billabongs*, or drainage depressions, in widely spaced valleys that form a uniform pattern shared with the neighbouring Mitchell and Gilbert basins.

The tropical savanna woodland of the Staaten region comprises tall dense grasses, together with various densities of mainly Eucalypt trees, predominantly Melaleuca.

A continually wet January in 2007 preceded a significant rainfall event on 7 February (see Figure 5.4). The gauge at Dorunda peaked at around 7.2m on 10 February, at which time a substantial part of the lower reaches of the Staaten basin were flooded.

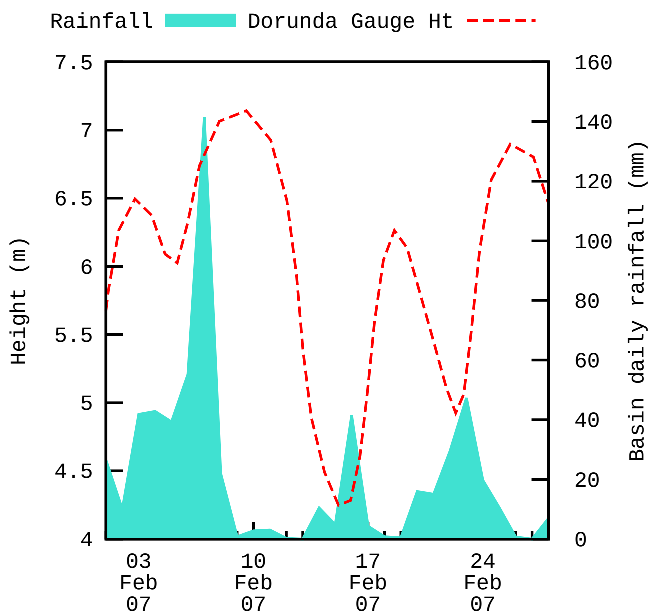

Figure 5.4: Staaten basin rainfall (blue) and river height (red) at Dorunda gauging station on the Staaten river in early 2007

The extent of the flood at this time in the Staaten Basin can be seen in the MODIS Band 6 image in the left of Figure 5.5. From the image on the right, it can be seen that the only open water visible from the GM data is along the coast, which represents the semi-permanent wetlands of the coastal South-east Karumba Plain Aggregation. The inability to distinguish the presence of flooding is representative of all the GM radar data seen during this event.

The relative separability of water and land between the two instances is high-

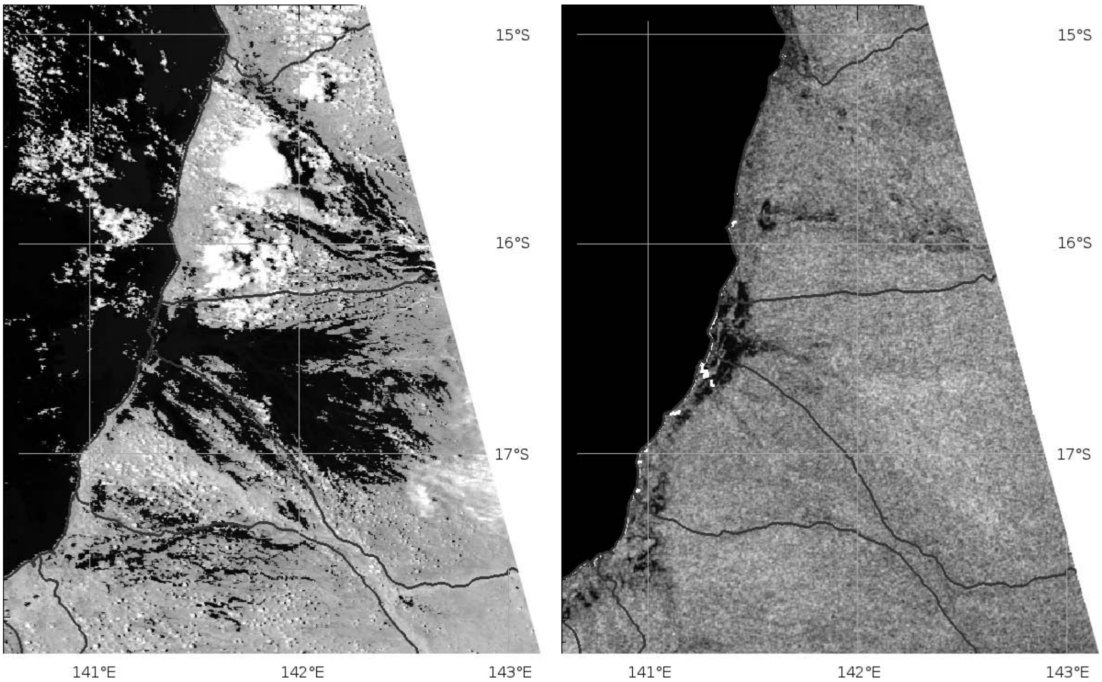

Figure 5.5: (left) Flooding (in black) of the Staaten river on 10 Feb 2007, derived from MODIS Band 6 reflectance values, and (right) the near-simultaneously acquired GM backscatter image

lighted in the density plots shown in Figure 5.6. Ground-projected values, normalised to an incidence angle of 30° (γ_{30}) for flooded regions are represented by the blue lines, non-flooded by red. The Flinders plot on the left shows that γ_{30} values for the flooded region appear to have at least two means, one at around -15 dB and another at around -10 dB, the latter made up largely of those pixels in the vicinity of the Norman River alluvial fan already discussed, that is susceptible to misclassification. The Staaten plot on the right shows that, beyond the tail of low values returned from the coastal wetlands, the flooded region shows a distribution around a mean that is perhaps a decibel higher than that of the non-flooded land.

The Staaten and the Flinders flooded regions are both very flat, and GM data was acquired at similar angles of incidence, and so it must be concluded that the vastly different radar responses represent differences in the nature of the vegetation, in the nature and pattern of the floods themselves, or a combination of the two. The positive displacement of the flooded density plot for the Staaten Basin indicates a higher set of backscatter values for the flooded region than

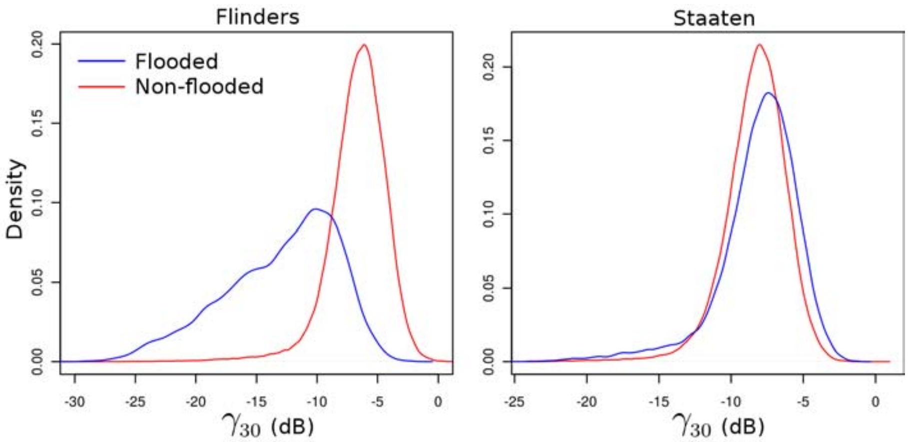

Figure 5.6: Backscatter value density plots of the Flinders (left) and Staaten (right) regions, during their respective flood events. Values from pixels representing flood waters, as identified in MODIS SWIR data, give the blue curve, non-flooded pixel values the red.

the surrounding land. We know that the C-Band signal used to produce GM data is liable to interact with structures at the physical scale of leaves and small branches of trees, and that the Staaten and the neighbouring basins do experience floods which reach the lower tree crown (see Figure 5.7). Flooding of this extent, which completely covers the grasses, tends to return a low value due to specular reflection and to attenuation and volume scattering from the upper branches.

Figure 5.7: Part of the Mitchell River during a flood (Source: Kowanyama Aboriginal Land and Natural Resources Management Office)

Where flood levels are much lower, the radar signal is liable to interact with grasses, and a flood level rising through the height of the grass and then covering it should be characterised by an increase in backscatter due to dihedral scattering, followed by a sharp drop in value at total inundation. Grasses form the tallest stratum growth form of the Flinders flooded region.

5.3 Theoretical Basis

As has been seen, the two regions under study have different land cover regimes. Both are extensively covered by grasses—in the case of the Flinders flood region, these are dominated by Dichanthium Sericeum, or Bluegrass (see Figure 5.8), the stems and leaves of which stand erect and rarely reach 30 cm in height (FAO, 2012). The major contrast in the Staaten region is the woody over-storey of ironwood / eucalypt species, with various grass species (Themeda Triandra, Heteropogon Contortus, Heteropogon Triticeus, Sorghum Plumosum, Chrysopogon Fallax, Alloteropsis Semialata, Eriachne Obtusa) which can grow up to anywhere between 70 and 300 cm tall, depending on phenology and fire history (see Figure 5.9).

Figure 5.8: Dichanthium Sericeum, < 30 cm (Image: D. Greig, Source: ANH (2012)

Figure 5.9: Sorghum Plumosum, 70–300 cm (Image: L. Wallis, Source: GBIF (2012)

The characteristics of radar backscatter reflected from a surface comprising water with emergent vegetation has been extensively studied (Costa & Telmer, 2006; Grings *et al.*, 2009; Henderson & Lewis, 2008; Hess *et al.*, 2003; Noernberg *et al.*, 1999; Parmuchi *et al.*, 2002; Pope *et al.*, 1997; Rosenqvist *et al.*, 2007; Silva *et al.*, 2008; Töyrä & Pietroniro, 2005; Töyrä *et al.*, 2002; Wang *et al.*, 1995). Some work presents evidence as to the merits, or otherwise, of the use of C-band horizontally co-polarised radar (C-HH, in which both the sent and received signals are filtered in the horizontal plane). Töyrä & Pietroniro (2005) note that SAR has difficulty separating inundated shrub or forest from other vegetation which is dry. They tackle this problem with the use of auxiliary visible/infrared (VIR) data. Pope *et al.* (1997) identify an apparent threshold in the height and density of grasses that determines the response (whether rising or falling) of backscatter to inundation, and suggest that the use of C-HH data to detect partial flooding in marshes with sparse cover *"will probably not be possible"*. This conclusion is shared by Pope *et al.* (1992), who note the lack of distinction between flooded emergent grasses and non-flooded grasses using C-HH. Another potential problem with C-HH data is that, due to the polarisation of incident radiation on the surface of water, co-polarised signals (HH and VV) are more susceptible to Bragg resonance than cross-polarised, although HH appears less so than VV (Liebe *et al.*, 2009).

For both C- and L-band data, Wang *et al.* (1995) found that HH data displayed a greater flooded/non-flooded backscatter ratio than VV in their study of response to flooding in the Amazon forests, as was the case for Grings *et al.* (2009) when exploring the use of Envisat ASAR data to estimate water storage in the marshes of the Paraná Delta in Argentina.

In studies of aquatic or flooded vegetation, the presence of water is generally manifest in a higher backscatter signal (e.g. Bartsch *et al.* (2008); Costa & Telmer (2006)), but this is not always the case. While total submersion of vegetation, in the absence of Bragg scattering, results in a low backscatter response due to specular reflection away from the sensor, the behaviour of the signal response as the water rises to that point depends on several factors.

Grings *et al.* (2009) found that verticality of the vegetation determined the behaviour of backscatter from flooded marshes: they observed that the response went *up* when the inundated marsh was mainly of vertical orientation, and *down* when of random orientation, a finding shared by Silva *et al.* (2008), Töyrä *et al.* (2001) and Pope *et al.* (1997). The latter describe a similar trend reversal in terms of vegetation density, observing an increasing backscatter value with flooding where the density of emergent Cattail and Saw Grass was greater than 60% cover, and a decrease in densities less than 50%. Flooding was also associated with a decrease in backscatter where small-stemmed rushes occurred at 50%–80% cover (Pope *et al.*, 1997).

Costa & Telmer (2006) used RADARSAT and JERS-1 data to examine the lakes of the Brazilian Pantanal. They found that taller denser aquatic species give the highest C-band backscatter values due to dihedral scattering. However, Ramsey (1998) found that in taller marshes, C-band and X-band returns were dominated by volume scattering, with dihedral scattering being predominant in shorter marsh grasses.

Kasischke *et al.* (2003) studied ERS SAR data at 13 sites in the South Florida wetlands, and found that in all but one of the study sites, radar backscatter decreased with increasing water level. The one exception, i.e. where backscatter increased with increasing water level, was the site with the highest above-ground biomass.

It is clear that certain combinations of structural orientation / homogeneity, vegetation density and spatial coverage preclude the ability to distinguish flooded and non-flooded vegetation, as was found by Parmuchi *et al.* (2002) in the case of marshes in the Paraná Delta, despite the knowledge that there existed a large difference in water levels between data acquisitions. The vegetation species in this case was *Scirpus giganteus* with 100% coverage, which comprised vertical stems rising to 1.5–2m. This inability to distinguish between flooded and non-flooded states would seem to contradict the findings of Grings *et al.* (2009), mentioned above, who apparently observed a marked separability between ASAR readings in flooded and non-flooded states of the same species (identified in this case as *Cortadera*), in the same region. Marsh density and biomass conditions during winter are suggested as possible reasons for the phenomenon by Parmuchi *et al.* (2002).

Considering the varied results, it seems that the flooding of grasslands may be observed either as a drop in backscatter due to specular reflection, or a rise due to dihedral scattering, both of which may conceivably be experienced within the bounds of a single pixel. Pope *et al.* (1997) refers to the trade off between increasing backscatter from dihedral interactions and decreasing backscatter from forward scattering. The determination as to which of these is dominant, is governed by some vegetation cover threshold, which may vary between species and growth stage. It seems unavoidable that there must be a range of cover within which the presence of flooding is undetectable with radar data. In either case, the detectability of water depends on the amount of attenuation present through volume scattering above the water level. Töyrä & Pietroniro (2005) note this fact, finding difficulty separating inundated shrub or forest from non-flooded vegetation or bare soil without the help of auxiliary data in the form of optical imagery. Pope *et al.* (1997) acknowledges that there *"appears to be an important height-density threshold in C-HH"*. Töyrä *et al.* (2001) found that their ability to detect flooded sedges and grasses was confined to the summer when the newly-grown stalks were upright, and that in the spring, the dihedral backscatter became attenuated by brown vegetation and thatching.

The mechanisms which conspire to render the Staaten flood invisible using GM data can only be understood by measuring backscatter responses under known vegetation and flood conditions.

5.4 Method

GM data covering the two flood events was preprocessed according to methods described in Chapter 2. A list of data used may be found in Appendix B.

The ability to use GM data to map the Flinders flood was tested by classifying flooded and non-flooded pixels using the methods described in Chapter 4 O'Grady *et al.* (2011), which involve a region-growing algorithm and track-for-track baseline image deduction. This was done on three dates for which near-simultaneous cloud-free MODIS data were available, in order that the accuracy of the map could be tested. Kappa tests (Cohen, 1960; Foody, 2006; Hunt *et al.*, 2010; Tolpekin & Stein, 2009) were carried out to this end.

In order to analyse the radar response to varying water levels in the savanna of the western Cape York river basins, a series of capacitance-type water level loggers (Fig. 5.11) was set up across a transect running south from the Mitchell River, over a distance of 22km, approximately 2km apart (see Fig. 5.10). These

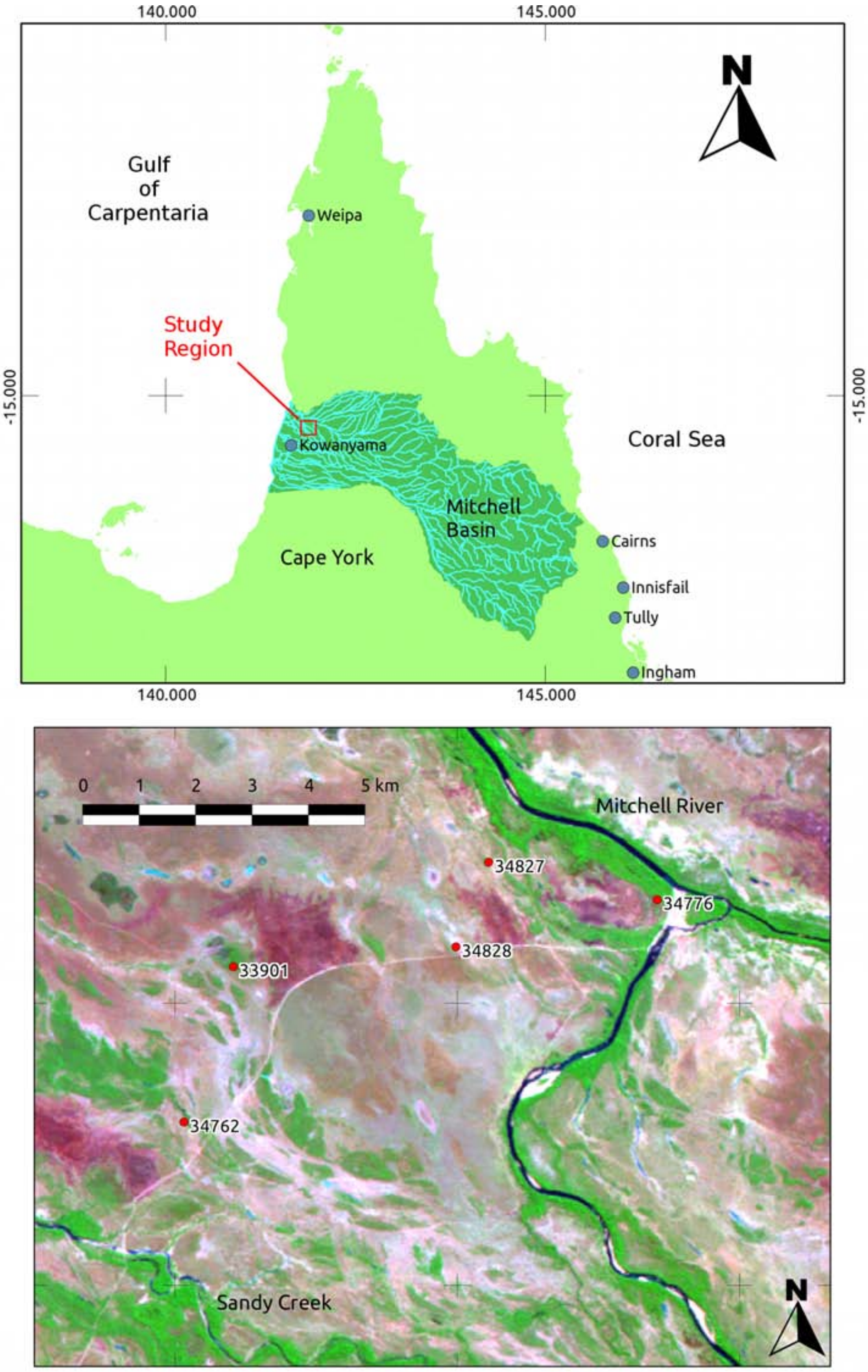

Figure 5.10: Location of water height loggers in the Mitchell floodplain

recorded data over the period of one year, including dry periods and periods of flooding at various depths.

Figure 5.11: Capacitance loggers set up in the Mitchell floodplain (as numbered). The main channel of the Mitchell near Shelfo Station is shown in its dry season state in the lower right-hand image

5.5 Results and Discussion

5.5.1 Flinders

Figure 5.12 shows the backscatter response at arbitrary points in the Flinders floodplain from the middle of the 2008/9 wet season through a complete wet-dry-wet season cycle. From this plot, it can be seen that the tussocky grasses dominating the floodplain produce high backscatter values, between -5 and -9 dB at the height of the wet season, and low values of -11 to -13 decibels during the dry. Total submersion of the grasses in February 2009 produced a backscatter value of around -17 dB, but the same sample point a few weeks later returned a value at the high end of the observed range. Where no flooding occurred, the range of values at any time throughout the year across the sample points was fairly consistent at -3 to -4 dB.

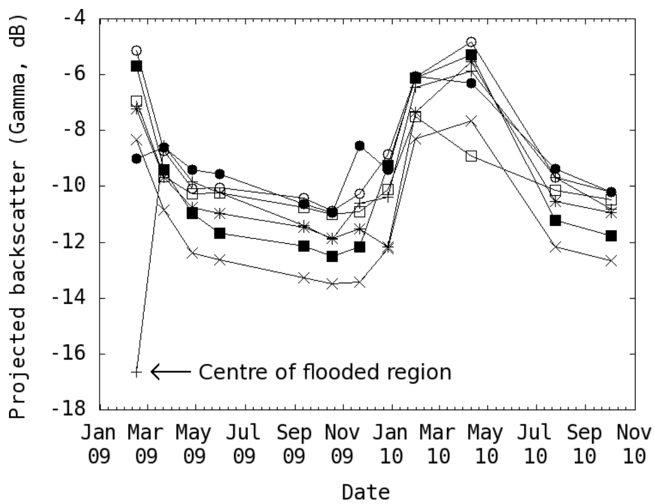

Figure 5.12: Variation of average GM backscatter values through the year from the same orbit track, at various points in the Flinders floodplain

The seasonal variation of backscatter values is consistent with findings by others (e.g. Bartsch *et al.* (2008); Kasischke *et al.* (2003); Wang *et al.* (1995)) as to the domination of backscatter signals by soil moisture. In fact, high soil-moisture response is all but indistinguishable from the response of semi-submerged grasses causing dihedral backscatter.

The build-up of water from dry soil through to increased wetness, to inundation, to reduction in water level below the top of vegetation and increased dihedral scattering may be seen in Figure 5.13.

On 31 January, the dry conditions across the floodplain are evident from the general low backscatter values below around -10 dB. By 15 February the flooding can clearly be seen, surrounded by much higher (-5 – 0 dB) backscatter corresponding to wet soil and dihedral scattering. In the next two images showing

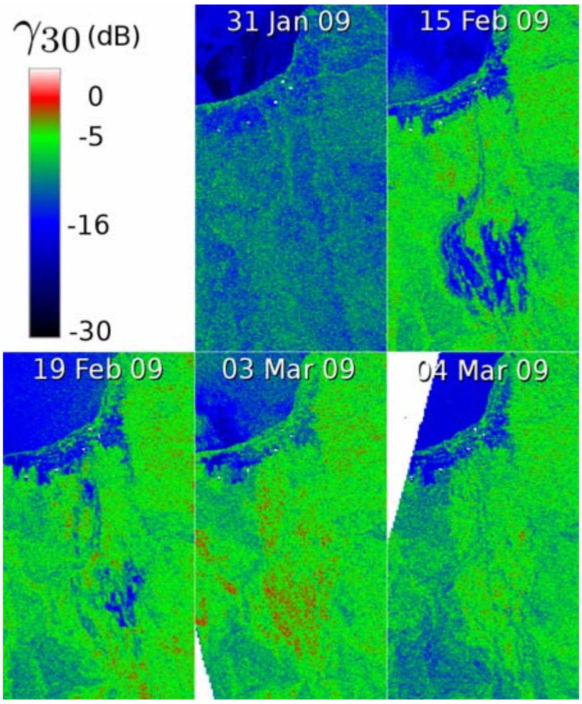

Figure 5.13: Progression of projected backscatter (γ_{30}) values in the Flinders region before and after the flood event.

19 February and 3 March, the area of total inundation represented by the homogeneous region of values at or below -16 dB reduces, and the radar-bright areas, tending towards zero loss, increase, as the flood water drops below the height of the vegetation, and interactions between the water surface and emergent vegetation result in dihedral scattering. Between 4 March and 9 March these areas are replaced by lower pixel values as the water level drops.

The effect of incidence angle on dihedral scattering is evident when comparing the images in Fig. 5.14, taken 11 hours apart on 9 and 10 March 2009. The former was taken was taken on an ascending orbit, where the data corresponding to the flooded region was acquired at a high incidence angle ($\approx 40°$). The latter was acquired on a descending orbit, with the flooded region corresponding to lower incidence angles ($\approx 15°$). The normalisation process with respect to incidence angle, using parameters derived from the methods described in Chapter3, and the classification described in Chapter 4 and in O'Grady *et al.* (2011), mitigate this effect to a large extent.

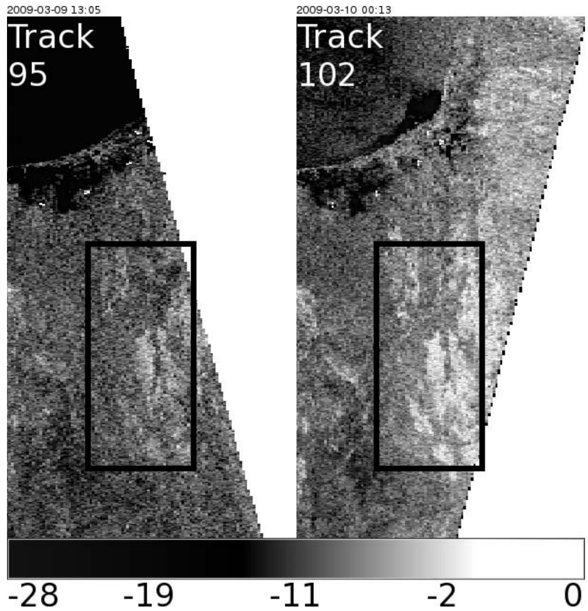

Figure 5.14: Two GM images of the Flinders floodplain, acquired 11 hours apart on 9–10 March 2009. On the left, the region of interest (ROI) is on the outside of the swath of an ascending orbit, where incidence angles are around 40°. On the right, the ROI is on the inside of a descending orbit, with incidence angles around 15°.

Progression of flooding

In order to observe the various states of vegetation–water interaction through the Flinders flood, an unsupervised classification was performed on the time series of images that were acquired through the flood event. This resulted in the grouping together of those areas with a similar behaviour of backscatter response over time.

Figure 5.15 follows the progress of the mean backscatter returned by four value groups, from the resultant classification, through the flood event. Prior to the build-up of flood water in late January 2009, pixels in the red, blue and orange classes showed a mean backscatter values of -11 dB consistent with dry soil. The green class, dominated by the highly-weathered bedrock to the southwest of the region, and the dry sand of the coastal areas to the north, returned a lower mean value of -12 dB, consistent with absorption and specular reflection. The next period, up to 15 February, sees a peaking of the gauge height at Walkers Bend of around 15 m. The blue-red class values dive to -15 dB, where total submersion is reached. It is unfortunate that no GM data were available earlier in February,

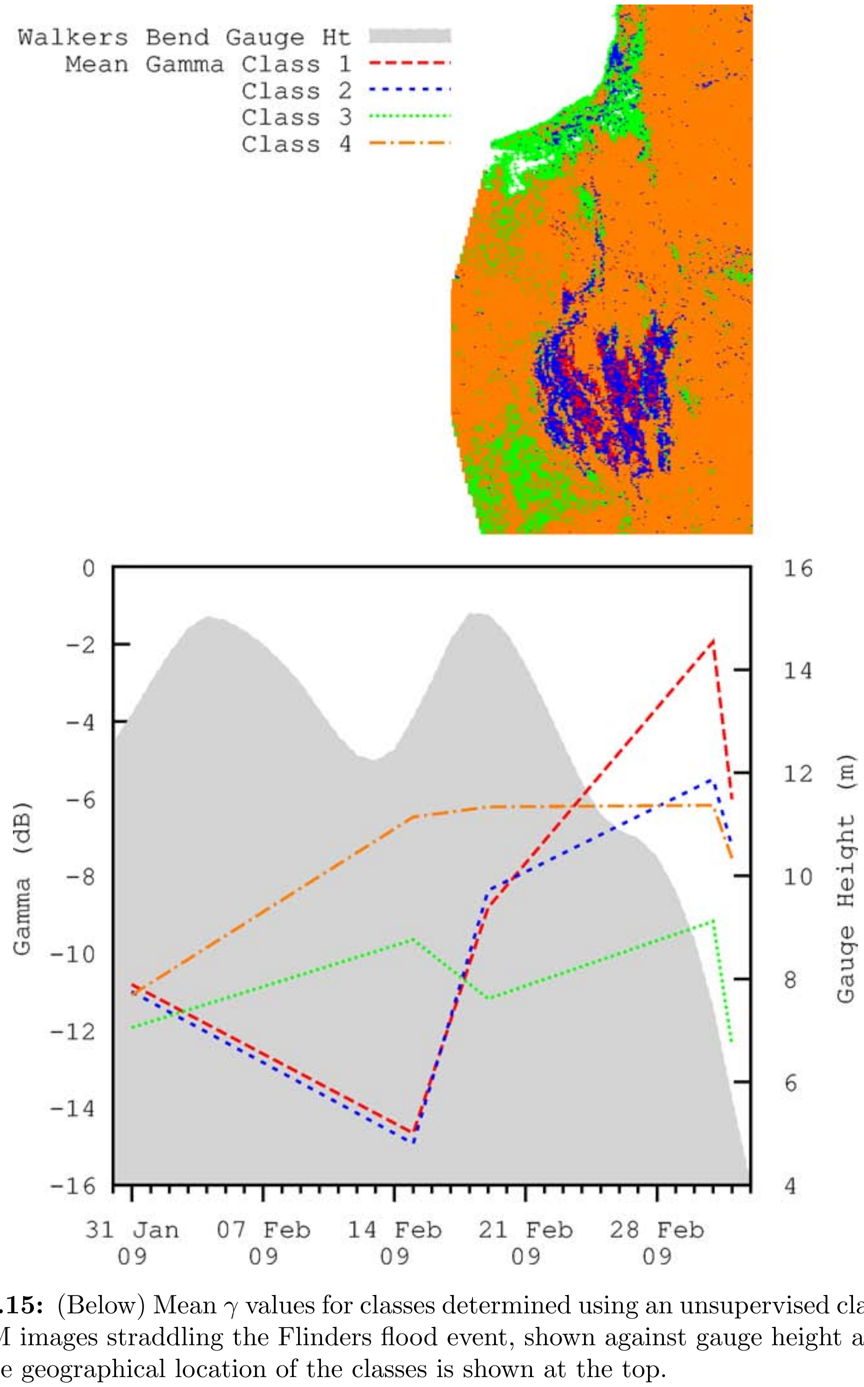

Figure 5.15: (Below) Mean γ values for classes determined using an unsupervised classification of five GM images straddling the Flinders flood event, shown against gauge height at Walker's Bend. The geographical location of the classes is shown at the top.

when we would expect to see, for these two classes, the backscatter values rise due to dihedral scattering, prior to total submersion. However, we do see this occur as the waters recede. In early March we see the blue class values approach those of the orange class at around -6 dB, representing those areas where the flood has drained, exposing wet soil. The red class values peak at an average of -2 dB, and represent those areas where the grasses remain emergent through the remnant flood waters. The orange class shows those areas which did not flood, and the progression from dry soils to wet soils can be seen between late January and mid February, where they remain fairly constant at around -6 dB until the gauge height at Walkers Bend is seen to drop off in early March. At this time, the average backscatter values for all of the classes begin their descent to their normal values for the time of year (driven by soil moisture), averaging around -9 dB.

Class map of Flinders flood

The full extend of the Flinders flood was mapped using the preprocessing, image differencing, thresholding and classification techniques described in Section 4.4.

The results of the subsequent classification of flooded and non-flooded pixels are shown in Figure 5.16. Correctly classified water and land are shown in blue and yellow respectively, and pixels incorrectly classified as water and land are shown in cyan and red. The κ-statistic resulting from the error analysis on the 15-February classification is 0.70 (see Table 5.1). No hard and fast rule exists to determine a definitive interpretation of the κ value, though some attempts have been offered (e.g. Fleiss (1981); Landis & Koch (1977)). In all assessments, a κ-statistic value 0.7 ranks highly, indicating a good classification result. It is significant that errors of omission, where water is classified incorrectly as land, are concentrated to the greater part on the north-east area, which actually represents the lower reaches of the Norman River. This error is demonstrated best in the classification for 3 March, seen in the lower left image in Figure 5.16.

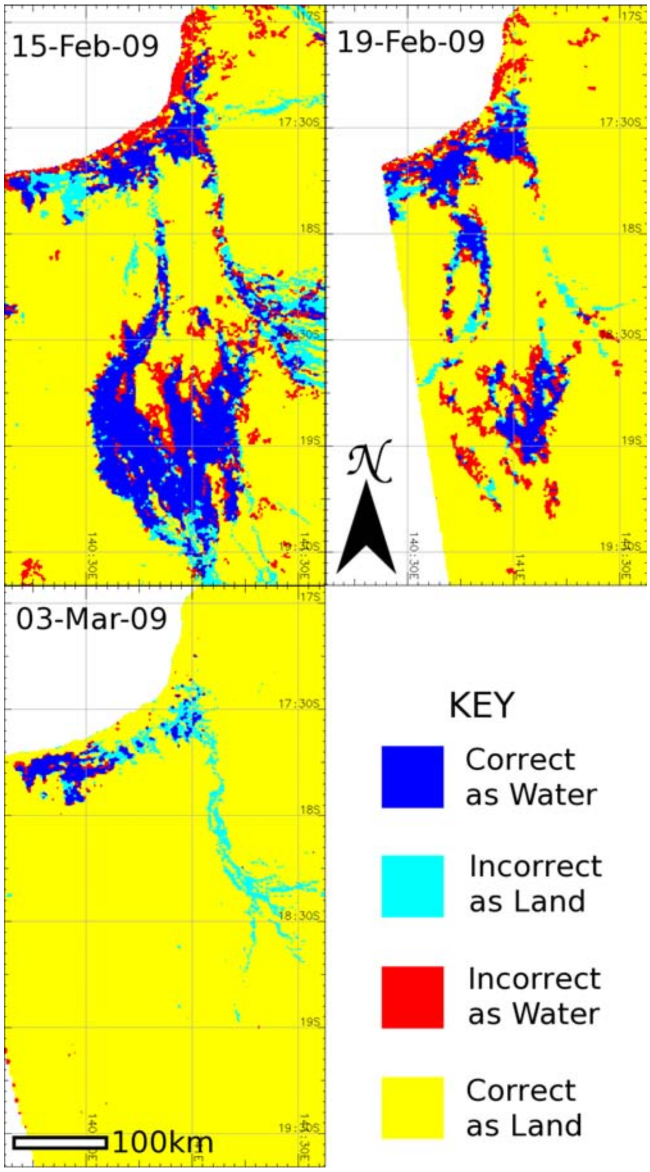

Figure 5.16: Accuracy of flood classification using GM data against a MODIS Band 6 threshold classification, at various stages of the flood.

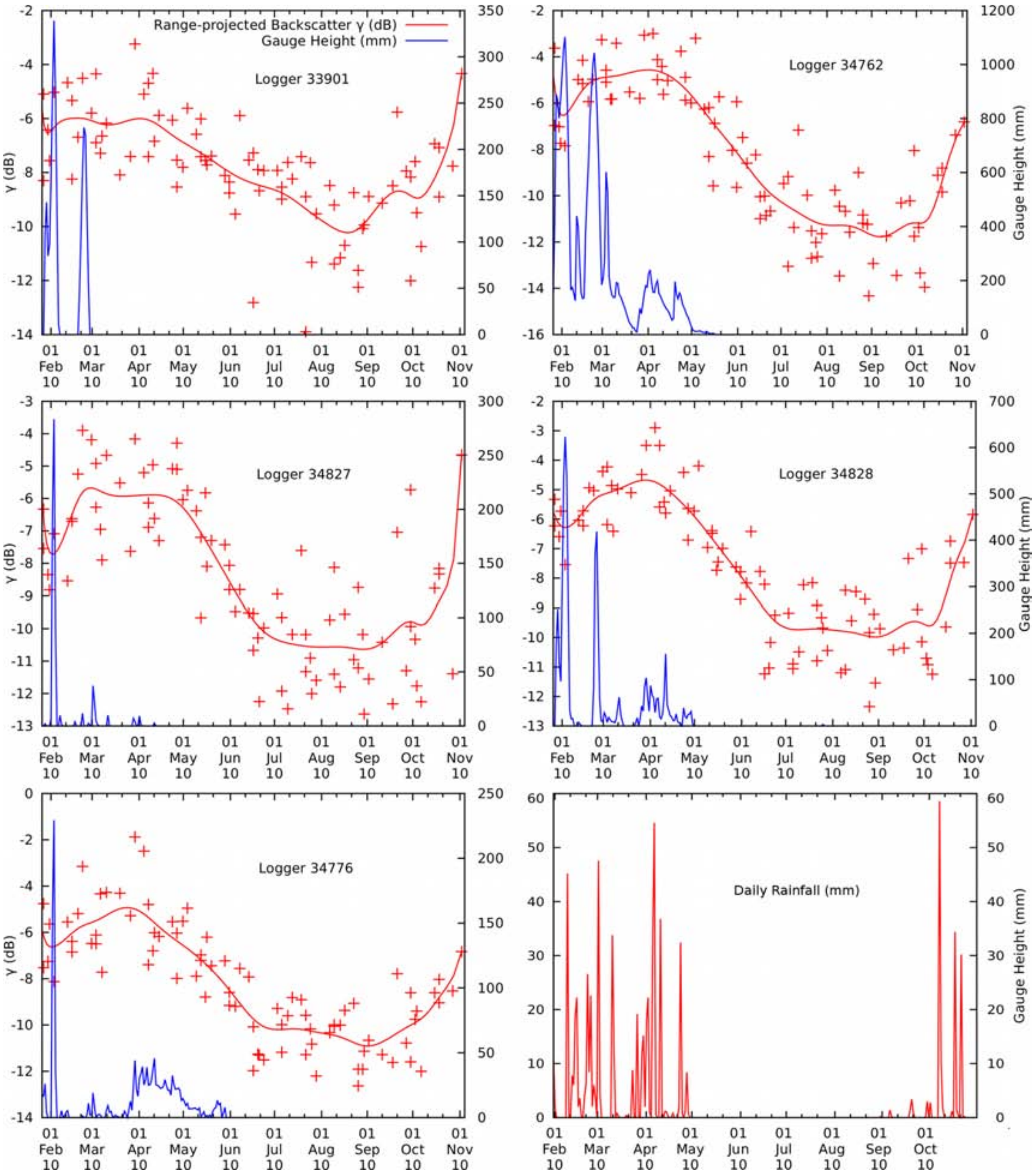

Figure 5.17: Water level measured at five logger locations (in blue) in the Mitchell floodplain over a nine month period, together with ground-range projected backscatter (γ_{30}, in red) derived from GM data. The bottom right-hand plot shows daily rainfall at Kowanyama Airport for the same period (Courtesy Australian Bureau of Meteorology http://www.bom.gov.au) Logger locations were shown in Fig. 5.10

		MODIS B6		
	Class	*Land*	*Water*	**Row Sum**
G	*Land*	102136	10758	**112894**
M	*Water*	10941	42209	**53150**
	Col Sum	**113077**	**52967**	**166044**

Class	% Commission	% Ommission	Estimated κ
Land	9.529293	9.675708	0.701270
Water	20.585136	20.310760	0.697725

κ	κ Variance
0.699493	0.000003

Obs Correct	Total Obs	% Observed Correct
144345	166044	86.931777

Table 5.1: Kappa (κ) results from the accuracy test performed on the classification of flooding in the Flinders basin on 15 February 2009

5.5.2 Staaten

Figure 5.17 shows the backscatter values being returned under certain flood levels in very similar environmental conditions to the Staaten flood, in the neighbouring Mitchell floodplain. Five data loggers were set up and left for one year, recording water height above ground level hourly. The results are plotted in Figure 5.17. Although the loggers were a few kilometres apart, the region is extremely flat, at around 11m above sea level. The three loggers furthest away from the Mitchell channel (33901, 34762, 34828) recorded two peaks, in early and late February, taking the water height up to between 200 and 1100 mm. It is only the first peak in early February, however, common to all of the logger data, which causes a discernible drop in the backscatter (γ) value which we would expect to see due to specular reflection on open water. In the case of loggers 33901 and 34827, it is certainly true that a water height of at least 300mm would be required to submerge the grasses, and this height was only achieved during this peak.

We can determine from the plots that values returned during the flooded period are of a broad range whose mean tends to follow the range of values expected as a result of soil moisture alone, at this time of year. We have seen the seasonal trend of backscatter values in the Flinders region in Figure 5.12, in which the low backscatter values during the dry season reflect the extremely low soil moisture content during that period.

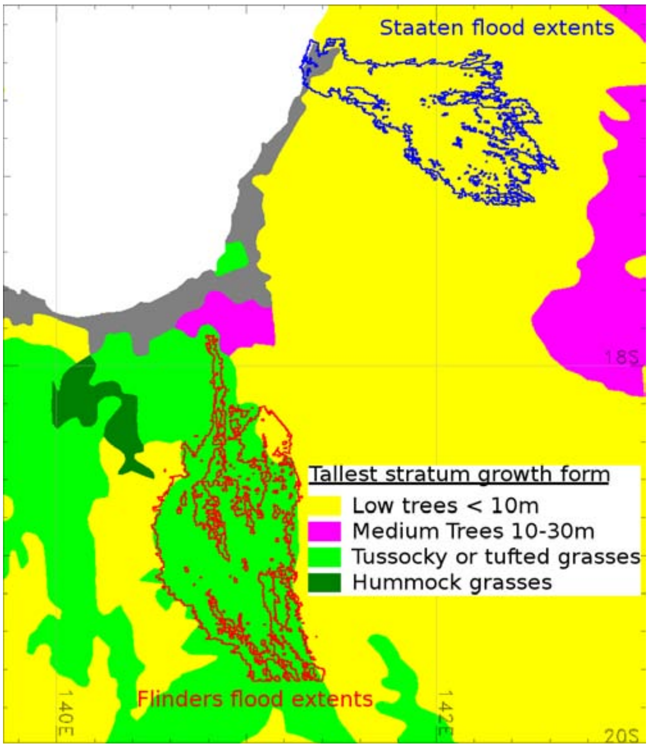

Figure 5.18: Tallest stratum growth-form in flooded areas

In the tussock grass-dominated Flinders floodplain, we see, in late January 2009, when the soil was dry, a backscatter value across the floodplain of around -11 dB. From this point, we see the flooded region drop to -15 dB, and then rise sharply as the flood recedes. This is consistent with the findings by others that short, more vertically oriented grasses are more inclined to return a response resulting from dihedral scattering. Another difference between the two regions is the presence of trees in the Mitchell and Staaten floodplains, in contrast to the Flinders flood region, the tallest stratum growth form of which is grass (see Figure 5.18). We know that C-Band radar will interact with structures of the order of scale of the small branches and foliage within the canopy of the eucalypts which dominate the Mitchell and Staaten, which can only serve to *dilute* the signature resulting from the grass and water interactions, with volume scatter.

5.6 Conclusion

From the classification and accuracy test performed using the Flinders data, GM data was shown to be a useful tool in the mapping of floods, given favourable surface conditions. It was mentioned in section 5.5 that the errors of omission in this classification were concentrated in the Norman River section of the study region. This is the section of the greater Flinders floodplain that shares a similar vegetation growth form class to the Staaten region, as can be seen in Figure 5.18.

Findings by others regarding the influence of vertical orientation and above-surface density in grasses on C-HH data is mixed. We found that in the short, vertically-oriented bluegrass of the Flinders floodplain, during partial inundation, a lower water level produced a higher backscatter value as dihedral scattering increased. In the denser, thatched grasses of the Mitchell and Staaten floodplains, the presence of water was barely distinguishable. Our findings straddle the demarcation of the expected radar response in flooded grasslands and wooded savanna, depending on the nature of vegetation. To model precisely the synergy between vegetation structure, density, orientation and phenology may not be possible, given the diversity of species and distribution. It is clear that certain environmental conditions preclude the use of GM data for the monitoring of floods. When radar is used to detect the presence of flooding, we rely on a low return in the case of total inundation, due to specular reflection, and on a high return where emergent vegetation is present, due to dihedral scattering.

The benefits of the use C-HH radar data to monitor shallow but extensive flooding may therefore come with the cost of a similar study on a floodplain-by-floodplain basis as needed, to calibrate thresholds, or to discount the use of C-band radar entirely.

Chapter 6

Conclusion

6.0.1 Research questions

The research questions posed in Section 1.6.1 were addressed as follows:

How does radar backscatter vary with incidence angle for different surface conditions? How does this affect the segmentation of open water? The variation of backscatter with incidence angle showed a close fit ($R^2 = 0.8$) to a sinusoidal model over open water, but a far less close fit ($R^2 = 0.2$) over land, due, most likely, to environmental variations of the target areas throughout the time series over which the regression was carried out. Despite this, the slope of a linear approximation to the model showed clear regional clustering. This clustering, when compared with various land cover classifiers, was found to correlate best with regolith.

The slope of the linear approximation to the variation of backscatter with incidence angle proved less sensitive to soil moisture and to Bragg resonance than the absolute backscatter values themselves, suggesting a potential avenue of research into more accurate mapping of water, in the event of future C-Band missions providing sufficiently frequent coverage.

The calculation of slope and offset of the linear model for particular regions of interest provided a reasonable means to normalise individual GM images with respect to incidence angle through the rest of the research done for this thesis.

Under what vegetation conditions (vegetation type, size, density, orientation) does multihedral backscatter distort the radar signal so as to make flood water indistinguishable from its surroundings? The short, vertically-oriented bluegrass of the Flinders floodplain demonstrated a predictable backscatter signature throughout the process of soil saturation, partial flooding and total inundation, allowing a flood to be mapped to a high level of accuracy (κ-statistic = 0.7).

The inundation of the taller, denser thatched grasses of the Mitchell/Staaten floodplains returned backscatter signals that were indistinguishable from the surrounding wet soil and vegetation through periods of partial inundation, with the only predictable signal being the fall in backscatter values at total inundation.

Prior knowledge of vegetation characteristics of the Flinders region would further increase the accuracy of the flood classification, by segregating the image into regions of greater and lesser certainty.

How can we separate dry soil/sand from floods through arid regions? How significant is this problem? Track-for-track image differencing techniques can be used to to eliminate ambiguity between low backscatter response due to specular reflection on flood waters and low backscatter response due to absorption in dry sand.

The problem was found to be potentially significant, with, in one example, the area of absorption surrounding flood waters in one GM image having the same order of scale as that of the specular reflection on the flood itself.

The work done to resolve this problem also demonstrated the ability of GM data to fill-in the flood mapping function during critical early stages of a major flood, were VIR data were unavailable due to cloud cover, and also demonstrated the stability of the backscatter threshold for flood demarcation, in comparison to that for SWIR reflectance from MODIS images.

The combination of techniques and data sources allowed a large flood to be mapped in its entirety over the course of several months.

How can the processing of such a large dataset be managed? How can we automate the download, registration and orthorectification of

a high volume of GM data files to allow efficient analysis? The open source geospatial community, led by the Open Source Geospatial Foundation (OSGeo[1]) play a vital role in the provision of fundamental tools to read, write and process most file formats used by the GIS field, and these are relied upon by both commercial and non-commercial software providers.

By developing the scripts used in this thesis, I have demonstrated that open source tools can be used throughout the whole data download, registration, pre-processing and analysis process, allowing control, transparency, flexibility and efficiency, at very little cost.

The primary reason for the decision to take the time to carry out this stage of the work, rather than relying on bespoke software such as ESA's NEST tools, was the fact that the whole process could be carried out using the university's high-performance computing system, in a parallel processing environment. It is easy to underestimate the resultant advantage of being able to run and re-run scripts many times, tweaking parameters in each case, making and correcting mistakes without having to wait a considerable time to find out that a mistake may have been made in the first place. A fast and efficient processing system allows for an environment of exploration, in which trial-and-error can lead to new paths in the research, as it has done for many people in all fields of research.

6.1 In summary

I have investigated the potential role that Envisat ASAR Global Monitoring Mode data plays in the mapping of broad scale flooding. Now that Envisat is no longer operational, although we have alternative C-band satellite sensor data available to us, we await a contender for GM data which matches its coverage and ready availability. We can be sure that, as technology in processing circuitry, data storage capacity and, in particular, battery power storage and solar recharge capabilities advance, we may not have to rely on such coarse spatial resolution as that of GM data. Any increase in resolution will pose further challenges to the processing involved in the type of research that makes use of large time series,

[1] http://www.osgeo.org/

such as that with which I have dealt here. Depending on the scales being looked at, the type of pre-processing described in Chapter 2 may involve generalisation computations where they were absent here, in order that resultant data sets were spatially comparable to other data with which they were to be compared. We can see this process happening even with GM data at its 1km resolution, where for example, soil moisture products have been derived and compared to similar products that have 25km or even 50km spatial resolutions. The foreseen finer spatial resolutions to be dealt with in the next generation of research will present plenty of new opportunity to gain a better understanding of the complexities of backscatter response. To take advantage of these resolutions, orthorectification must be carried out in compliance with comprehensive and proven techniques as set out by, for example van Zyl *et al.* (1993) and Ulander (1996), using a similarly fine-scaled DEM. More careful consideration will need to be given to georeferencing, though it is expected that much of this preprocessing will be offered by the data providers, as was the case, for example, with L-band ALOS PALSAR. Given such anticipated increased requirements in terms of processing, it is felt that the principles described in this thesis, in the use of universally available open source data interoperability tools, open platform scripting and GIS software and multi-threading techniques that can easily be ported to super-computers such as JCU's HPC, will continue to offer the best solutions.

Whilst the use, on the same broad scale, of data at a much finer resolution, will lead to less ambiguity caused by the aggregation of sub-pixel backscatter responses from a surface of varied structural, textural and dielectric properties, many factors which contribute to the complexities faced with the use of GM data will remain. The availability of finer resolution data at a similar temporal frequency as GM will open the path for the extension of work described here. More precise matching of radar response with topographical parameters will lead to a better understanding of the variance of backscatter with incidence angle. Flooding extents will be able to be mapped with greater precision. Reduced pixel-mixing will lead to better segregation of soil moisture, for example, from dihedral scatter at the boundaries of floods. Partially flooded vegetation may be more precisely matched with radar response categorically in terms of vegetation species, which, we have learnt, is vital in order to interpret backscatter from such environments to derive the presence of water, or even its relative height.

At the outset of the work described here, the decision was made to concentrate on GM as a primary source of data with which to investigate the mapping of floods. This decision was made for a number of reasons. The time constraints governing most Ph.D.. research (which are really the manifestation of *financial* constraints), impose the necessary trade-off between depth of research and scope. The temporal frequency of GM data provided a huge time series with which to investigate the behaviour of backscatter against various topographical parameters, as well as giving me the opportunity to test the availability of data in flood events against VIR alternatives. Also, from research by others it was found that, of all possible wave bands and polarisation configurations, the C-HH configuration offered by GM data might well be the best one for the job. It is worth noting here that one of the most confounding problems found in all research in the detection of water using both C- and L-band data was the phenomenon of Bragg Resonance. As I have discussed, this is dependent on the orientation, as well as relative scale, of regular waves on the surface of the water. As such the effect is far reduced using a cross-polarised, C-HV or C-VH configuration, although this may come at the cost of a lower radiometric resolution on surfaces where no polarity shift has occurred. Sentinel-1 will provide both cross-polarised configurations (ESA, 2012b).

From my initial review of literature on the subject of water detection using radar remote sensing, fundamental questions emerged: What were the effects of incidence angle on backscatter? How could specular reflection be distinguished from absorption in flooded arid regions? How did backscatter response vary with vegetation conditions under partial inundation? To answer these questions, I devised a means to process and manage the large dataset, necessary for such analysis at a pixel-by-pixel level. I used regression to gain values, for each pixel and under seasonal conditions, of slope and intercept in a linear approximation of the relationship between incidence angle and backscatter, by which to normalise the data. I managed to further mitigate incidence angle effects through image differencing, and with this method I also separated flood from desert, successfully tackling a problem that had not been dealt with before. In this way I captured the progress of an entire flood event, stretching across a thousand kilometres over a hundred days. I investigated radar response to total and partial submersion of vegetation in two regions in the tropical savanna of northern Queensland, and gained an understanding of the interaction of radar with different vegetative conditions, adding to a field of research that was, and is, in great need of further investigation. The study reinforced my conviction in the ability of GM data to map a large rapid flood event covering nine thousand kilometres with open water, while at the same time highlighting the failure of GM to capture a similarly sized event in a neighbouring region, with a population close to zero; where floods, even on this scale, can conceivably pass by unnoticed.

In attempting to answer these questions, other questions inevitably arose, and some were answered. I observed the correlation between the variation of backscatter with incidence angle and regolith. I found that the unique and highly separable value of $\Delta\gamma/\Delta\alpha$ on open water appeared to be relatively independent of Bragg Resonance, paving the way to the possibility of taking advantage of this fact to map flooding using C-HH data under unfavourable wind conditions, with impunity. Further, it was found the this opportunity was unlikely to be met using GM data, due to margins of error in consecutive images where the difference in incidence angle was insufficient. The question of how to optimise radiometric thresholding was answered with a unique incremental threshold convergence method using complementary MODIS data, in a process which highlighted both the stability of the resultant GM-derived threshold, and the instability of the MODIS SWIR reflectance threshold for open water.

The understanding gained from this research, and the questions raised, coincide well with the opportunity offered by JCU for further research, to use radar and optical/thermal satellite data to contribute to knowledge being gathered by a team under the Hydrology Department, as well as to investigate further the interaction of radar with vegetation and water in a tropical floodplain. I look forward to this work, and to the discoveries that await the field of remote sensing as new satellite missions come online.

6.2 Beyond the thesis

6.2.1 C-band synthetic aperture radar

On 8 April 2012, while the conclusions to this thesis were being written, the European Space Agency lost contact with Envisat. After spending a month trying to restore contact to the satellite, ESA declared the mission at an end on 9 May. As with many successful earth observation satellite missions, Envisat was in operation for well over its planned lifetime, having been in orbit since 2002.

With the corresponding loss of the ASAR sensor, there is a gap in availability of data data similar to ASAR's GM mode, with its temporal frequency and availability. In the short term, this will have an immediate effect on research such as this, which seeks to take advantage of this particular data mode that has been peculiar to Envisat ASAR, and at least one systematically generated product derived from GM data, that being ESA's Tiger Innovator project *Soil moisture for Hydrometeorological Applications over SADC* (SHARE) (Bartsch *et al.*, 2008).

Thankfully, the end of Envisat does not mark the end of satellite C-band radar availability. The Canadian Space Agency's (CSA) remarkable Radarsat-1 has been earmarked to fill part of the gap left by Envisat's demise (Boucher, 2012). Radarsat-1, launched on a 5 year mission in November 1995, is still going strong in May 2012. Though having no GM mode as such, Radarsat-1 does have a wide ScanSAR mode with a nominal resolution of 100m, as well as fine-beam modes operating up to an 8m nominal resolution. The later Radarsat-2 satellite, launched in December 2007 and being capable of dual-sided imaging to a nominal resolution of 3m, also adds to the available list of C-band data. Further to this, CSA are planning the continuation and improvement of Radarsat-1 and -2 in the planned launches in 2016 and 2017 of the RADARSAT Constellation, which is intended to provide daily C-band SAR coverage of 95% of the world (CSA, 2012).

ESA has been planning to launch its next C-band SAR sensor aboard the Sentinel-1 mission in 2013 (ESA, 2012b), and the cessation of operation of Envisat gives this mission renewed significance. Sentinel-1 will be one of a string of satellites launched under a programme entitled *Global Monitoring for Environ-*

ment and Security (GMES), headed by the European Commission in partnership with the ESA and the European Environment Agency (ESA, 2012a). The subsequent Sentinels 2–5 will include high resolution VIR sensors for the monitoring of land, ocean and atmosphere.

The Indian Space Research Organisation (ISRO) launched its *Radar Imaging Satellite-1* (RISAT-1) on 26 April 2012 (ISRO, 2012), though the future availability of data from the C-band SAR sensor on board to the global scientific community is unclear.

6.2.2 Mary River, Northern Territory

The need to monitor greenhouse gas emissions from floodplains in Australia

One vital component in gauging the extent of the greenhouse-gas-induced climate change problem is the monitoring of emissions. The United Nations Convention on Climate Change (UNCCC) identified the systematic observation of surface greenhouse gases as an essential component of climate change policy (Onoda, 2008). Currently there are large uncertainties in surface fluxes of CO_2, CH_4 and N_2O, but an increasing feedback between climate change and greenhouse gasses is expected (Bréon & Ciais, 2010). The Global Warming Potential (GWP) of CH_4 is 25 times that of CO_2 (Dalal *et al.*, 2008), which amounts to 20% of the total global warming effect. To put the GWP of CH_4 in context, Dalal *et al.* (2008) tell us that, since 1750, CO_2 concentrations have gone up by 33%, while CH_4 concentrations have gone up by 75%.

Somewhere between a quarter and a third of global CH_4 emissions come from wetlands and lake sediments (Chen *et al.*, 2011; Dalal *et al.*, 2008). The feedback between climate change and methanogenesis in such environments in Australia is poorly understood, due to a lack of research data, but we do know that there is a positive feedback between atmospheric CO_2 concentrations and CH_4 emissions (Dalal *et al.*, 2008). Law & Garnett (2011) assess the use of the National Carbon Accounting Toolbox (NCAT) for estimating and mapping carbons stocks in Australia's Northern Territory, and conclude that further work is needed on soils, fire, grasslands, wetlands and woody debris in order to improve the validity of NCAT for carbon estimates.

The role of C-band radar

Soil and vegetation characteristics are major factors governing the production and emission of CH_4 in wetlands. In addition, the hydrodynamics of wetland systems are crucially important to understand, for a number of reasons. Flooded wetlands can produce forty times the amount of CH_4 as wet soils (Arnell, 2002). In dry ecosystems, methane fluxes are linked largely to soil porosity, whereas, once flooded, methane emissions are a function of vegetation characteristics and the actual level of the water (Chen *et al.*, 2011; Dalal *et al.*, 2008). Also, the very dynamic density and composition of aquatic vegetation in a floodplain are governed by its hydrology and morphology (Coops *et al.*, 1999).

Vegetation types determine relative CH_4 emissions. There is a positive correlation between the distribution of vegetation with well-developed aerenchyma and CH_4 production and emission. Such emissions may also be influenced by the provision of carbon substrates though the roots. In addition, vegetation can be an indicator of soil types, which in turn effect CH_4 production through relative levels of trace elements, electron acceptors, pH and salinity (Dalal *et al.*, 2008).

Research is currently underway by a team here at JCU, monitoring greenhouse gas emissions in a section of the Mary River floodplain in the Northern Territory. The intention is to upscale results to the broader floodplain, and beyond, based on common indicators that can be correlated to the results. In light of what has been discussed here, data must be collected in terms of vegetation type, density and phenology, as well as the hydrodynamics of the flood plain - water height, flood duration and water body connectivity. Cost and practical accessibility limit the provision of large scale data of this sort to remote sensing as a method. Research described in this thesis has outlined the limitations of VIR data alone as a continuous monitoring tool, due to cloud cover. We have seen that microwave radar data are largely free from this problem, and that C-band data, in particular, have been the radar data of choice for many studies of aquatic vegetation. We have also seen that C-band radar allows us to determine the presence of water and, in certain vegetation environments, gives us an indication of the level of submersion of aquatic vegetation.

We have also learnt the important limitations of C-band data. The disadvantage of coarseness of scale suffered by GM data is somewhat irrelevant, given that there remains no similar contender with a 500m pixel spacing. However, as mentioned, Radarsat-1 and -2 do provide an invaluable stepping-stone until the advent of ESA's Sentinel mission, at which time we can hope for a 1–3 day repeat coverage once again (ESA, 2012b). Other limitations, such as we found in the ambiguity of signal in the Staaten grasslands under flood, are peculiar to a particular vegetation regime. In this regard, the particular conditions of the Mary River ecosystem can be evaluated on their own merits. In addition to radar, VIR remote sensing will necessarily be used to distinguish, as needed, the vegetation types and stages. Such requirements can be met by a number of available satellite sensors, depending on the resolution required, ranging from MODIS and Landsat TM at 500, 250 or 30m resolutions, all the way to the 0.3m panchromatic, 2m VIR and the almost daily revisit time offered by DigitalGlobe's WorldView-2 (DigitalGlobe, 2012).

Participation in the research at Mary River constitutes not only a contribution as a tool to upscale the observed data, but also provides the opportunity to answer questions arising from the work described in Chapter 5 and by others, surrounding the complex relationship of C-band backscatter, with water level and structure, density, orientation and height of emergent vegetation.

6.2.3 Combination with other data types

The satellite Gravity Recovery and Climate Experiment (GRACE) is a twin satellite mission which provides data in the form of a set of Stokes coefficients to a truncated spherical harmonic expansion of the geoid. The data are used to compute gravity anomalies, which are deviations from the large-scale gravity field, caused by density variations in the subsurface. As ground and surface water constitute a substantial fluid mass with significant variation over time, GRACE's potential contribution to the field of hydrology is clear. A significant amount of literature directly related to GRACE data are devoted to the establishment of the accuracy of the reduction process used to derive the anomaly figures, as this is a complex procedure. The further derivation of hydrological parameters, and the apportioning of values to various components of the hydrological cycle are even more complex. GM data allows us the opportunity to test the relationship of observed rainfall extent and relative soil moisture with GRACE anomaly derivations for the Australian region, forming a component of the ground-truthing work necessary to increase the accuracy of GRACE derived products. I am currently involved in discussions towards the design of a research model to take advantage of this opportunity.

Back in Section 4.6.3 I commented on the potential of the future Surface Water and Ocean Topography (SWOT) mission, to be launched in 2020. Using wide-swath altimetry technology, SWOT will provide temporal and spatial variations in water volumes stored in rivers, lakes, and wetlands at unprecedented resolution (Biancamaria *et al.*, 2010). SWOT will generate a global 3D mapping of all terrestrial water bodies whose surface area exceeds 250 m^2 and rivers whose width exceeds 100 m (Biancamaria *et al.*, 2010). The principal instrument of SWOT will be a K_a-band Radar Interferometer (KaRIN), which will provide heights and co-registered all-weather imagery of water over 2 swaths, each 60 km wide, with an expected precision of 1 cm/km for water slopes, and absolute height level precision of 10 cm/km^2. The high spatial and radiometric resolution of SWOT data, with repeat coverage occurring at least twice every 21 days, will enable cross-validation of C-band derived flood extents, facilitate volume calculations and add precision to the derivation of GRACE products. The contribution of SWOT to flood mapping will be enormous.

6.2.4 Characteristics of fire occurrence and spread under a changing Australian environment

Tropical savannas (TS) cover more than one third of the continent of Australia (Landsberg *et al.*, 2011). Globally, they contain almost 15% of the world's carbon stock, and contribute 38%, 19% and 59% of emissions of CO_2, CH_4 and NO_2 respectively (Spessa *et al.*, 2005). This makes TS a significant component of the global greenhouse gas budget. The TS landscapes of northern Australia are dynamic, continually changing due to anthropogenic and natural effects. One important feature straddling both of these categories is fire. In their study of fire patterns in two regions within the TS in northern Australia, Felderhof & Gillieson (2006) found that up to 74% of of the Cape York study region burnt in a single year, and determined that an understanding of fire patterns in the TS was a necessary step towards understanding the vegetation dynamics in the region.

Fire patterns are determined by ignition and propagation characteristics (Chuvieco *et al.*, 2004). Propagation depends on fuel and environmental conditions. Ignition depends on man or nature, and the latter takes the form of lightning (Felderhof & Gillieson, 2006). Neilson (1995) models fire likelihood on lightning conditions and intensity of rainfall in summer, as do M.B. & Pivello (2000), who note that most fires occur in the transition from the dry to the wet season. In the context of greenhouse gas emissions, it is expected that lightning occurrences will increase, with an increased concentration of CO_2 in the atmosphere (Cardoso *et al.*, 2008).

Many researches have used remote sensing in an attempt to gauge fire risk. Chuvieco *et al.* (2004) cite three disadvantages in their endeavours to this end, being insufficient temporal frequency, obscuration by cloud cover and calibration difficulties. Certainly the GM data used in this thesis would overcome the first two of these - to the third problem it may offer its own brand of challenges. The authors also highlight the disadvantage with their VIR data in the case of dead fuel, in that wetness is not followed by greenness, and therefore the moisture content is less discernible. Spessa *et al.* (2005), in their investigation into the relationship of fire frequency, rainfall and vegetation patterns in northern Australia, used a Normalised Difference Vegetation Index (NDVI) to distinguish vegetation patterns, but note potential errors due to differences in “background soil colour”. The importance of dead fuel moisture to the spread of fire in grasslands is emphasised by Sullivan (2010), who also reiterate the difficulty in measuring this parameter. They also list the grass curing rate as a factor influencing fire spread, and note that whilst rainfall does not slow down the curing rate of annual grasses (which continue to cure once they have started), it does slow down the curing rate in perennial grasses through regeneration.

The scale of TS regions under study confine any broad-reaching real-time fire occurrence or likelihood mapping to remote sensing. Apart from the use of thermal infrared data to detect fire occurrences directly, VIR reflectance data is limited in its response purely to surface reflection. Thermal emissions have been used to some effect by, for example, Vidal *et al.* (1994), who relate fire occurrences to the ratio between actual and potential evapotranspiration (AET/PET) derived from daily NOAA-AVHRR surface temperatures and synoptic air temperature (Leblon, 2005).

Little work has been done to explore the use of radar to add a measure of biomass density to fire likelihood detection. Leblon (2005) explore the use of Radarsat-1 to help determine the fuel moisture component of fire probability, but find that the 35 day revisit time is prohibitive, and see the contribution to the signal by soil moisture as noise. As we have seen in Chapter 5, it is important to know the characteristics of the vegetation species that cover the region of interest, as, depending on the density, structure and orientation of grasses, C-band backscatter may represent the wetness/dryness of the grass almost independently of the surface beneath. As discussed, the context of vegetation species is also crucial where rainfall may or may not effect fuel curing.

Bartsch *et al.* (2008) showed how GM data could provide an effective and, at 1km resolution, spatially fine (compared to alternatives) soil moisture product. We have shown that in some grasslands, C-band backscatter is representative of the wetness of grasses, rather than the surface below. The temporal frequency of GM data allows us to see, during the dry season, where in the savanna rain has recently fallen.

Figure 6.1 shows four GM images over the Flinders region in Queensland during the dry season. The top left image shows the low backscatter values where no rain has fallen recently, whereas the other images show where rain has fallen in the previous 24 hours or so. It may be, that analysis of the time taken for the radar response to drop, following a rain event, could give us an indication as to whether the backscatter is representative of the soil moisture, or the wetness of the vegetation. Where soil moisture is represented, the use of X-band data could be explored, the shorter wavelength of which ensures interaction of the radar sig-

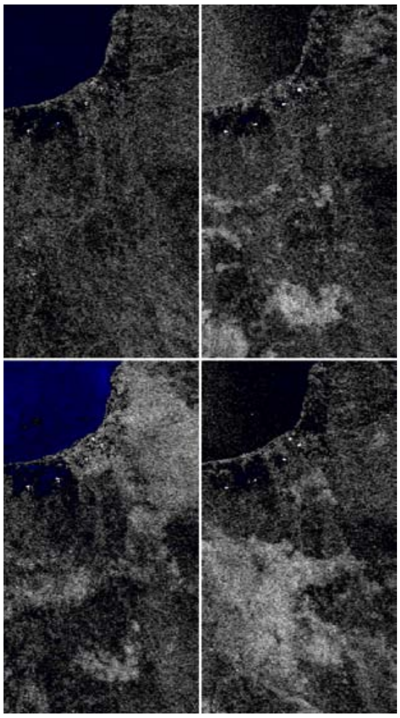

Figure 6.1: Four images of the Flinders region in Queensland, in which the high backscatter response following rainfall is manifest as bright patches against the otherwise low response due to dry surface conditions

nal with the smaller structured grass components. At the very least, with GM data we can conceivably generate maps showing rainless periods throughout the dry season. Work by Felderhof & Gillieson (2006) shows us how to effectively map fires in Australia's tropical savannas over long periods using remote sensing. With such data sets, the path has been laid for us to analyse any correlation between fire distribution and spread, with products derived from radar data, together with VIR and thermal imagery. Although Envisat is no longer operational, its wealth of data remains for much potential future research, especially in the analysis of the relationship of backscatter with environmental conditions. In light of the importance of tropical savannas globally, and of fire patterns within those savannas, it is surely an avenue of research worth exploring.

Appendix A - Scripts

GrassAscii.pm

A perl module building a class with the ability to read and write GRASS GIS native ASCII raster images.

Listing 1: GrassAscii.pm

```perl
package GrassAscii;
use strict;
use warnings;

sub new {
    my $class = shift;
    my $fullpath = shift or die "You must argue a full path\n";
    my $self = {
        FULLPATH => $fullpath,
        NORTH => undef,
        SOUTH => undef,
        EAST => undef,
        WEST => undef,
        ROWS => undef,
        COLS => undef,
        NULL => undef,
        TYPE => 'float',
        MULTIPLIER => 1,
        DECIMAL_PLACES => 2,
        DATA => []
    };
    bless($self, $class);
    return $self;
}

sub write_ascii {
    my $self = shift;
    if (@_) { ($self->{TYPE}, $self->{DECIMAL_PLACES}) = @_ }
    my $dps = $self->{DECIMAL_PLACES};
    open my $output, ">".$self->{FULLPATH} or die "Could not edit/create ".↩
        $self->{FULLPATH}."\n";
```

```
        foreach my $field qw (NORTH SOUTH EAST WEST ROWS COLS NULL TYPE MULTIPLIER) {
            if (defined($self->{$field})) {
                print $output lc($field).":\t".$self->{$field}."\n";
            }
        }
        foreach my $datarow (@{$self->{DATA}}) {
            my @rowdata = map(sprintf("%.$dps"."f",$_), @$datarow);
            print $output join("\t",@rowdata)."\n";
        }
    close $output;
}

sub read_header {
    my $self = shift;
    open my $input, $self->{FULLPATH} or die "Could not open ".$self->{FULLPATH}."\n";
    while (my $line = <$input>) {
        if ($line =~ /^([a-z]+):(\s*|\t)(\w+)$/) {
            $self->{uc($1)} = $3;
        } else {
            return 1;
        }
    }
    0;
}

sub read_data {
    my $self = shift;
    open my $input, $self->{FULLPATH};
    my @data;
    while (my $row = <$input>) {
        unless ($row =~ /^[a-z]/) {
            my @rowdata = split(/\t|\s/,$row);
            push @data, \@rowdata;
        }
    }
    $self->{DATA} = \@data;
    close $input;
}

1;
```

ORTHO.pm

A perl module building a child class of GrassAscii, which reads raster value data generated by the GM module and performs orthorectification.

Listing 2: ORTHO.pm

```
package ORTHO;
use Math::Trig;
```

```perl
use GrassAscii;

@ISA = ("GrassAscii");

use strict;
use warnings;


my $P = 500; #pixel size

sub new {
    my $class = shift;
    my ($root, $R) = @_ or die "You need to argue a root and a satellite radius.\n";
    my $self  = $class->GrassAscii::new($root.'.ORTHO');
    $self->{ROOT} = $root;
    $self->{R} = $R;
    $self->{HEIGHT} = undef;
    $self->{WIDTH} = undef;
    $self->{MARGIN} = 2; #How much to trim the edges by
    bless($self, $class);
    return $self;
}

sub fix_header {
    my $self = shift;
    $self->{NORTH} = sprintf("%.0f",$self->{HEIGHT} - $self->{MARGIN});
    $self->{SOUTH} = $self->{MARGIN};
    $self->{EAST} = sprintf("%.0f",$self->{WIDTH} - $self->{MARGIN});
    $self->{WEST} = $self->{MARGIN};
    $self->{ROWS} = sprintf("%.0f",$self->{HEIGHT});
    $self->{COLS} = sprintf("%.0f",$self->{WIDTH});
    $self->{NULL} = 0;
    $self->{TYPE} = 'int';
    $self->{DECIMAL_PLACES} = 0;
}

sub get_r { #radius at geographic lattitude
    my $lat = shift;
    my $flat = 1 / 298.257223560; #flattening
    my $a = 6378137; # Equatorial radius of WGS84 ellipsoid
    my $theta = atan((1 - $flat)**2 * tan(deg2rad($lat)));
    my $radius = $a * (1 - ($flat * (sin($theta))**2));
    return $radius;
}

# Note check_dimensions() must initialize $WIDTH and $HEIGHT
sub check_dimensions {
    my $self = shift;
    my %colsrows = (cols => undef, rows => undef);
    foreach my $thing ('cols','rows') {
        $colsrows{$thing} = get_dim($thing, $self->{ROOT}.'.DATA') or die "Data appears to have no dimensions\n";
        foreach my $field ('DEM','LAT','SRT') {
            my $dim = get_dim($thing,$self->{ROOT}.".$field");
            unless ($dim == $colsrows{$thing}) { return 0 }
        }
    }
    $self->{WIDTH} = $colsrows{cols};
    $self->{HEIGHT} = $colsrows{rows};
    return 1;
}
```

```perl

sub get_dim {
    my ($thing, $fullpath) = @_;
    my $output = 0;
    my $response = `grep $thing $fullpath`;
    chomp $response;
    if ($response =~ /:[\t\s](\d+)$/) {
        $output = 1 * $1;
    }
    return $output;
}

sub orthorectify {
    my $self = shift;
    die "The data files are not the same size. Aborting\n" unless (check_dimensions($self));
    print "Orthorectifying...\n";
#   First to get past the headers
    open DEM, $self->{ROOT}.".DEM" or die "Couldn't open ".$self->{ROOT}.".DEM\n";
    open DATA, $self->{ROOT}.".DATA" or die "Couldn't open ".$self->{ROOT}.".DATA\n";
    open LAT, $self->{ROOT}.".LAT" or die "Couldn't open ".$self->{ROOT}.".LAT\n";
    open SRT, $self->{ROOT}.".SRT" or die "Couldn't open ".$self->{ROOT}.".SRT\n";
    open THETA, $self->{ROOT}.".THETA" or die "Couldn't open ".$self->{ROOT}.".THETA\n";

    my %type = (DEM => [], DATA => [], LAT => [], SRT => [], THETA => []);
    my %handles = (DEM => *DEM, DATA => *DATA, LAT => *LAT, SRT => *SRT, THETA => *THETA);

    foreach my $key (keys %handles) {
        my $line = 'x';
        while ($line =~ /^[a-z]/) {
            local *FH = $handles{$key};
            $line = <FH>;
        }
        my @row = split(/\t|\s/,$line);
        $type{$key} = \@row;
    }

    foreach (my $row = 0; $row < $self->{HEIGHT}; $row++){

        my $phi_max = 0;
        my @newrasterrow = ();
        my @contributions = ();
        my @displacements = ();
        my @shadows = ();

        for (my $i = 0; $i < $self->{WIDTH}; $i++) {
            push @newrasterrow, 0;
            push @contributions, 0;
            push @displacements, 0;
            push @shadows, 0;
        }
    # First pass to establish contributions (see notes 2 April 2011)

        for (my $col = 0; $col < $self->{WIDTH}; $col++) {

            my $h = $type{DEM}->[$col];
```

```perl

            unless ($h eq '*') { # because these represent null values in DEM
                my $radians = $type{THETA}->[$col] * 3.1415927 / 180;
                my $s = 299792458 * $type{SRT}->[$col] * 10**(-9) / 2; # Slant range distance in metres to Ellipsoid !Corrected!
                my $phi = asin($s * sin($radians) / sqrt($s**2 + $h**2 - (2 * $s * $h * cos($radians)))); #to calc shadow see notes 7 April 2011

                if ($phi_max > $phi) { #This must be shadow - update phi_max, shadow and leave
                    $shadows[$col] = 1;
                } else { # carry on with contributions
                    $phi_max = $phi;

                    my $r = get_r($type{LAT}->[$col]);

                    my $big_omega = acos((($r + $h)**2 + ($self->{R})**2 - $s**2) / (2 * ($r + $h) * $self->{R}));
                    my $small_omega = acos(($r**2 + ($self->{R})**2 - $s**2)/(2 * $r * $self->{R}));
                    my $delta = $r * ($big_omega - $small_omega);
                    my $displacement = $delta / $P; # Number of cols as decimal fraction
                    $displacements[$col] = $displacement; #Store for second pass
                    my $int = int($displacement);

                    if (($col - $int) >= 0 && ($col - $int) < $self->{WIDTH}) {
                        $contributions[$col - $int] += (1 - $displacement + $int);
                    }
                    if (($col - $int - 1) >= 0 && ($col - $int - 1) < $self->{WIDTH}) {
                        $contributions[$col - $int - 1] += ($displacement - $int);
                    }
                }
            }
        }

    # OK now for second pass to place values

        for (my $col = 0; $col < $self->{WIDTH}; $col++) {

            my $h = $type{DEM}->[$col];
            unless (($h eq '*') || ($shadows[$col] == 1)) { # because these represent null values in DEM or shadow, respectively
                my $displacement = $displacements[$col];
                my $int = int($displacement);
                if (($col - $int) >= 0 && ($col - $int) < $self->{WIDTH} && ($col - $int - 1) >= 0 && ($col - $int - 1) < $self->{WIDTH}) {
                    if ($contributions[$col - $int - 1]) { #Just avoiding divisions by zero
                        $newrasterrow[$col] = ($displacement - $int) * $type{DATA}->[$col - $int - 1] / $contributions[$col - $int - 1];
                    }
                    if ($contributions[$col - $int]) { # again, avoiding divisions by zero
```

```
                            $newrasterrow[$col] += (1 - $displacement + $int) * ↩
                                $type{DATA}->[$col - $int] / $contributions[$col - ↩
                                $int];
                        }
                    }

                }
            }
#           @chars = map(chr, @nums)
            my @int_row = map(int, @newrasterrow);
            push @{$self->{DATA}}, \@int_row;
            foreach my $key (keys %handles) {
                local *FH = $handles{$key};
                my @thisrow = split(/\t|\s/,<FH>);
                $type{$key} = \@thisrow;
            }
        }
        fix_header($self);

        close DEM;
        close DATA;
        close LAT;
        close SRT;
}

sub trim_edges() {
    my $self = shift;
    for (my $i = 0; $i < $self->{MARGIN}; $i++) {
        pop(@{$self->{DATA}});
        shift(@{$self->{DATA}});
        foreach my $row (@{$self->{DATA}}) {
            pop(@$row);
            shift(@$row);
        }
        $self->{WIDTH} -= 2;
        $self->{HEIGHT} -= 2;
    }
}

1;
```

ALPHA.pm

A perl child class of GrassAscii, which calculates local incidence angles α from nominal incidence angles θ.

Listing 3: ALPHA.pm

```
package ALPHA;
use GrassAscii;
use Math::Trig;

```

```perl
@ISA = ("GrassAscii");

use strict;
use warnings;

my $P = 500; # Pixel spacing

sub new {
    my $class = shift;
    my $root = shift or die "You must argue a fullpath root\n";
    my $self  = $class->GrassAscii::new($root.'.ALPHA');
    $self->{ROOT} = $root;
    bless ($self, $class);
    return $self;
}

sub create_alpha {
    my $self = shift;
    my %ascii;

    print "Creating Alpha...\n";

    foreach my $type qw(DEM THETA) {
        $ascii{$type} = new GrassAscii($self->{ROOT}.".$type");
        $ascii{$type}->read_header();
    }

    die "Cols and Rows are not equal\n" unless (check_dims(\%ascii));
    foreach my $type qw(DEM THETA) {

        $ascii{$type}->read_data();
    }
    my $dnull = '*';

    my $tempfile = $self->{ROOT}.'.TEMP';
    open TEMPDATA, ">$tempfile";

    for (my $rows = 1; $rows < ($ascii{THETA}->{ROWS} - 1); $rows++) {
        my @output_row;
        for (my $cols = 1; $cols < ($ascii{THETA}->{COLS} - 1); $cols++) {
            my ($a, $b, $c, $d, $f, $g, $h, $i) = (
                $ascii{DEM}->{DATA}[$rows - 1][$cols + 1],
                $ascii{DEM}->{DATA}[$rows][$cols + 1],
                $ascii{DEM}->{DATA}[$rows + 1][$cols + 1],
                $ascii{DEM}->{DATA}[$rows - 1][$cols],
                $ascii{DEM}->{DATA}[$rows + 1][$cols],
                $ascii{DEM}->{DATA}[$rows - 1][$cols - 1],
                $ascii{DEM}->{DATA}[$rows][$cols - 1],
                $ascii{DEM}->{DATA}[$rows + 1][$cols - 1]
            );
            my $alpha = 0;
            unless (($a eq $dnull)||($b eq $dnull)||($c eq $dnull)||($d eq $dnull)
            ||($f eq $dnull)||($g eq $dnull)||($h eq $dnull)||($i eq $dnull)) {
                my $theta = deg2rad($ascii{THETA}->{DATA}[$rows][$cols]);
                my $s = $i - $a + $c - $g + $f - $d;
                my $t = $a - $i - $g + $c + $b - $h;
                my $L = sqrt($s**2 + (36 * $P**2) + $t**2);
                my $A = $s/$L;
                my $C = (6 * $P)/$L;
                $alpha = 180 * acos(($C * cos($theta)) - ($A * sin($theta))) / 3.1415927;
```

```
            }
            push (@output_row, ($alpha ? $alpha : 0));
        }
        print TEMPDATA join("\t",@output_row)."\n";
    }
    close TEMPDATA;

    $self->{NORTH} = $ascii{THETA}->{NORTH} - 1;
    $self->{SOUTH} = $ascii{THETA}->{SOUTH} + 1;
    $self->{EAST} = $ascii{THETA}->{EAST} - 1;
    $self->{WEST} = $ascii{THETA}->{WEST} + 1;
    $self->{ROWS} = $ascii{THETA}->{ROWS} - 2;
    $self->{COLS} = $ascii{THETA}->{COLS} - 2;
    $self->{NULL} = 0;
    $self->{TYPE} = 'float';
    $self->{MULTIPLIER} = 1;
    %ascii = ();
    feed_back_data_from_file($self);
}

sub feed_back_data_from_file {
    my $self = shift;
    my $tempfile = $self->{ROOT}.'.TEMP';
    open INDATA, $tempfile;
    while (<INDATA>) {
        my @cols = split(/\t/);
        push @{$self->{DATA}}, \@cols;
    }
    close INDATA;
}

sub check_dims {
    my $asciis = shift;
    my $output = 0;
    if (my @keys = keys %$asciis) {
        $output = 1;
        for (my $i = 1; $i < (@keys); $i++) {
            foreach my $dim qw(ROWS COLS) {
                $output = 0 unless ($asciis->{$keys[$i]}{$dim} == $asciis->{
                    $keys[0]}{$dim});
            }
        }
    }
    return $output;
}
```

GM.pm

A perl module that is responsible for reading a GM data file, extracting geometric parameters, and interpolating tie point data to create raster surfaces for the incidence angle at the WGS84 ellipsoid (θ), the slant range time (SRT), and latitude (LAT), all of which are necessary for preprocessing calculations:

Listing 4: GM.pm

```
package GM;
use MY_CONFIG;
use Math::Trig;
use strict;
use warnings;

my $config = new MY_CONFIG('config');

my $PDS = $config->{PDS};
my $GDALINFO = $config->{GDALINFO};

sub new {
    my $class = shift;
    my $self = {};
    $self->{FULLPATH} = shift;
    $self->{WIDTH} = undef;
    $self->{HEIGHT} = undef;
    $self->{TIEPOINTS} = [];
    $self->{SAMPLE_NUMBERS} = [];
    bless ($self, $class);
    return $self;
}

sub get_R {
    my $self = shift;
    my $fullpath = $self->{FULLPATH};
    my @response = `$PDS -ds 2 -field orbit_state_vectors $fullpath`;
    chomp @response;
    my @keys = split(/\t/,$response[3]);
    my @values = split(/\t/,$response[4]);
    my %hash;
    for (my $i = 0; $i <= $#keys; $i++) {
        $hash{$keys[$i]} = $values[$i];
    }
    my $R = sqrt(($hash{'orbit_state_vectors[2].x_pos_1'})**2 + ($hash{'↩
        orbit_state_vectors[2].y_pos_1'})**2 + ($hash{'orbit_state_vectors[2].↩
        z_pos_1'})**2) / 100; # as they are in cm.
    return (1 * sprintf("%.0f",$R));
}

sub interpolate {
    my $self = shift;
    my $root = $self->{FULLPATH};
    $root =~ s/\.N1//;
    my @theta; #Nominal Incidence Angles
    my @srt; #Slant Range Times
    my @lat; # Latitudes
    my %all = (theta => \@theta, srt => \@srt, lat => \@lat);
    print "Interpolating...\n";
    #Create empty raster arrays
    foreach my $key (keys %all) {
        for (my $i = 0; $i < $self->{HEIGHT}; $i++) {
            my @temp;
            for (my $j = 0; $j < $self->{WIDTH}; $j++) {
                push @temp, 0;
            }
            push @{$all{$key}}, \@temp;
        }
    }
    # Inerpolate across rows
```

```perl

    foreach my $tp_row (@{$self->{TIEPOINTS}}) {
        my $this_raster_row = $self->{HEIGHT} - ($tp_row->[0]{'yx'}[0] + 0.5);

        for (my $tp_col = 0; $tp_col < 10; $tp_col++) {
            my %last_sample_value;
            my %next_sample_value;
            my $last_sample_col = $self->{SAMPLE_NUMBERS}[$tp_col] - 1;
            my $next_sample_col = $self->{SAMPLE_NUMBERS}[$tp_col + 1] -1;

            foreach my $field (keys %all) {
                $last_sample_value{$field} = $tp_row->[$tp_col]{$field};
                $next_sample_value{$field} = $tp_row->[$tp_col + 1]{$field};
            }
            for (my $raster_col = $self->{SAMPLE_NUMBERS}[$tp_col] - 1; $raster_col < $self->{SAMPLE_NUMBERS}[$tp_col + 1] -1; $raster_col++) {
                my %thisvalue;

                foreach my $fld (keys %all) {
                    $thisvalue{$fld} = (($next_sample_value{$fld} - $last_sample_value{$fld})
                    * ($raster_col - $last_sample_col) / ($next_sample_col - $last_sample_col))
                    + $last_sample_value{$fld};
                    $all{$fld}[$this_raster_row][$raster_col] = $thisvalue{$fld};
                }

            }
        }
        foreach my $fd (keys %all) {
            $all{$fd}[$this_raster_row]->[$self->{SAMPLE_NUMBERS}[10] - 1] = $tp_row->[10]{$fd};
        }
    }

    # Now interpolate down columns

    for (my $rast_col = 0; $rast_col < $self->{WIDTH}; $rast_col++) {
        for (my $tiepoint_row = 0; $tiepoint_row < scalar(@{$self->{TIEPOINTS}}) - 1; $tiepoint_row++) {
            my $last_sample_raster_row = $self->{HEIGHT} - ($self->{TIEPOINTS}[$tiepoint_row][0]{'yx'}[0] + 0.5);
            my $next_sample_raster_row = $self->{HEIGHT} - ($self->{TIEPOINTS}[$tiepoint_row + 1][0]{'yx'}[0] + 0.5);

            for (my $raster_row = $last_sample_raster_row; $raster_row < $next_sample_raster_row; $raster_row++) {
                my $proportion = ($raster_row - $last_sample_raster_row) / ($next_sample_raster_row - $last_sample_raster_row);

                foreach my $feld (keys %all) {
                    my $this_value = $proportion
                    * ($all{$feld}->[$next_sample_raster_row][$rast_col] - $all{$feld}->[$last_sample_raster_row][$rast_col])
                    + $all{$feld}->[$last_sample_raster_row][$rast_col];

                    $all{$feld}->[$raster_row][$rast_col] = $this_value;
                }

            }
```

```
        }
    }
    output_rasters(\%all, $root, $self);
}

sub output_rasters {
    my ($all, $root, $self) = @_;
    foreach my $field (keys %$all) {
        output_raster($all->{$field}, uc($field), $root, $self);
    }
}

sub output_raster {
    my ($data, $suffix, $root, $self) = @_;
    my $fullpath = "$root.$suffix";
    open my $output, ">$fullpath" or die "Couldn't create/edit $fullpath\n";
        my $north = sprintf("%.0f",$self->{HEIGHT});
        my $east = sprintf("%.0f",$self->{WIDTH});
        print $output <<"EOF";
north:  $north
south:  0
east:   $east
west:   0
rows:   $north
cols:   $east
type:   float
null:   0
EOF
        foreach my $datarow (@$data) {
            my @row = map {sprintf("%.2f",$_)} @$datarow;
            print $output join("\t", @row)."\n";
        }
    close $output;
}

sub create_points_file {
    my $self = shift;
    my ($points_path, $reverse) = @_ or die "Points file path not specified. Aborting.\n";
    open POINTS, ">$points_path" or die "Cannot create/edit POINTS file $points_path\n";
        print POINTS "# Neareast\tNearnorth\tFareast\tFarnorth\tInclude\n";
        my $tiepoints = $self->{TIEPOINTS};
        for (my $i = 0; $i < (@$tiepoints); $i++) {
            for (my $j = 0; $j < 11; $j++) {
                my $x = $tiepoints->[$i][$j]{'yx'}[1];
                my $y = $tiepoints->[$i][$j]{'yx'}[0];
                my $long = $tiepoints->[$i][$j]{'long'};
                my $lat = $tiepoints->[$i][$j]{'lat'};
                my $local = "$x\t$y";
                my $destination = "$long\t$lat";
                my $output = ($reverse ? "$destination\t$local\t1\n" : "$local\t$destination\t1\n");
                print POINTS $output;
            }
        }
    close POINTS;
}

sub open {
    my $self = shift;
    ($self->{WIDTH}, $self->{HEIGHT}) = @{get_dimensions($self->{FULLPATH})};
```

```perl
    ($self->{TIEPOINTS}, $self->{SAMPLE_NUMBERS}) = @{get_tiepoints($self)};
}

sub get_root {
    my $fullpath = shift;
    my $output = 0;
    if ($fullpath =~ /(ASA.+)\.N1/) {
        $output = $1;
    }
    return $output;
}

sub get_tiepoints {
    my $self = shift;
    my $fullpath = $self->{FULLPATH};
    my @datarows = `$PDS -ds 7 -field first_line_tie_points,last_line_tie_points $fullpath`;
    chomp @datarows;
    my $num_records = scalar(@datarows) - 4;
    my $delta_y = $self->{HEIGHT} / $num_records;
    my $Y = $self->{HEIGHT} + $delta_y - 0.5;
    my @keys = split(/\t/, $datarows[3]);
    my @tiepoints;
    my @sample_numbers;
    for (my $datarow = 4; $datarow <= $#datarows; $datarow++) {

        my %hash;
        my @values = split(/\t/,$datarows[$datarow]);
        for (my $i = 0; $i <= $#keys; $i++) {
            $hash{$keys[$i]} = $values[$i];
        }
        foreach my $prefix (('first', 'last')) {
            if (($prefix eq 'first') || ($datarow == $#datarows)) {
                my @tiepoint_row;
                $Y = ($prefix eq 'last') ? ($Y - ($delta_y - 1)) : ($Y - $delta_y);
                for (my $i = 0; $i < 11; $i++) {

                    my $theta = $hash{$prefix."_line_tie_points.angles\[$i\]"};
                    my $x = $hash{$prefix."_line_tie_points.samp_numbers\[$i\]"} - 0.5;
                    my $y = $Y;
                    my $srt = $hash{$prefix."_line_tie_points.slant_range_times\[$i\]"};
                    my $lat = $hash{$prefix."_line_tie_points.lats\[$i\]"};
                    my $long = $hash{$prefix."_line_tie_points.longs\[$i\]"};
                    my %hash_out = (theta => $theta,
                        yx => [$y, $x],
                        srt => $srt,
                        lat => $lat,
                        long => $long);

                    push @tiepoint_row, \%hash_out;
                    if ($prefix eq 'last') { push @sample_numbers, 1 * $hash{$prefix."_line_tie_points.samp_numbers\[$i\]"} }
                }
                push @tiepoints, \@tiepoint_row;
            }
        }


    }
```

```
    return [\@tiepoints, \@sample_numbers];
}

sub get_dimensions {
    my ($fullpath) = @_;
    my ($width, $height) = (0, 0);
    my $response = `$GDALINFO $fullpath | grep 'Lower Right' `;
    if ($response =~ /\(\s*([\d.]+),\s*([\d.]+)\)/) {
        $height = $2;
        $width = $1;
    }
    return [$width, $height];
}

1;
```

process_gm.pl

The perl script which uses the methods in modules above to implement the pre-processing of a batch of GM data files. The script runs within its own GRASS GIS environment, creating a unique MAPSET which is destroyed once complete. In this way the routine can be run multiple times simultaneously within one GRASS instance, without falling foul of any locks.

Listing 5: process_gm.pl

```
#!/usr/bin/perl
use lib '/home/damien/Modules';

use GM;
use ORTHO;
use ALPHA;
use MY_CONFIG;
use strict;
use warnings;

my $config = new MY_CONFIG('config');
my $GISDBASE = $config->{GISDBASE};
my $DEM_LOCATION = $config->{DEM_LOCATION}; #'North_Aus';
my $DEM_NAME = $config->{DEM_NAME};
my $LOCATION = $config->{LOCATION};
my $time = time();

# We'll just search the current directory for GM N1 files
# Note: This must be done from within a Grass shell.

my ($BATCH) = $ARGV[0] or die "You must argue a batch number\n";
my ($search_dir) = $ARGV[1] or die "You must argue a search directory (full ↩
    path)\n";

```

```perl
my @fullpaths = `/usr/bin/find $search_dir -type l -name 'ASA*.N1'`;
chomp @fullpaths;

die "No GM files found\n" unless (scalar(@fullpaths));

# OK, what follows is the main procedure - a sequence of commands, most of which are defined below in sub-procedures. I know, I know, it's ugly, but all of the necessary (and more beautiful) algorithm structures have been set up in the modules called at the top. This is just the final implementation.

foreach my $fullpath (@fullpaths) {
    next unless check_latitude($fullpath);
    mapset($DEM_LOCATION, "M$BATCH");
    delete_old_location();
    recreate_dem_group();
    bring_in_raw($fullpath);
    target_dem();
    my $gm = new GM($fullpath);
    $gm->open();
    $gm->create_points_file("$GISDBASE/L$BATCH/PERMANENT/group/temp/POINTS"); #replace dodgy imported one
    $gm->create_points_file("$GISDBASE/$DEM_LOCATION/M$BATCH/group/G$BATCH/POINTS",1);#reversed to bring in dem
    rectify_dem();
    $gm->interpolate();
    my $root = $fullpath;
    $root =~ s/\.N1//;
    my $R = $gm->get_R();
    $gm = 0; #Free memory?
    mapset("L$BATCH",'PERMANENT');
    ascify_data_and_dem($root);
    my $ortho = new ORTHO($root, $R);
    $ortho->orthorectify();
    $ortho->write_ascii('int',0);
    $ortho = 0; #Free memory?
    my $alpha = new ALPHA($root);
    $alpha->create_alpha();
    $alpha->write_ascii('float',2);
    $alpha = 0; #Free memory?
    import_asciis($root);
    create_output_group();
    set_target();
    copy_points_file();
    rectify_output_group();
    mapset($LOCATION, "M$BATCH");
    output_tif($root);
    clean_up($root);
}

rid_gis_folders();

print "That took ".(time() - $time)." seconds\n";

sub check_latitude {
    my $fullpath = shift;
    my @lats;
    my @result = `gdalinfo $fullpath `;
    foreach my $line (@result) {#(595.5,480.5) -> (-70.374488,-10.937347,0)
        if ($line =~ /\(([\d.,]+)\)\s\->\s\(-?[\d.]+,-?([\d.]+),.+/) {
            push @lats, $1;
        }
```

```
    }
#   @articles = sort {$b <=> $a} @files;
    my @sorted = sort {$a <=> $b} @lats;
    return ($sorted[0] < 60);
}

sub rid_gis_folders {
    unlink "$GISDBASE/L$BATCH";
    unlink "$GISDBASE/$LOCATION/M$BATCH";
    unlink "$GISDBASE/$DEM_LOCATION/M$BATCH";
}

sub clean_up {
    my $root = shift;
    my @extensions = qw(ALPHA ORTHO THETA LAT SRT DATA DEM TEMP);
    my @files = map("$root.$_", @extensions);
    unlink @files;
}

sub output_tif {
    my $root = shift;
    my $command = <<"EOF";
g.region zoom=ORTHO.r
r.mapcalc 'ALPHA = round(100 * ALPHA.r)'
r.mapcalc 'ORTHO = round(ORTHO.r)'
g.remove group=output
i.group group=output input=ORTHO,ALPHA
r.out.gdal -c input=output format=GTiff type=UInt16 output=$root.tif
EOF
    system $command;
}

sub rectify_output_group {
    system "i.rectify -a group=output extension=.r order=3 ";
}

sub copy_points_file {
    system "/bin/cp $GISDBASE/L$BATCH/PERMANENT/group/temp/POINTS $GISDBASE/L$BATCH/PERMANENT/group/output/POINTS ";
}

sub create_output_group {
    system "i.group group=output input=ORTHO,ALPHA ";
}

sub import_asciis {
    my $root = shift;
    my $command = <<"EOF";
r.in.ascii input=$root.ORTHO output=ORTHO
r.in.ascii input=$root.ALPHA output=ALPHA
EOF
    system $command;
}

sub set_target {
    system "i.target group=output location=$LOCATION mapset=M$BATCH ";
}

sub ascify_data_and_dem {
    my ($root) = @_;
    system "r.out.ascii -i input=$DEM_NAME.r output=$root.DEM null=* ";
    system "r.out.ascii -i input=temp.1 output=$root.DATA null=0 ";
```

```
}

sub rectify_dem {
    system "i.rectify -c group=G$BATCH input=$DEM_NAME extension=.r order=3 ";
}

sub bring_in_raw {
    my ($fullpath) = @_;
    system "r.in.gdal input=$fullpath output=temp location=L$BATCH --overwrite";
}

sub target_dem {
    system "i.target group=G$BATCH location=L$BATCH mapset=PERMANENT ";
}

sub recreate_dem_group {
    my $result = `g.list group `;
    system "g.remove group=G$BATCH " if $result =~ /G$BATCH/;
    system "i.group group=G$BATCH input=$DEM_NAME ";
}

sub delete_old_location {
    system "/bin/rm -r $GISDBASE/L$BATCH " if -d "$GISDBASE/L$BATCH";
}

sub mapset {
    my ($location, $mapset) = @_;
    my $gisenv = `g.gisenv `;
    if ($gisenv =~ /LOCATION_NAME='([\w\d]+)';\nMAPSET='([\w\d]+)';\n/) {
        unless ($1 eq $location && $2 eq $mapset) {
            system "g.mapset -c location=$location mapset=$mapset ";
            system "g.mapset -c location=$location mapset=$mapset ";# Deliberately done twice
        }
        system "g.region -d ";
    } else {
        die "You need to be within a Grass shell\n";
    }
}
```

pbs.pl

This perl script looks for all GM data files under the current directory and separates them into batches, creating a directory for each batch and symbolic links within each to those folders. Each batch will then be processed concurrently. Two batch scripts are then created by the main script for each batch - one being the instructions for Grass GIS, the other being the PBS batch script. The latter is submitted to the HPC server. The start of each PBS script sets the GRASS_BATCH_JOB variable to point to the individual Grass batch script, and starts a new instance of GRASS GIS, creating a unique temporary MAPSET within which to work.

Listing 6: pbs.pl

```
#!/usr/bin/perl

use strict;
use warnings;

my @GMs = `find \`pwd\` -type f -name 'ASA_GM*.N1'`;
chomp @GMs;

my ($prefix, $number_of_batches) = @ARGV;
my $lastbatch = ($#GMs > $number_of_batches ? $number_of_batches : $#GMs);
my $files_per_folder = int(($#GMs + 1) / ($lastbatch + 1));
my $index = 0;
my $localdir = `pwd`;
my @folders;

for (my $batch = 0; $batch <= $lastbatch; $batch++) {
    mkdir "$prefix$batch" or die "Couldn't create folder $prefix$batch\n";
    push @folders, $prefix$batch;
    for (1..$files_per_folder) {
        system "ln -s $GMs[$index] $prefix$batch/";
        $index++;
    }
}

# Now to get remainders, if there are any
for (my $i = $index; $i <= $#GMs; $i++) {
    my $put_it_in = $#GMs - $i;
    system "ln -s $GMs[$i] $prefix$put_it_in/";
}

foreach my $folder (@folders) {
    open my $grassbatch, ">grassbatch$folder" or die "Couldn't create ↩
        grassbatch$folder\n";
    print $grassbatch '#!/bin/bash'."\n";
    print $grassbatch "process_gm.pl $folder `pwd`/$folder\n";
    close $grassbatch;
    chmod 0755, "grassbatch$folder";
    open my $pbsbatch, ">pbsbatch$folder" or die "Couldn't create ↩
        pbsbatch$folder\n";
    print $pbsbatch <<'EOF';
#!/bin/bash
#PBS -c s
#PBS -j oe
#PBS -m ae
#PBS -N Preprocess_GM_Files
#PBS -M damien.ogrady@my.jcu.edu.au
#PBS -l walltime=9999:00:00
#PBS -l pmem=8gb

echo "------------------------------------------------------------"
echo " This job is allocated 1 cpu on "
cat $PBS_NODEFILE
echo "------------------------------------------------------------"
```

```
echo "PBS: Submitted to $PBS_QUEUE@$PBS_O_HOST"
echo "PBS: Working directory is $PBS_O_WORKDIR"
echo "PBS: Job identifier is $PBS_JOBID"
echo "PBS: Job name is $PBS_JOBNAME"
echo "————————————————————————————————————————————————————"

cd $PBS_O_WORKDIR
source /etc/profile.d/modules.sh
module load grass
EOF
    print $pbsbatch "export GRASS_BATCH_JOB=$localdir/grassbatch$folder\n";
    print $pbsbatch "grass64 -c -text /home/Damien/Grassdata/World/M$folder\n";
    close $pbsbatch;
    chmod 0755, "pbsbatch$folder";
    system "qsub pbsbatch$folder";
}
```

regression.pl

This perl script uses GDAL to carry out regression as described in section 3.4.1. GRASS GIS is only used at the very end to create visual interpretations.

Listing 7: regression.pl

```
#!/usr/bin/perl
use strict;
use warnings;
use lib '/home/damien/Modules';
use GRASSSESSION;
use Geo::GDAL;
use MY_CONFIG;

my $SPECIFIC_DIRECTORY = undef; # speaks for itself. Comes from command line args !!NB!! NOT fullpath, just a name
my $raw_files = get_arguments();
my $config = new MY_CONFIG('config');

my $RESOLUTION = $config->{RESOLUTION}; #Full will be 0.05
my $TARGET_DIRECTORY = $config->{TARGET_DIRECTORY}; # Root location for regression, world and timestamp maps
my $MASK_DIRECTORY = $config->{MASK_DIRECTORY}; # location of the MASK.tif file
my $GISDBASE = $config->{GISDBASE};
my $LOCATION = $config->{LOCATION};
my ($N, $S, $E, $W) = ($config->{N},$config->{S},$config->{E},$config->{W}); # Defining the north, south, east and west limits
my $WKT = $config->{WKT};
$config = undef;


### This is the main procedure ###

foreach my $fullpath (@$raw_files) {
```

```
    my $root = get_root($fullpath) or die "Something wrong with the full path $fullpath\n";
    if ($root) {
        my $dn_dataset = Geo::GDAL::Open( $fullpath );
        if (within_bounds($dn_dataset)) {
#           eval {
                my $clipped_dn_dataset = clip_dn($root, $dn_dataset);#contains dn and alpha
                my $sigma_alpha_dataset = create_sigmaalpha($root, $clipped_dn_dataset);
                update_regression($sigma_alpha_dataset, $clipped_dn_dataset);

#           };

#           print LOG "Error for $fullpath: $@" if $@;
        } else {
            print "File with root $root not within bounds\n";
        }

        delete_temporary_files($root);
    }
}
grass_calc_and_output();

### End of main procedure ###

sub grass_calc_and_output {
    my $grass = new GRASSSESSION($GISDBASE);
    $grass->setLocation($LOCATION);
    foreach my $prefix qw(N SumX SumX2 SumY SumY2 SumXY SumGamma) {
        $grass->addCommand("r.in.gdal input=$TARGET_DIRECTORY/$SPECIFIC_DIRECTORY/$prefix.tif output=$prefix --overwrite");
#       $grass->addCommand("rm $TARGET_DIRECTORY/$SPECIFIC_DIRECTORY/$prefix.tif");
    }
    my $command = <<"GCAO";
    r.mapcalc 'B=eval(numerator = (N * SumXY) - (SumX * SumY), denominator = (N * SumX2) - pow(SumX, 2), numerator / denominator)'
    r.mapcalc 'A = (SumY - (B * SumX))/N'
    r.mapcalc 'R2 = eval(numerator = (N * SumXY) - (SumX * SumY), \\
        denominator = sqrt((N * SumX2) - pow(SumX, 2)) * sqrt((N * SumY2) - pow(SumY, 2)), R = numerator / denominator, pow(R,2))'
    r.mapcalc 'SD = sqrt((SumY2 / N) - pow(SumY / N, 2))'
    r.colors.stddev SD
    r.colors.stddev B
    r.mapcalc 'MEANGAMMA = eval(mg = SumGamma / N, \\
        if(mg > 255, 255, mg))'

    echo '0% red
    0 red
    70 green
    140 0 128 0
    160 blue
    255 0 0 128' | r.colors MEANGAMMA col=rules

    r.out.png input=MEANGAMMA output=$TARGET_DIRECTORY/MEANGAMMA_$SPECIFIC_DIRECTORY.png
    r.out.png input=SD output=$TARGET_DIRECTORY/SD_$SPECIFIC_DIRECTORY.png
GCAO
    $grass->addCommand($command);
    foreach my $suffix qw(B A R2 MEANGAMMA SD) {
        my $type = ($suffix eq 'OUTPUT' ? 'Byte' : 'Float32');
```

```
        $grass->addCommand("r.out.gdal input=$suffix output=$TARGET_DIRECTORY/$SPECIFIC_DIRECTORY/$suffix.tif type=$type format=GTiff nodata=0");
    }
    $grass->run();
}

sub get_root {
    my $fullpath = shift;
    if ($fullpath =~ /(ASA_GM.+)\.tif/) {
        return $1;
    }
}

sub get_mask_data {
    my ($clipped_dn_dataset) = @_;
    my $mask_dataset = Geo::GDAL::Open( "$MASK_DIRECTORY/MASK.tif" ) or die "Couldn't open mask $MASK_DIRECTORY/MASK.tif\n";
    my $mask_band = $mask_dataset->GetRasterBand(1);
    my ($minx, $maxx, $miny, $maxy, $dx, $dy, $width, $height, $xoff, $yoff) = @{get_gridding_data($clipped_dn_dataset)};
    my $data = $mask_band->ReadTile($xoff, $yoff, $width, $height);
    return $data;
}

sub delete_temporary_files {
    my ($root) = @_;
    foreach ('ALPHA','SIGMAALPHA','DN','CLIP') {
        unlink("$_$root.tif");
    }
}

sub clip_dn {
    my ($root, $dn_dataset) = @_;
    my ($minx, $maxx, $miny, $maxy, $dx, $dy, $width, $height, undef, undef) = @{get_gridding_data($dn_dataset)};
    my $west = $minx < $W ? $W : $minx;
    my $east = $maxx > $E ? $E : $maxx;
    my $north = $maxy > $N ? $N : $maxy;
    my $south = $miny < $S ? $S : $miny;

    my $xoff = sprintf("%.0f",($west - $minx)/$dx);
    my $yoff = sprintf("%.0f",abs(($north - $maxy)/$dy));
    my $xsize = sprintf("%.0f",($east - $west)/$dx);
    my $ysize = abs(sprintf("%.0f",($north - $south)/$dy));

    my $dn_band = $dn_dataset->GetRasterBand(1);
    my $alpha_band = $dn_dataset->GetRasterBand(2);

    my $dn_data = $dn_band->ReadTile($xoff, $yoff, $xsize, $ysize);
    my $alpha_data = $alpha_band->ReadTile($xoff, $yoff, $xsize, $ysize);

    my $dataset = Geo::GDAL::Driver('GTiff')->Create("CLIP$root.tif", $xsize, $ysize, 2, 'UInt16');
    $dataset->GeoTransform($west, $RESOLUTION, 0, $north, 0, -$RESOLUTION);
    $dataset->SetProjection($WKT);

    my $dn_band_out = $dataset->Band(1);
    $dn_band_out->NoDataValue(65535);
    $dn_band_out->WriteTile($dn_data);

    my $alpha_band_out = $dataset->Band(2);
    $alpha_band_out->NoDataValue(65535);
```

```perl
    $alpha_band_out->WriteTile($alpha_data);

    return $dataset;
}

sub get_gridding_data {
    my ($dataset) = @_;
    my ($minx, $dx, undef, $maxy, undef, $dy) = $dataset->GeoTransform();
    my ($width, $height) = $dataset->Size;
    my ($maxx, $miny) = (($minx + ($dx * $width)), ($maxy - (abs($dy) * $height)));
    my $xoff = sprintf("%.0f",($minx - $W)/$dx);
    my $yoff = sprintf("%.0f",($maxy - $N)/$dy);

    my $output = [$minx, $maxx, $miny, $maxy, $dx, $dy, $width, $height, $xoff, $yoff];
    return $output;
}

sub within_bounds {
    my ($dn_dataset) = @_;
    my ($minx, $maxx, $miny, $maxy) = @{get_gridding_data($dn_dataset)};
    return ($miny < $N) && ($maxy > $S) && ($minx < $E) && ($maxx > $W);
}

sub update_regression { # In this case using psi - a power of cosine alpha. See notes 1 Dec 09.
    my ($sigma_alpha_dataset, $clipped_dn_dataset) = @_;
#   my $regression_dataset = get_regression_dataset();
    my ($N_band, $SumY_band, $SumX_band, $SumXY_band, $SumX2_band, $SumY2_band, $SumGamma_band) = @{get_regression_bands()};
    my ($minx, $maxx, $miny, $maxy, $dx, $dy, $width, $height, $xoff, $yoff) = @{get_gridding_data($sigma_alpha_dataset)};

    my $N_data = $N_band->ReadTile($xoff, $yoff, $width, $height);
    my $SumY_data = $SumY_band->ReadTile($xoff, $yoff, $width, $height);
    my $SumX_data = $SumX_band->ReadTile($xoff, $yoff, $width, $height);
    my $SumXY_data = $SumXY_band->ReadTile($xoff, $yoff, $width, $height);
    my $SumX2_data = $SumX2_band->ReadTile($xoff, $yoff, $width, $height);
    my $SumY2_data = $SumY2_band->ReadTile($xoff, $yoff, $width, $height);
    my $SumGamma_data = $SumGamma_band->ReadTile($xoff, $yoff, $width, $height);

    my $Sigma_alpha_band = $sigma_alpha_dataset->GetRasterBand(1);
    my $Sigma_alpha_nodata = $Sigma_alpha_band->GetNoDataValue;
    my $Sigma_alpha_data = $Sigma_alpha_band->ReadTile;

    my $alpha_band = $clipped_dn_dataset->GetRasterBand(2);
    my $alpha_nodata = $alpha_band->GetNoDataValue;
    my $alpha_data = $alpha_band->ReadTile;

    print "Updating regression...\n";

    for (my $Row=0; $Row<$height; $Row++) {
        for (my $Col=0; $Col<$width; $Col++) {
            if ($Sigma_alpha_data->[$Row][$Col] && ($Sigma_alpha_data->[$Row][$Col] != 65535)
            && $alpha_data->[$Row][$Col] && ($alpha_data->[$Row][$Col] != 65535)) {
                my $Y = $Sigma_alpha_data->[$Row][$Col];
                my $alpha = $alpha_data->[$Row][$Col] / 100;
                $alpha += 360 if $alpha < 0;
```

```
                    my $X = -100 * log10(cos(3.1415927 * $alpha / 180));
                    my $gamma = $Y - $X;
                    $N_data->[$Row][$Col] += 1;
                    $SumY_data->[$Row][$Col] += $Y;
                    $SumX_data->[$Row][$Col] += $X;
                    $SumXY_data->[$Row][$Col] += ($X * $Y);
                    $SumX2_data->[$Row][$Col] += ($X ** 2);
                    $SumY2_data->[$Row][$Col] += ($Y ** 2);
                    $SumGamma_data->[$Row][$Col] += $gamma;
                }
            }
        }

        $N_band->WriteTile($N_data, $xoff, $yoff);
        $SumY_band->WriteTile($SumY_data, $xoff, $yoff);
        $SumX_band->WriteTile($SumX_data, $xoff, $yoff);
        $SumXY_band->WriteTile($SumXY_data, $xoff, $yoff);
        $SumX2_band->WriteTile($SumX2_data, $xoff, $yoff);
        $SumY2_band->WriteTile($SumY2_data, $xoff, $yoff);
        $SumGamma_band->WriteTile($SumGamma_data, $xoff, $yoff);

}
# $N_band, $SumY_band, $SumX_band, $SumXY_band, $SumX2_band, $psi_band

# Byte/Int16/UInt16/UInt32/Int32/Float32/Float64/
#                   CInt16/CInt32/CFloat32/CFloat64}
sub get_regression_bands {
    my $bands = [
        ['N','UInt16'],
        ['SumY','UInt16'],
        ['SumX','Float32'],
        ['SumXY','Float32'],
        ['SumX2','Float32'],
        ['SumY2','Float32'],
        ['SumGamma','UInt16']
        ];
    my @output;

    foreach (@$bands) {
        my ($name, $datatype) = @$_;
        my $path = "$TARGET_DIRECTORY/$SPECIFIC_DIRECTORY";
        if (-e "$path/$name.tif") {
            my $dataset = Geo::GDAL::Open("$path/$name.tif",'Update');
            my $band = $dataset->GetRasterBand(1);
            push (@output, $band);
        } else {
            my $width = sprintf("%.0f",($E - $W) / $RESOLUTION);
            my $height = sprintf("%.0f",($N - $S) / $RESOLUTION);
            print "Creating $path/$name.tif...\n";
#           my $dataset;
#           eval{
            mkdir $path unless -d $path;
            my $dataset = Geo::GDAL::Driver('GTiff')->Create("$path/$name.tif",
                $width, $height, 1, $datatype);
#           };
#           print STDERR "Error: $@";
            $dataset->GeoTransform($W, $RESOLUTION, 0, $N, 0, -$RESOLUTION);
            $dataset->SetProjection($WKT);
            my $band = $dataset->Band(1);
            $band->Fill(0);
            $band->NoDataValue(0);
            push (@output, $band);
```

```perl
        }
    }
    return \@output;
}

sub create_sigmaalpha {
    my ($root, $clipped_dn_dataset) = @_;
    my ($width, $height) = $clipped_dn_dataset->Size;
    my ($minx, $dx, undef, $maxy, undef, $dy) = $clipped_dn_dataset->GeoTransform();
    my $alpha_band = $clipped_dn_dataset->GetRasterBand(2);
    my $alphas = $alpha_band->ReadTile;
    my $dn_band = $clipped_dn_dataset->GetRasterBand(1);
    my $dn_nodata = $dn_band->GetNoDataValue;
    my $dns = $dn_band->ReadTile;
    my $mask_data = get_mask_data($clipped_dn_dataset);

    my $name = "SIGMAALPHA$root.tif";      # name (without extension) for the new raster
    my $datatype = 'UInt16';# datatype for the values in pixels
    my $nodata = 0;           # nodata value
    my @data = ();             # pixel values, stored in this example in a hash

    my $dataset = Geo::GDAL::Driver('GTiff')->Create($name, $width, $height, 1, $datatype);
    $dataset->GeoTransform($minx, $dx, 0, $maxy, 0, $dy);
    $dataset->SetProjection($WKT);
    my $band = $dataset->Band(1);
    $band->NoDataValue($nodata);

    print "Creating SigmaAlpha for $root...\n";

#   die "DN and ALPHA maps are different sizes\n" unless ($alpha_dataset->Size == ($width, $height));
    for (my $row=0; $row<$height; $row++) {
        my @rowvalue;
        for (my $col=0; $col<$width; $col++) {
            my $value = $nodata;
            if (($dns->[$row][$col] != 65535)
            && $dns->[$row][$col]
            && ($alphas->[$row][$col] != 65535)
            && $alphas->[$row][$col]
            && $mask_data->[$row][$col]) {
                my $alpha = $alphas->[$row][$col] / 100;
                $alpha += 360 if $alpha < 0;
                $value = sprintf("%.0f",(-100 * log10((($dns->[$row][$col] ** 2)/21900000) * sin((3.1415927/180) * $alpha))));
                if ($value < 0) {
                    $value = 0;
                } elsif ($value > 65534) {
                    $value = 65534;
                }
            }
            push (@rowvalue,$value);
        }
        push (@data,\@rowvalue);
    }

    $band->WriteTile(\@data);
    return $dataset;
}
```

```perl
sub log10 {
    my $n = shift;
    return log($n)/log(10) unless $n < 0;
    0;
}

sub get_arguments {
    die "You must argue a directory and some raw data filename(s)\n" if (@ARGV) == 0;
    $SPECIFIC_DIRECTORY = shift @ARGV;
    my @output;
    foreach my $raw (@ARGV) {
        die "Sorry, but the argument(s) must contain the FULL, not RELATIVE, path\n" unless $raw =~ /^\//;
        push(@output, $raw);
    }
    return \@output;
}
```

Appendix B - Data

All GM data was acquired systematically via download from ESA's Kiruna and ESRIN ground stations, made available in a two-week moving window through the Category 1 Fast Track Registration agreement, under the project number C1P.5908 (ESA, 2007a).

All MODIS data was obtained from http://lpdaac.usgs.gov , maintained by the NASA Land Processes Distributed Active Archive Center (LP DAAC) at the USGS/Earth Resources Observation and Science (EROS) Center, Sioux Falls, South Dakota. 2003. Data for the images were provided by NASA.

Chapter 3

Radar data

All GM data for the year 2009 between latitudes 10° S and 29° S in the following orbit tracks: 9, 16, 23, 30, 38, 44, 52, 59, 66, 73, 87, 95, 102, 109, 116, 130, 138, 145, 152, 159, 173, 181, 188, 195, 202, 206, 209, 216, 224, 231, 238, 245, 252, 259, 267, 281, 288, 295, 302, 316, 324, 331, 338, 345, 359, 367, 374, 381, 388, 402, 410, 417, 424, 431, 445, 453, 460, 467, 474, 481, 488, 496.

Dominant vegetation species, vegetation growth form

Title: Vegetation - Post-European Settlement (1988)
Custodian: Geoscience Australia

Metadata: http://www.ga.gov.au/meta/ANZCW0703005426.html

Geology

Title: Surface geology of Australia 1:1,000,000 scale, Queensland - 2nd edition

Authors: Whitaker, A.J., Champion, D.C., Sweet, I.P., Kilgour, P. and Connolly, D.P.

Custodian: Geoscience Australia

Further information: http:/www.ga.gov.au

Soil type

Title: Digital Atlas of Australian Soils - Soil Landscapes Map

Custodian: Department of Agriculture Fisheries and Forestry: Australian Bureau of Agricultural and Resource Economics and Sciences

Metadata: http://adl.brs.gov.au/anrdl/metadata_files/pa_daaslr9abd_00111a01.xml

Regolith

Title: Regolith landforms polygon dataset AGSOCAT (AGSO catalogue) Number : 21805

Custodian: Geoscience Australia

Metadata: http://www.agso.gov.au/databases/catalog/agsocat.html

MODIS

Satellite	Year	Day	H	V
Aqua	2011	130	30	12
Aqua	2011	130	31	10
Aqua	2011	130	31	11

Chapter 5

Radar data

The following lists, each entry comprises 5 numbers representing the following:

1. Date of acquisition (yyyymmdd)
2. Time of acquisition (hhmmss)
3. Orbit cycle
4. Orbit track
5. Absolute orbit

GM Data used in Chapter 5

20050125 001330 034 00102 15186	20060403 000450 046 00288 21384	20060406 001031 046 00331 21427
20070208 125110 055 00238 25843	20070212 000458 055 00288 25893	20070215 001038 055 00331 25936
20090131 000734 076 00059 36185	20090203 123426 076 00109 36235	20090206 124102 076 00152 36278
20090209 124523 076 00195 36321	20090213 140138 076 00253 36379	20090214 132804 076 00267 36393
20090215 125745 076 00281 36407	20090217 133457 076 00310 36436	20090218 004227 076 00317 36443
20090219 001026 076 00331 36457	20090219 123234 076 00338 36464	20090220 134155 076 00353 36479
20090221 004813 076 00360 36486	20090221 130757 076 00367 36493	20090222 001753 076 00374 36500
20090222 123813 076 00381 36507	20090222 141833 076 00382 36508	20090222 234610 076 00388 36514
20090223 012659 076 00389 36515	20090224 131443 076 00410 36536	20090225 002325 076 00417 36543
20090225 124234 076 00424 36550	20090227 131927 076 00453 36579	20090228 002814 076 00460 36586
20090228 124932 076 00467 36593	20090228 142952 076 00468 36594	20090228 235646 076 00474 36600
20090301 013916 076 00475 36601	20090301 135910 076 00482 36608	20090302 010606 076 00489 36615
20090302 132510 076 00496 36622	20090303 003354 077 00002 36629	20090303 125349 077 00009 36636
20090304 000157 077 00016 36643	20090305 133059 077 00038 36665	20090306 003934 077 00045 36672
20090307 122910 077 00066 36693	20090307 233835 077 00073 36700	20090308 133759 077 00081 36708
20090309 004520 077 00088 36715	20090309 130507 077 00095 36722	20090310 001316 077 00102 36729
20090310 123428 077 00109 36736	20090310 234342 077 00116 36743	20090311 134339 077 00124 36751
20090312 005106 077 00131 36758	20090312 131047 077 00138 36765	20090313 002039 077 00145 36772
20090313 124103 077 00152 36779	20090313 234849 077 00159 36786	20090314 134933 077 00167 36794
20090315 005744 077 00174 36801	20090315 131637 077 00181 36808	20090316 002611 077 00188 36815
20090316 124532 077 00195 36822	20090316 235430 077 00202 36829	20090317 013619 077 00203 36830
20090317 135550 077 00210 36837	20090318 010335 077 00217 36844	20090318 132216 077 00224 36851
20090319 003152 077 00231 36858	20090319 125058 077 00238 36865	20090320 000015 077 00245 36872
20090320 140137 077 00253 36880	20090322 003642 077 00274 36901	20090322 125637 077 00281 36908
20090323 000446 077 00288 36915	20090323 122630 077 00295 36922	20090324 011441 077 00303 36930
20090324 133455 077 00310 36937	20090325 004321 077 00317 36944	20090325 130759 077 00324 36951
20090326 001144 077 00331 36958	20090326 123232 077 00338 36965	20090326 141306 077 00339 36966
20090326 234112 077 00345 36972	20090327 012122 077 00346 36973	20090327 134048 077 00353 36980
20090329 001751 077 00374 37001	20090329 123812 077 00381 37008	20090330 012657 077 00389 37016
20090330 134627 077 00396 37023	20090331 005451 077 00403 37030	20090331 131343 077 00410 37037
20090401 002323 077 00417 37044	20090401 124232 077 00424 37051	20090401 142410 077 00425 37052
20090401 235133 077 00431 37058	20090402 013313 077 00432 37059	20090402 135254 077 00439 37066
20090403 005943 077 00446 37073	20090403 131925 077 00453 37080	20090404 142949 077 00468 37095
20090404 235643 077 00474 37101	20090405 013913 077 00475 37102	20090405 135841 077 00482 37109
20090406 010603 077 00489 37116	20090406 132506 077 00496 37123	20090407 125407 078 00009 37137
20090408 000154 078 00016 37144	20090408 140428 078 00024 37152	20090408 233257 078 00030 37158
20090409 011142 078 00031 37159	20090409 133056 078 00038 37166	20090410 003931 078 00045 37173
20090410 125925 078 00052 37180	20090411 141014 078 00067 37195	20090411 233832 078 00073 37201
20090412 133757 078 00081 37209	20090413 004517 078 00088 37216	20090413 130505 078 00095 37223
20090414 001313 078 00102 37230	20090414 123425 078 00109 37237	20090414 141546 078 00110 37238
20090414 234339 078 00116 37244	20090415 134336 078 00124 37252	20090416 005103 078 00131 37259
20090416 131044 078 00138 37266	20090417 002037 078 00145 37273	20090417 142120 078 00153 37281
20090417 234846 078 00159 37287	20090418 134932 078 00167 37295	20090420 002609 078 00188 37316
20090420 124522 078 00195 37323	20090420 142701 078 00196 37324	20090420 235409 078 00202 37330
20090421 013618 078 00203 37331	20090421 135549 078 00210 37338	20090422 010334 078 00217 37345
20090422 132216 078 00224 37352	20090423 003102 078 00231 37359	20090423 125132 078 00238 37366
20090423 235919 078 00245 37373	20090424 140137 078 00253 37381	20090425 010942 078 00260 37388
20090425 132803 078 00267 37395	20090426 125637 078 00281 37409	20090427 000446 078 00288 37416

Continued on next page

GM Data used in Chapter 5

20090427 122630 078 00295 37423	20090427 140723 078 00296 37424	20090427 233547 078 00302 37430
20090428 011434 078 00303 37431	20090429 130217 078 00324 37452	20090430 001026 078 00331 37459
20090430 123233 078 00338 37466	20090501 012035 078 00346 37474	20090502 004813 078 00360 37488
20090502 130757 078 00367 37495	20090503 001753 078 00374 37502	20090503 123813 078 00381 37509
20090503 141833 078 00382 37510	20090504 012659 078 00389 37517	20090504 134628 078 00396 37524
20090505 005359 078 00403 37531	20090505 131345 078 00410 37538	20090506 002325 078 00417 37545
20090506 124234 078 00424 37552	20090506 142412 078 00425 37553	20090506 235136 078 00431 37559
20090507 013315 078 00432 37560	20090508 005945 078 00446 37574	20090509 002814 078 00460 37588
20090509 124932 078 00467 37595	20090509 142952 078 00468 37596	20090510 013916 078 00475 37603
20090510 135845 078 00482 37610	20090511 010606 078 00489 37617	20090511 132510 078 00496 37624
20090512 003354 079 00002 37631	20090512 125410 079 00009 37638	20090513 140432 079 00024 37653
20090513 233301 079 00030 37659	20090514 011146 079 00031 37660	20090515 003934 079 00045 37674
20090515 125928 079 00052 37681	20090516 000737 079 00059 37688	20090516 141017 079 00067 37696
20090517 011728 079 00074 37703	20090517 133800 079 00081 37710	20090518 004520 079 00088 37717
20090518 130507 079 00095 37724	20090519 001316 079 00102 37731	20090519 123428 079 00109 37738
20090519 141549 079 00110 37739	20090519 234342 079 00116 37745	20090520 012347 079 00117 37746
20090520 134339 079 00124 37753	20090521 005106 079 00131 37760	20090521 131047 079 00138 37767
20090522 002040 079 00145 37774	20090522 142123 079 00153 37782	20090523 013009 079 00160 37789
20090523 134934 079 00167 37796	20090524 005653 079 00174 37803	20090524 131638 079 00181 37810
20090525 002612 079 00188 37817	20090525 124524 079 00195 37824	20090525 142703 079 00196 37825
20090525 235412 079 00202 37831	20090526 013620 079 00203 37832	20090526 135552 079 00210 37839
20090527 010317 079 00217 37846	20090527 132218 079 00224 37853	20090528 003105 079 00231 37860
20090530 010857 079 00260 37889	20090530 132805 079 00267 37896	20090531 003644 079 00274 37903
20090531 125639 079 00281 37910	20090601 000448 079 00288 37917	20090601 122917 079 00295 37924
20090601 140726 079 00296 37925	20090601 233549 079 00302 37931	20090602 011437 079 00303 37932
20090602 133458 079 00310 37939	20090603 004228 079 00317 37946	20090603 130219 079 00324 37953
20090604 001028 079 00331 37960	20090604 123235 079 00338 37967	20090605 012037 079 00346 37975
20090605 134051 079 00353 37982	20090606 004815 079 00360 37989	20090606 130759 079 00367 37996
20090607 001755 079 00374 38003	20090607 123815 079 00381 38010	20090607 141835 079 00382 38011
20090607 234612 079 00388 38017	20090608 012701 079 00389 38018	20090612 005947 079 00446 38075
20090618 133100 080 00038 38168	20090619 003936 080 00045 38175	20090619 125930 080 00052 38182
20090620 141019 080 00067 38197	20090620 233837 080 00073 38203	20090621 011729 080 00074 38204
20090622 004522 080 00088 38218	20090622 130509 080 00095 38225	20090623 001318 080 00102 38232
20090623 123430 080 00109 38239	20090623 141551 080 00110 38240	20090623 234344 080 00116 38246
20090624 012349 080 00117 38247	20090624 134341 080 00124 38254	20090625 005108 080 00131 38261
20090625 131048 080 00138 38268	20090703 140140 080 00253 38383	20090704 010857 080 00260 38390
20090704 132805 080 00267 38397	20090705 003644 080 00274 38404	20090706 000448 080 00288 38418
20090706 122633 080 00295 38425	20090706 140725 080 00296 38426	20090706 233549 080 00302 38432
20090707 011436 080 00303 38433	20090707 133458 080 00310 38440	20090708 004228 080 00317 38447
20090708 130219 080 00324 38454	20090709 001027 080 00331 38461	20090710 134050 080 00353 38483
20090711 004814 080 00360 38490	20090711 130758 080 00367 38497	20090712 001754 080 00374 38504
20090712 123814 080 00381 38511	20090712 234611 080 00388 38518	20090713 012700 080 00389 38519
20090713 134630 080 00396 38526	20090714 005400 080 00403 38533	20090714 131346 080 00410 38540
20090715 002326 080 00417 38547	20090715 124235 080 00424 38554	20090715 142413 080 00425 38555
20090715 235137 080 00431 38561	20090716 135258 080 00439 38569	20090717 005947 080 00446 38576
20090717 131928 080 00453 38583	20090718 002815 080 00460 38590	20090718 124932 080 00467 38597
20090718 235646 080 00474 38604	20090719 013917 080 00475 38605	20090719 135845 080 00482 38612
20090720 010607 080 00489 38619	20090720 132511 080 00496 38626	20090721 125349 081 00009 38640

Continued on next page

GM Data used in Chapter 5

20090722 000158 081 00016 38647	20090722 140433 081 00024 38655	20090723 011146 081 00031 38662
20090723 133059 081 00038 38669	20090724 125929 081 00052 38683	20090725 000737 081 00059 38690
20090725 122911 081 00066 38697	20090725 233835 081 00073 38704	20090726 011728 081 00074 38705
20090726 133800 081 00081 38712	20090727 004521 081 00088 38719	20090727 130508 081 00095 38726
20090728 001317 081 00102 38733	20090728 123428 081 00109 38740	20090728 141550 081 00110 38741
20090728 234343 081 00116 38747	20090729 012348 081 00117 38748	20090729 134340 081 00124 38755
20090730 131048 081 00138 38769	20090731 002040 081 00145 38776	20090731 124104 081 00152 38783
20090731 234850 081 00159 38790	20090801 013010 081 00160 38791	20090801 134934 081 00167 38798
20090802 005653 081 00174 38805	20090802 131638 081 00181 38812	20090803 002612 081 00188 38819
20090803 124524 081 00195 38826	20090803 142703 081 00196 38827	20090803 235412 081 00202 38833
20090804 013620 081 00203 38834	20090807 140139 081 00253 38884	20090808 010857 081 00260 38891
20090808 132805 081 00267 38898	20090809 003644 081 00274 38905	20090809 125639 081 00281 38912
20090810 000448 081 00288 38919	20090810 140725 081 00296 38927	20090810 233549 081 00302 38933
20090811 011436 081 00303 38934	20090811 133457 081 00310 38941	20090812 004227 081 00317 38948
20090812 130218 081 00324 38955	20090813 001027 081 00331 38962	20090813 123234 081 00338 38969
20090814 134050 081 00353 38984	20090815 004814 081 00360 38991	20090815 130758 081 00367 38998
20090816 001754 081 00374 39005	20090816 001754 081 00374 39005	20090816 123814 081 00381 39012
20090816 234611 081 00388 39019	20090817 012659 081 00389 39020	20090817 134629 081 00396 39027
20090818 005400 081 00403 39034	20090818 131345 081 00410 39041	20090819 002326 081 00417 39048
20090819 124234 081 00424 39055	20090819 142413 081 00425 39056	20090821 131928 081 00453 39084
20090822 002814 081 00460 39091	20090822 124931 081 00467 39098	20090822 142952 081 00468 39099
20090822 235645 081 00474 39105	20090823 013916 081 00475 39106	20090824 010606 081 00489 39120
20090824 010606 081 00489 39120	20090824 132510 081 00496 39127	20090825 003353 082 00002 39134
20090825 125410 082 00009 39141	20090826 000157 082 00016 39148	20090826 140432 082 00024 39156
20090827 011145 082 00031 39163	20090827 133058 082 00038 39170	20090828 003933 082 00045 39177
20090828 125928 082 00052 39184	20090829 000736 082 00059 39191	20090829 122910 082 00066 39198
20090829 141016 082 00067 39199	20090829 233834 082 00073 39205	20090830 011727 082 00074 39206
20090831 004519 082 00088 39220	20090831 130507 082 00095 39227	20090901 001315 082 00102 39234
20090901 123427 082 00109 39241	20090901 141548 082 00110 39242	20090902 012346 082 00117 39249
20090902 134338 082 00124 39256	20090903 005105 082 00131 39263	20090903 131046 082 00138 39270
20090904 002038 082 00145 39277	20090904 124102 082 00152 39284	20090904 142122 082 00153 39285
20090904 234848 082 00159 39291	20090905 013008 082 00160 39292	20090906 005651 082 00174 39306
20090906 131636 082 00181 39313	20090907 002610 082 00188 39320	20090907 124522 082 00195 39327
20090907 142701 082 00196 39328	20090908 013618 082 00203 39335	20090908 135549 082 00210 39342
20090909 010315 082 00217 39349	20090909 132215 082 00224 39356	20090910 003102 082 00231 39363
20090910 125131 082 00238 39370	20090910 143240 082 00239 39371	20090910 235918 082 00245 39377
20090912 010854 082 00260 39392	20090912 132802 082 00267 39399	20090913 003641 082 00274 39406
20090913 125636 082 00281 39413	20090914 000444 082 00288 39420	20090914 140722 082 00296 39428
20090915 011433 082 00303 39435	20090915 133454 082 00310 39442	20090916 004224 082 00317 39449
20090916 130215 082 00324 39456	20090917 001023 082 00331 39463	20090917 123230 082 00338 39470
20090917 141304 082 00339 39471	20090917 234110 082 00345 39477	20090918 012032 082 00346 39478
20090919 004810 082 00360 39492	20090919 130754 082 00367 39499	20090920 001750 082 00374 39506
20090920 123810 082 00381 39513	20090920 141830 082 00382 39514	20090921 012655 082 00389 39521
20090921 134625 082 00396 39528	20090922 005355 082 00403 39535	20090922 131341 082 00410 39542
20090923 002321 082 00417 39549	20090923 124230 082 00424 39556	20090923 142408 082 00425 39557
20090923 235132 082 00431 39563	20090924 013311 082 00432 39564	20090925 005941 082 00446 39578
20090925 131923 082 00453 39585	20090926 002809 082 00460 39592	20090926 124927 082 00467 39599
20090926 142947 082 00468 39600	20090927 013911 082 00475 39607	20090927 135839 082 00482 39614

Continued on next page

GM Data used in Chapter 5

20090928 010601 082 00489 39621	20090928 132632 082 00496 39628	20090929 125405 083 00009 39642
20090930 000152 083 00016 39649	20090930 140426 083 00024 39657	20090930 233255 083 00030 39663
20091001 011140 083 00031 39664	20091002 003928 083 00045 39678	20091002 125923 083 00052 39685
20091003 000732 083 00059 39692	20091003 122905 083 00066 39699	20091003 141011 083 00067 39700
20091004 011722 083 00074 39707	20091004 133754 083 00081 39714	20091005 004515 083 00088 39721
20091005 130502 083 00095 39728	20091006 001311 083 00102 39735	20091006 123423 083 00109 39742
20091006 141544 083 00110 39743	20091006 234337 083 00116 39749	20091007 012342 083 00117 39750
20091008 005101 083 00131 39764	20091008 131042 083 00138 39771	20091009 002034 083 00145 39778
20091009 124058 083 00152 39785	20091009 142118 083 00153 39786	20091010 013004 083 00160 39793
20091012 142657 083 00196 39829	20091012 235406 083 00202 39835	20091013 013615 083 00203 39836
20091013 135546 083 00210 39843	20091014 010311 083 00217 39850	20091014 132212 083 00224 39857
20091015 003059 083 00231 39864	20091015 125128 083 00238 39871	20091015 235915 083 00245 39878
20091016 140133 083 00253 39886	20091017 010851 083 00260 39893	20091017 132759 083 00267 39900
20091018 125633 083 00281 39914	20091019 000442 083 00288 39921	20091019 122627 083 00295 39928
20091019 140719 083 00296 39929	20091019 233543 083 00302 39935	20091020 011431 083 00303 39936
20091020 133452 083 00310 39943	20091021 004222 083 00317 39950	20091021 130213 083 00324 39957
20091022 001022 083 00331 39964	20091022 141303 083 00339 39972	20091022 234108 083 00345 39978
20091023 012031 083 00346 39979	20091023 134045 083 00353 39986	20091024 130752 083 00367 40000
20091025 001749 083 00374 40007	20091025 123809 083 00381 40014	20091025 141829 083 00382 40015
20091025 234606 083 00388 40021	20091026 012654 083 00389 40022	20091026 134624 083 00396 40029
20091027 005355 083 00403 40036	20091027 131340 083 00410 40043	20091028 142408 083 00425 40058
20091028 235131 083 00431 40064	20091029 013311 083 00432 40065	20091031 124927 083 00467 40100
20091031 142947 083 00468 40101	20091031 235641 083 00474 40107	20091101 135840 083 00482 40115
20091102 010602 083 00489 40122	20091102 132505 083 00496 40129	20091103 003349 084 00002 40136
20091103 125344 084 00009 40143	20091104 000152 084 00016 40150	20091104 140427 084 00024 40158
20091104 233256 084 00030 40164	20091105 011141 084 00031 40165	20091106 003929 084 00045 40179
20091106 125923 084 00052 40186	20091107 000732 084 00059 40193	20091107 141012 084 00067 40201
20091108 011747 084 00074 40208	20091108 133755 084 00081 40215	20091109 004515 084 00088 40222
20091109 130502 084 00095 40229	20091110 001339 084 00102 40236	20091110 141544 084 00110 40244
20091110 234337 084 00116 40250	20091111 012342 084 00117 40251	20091111 134334 084 00124 40258
20091112 005101 084 00131 40265	20091112 131042 084 00138 40272	20091113 002034 084 00145 40279
20091113 142118 084 00153 40287	20091114 013004 084 00160 40294	20091114 134929 084 00167 40301
20091115 005647 084 00174 40308	20091115 131632 084 00181 40315	20091116 002606 084 00188 40322
20091116 124518 084 00195 40329	20091116 142657 084 00196 40330	20091116 235406 084 00202 40336
20091117 013614 084 00203 40337	20091117 055648 084 00206 40340	20091117 135545 084 00210 40344
20091118 010311 084 00217 40351	20091118 132212 084 00224 40358	20091119 143236 084 00239 40373
20091119 235914 084 00245 40379	20091120 140133 084 00253 40387	20091121 010850 084 00260 40394
20091121 132758 084 00267 40401	20091122 003637 084 00274 40408	20091122 125632 084 00281 40415
20091123 000441 084 00288 40422	20091123 122625 084 00295 40429	20091123 140718 084 00296 40430
20091123 233542 084 00302 40436	20091124 011429 084 00303 40437	20091124 133451 084 00310 40444
20091125 004221 084 00317 40451	20091125 004223 084 00317 40451	20091126 123227 084 00338 40472
20091126 141259 084 00339 40473	20091126 234109 084 00345 40479	20091126 234109 084 00345 40479
20091127 012031 084 00346 40480	20091127 012031 084 00346 40480	20091127 134040 084 00353 40487
20091128 004804 084 00360 40494	20091128 130752 084 00367 40501	20091129 001746 084 00374 40508
20091129 123804 084 00381 40515	20091129 141824 084 00382 40516	20091130 012652 084 00389 40523
20091130 134624 084 00396 40530	20091201 005350 084 00403 40537	20091202 002317 084 00417 40551
20091202 124228 084 00424 40558	20091202 142408 084 00425 40559	20091202 235128 084 00431 40565
20091203 013306 084 00432 40566	20091203 135250 084 00439 40573	20091204 005936 084 00446 40580

Continued on next page

GM Data used in Chapter 5

20091204 131921 084 00453 40587	20091205 002808 084 00460 40594	20091205 124806 084 00467 40601
20091205 142947 084 00468 40602	20091206 135837 084 00482 40616	20091207 010600 084 00489 40623
20091208 125342 085 00009 40644	20091209 000148 085 00016 40651	20091209 140423 085 00024 40659
20091209 233254 085 00030 40665	20091210 011140 085 00031 40666	20091210 133052 085 00038 40673
20091211 003928 085 00045 40680	20091211 003928 085 00045 40680	20091211 125919 085 00052 40687
20091212 000728 085 00059 40694	20091212 123110 085 00066 40701	20091212 141007 085 00067 40702
20091213 011723 085 00074 40709	20091213 133749 085 00081 40716	20091214 004515 085 00088 40723
20091215 001308 085 00102 40737	20091215 123418 085 00109 40744	20091215 141539 085 00110 40745
20091215 234332 085 00116 40751	20091216 012341 085 00117 40752	20091216 134335 085 00124 40759
20091217 005057 085 00131 40766	20091217 131042 085 00138 40773	20091218 002032 085 00145 40780
20091218 124054 085 00152 40787	20091218 142113 085 00153 40788	20091219 013001 085 00160 40795
20091219 134929 085 00167 40802	20091220 005644 085 00174 40809	20091221 002604 085 00188 40823
20091221 124519 085 00195 40830	20091221 142659 085 00196 40831	20091221 235403 085 00202 40837
20091222 013611 085 00203 40838	20091222 135545 085 00210 40845	20091223 010312 085 00217 40852
20091223 132213 085 00224 40859	20091224 003100 085 00231 40866	20091224 125055 085 00238 40873
20091224 143238 085 00239 40874	20091225 140132 085 00253 40888	20091226 010853 085 00260 40895
20091227 003640 085 00274 40909	20091227 125633 085 00281 40916	20091228 000440 085 00288 40923
20091228 122628 085 00295 40930	20091228 140717 085 00296 40931	20091228 233544 085 00302 40937
20091229 011427 085 00303 40938	20091229 133449 085 00310 40945	20091230 004224 085 00317 40952
20091230 130214 085 00324 40959	20091231 001020 085 00331 40966	20091231 123228 085 00338 40973
20091231 141300 085 00339 40974	20100101 012032 085 00346 40981	20100102 004805 085 00360 40995
20100102 130754 085 00367 41002	20100103 001748 085 00374 41009	20100103 123806 085 00381 41016
20100103 141825 085 00382 41017	20100103 234604 085 00388 41023	20100104 012654 085 00389 41024
20100104 134626 085 00396 41031	20100105 005352 085 00403 41038	20100105 131341 085 00410 41045
20100106 002319 085 00417 41052	20100106 124230 085 00424 41059	20100106 142410 085 00425 41060
20100107 013308 085 00432 41067	20100108 005938 085 00446 41081	20100108 131924 085 00453 41088
20100109 002810 085 00460 41095	20100109 124809 085 00467 41102	20100109 142949 085 00468 41103
20100109 235639 085 00474 41109	20100110 135839 085 00482 41117	20100111 010603 085 00489 41124
20100111 132506 085 00496 41131	20100112 003350 086 00002 41138	20100112 125345 086 00009 41145
20100113 000151 086 00016 41152	20100113 140426 086 00024 41160	20100114 011144 086 00031 41167
20100115 003931 086 00045 41181	20100115 125921 086 00052 41188	20100116 000731 086 00059 41195
20100116 123113 086 00066 41202	20100116 141010 086 00067 41203	20100116 233831 086 00073 41209
20100117 011725 086 00074 41210	20100117 133751 086 00081 41217	20100118 004518 086 00088 41224
20100118 130504 086 00095 41231	20100119 001310 086 00102 41238	20100119 123419 086 00109 41245
20100119 141541 086 00110 41246	20100120 012343 086 00117 41253	20100121 005059 086 00131 41267
20100121 131043 086 00138 41274	20100122 002034 086 00145 41281	20100122 123942 086 00152 41288
20100122 142115 086 00153 41289	20100122 234843 086 00159 41295	20100123 013002 086 00160 41296
20100123 134930 086 00167 41303	20100124 005645 086 00174 41310	20100124 131634 086 00181 41317
20100125 002605 086 00188 41324	20100125 124801 086 00195 41331	20100125 142700 086 00196 41332
20100126 013612 086 00203 41339	20100127 010313 086 00217 41353	20100127 132213 086 00224 41360
20100128 003100 086 00231 41367	20100128 125056 086 00238 41374	20100128 143239 086 00239 41375
20100128 235913 086 00245 41381	20100129 140132 086 00253 41389	20100130 011024 086 00260 41396
20100130 132800 086 00267 41403	20100131 003640 086 00274 41410	20100131 125633 086 00281 41417
20100201 000440 086 00288 41424	20100201 122628 086 00295 41431	20100202 011427 086 00303 41439
20100202 133449 086 00310 41446	20100203 004224 086 00317 41453	20100203 130213 086 00324 41460
20100204 001020 086 00331 41467	20100204 123145 086 00338 41474	20100204 141259 086 00339 41475
20100204 234106 086 00345 41481	20100205 012031 086 00346 41482	20100205 134040 086 00353 41489
20100206 004805 086 00360 41496	20100206 130753 086 00367 41503	20100207 123804 086 00381 41517

Continued on next page

GM Data used in Chapter 5

20100207 234603 086 00388 41524	20100208 134625 086 00396 41532	20100209 005351 086 00403 41539
20100209 131340 086 00410 41546	20100210 002318 086 00417 41553	20100210 124229 086 00424 41560
20100210 142409 086 00425 41561	20100210 235129 086 00431 41567	20100211 013307 086 00432 41568
20100211 135250 086 00439 41575	20100212 005617 086 00446 41582	20100212 131922 086 00453 41589
20100213 002521 086 00460 41596	20100213 002808 086 00460 41596	20100213 124805 086 00467 41603
20100213 235637 086 00474 41610	20100214 013203 086 00475 41611	20100214 122359 086 00481 41617
20100214 135837 086 00482 41618	20100215 010152 086 00489 41625	20100215 010601 086 00489 41625
20100215 132504 086 00496 41632	20100216 125341 087 00009 41646	20100216 235939 087 00016 41653
20100217 013445 087 00017 41654	20100217 122953 087 00023 41660	20100217 140424 087 00024 41661
20100217 233254 087 00030 41667	20100218 133052 087 00038 41675	20100219 003637 087 00045 41682
20100219 003929 087 00045 41682	20100220 000534 087 00059 41696	20100220 123110 087 00066 41703
20100220 123554 087 00066 41703	20100220 141007 087 00067 41704	20100220 141618 087 00067 41704
20100220 233829 087 00073 41710	20100221 011209 087 00074 41711	20100221 133749 087 00081 41718
20100222 004215 087 00088 41725	20100222 004515 087 00088 41725	20100222 130500 087 00095 41732
20100223 123418 087 00109 41746	20100223 142207 087 00110 41747	20100223 233918 087 00116 41753
20100223 234332 087 00116 41753	20100224 011706 087 00117 41754	20100224 134334 087 00124 41761
20100225 004751 087 00131 41768	20100225 131040 087 00138 41775	20100226 001655 087 00145 41782
20100226 002032 087 00145 41782	20100226 123941 087 00152 41789	20100226 142113 087 00153 41790
20100226 234458 087 00159 41796	20100227 012153 087 00160 41797	20100227 013001 087 00160 41797
20100227 134929 087 00167 41804	20100227 135622 087 00167 41804	20100228 005329 087 00174 41811
20100301 002233 087 00188 41825	20100301 002604 087 00188 41825	20100301 124517 087 00195 41832
20100301 235403 087 00202 41839	20100302 012912 087 00203 41840	20100302 122110 087 00209 41846
20100302 135544 087 00210 41847	20100303 005904 087 00217 41854	20100303 010312 087 00217 41854
20100303 132212 087 00224 41861	20100304 002811 087 00231 41868	20100304 003059 087 00231 41868
20100304 125053 087 00238 41875	20100304 143238 087 00239 41876	20100304 235644 087 00245 41882
20100305 013457 087 00246 41883	20100305 140132 087 00253 41890	20100306 010440 087 00260 41897
20100307 003349 087 00274 41911	20100307 003639 087 00274 41911	20100307 125632 087 00281 41918
20100307 130442 087 00281 41918	20100308 000238 087 00288 41925	20100308 013724 087 00289 41926
20100308 122628 087 00295 41932	20100308 123255 087 00295 41932	20100308 140717 087 00296 41933
20100308 141320 087 00296 41933	20100308 233543 087 00302 41939	20100309 010941 087 00303 41940
20100309 133449 087 00310 41947	20100310 003927 087 00317 41954	20100311 000826 087 00331 41968
20100311 123227 087 00338 41975	20100311 141259 087 00339 41976	20100311 141910 087 00339 41976
20100311 233629 087 00345 41982	20100311 234110 087 00345 41982	20100312 011441 087 00346 41983
20100312 134040 087 00353 41990	20100313 004459 087 00360 41997	20100313 004805 087 00360 41997
20100313 130850 087 00367 42004	20100314 001404 087 00374 42011	20100314 123806 087 00381 42018
20100314 141825 087 00382 42019	20100314 234603 087 00388 42025	20100315 011930 087 00389 42026
20100315 012653 087 00389 42026	20100315 135334 087 00396 42033	20100316 005041 087 00403 42040
20100316 131427 087 00410 42047	20100317 001945 087 00417 42054	20100317 002319 087 00417 42054
20100317 124231 087 00424 42061	20100317 142410 087 00425 42062	20100317 234750 087 00431 42068
20100318 012420 087 00432 42069	20100318 013308 087 00432 42069	20100318 135252 087 00439 42076
20100318 135913 087 00439 42076	20100319 005619 087 00446 42083	20100319 131923 087 00453 42090
20100320 002523 087 00460 42097	20100320 002810 087 00460 42097	20100320 142949 087 00468 42105
20100320 235350 087 00474 42111	20100320 235638 087 00474 42111	20100321 122401 087 00481 42118
20100321 135839 087 00482 42119	20100322 010154 087 00489 42126	20100322 010603 087 00489 42126
20100322 132506 087 00496 42133	20100323 125343 088 00009 42147	20100324 233257 088 00030 42168
20100325 010710 088 00031 42169	20100325 011203 088 00031 42169	20100325 133054 088 00038 42176
20100326 003644 088 00045 42183	20100326 003931 088 00045 42183	20100326 125921 088 00052 42190
20100327 141009 088 00067 42205	20100327 141620 088 00067 42205	20100327 233831 088 00073 42211

Continued on next page

GM Data used in Chapter 5

20100328 011211 088 00074 42212	20100328 133751 088 00081 42219	20100329 004216 088 00088 42226
20100329 004609 088 00088 42226	20100329 130501 088 00095 42233	20100330 001115 088 00102 42240
20100330 123726 088 00109 42247	20100330 141541 088 00110 42248	20100330 142209 088 00110 42248
20100330 234333 088 00116 42254	20100331 011707 088 00117 42255	20100401 131041 088 00138 42276
20100402 001656 088 00145 42283	20100402 002033 088 00145 42283	20100402 124056 088 00152 42290
20100402 142114 088 00153 42291	20100402 234458 088 00159 42297	20100402 234842 088 00159 42297
20100403 012153 088 00160 42298	20100403 013005 088 00160 42298	20100403 134930 088 00167 42305
20100403 134930 088 00167 42305	20100403 135623 088 00167 42305	20100403 135623 088 00167 42305
20100404 005329 088 00174 42312	20100405 002604 088 00188 42326	20100405 124517 088 00195 42333
20100405 142659 088 00196 42334	20100405 235403 088 00202 42340	20100406 012656 088 00203 42341
20100406 013611 088 00203 42341	20100406 122110 088 00209 42347	20100406 135544 088 00210 42348
20100407 005904 088 00217 42355	20100407 010312 088 00217 42355	20100407 132212 088 00224 42362
20100408 002811 088 00231 42369	20100408 125052 088 00238 42376	20100408 143237 088 00239 42377
20100408 235644 088 00245 42383	20100409 013209 088 00246 42384	20100409 140131 088 00253 42391
20100410 010439 088 00260 42398	20100410 010852 088 00260 42398	20100410 132759 088 00267 42405
20100411 003348 088 00274 42412	20100411 003638 088 00274 42412	20100411 125631 088 00281 42419
20100411 130441 088 00281 42419	20100412 000237 088 00288 42426	20100412 123254 088 00295 42433
20100412 140716 088 00296 42434	20100412 141319 088 00296 42434	20100412 233542 088 00302 42440
20100413 010939 088 00303 42441	20100414 003926 088 00317 42455	20100414 004222 088 00317 42455
20100414 130210 088 00324 42462	20100415 000824 088 00331 42469	20100415 123226 088 00338 42476
20100415 141257 088 00339 42477	20100415 141908 088 00339 42477	20100415 233627 088 00345 42483
20100415 234108 088 00345 42483	20100416 134038 088 00353 42491	20100417 004457 088 00360 42498
20100417 004803 088 00360 42498	20100417 130749 088 00367 42505	20100418 001401 088 00374 42512
20100418 123803 088 00381 42519	20100418 234601 088 00388 42526	20100419 011928 088 00389 42527
20100419 012651 088 00389 42527	20100419 134623 088 00396 42534	20100419 135332 088 00396 42534
20100420 005038 088 00403 42541	20100420 131338 088 00410 42548	20100421 002316 088 00417 42555
20100421 124228 088 00424 42562	20100421 142407 088 00425 42563	20100421 234747 088 00431 42569
20100421 235127 088 00431 42569	20100422 012652 088 00432 42570	20100422 013309 088 00432 42570
20100422 135249 088 00439 42577	20100422 135249 088 00439 42577	20100422 135914 088 00439 42577
20100423 005616 088 00446 42584	20100423 131921 088 00453 42591	20100424 002520 088 00460 42598
20100424 124803 088 00467 42605	20100424 142946 088 00468 42606	20100424 235718 088 00474 42612
20100425 012931 088 00475 42613	20100425 122358 088 00481 42619	20100425 135836 088 00482 42620
20100426 010150 088 00489 42627	20100426 010600 088 00489 42627	20100426 132503 088 00496 42634
20100427 235938 089 00016 42655	20100428 013746 089 00017 42656	20100428 122952 089 00023 42662
20100428 140423 089 00024 42663	20100428 233253 089 00030 42669	20100429 133051 089 00038 42677
20100430 003636 089 00045 42684	20100430 003928 089 00045 42684	20100430 125918 089 00052 42691
20100501 000533 089 00059 42698	20100501 122859 089 00066 42705	20100501 123553 089 00066 42705
20100501 141006 089 00067 42706	20100501 233828 089 00073 42712	20100502 011208 089 00074 42713
20100502 133748 089 00081 42720	20100503 004214 089 00088 42727	20100503 004515 089 00088 42727
20100503 130459 089 00095 42734	20100504 001112 089 00102 42741	20100504 123417 089 00109 42748
20100504 141538 089 00110 42749	20100504 142207 089 00110 42749	20100504 233917 089 00116 42755
20100504 234331 089 00116 42755	20100505 011705 089 00117 42756	20100505 134334 089 00124 42763
20100506 004750 089 00131 42770	20100506 131039 089 00138 42777	20100507 001654 089 00145 42784
20100507 002031 089 00145 42784	20100507 142112 089 00153 42792	20100507 234840 089 00159 42798
20100508 012151 089 00160 42799	20100508 013004 089 00160 42799	20100508 134928 089 00167 42806
20100508 135622 089 00167 42806	20100509 005328 089 00174 42813	20100509 131631 089 00181 42820
20100510 002232 089 00188 42827	20100510 002603 089 00188 42827	20100510 124516 089 00195 42834
20100510 142819 089 00196 42835	20100510 235401 089 00202 42841	20100511 013609 089 00203 42842

Continued on next page

GM Data used in Chapter 5

20100511 122109 089 00209 42848	20100512 005902 089 00217 42856	20100512 010307 089 00217 42856
20100512 132211 089 00224 42863	20100513 002810 089 00231 42870	20100513 003058 089 00231 42870
20100513 125051 089 00238 42877	20100513 143359 089 00239 42878	20100513 235640 089 00245 42884
20100514 013455 089 00246 42885	20100514 122648 089 00252 42891	20100514 140130 089 00253 42892
20100515 010851 089 00260 42899	20100515 132956 089 00267 42906	20100516 125630 089 00281 42920
20100517 000236 089 00288 42927	20100517 013722 089 00289 42928	20100517 122626 089 00295 42934
20100517 123253 089 00295 42934	20100517 140715 089 00296 42935	20100517 141318 089 00296 42935
20100517 233541 089 00302 42941	20100518 010939 089 00303 42942	20100518 133447 089 00310 42949
20100519 003925 089 00317 42956	20100519 004222 089 00317 42956	20100519 130210 089 00324 42963
20100520 123225 089 00338 42977	20100520 141908 089 00339 42978	20100520 233627 089 00345 42984
20100520 234107 089 00345 42984	20100521 011439 089 00346 42985	20100521 134038 089 00353 42992
20100522 004457 089 00360 42999	20100522 004803 089 00360 42999	20100522 130749 089 00367 43006
20100523 001401 089 00374 43013	20100523 123803 089 00381 43020	20100523 141823 089 00382 43021
20100523 234207 089 00388 43027	20100524 011928 089 00389 43028	20100524 012651 089 00389 43028
20100524 134623 089 00396 43035	20100525 005039 089 00403 43042	20100525 131338 089 00410 43049
20100526 001942 089 00417 43056	20100526 002316 089 00417 43056	20100526 142551 089 00425 43064
20100526 234747 089 00431 43070	20100526 235127 089 00431 43070	20100527 013309 089 00432 43071
20100527 135249 089 00439 43078	20100527 135910 089 00439 43078	20100528 005616 089 00446 43085
20100528 131921 089 00453 43092	20100529 002520 089 00460 43099	20100529 002807 089 00460 43099
20100529 124804 089 00467 43106	20100529 142946 089 00468 43107	20100529 235347 089 00474 43113
20100529 235636 089 00474 43113	20100530 013223 089 00475 43114	20100530 122358 089 00481 43120
20100531 010600 089 00489 43128	20100531 132705 089 00496 43135	20100601 003058 090 00002 43142
20100601 003347 090 00002 43142	20100601 125340 090 00009 43149	20100601 235939 090 00016 43156
20100602 013747 090 00017 43157	20100602 122953 090 00023 43163	20100602 140424 090 00024 43164
20100602 233254 090 00030 43170	20100603 010708 090 00031 43171	20100603 133052 090 00038 43178
20100604 003928 090 00045 43185	20100604 125918 090 00052 43192	20100605 000533 090 00059 43199
20100605 122900 090 00066 43206	20100605 141007 090 00067 43207	20100605 141618 090 00067 43207
20100605 233828 090 00073 43213	20100606 011209 090 00074 43214	20100606 133749 090 00081 43221
20100607 004214 090 00088 43228	20100607 004515 090 00088 43228	20100607 130555 090 00095 43235
20100608 001113 090 00102 43242	20100608 123417 090 00109 43249	20100608 141538 090 00110 43250
20100608 142205 090 00110 43250	20100608 234331 090 00116 43256	20100609 011705 090 00117 43257
20100610 004750 090 00131 43271	20100610 131039 090 00138 43278	20100611 001654 090 00145 43285
20100611 002031 090 00145 43285	20100611 123940 090 00152 43292	20100611 142112 090 00153 43293
20100611 234456 090 00159 43299	20100611 234840 090 00159 43299	20100612 013003 090 00160 43300
20100612 134928 090 00167 43307	20100612 135621 090 00167 43307	20100613 005327 090 00174 43314
20100613 131629 090 00181 43321	20100614 002231 090 00188 43328	20100614 002602 090 00188 43328
20100614 124515 090 00195 43335	20100614 235401 090 00202 43342	20100615 012931 090 00203 43343
20100615 013609 090 00203 43343	20100615 122108 090 00209 43349	20100615 135542 090 00210 43350
20100616 005902 090 00217 43357	20100616 010310 090 00217 43357	20100616 132415 090 00224 43364
20100617 002809 090 00231 43371	20100617 003057 090 00231 43371	20100617 125051 090 00238 43378
20100617 143236 090 00239 43379	20100617 235639 090 00245 43385	20100618 013515 090 00246 43386
20100618 122648 090 00252 43392	20100618 140130 090 00253 43393	20100619 010438 090 00260 43400
20100620 003347 090 00274 43414	20100620 003637 090 00274 43414	20100620 125630 090 00281 43421
20100620 130439 090 00281 43421	20100621 000235 090 00288 43428	20100621 013721 090 00289 43429
20100621 122625 090 00295 43435	20100621 140714 090 00296 43436	20100621 141318 090 00296 43436
20100621 233541 090 00302 43442	20100622 010938 090 00303 43443	20100622 133446 090 00310 43450
20100623 003924 090 00317 43457	20100623 130209 090 00324 43464	20100624 000823 090 00331 43471
20100624 123224 090 00338 43478	20100624 141256 090 00339 43479	20100624 141910 090 00339 43479

Continued on next page

GM Data used in Chapter 5

20100624 233626 090 00345 43485	20100624 234107 090 00345 43485	20100625 011438 090 00346 43486
20100625 134037 090 00353 43493	20100626 004456 090 00360 43500	20100626 004802 090 00360 43500
20100626 130750 090 00367 43507	20100627 001401 090 00374 43514	20100627 123803 090 00381 43521
20100627 141822 090 00382 43522	20100627 142458 090 00382 43522	20100627 234600 090 00388 43528
20100628 011927 090 00389 43529	20100628 012650 090 00389 43529	20100628 134623 090 00396 43536
20100628 135331 090 00396 43536	20100629 005038 090 00403 43543	20100629 131338 090 00410 43550
20100630 001942 090 00417 43557	20100630 002316 090 00417 43557	20100630 124228 090 00424 43564
20100630 142553 090 00425 43565	20100630 234747 090 00431 43571	20100630 235127 090 00431 43571
20100701 012652 090 00432 43572	20100701 013305 090 00432 43572	20100701 135248 090 00439 43579
20100702 005615 090 00446 43586	20100702 131920 090 00453 43593	20100703 002520 090 00460 43600
20100703 002807 090 00460 43600	20100703 124803 090 00467 43607	20100703 142945 090 00468 43608
20100703 235346 090 00474 43614	20100703 235635 090 00474 43614	20100704 013222 090 00475 43615
20100704 122357 090 00481 43621	20100704 135835 090 00482 43622	20100705 010150 090 00489 43629
20100705 010559 090 00489 43629	20100705 132502 090 00496 43636	20100706 125342 091 00009 43650
20100706 235938 091 00016 43657	20100707 013746 091 00017 43658	20100707 122952 091 00023 43664
20100707 140423 091 00024 43665	20100707 233253 091 00030 43671	20100708 010708 091 00031 43672
20100709 003636 091 00045 43686	20100709 003928 091 00045 43686	20100709 125918 091 00052 43693
20100710 000533 091 00059 43700	20100710 122859 091 00066 43707	20100710 123553 091 00066 43707
20100710 141006 091 00067 43708	20100710 141617 091 00067 43708	20100710 233828 091 00073 43714
20100711 011208 091 00074 43715	20100711 133748 091 00081 43722	20100712 004259 091 00088 43729
20100712 004515 091 00088 43729	20100712 130459 091 00095 43736	20100713 001112 091 00102 43743
20100713 141538 091 00110 43751	20100713 142205 091 00110 43751	20100713 234331 091 00116 43757
20100714 011705 091 00117 43758	20100714 134334 091 00124 43765	20100715 004750 091 00131 43772
20100715 131039 091 00138 43779	20100716 001654 091 00145 43786	20100716 002031 091 00145 43786
20100716 124054 091 00152 43793	20100716 142112 091 00153 43794	20100717 012152 091 00160 43801
20100717 013004 091 00160 43801	20100717 134928 091 00167 43808	20100718 131632 091 00181 43822
20100719 002232 091 00188 43829	20100719 002603 091 00188 43829	20100719 124516 091 00195 43836
20100719 142657 091 00196 43837	20100719 235420 091 00202 43843	20100720 013609 091 00203 43844
20100720 122109 091 00209 43850	20100720 135543 091 00210 43851	20100721 005903 091 00217 43858
20100721 005903 091 00217 43858	20100721 010311 091 00217 43858	20100721 132416 091 00224 43865
20100722 002810 091 00231 43872	20100722 003058 091 00231 43872	20100722 125052 091 00238 43879
20100722 235834 091 00245 43886	20100723 013456 091 00246 43887	20100723 122649 091 00252 43893
20100723 140131 091 00253 43894	20100724 010439 091 00260 43901	20100724 010851 091 00260 43901
20100724 132758 091 00267 43908	20100725 003348 091 00274 43915	20100725 125631 091 00281 43922
20100725 130441 091 00281 43922	20100726 000237 091 00288 43929	20100726 013723 091 00289 43930
20100726 122627 091 00295 43936	20100726 123254 091 00295 43936	20100726 141319 091 00296 43937
20100726 233542 091 00302 43943	20100727 010939 091 00303 43944	20100727 133447 091 00310 43951
20100728 003926 091 00317 43958	20100728 004222 091 00317 43958	20100728 130210 091 00324 43965
20100729 000824 091 00331 43972	20100729 123226 091 00338 43979	20100729 141258 091 00339 43980
20100729 141912 091 00339 43980	20100729 234108 091 00345 43986	20100730 011439 091 00346 43987
20100730 134039 091 00353 43994	20100731 004458 091 00360 44001	20100731 004804 091 00360 44001
20100801 001402 091 00374 44015	20100801 123804 091 00381 44022	20100801 141824 091 00382 44023
20100801 142500 091 00382 44023	20100801 234208 091 00388 44029	20100801 234602 091 00388 44029
20100802 012652 091 00389 44030	20100802 134624 091 00396 44037	20100803 005040 091 00403 44044
20100803 131340 091 00410 44051	20100804 001944 091 00417 44058	20100804 002318 091 00417 44058
20100804 124230 091 00424 44065	20100804 142555 091 00425 44066	20100804 234749 091 00431 44072
20100804 235129 091 00431 44072	20100805 012654 091 00432 44073	20100805 135912 091 00439 44080
20100806 005618 091 00446 44087	20100806 131922 091 00453 44094	20100807 002522 091 00460 44101

Continued on next page

GM Data used in Chapter 5

20100807 002809 091 00460 44101	20100807 124805 091 00467 44108	20100807 142948 091 00468 44109
20100807 235349 091 00474 44115	20100807 235637 091 00474 44115	20100808 013224 091 00475 44116
20100808 122400 091 00481 44122	20100808 135838 091 00482 44123	20100809 010602 091 00489 44130
20100809 132505 091 00496 44137	20100810 003349 092 00002 44144	20100810 235941 092 00016 44158
20100811 013749 092 00017 44159	20100811 122954 092 00023 44165	20100811 140425 092 00024 44166
20100811 233256 092 00030 44172	20100812 010710 092 00031 44173	20100812 133053 092 00038 44180
20100813 003638 092 00045 44187	20100813 003930 092 00045 44187	20100813 125920 092 00052 44194
20100814 122901 092 00066 44208	20100814 123555 092 00066 44208	20100814 141008 092 00067 44209
20100814 233830 092 00073 44215	20100815 011210 092 00074 44216	20100815 133750 092 00081 44223
20100816 004216 092 00088 44230	20100816 004516 092 00088 44230	20100816 130501 092 00095 44237
20100817 001114 092 00102 44244	20100817 123418 092 00109 44251	20100817 141540 092 00110 44252
20100817 142206 092 00110 44252	20100817 234333 092 00116 44258	20100818 011706 092 00117 44259
20100818 134335 092 00124 44266	20100819 131040 092 00138 44280	20100820 001655 092 00145 44287
20100820 002032 092 00145 44287	20100820 142113 092 00153 44295	20100820 234458 092 00159 44301
20100820 234842 092 00159 44301	20100821 012153 092 00160 44302	20100821 013005 092 00160 44302
20100821 134929 092 00167 44309	20100821 135625 092 00167 44309	20100822 005329 092 00174 44316
20100822 131632 092 00181 44323	20100823 002604 092 00188 44330	20100823 124517 092 00195 44337
20100823 142658 092 00196 44338	20100823 235402 092 00202 44344	20100824 012932 092 00203 44345
20100824 013610 092 00203 44345	20100824 122110 092 00209 44351	20100825 005903 092 00217 44359
20100825 010311 092 00217 44359	20100825 132212 092 00224 44366	20100826 002811 092 00231 44373
20100826 125052 092 00238 44380	20100826 143237 092 00239 44381	20100826 235644 092 00245 44387
20100827 013517 092 00246 44388	20100827 122649 092 00252 44394	20100827 140131 092 00253 44395
20100828 010439 092 00260 44402	20100828 010852 092 00260 44402	20100828 132759 092 00267 44409
20100829 003348 092 00274 44416	20100829 003639 092 00274 44416	20100829 125631 092 00281 44423
20100830 000237 092 00288 44430	20100830 122627 092 00295 44437	20100830 123254 092 00295 44437
20100830 140716 092 00296 44438	20100830 141319 092 00296 44438	20100830 233542 092 00302 44444
20100831 010939 092 00303 44445	20100831 133447 092 00310 44452	20100901 003926 092 00317 44459
20100901 130210 092 00324 44466	20100902 000824 092 00331 44473	20100902 123226 092 00338 44480
20100902 141912 092 00339 44481	20100902 234108 092 00345 44487	20100903 011439 092 00346 44488
20100903 011439 092 00346 44488	20100903 134039 092 00353 44495	20100904 004803 092 00360 44502
20100904 130750 092 00367 44509	20100905 001402 092 00374 44516	20100905 123804 092 00381 44523
20100905 141823 092 00382 44524	20100905 142459 092 00382 44524	20100905 234207 092 00388 44530
20100905 234602 092 00388 44530	20100906 011929 092 00389 44531	20100906 012651 092 00389 44531
20100906 134624 092 00396 44538	20100907 005039 092 00403 44545	20100908 002317 092 00417 44559
20100908 124229 092 00424 44566	20100908 142408 092 00425 44567	20100908 234748 092 00431 44573
20100908 235128 092 00431 44573	20100909 012653 092 00432 44574	20100909 013310 092 00432 44574
20100909 135250 092 00439 44581	20100909 135250 092 00439 44581	20100909 135914 092 00439 44581
20100909 135914 092 00439 44581	20100910 005617 092 00446 44588	20100910 131921 092 00453 44595
20100911 002521 092 00460 44602	20100911 124804 092 00467 44609	20100911 142946 092 00468 44610
20100911 235347 092 00474 44616	20100911 235636 092 00474 44616	20100912 013223 092 00475 44617
20100912 122358 092 00481 44623	20100912 135836 092 00482 44624	20100913 010151 092 00489 44631
20100913 010151 092 00489 44631	20100913 010151 092 00489 44631	20100913 010600 092 00489 44631
20100913 132503 092 00496 44638	20100914 003058 093 00002 44645	20100914 003347 093 00002 44645
20100914 125936 093 00009 44652	20100914 235939 093 00016 44659	20100915 013747 093 00017 44660
20100915 122952 093 00023 44666	20100915 140423 093 00024 44667	20100915 233254 093 00030 44673
20100916 010708 093 00031 44674	20100916 133051 093 00038 44681	20100917 003635 093 00045 44688
20100917 125917 093 00052 44695	20100918 000532 093 00059 44702	20100918 122859 093 00066 44709
20100918 123552 093 00066 44709	20100918 141006 093 00067 44710	20100918 141617 093 00067 44710

Continued on next page

GM Data used in Chapter 5

20100918 233828 093 00073 44716	20100918 233828 093 00073 44716	20100919 011208 093 00074 44717
20100919 011208 093 00074 44717	20100919 133748 093 00081 44724	20100920 004213 093 00088 44731
20100920 004514 093 00088 44731	20100920 130458 093 00095 44738	20100921 123416 093 00109 44752
20100921 141537 093 00110 44753	20100921 142204 093 00110 44753	20100921 233916 093 00116 44759
20100921 234330 093 00116 44759	20100922 011703 093 00117 44760	20100922 134332 093 00124 44767
20100923 004748 093 00131 44774	20100923 131512 093 00138 44781	20100923 131512 093 00138 44781
20100924 001652 093 00145 44788	20100924 002029 093 00145 44788	20100924 124052 093 00152 44795
20100924 142110 093 00153 44796	20100924 234454 093 00159 44802	20100925 134926 093 00167 44810
20100925 135623 093 00167 44810	20100926 005325 093 00174 44817	20100926 131629 093 00181 44824
20100927 002229 093 00188 44831	20100927 002600 093 00188 44831	20100927 124513 093 00195 44838
20100927 142655 093 00196 44839	20100927 235359 093 00202 44845	20100928 012928 093 00203 44846
20100928 013607 093 00203 44846	20100928 122106 093 00209 44852	20100928 122106 093 00209 44852
20100928 135540 093 00210 44853	20100929 005900 093 00217 44860	20100929 010308 093 00217 44860
20100929 010308 093 00217 44860	20100930 002807 093 00231 44874	20100930 003055 093 00231 44874
20100930 125048 093 00238 44881	20100930 143424 093 00239 44882	20100930 235640 093 00245 44888
20101001 013205 093 00246 44889	20101001 122645 093 00252 44895	20101001 140127 093 00253 44896
20101002 010435 093 00260 44903	20101002 132754 093 00267 44910	20101003 003344 093 00274 44917
20101003 003634 093 00274 44917	20101003 125627 093 00281 44924	20101003 130436 093 00281 44924
20101004 000233 093 00288 44931	20101004 013719 093 00289 44932	20101004 122622 093 00295 44938
20101004 123249 093 00295 44938	20101004 140711 093 00296 44939	20101004 141315 093 00296 44939
20101004 233538 093 00302 44945	20101005 010935 093 00303 44946	20101005 133443 093 00310 44953
20101006 003921 093 00317 44960	20101006 004218 093 00317 44960	20101006 130206 093 00324 44967
20101007 000820 093 00331 44974	20101007 123139 093 00338 44981	20101007 141253 093 00339 44982
20101007 141907 093 00339 44982	20101007 233623 093 00345 44988	20101007 234103 093 00345 44988
20101008 011434 093 00346 44989	20101008 134034 093 00353 44996	20101009 004453 093 00360 45003
20101009 004758 093 00360 45003	20101009 130744 093 00367 45010	20050122 000751 034 00059 15143

References

A., L. & R., L. (2008). Fuel type characterization based on coarse resolution modis satellite data. *iForest - Biogeosciences and Forestry*, **1**, 60–64. 146

Abhyankar, A.A., Patwardhan, A. & Inamdar, A. (2007). Identification of threshold to classify water in radarsat-1 sar using irs 1d liss iii data and spatial correlation coefficient. In *Asian Association on Remote Sensing, Proceedings ACRS 2007*, http://www.aars-acrs.org/acrs/proceeding/ACRS2007/Papers/TS30.7.pdf. 27, 45

Ahmed, K.I. (2006). *ENVISAT ASAR for Land Cover Mapping and Change Detection*. Department of Urban Planning and Environment, School of Architecture and the Built Environment, Royal Institute of Technology (KTH), 100 44 Stockholm, Sweden, master of Science Thesis in Geoinformatics http://www.infra.kth.se/impgg/DOCS/EX-0611.pdf. 37, 48, 50, 54

Ahn, Y.H. & Shanmugam, P. (2006). Detecting the red tide algal blooms from satellite ocean color observations in optically complex northeast-asia coastal waters. *Remote Sensing of Environment*, **103**, 419–437. 146

Alpers, W. (1985). Theory of radar imaging of internal waves. *Nature*, **314**, 245–247. 143

Alsdorf, D., Rodriguez, E. & Lettenmaier, D. (2007). Measuring surface water from space. *Rev. Geophys.*, **45**. 60, 143, 144, 149

Amirmazlaghani, M., Amindavar, H. & Moghaddamjoo, A. (2009). Speckle suppression in sar images using the 2-d garch model. *IEEE Transactions on Image Processing*, **18**, 250–259. 39

ANH (2012). Australian plant image index. In *Australian National Herbarium*, Australian Government, Canberra, http://www.anbg.gov.au/photo/index.html, viewed May 2012. 156

Antoniol, G., Basco, C. & Ceccarelli, M. (2005). r.texture. In GRASS Development Team (2009). 46

Arnell, N. (2002). *Hydrology and Global Environmental Change*. Prentice Hall, Harlow, Essex. 2, 180

Array S. C. Inc. (2009). *NEST: Next ESA SAR Toolbox*. ESA / Array Systems Computing Inc., http://www.array.ca/nest/tiki-index.php. 40

Arzandeh, S. & Wang, J. (2002). Texture evaluation of radarsat imagery for wetland mapping. *Can. J. Remote Sensing*, **28**, 653–666. 46, 48, 54

Ashraf, M. & Majeed, A. (2006). *Water requirements of major crops for different agro-climatic zones of Balochistan*, vol. vii. The World Conservation Union (IUCN) Pakistan, Water Programme., Marker House, Zarghoon Road, Quetta, Pakistan. 122

Badji, M. & Dautrebande, S. (1997). Characterization of flood inundated areas and delineation of poor drainage soil using ERS-1 SAR imagery. *Hydrological Processes*, 1441–1450. 60

Baghdadi, N., Bernier, M., Gauthier, R. & Neeson, I. (2001). Evaluation of c-band sar data for wetlands mapping. *International Journal of Remote Sensing*, **22**, 71–88. 2, 26, 43, 44, 48, 88, 89, 91, 113

Baldassarre, G.D., Schumann, G. & Bates, P.D. (2009). A technique for the calibration of hydraulic models using uncertain satellite observations of ?ood extent. *Journal of Hydrology*, 276–282. 27, 47

Bartsch, A., Doubkova, M., Pathe, C., Sabel, D., Wagner, W. & Wolski, P. (2008). River flow & wetland monitoring with envisat asar global mode in the okavango basin and delta. In *Proceedings of the Second IASTED Africa Conference Water Resource Management (AfricaWRM 2008)*, 152–156, Gaborone, Botswana. 29, 146, 149, 157, 162, 178, 184

Bartsch, A., Wagner, W., Scipal, K., Pathe, C., Sabel, D. & Wolski, P. (2009). Global monitoring of wetlands—the value of envisat asar global mode. *Journal of Environmental Management*, **90**, 2226–2233. 35, 40, 146

Baup, F., Mougin, E., Hiernaux, P., Lopes, A., De Rosnay, P. & Chênerie, I. (2007). Radar signatures of sahelian surfaces in Mali using ENVISAT-ASAR data. *IEEE Transactions on Geoscience and Remote Sensing*, **45**, 2354–2363. 60

Ben Ayed, I., Mitiche, A. & Belhadj, Z. (2005). Multiregion level-set partitioning of synthetic aperture radar images. vol. 27, 793–800, IEEE Computer Soc., United States. 143

Biancamaria, S., Andreadis, K.M., Durand, M., Clark, E.A., Rodriguez, E., Mognard, N.M., Alsdorf, D.E., Lettenmaier, D.P. & Oudin, Y. (2010). Preliminary characterization of SWOT hydrology error budget and global capabilities. *IEEE Journal of Selected Topics in Applied Earth Observations and Remote Sensing*, **3**, 6–19. 145, 182

Bindlish, R., Crow, W. & Jackson, T. (2009). Role of passive microwave remote sensing in improving flood forecasts. *Geoscience and Remote Sensing Letters, IEEE*, **6**, 112–116. 87

Bonn, F. & Dixon, R. (2005). Monitoring flood extent and forecasting excess runoff risk with radarsat-1 data. *Natural Hazards*, **35**, 377–393. 2, 22, 23, 27, 34, 54, 87, 149

Boucher, M. (2012). Canada's RADARSAT-1 to fill in as ESA's Envisat service interrupted. In *SpaceRef*, SpaceRef, `http://spaceref.ca/missions-and-programs/canadian-space-agency/radarsat-1/canadas-radarsat-to-fill-in-as-esas-envisat-service-interrupted.html`, viewed 29 May 12. 178

Bouman, C. & Shapiro, M. (2004). i.smap. In GRASS Development Team (2009). 47

Bourgeau-Chavez, L.L., Kasischke, E.S., Brunzell, S.M., Mudd, J.P., Smith, K.B. & Frick, A.L. (2001). Analysis of space-borne sar data for wetland mapping in virginia riparian ecosystems. *International Journal of Remote Sensing*, **22**, 3665–3687. 26, 32, 50, 52

Bracaglia, M., Ferrazzoli, P. & Guerriero, L. (1995). A fully polarimetric multiple scattering model for crops. *Remote Sensing of the Environment*, **54**, 170–179. 34

Bréon, F.M. & Ciais, P. (2010). Spaceborne remote sensing of greenhouse gas concentrations. *Comptes Rendus Geoscience*, **342**, 412–424, the atmosphere seen from space. 179

Bukata, R. (2005). *Satellite Monitoring of Inland and Coastal Water Quality: Retrospection, Introspection, Future Directions*. Taylor and Francis, New York. 144

Campbell, J.B. (2007). *Introduction to Remote Sensing*. The Guilford Press, New York, 4th edn. 54

Cardoso, M.F., Nobre, C.A., Lapola, D.M., Oyama, M.D. & Sampaio, G. (2008). Longterm potential for fires in estimates of the occurrence of savannas in the tropics. *Global Ecology and Biogeography*, **17**, 222–235. 183

Chakraborty, D., Sen, G. & Hazra, S. (2009). High-resolution satellite image segmentation using holder exponents. *Journal of Earth System Science*, **118**, 609–617. 143

Chandran, R.V., Ramakrishnan, D., Chowdary, V.M., Jeyaram, A. & Jha, A.M. (2006). Flood mapping and analysis using air-borne synthetic aperture radar: A case study of july 2004 flood in baghmati river basin, bihar. *Current Science*, **90**, 249–256. 28, 54, 87

Chen, H., Wu, N., Wang, Y., Gao, Y. & Peng, C. (2011). Methane fluxes from alpine wetlands of Zoige Plateau in relation to water regime and vegetation under two scales. *Water, Air and Soil Pollution*, **217**, 173–183. 179, 180

Chen, J.M., Chen, X., Ju, W. & Geng, X. (2004). Distributed hydrological model for mapping evapotranspiration using remote sensing inputs. *Journal of Hydrology*, **305**, 15–39. 141

Chéret, V. & Denux, P. (2007). Mapping wildfire danger at regional scale with an index model integrating coarse spatial resolution remote sensing data. *Journal of Geophysical Research*, **112**. 146

Chuvieco, E., Aguado, I. & Dimitrakopoulos, A.P. (2004). Conversion of fuel moisture content values to ignition potential for integrated fire danger assessment. *Canadian Journal of Forest Research*, **34**, 2284–2284. 183

Ciuc, M., Bolon, P., Trouve, E., Buzuloiu, V. & Rudant, J.P. (2001). Adaptive-neighborhood multitemporal synthetic speckle removal in aperture radar images. *Applied Optics*, **40**, 5954–5966. 60

Cohen, J. (1960). A coefficient of agreement for nominal scales. *Educational and Psychological Measurement*, **XX**, 37–46. 121, 159

Colesanti, C. & Wasowski, J. (2006). Investigating landslides with space-borne synthetic aperture radar (SAR) interferometry. *Engineering Geology*, **88**, 173–199. 60

COLLINS, M.J. & KOPP, E.B. (2008). On the design and evaluation of multiobjective single-channel sar image segmentation algorithms. vol. 46, 1836–1846, IEEE Transactions on Geoscience and Remote Sensing. 144

CONESA-GARCIA, C., CASELLES-MIRALLES, V., SANCHEZ TOMAS, J.M. & GARCIA-LORENZO, R. (2010). Hydraulic geometry, gis and remote sensing, techniques against rainfall-runoff models for estimating flood magnitude in ephemeral fluvial systems. *Remote Sensing*, **2**, 2607–2628. 141

COOPS, H., HANGANU, J., TUDOR, M. & OOSTERBERG, W. (1999). Classification of Danube Delta lakes based on aquatic vegetation and turbidity. *Hydrobiologia*, **415**, 187–191. 180

COSSU, R., SCHOEPFER, E., BALLY, P. & FUSCO, L. (2009). *Near real-time SAR based processing to support flood monitoring*. ESA-ESRIN, Directorate of Earth Observation Programmes, Galileo Galilei, 00044 Frascati, Italy. 61

COSTA, M.P. & TELMER, K.H. (2006). Utilizing SAR imagery and aquatic vegetation to map fresh and brackish lakes in the brazilian Pantanal wetland. *Remote Sensing of Environment*, **105**, 204–213. 149, 156, 157, 158

CSA (2012). RADARSAT constellation. In *Canadian Space Agency*, Canadian Space Agency, http://www.asc-csa.gc.ca/eng/satellites/radarsat/default.asp, viewed 29 May 12. 178

DALAL, R.C., ALLEN, D.E., LIVESLEY, S.J. & RICHARDS, G. (2008). Magnitude and biophysical regulators of methane emission and consumption in the Australian agricultural, forest, and submerged landscapes: a review. *Plant Soil*, **309**, 43–76. 179, 180

DAVID, S., HOLECZ, F., MEIER, E. & NUESCH, D. (1998). Absolute radiometric correction in rugged terrain: A plea for integrated radar brightness. In *International Geoscience and Remote Sensing Symposium (IGARSS)*, vol. 1, 330–332. 41, 43, 45

DECHARME, B., OTTLÉ, C., SAUX-PICART, S., BOULAIN, N., CAPPELAERE, B., RAMIER, D. & ZRIBI, M. (2009). A new land surface hydrology within the noah-wrf land-atmosphere mesoscale model applied to semiarid environment: Evaluation over the Dantiandou Kori (Niger). *Advances in Meteorology*, **2009**, 1–13. 141

DHEERAVATH, V., THENKABAIL, P., CHANDRAKANTHA, G., NOOJIPADY, P., REDDY, G., BIRADAR, C., GUMMA, M. & VELPURI, M. (2010). Irrigated areas of india derived using modis 500 m time series for the years 20012003. *ISPRS Journal of Photogrammetry and Remote Sensing*, **65**, 42–59. 120

DIGITALGLOBE (2012). About the worldview-2 satellite. In *WorldView-2*, DigitalGlobe, http://worldview2.digitalglobe.com/about/, viewed 29 May 12. 181

ESA (2004). *Absolute calibration of ASAR level 1 products generated with PF-ASAR*. European Space Agency, ESRIN, Via Galileo Galilei, Casella Postale 64, 00044 Frascati (Rome), Italy, 1st edn. 14, 40, 42, 43, 88, 113

ESA (2007a). *ASAR Product Handbook*. European Space Agency, 8–10 rue Mario Nikis, 75738 Paris, 2nd edn. 12, 13, 29, 30, 32, 36, 40, 61, 72, 73, 114, 210

ESA (2007b). Asar products specifications. In *Envisat-1 Products Specifications*, vol. 8, European Space Agency. 30, 61, 146

ESA (2009a). Category-1 registration. In *Earth Observation: Principal Investigator Portal*, European Space Agency, http://eopi.esa.int/esa/esa?cmd=aodetail&aoname=Registration. 38

ESA (2009b). Esa data products: Envisat asar. In *Earthnet Online*, European Space Agency, http://earth.esa.int/object/index.cfm?fobjectid=1536. 90

ESA (2009c). Organisation of products. In *ESA Earthnet Online*, European Space Agency, http://envisat.esa.int. 45

ESA (2010). Enviview. In *Earthnet Online*, European Space Agency, Earth Observation Ground Segment Department User Services and Mission Planning Office Via Galileo Galilei 00044 Frascati (Rome) Italy. 79

ESA (2012a). About GMES. In ESA (2012b), viewed 29 May 12. 179

ESA (2012b). ESA's sentinel satellites. In *GMES Observing the Earth*, European Space Agency, http://www.esa.int/esaLP/SEMBRS4KXMF_LPgmes_0.html, viewed 29 May 12. 176, 178, 181, 228

Fair, C.C. (2011). Pakistan in 2010 flooding, governmental inefficiency, and continued insurgency. *Asian Survey*, **51**, 97–110. 108

FAO (2012). Dichanthium sericeum (r. br.) a. camus. In *Grassland Species*, Food and Agriculture Organization of the United Nations, http://www.fao.org/ag/AGP/AGPC/doc/Gbase/data/pf000216.htm, viewed May 2012. 156

Felderhof, L. & Gillieson, D. (2006). Comparison of fire patterns and fire frequency in two tropical savanna bioregions. *Austral Ecology*, **31**, 736–746. 183, 185

Fleiss, J.L. (1981). *Statistical methods for rates and proportions*. John Wiley, New York, 2nd edn. 166

Foody, G.M. (2006). What is the difference between two maps? a remote sensers view. *Journal of Geographical Systems*, **8**, 119–130. 121, 159

Frappart, F., Seyler, F., Martinez, J.M., León, J.G. & Cazenave, A. (2005). Floodplain water storage in the negro river basin estimated from microwave remote sensing of inundation area and water levels. *Remote Sensing of Environment*, **99**, 387–399. 1, 28, 54, 87

Fu, Y., Cao, Z. & Pi, Y. (2008). Multi-region segmentation of sar image by a multiphase level set approach. *Journal of Electronics (China)*, **25**, 556–561. 144

Galland, F., Nicolas, J., Sportouche, H., Roche, M., Tupin, F. & Refregier, P. (2009). Unsupervised synthetic aperture radar image segmentation using fisher distributions. vol. 47, 2966–2972, IEEE. 143

GBIF (2012). Sorghum plumosum. In *Atlas of Living Australia*, Global Biodiversity Information Facility, http://bie.ala.org.au/species/Sorghum+plumosum, viewed May 2012. 156

Gens, R. (2007). From sar data to information: Status, trends and future. In *THEMATIC PROCESSING, MODELING AND ANALYSIS OF REMOTELY SENSED DATA*, International Society for Photogrammetry and Remote Sensing, http://www.itc.nl/isprsc7/wg2/documents/keynote.pdf. 22, 23

GESDISC (2011). *Flooding in Pakistan caused by higher-than-normal monsoon rainfall*. Goddard Earth Sciences Data and Information Services Center, http://disc.sci.gsfc.nasa.gov, 1-Mar-2011 Accessed online. 111

Grandi, G.D.D., Lucas, R.M. & Kropacek, J. (2009). Analysis by wavelet frames of spatial statistics in sar data for characterizing structural properties of forests. *IEEE Transactions on Geoscience and Remote Sensing*, **47**, 494–507. 47

GRASS Development Team (2009). *Geographic Resources Analysis Support System (GRASS GIS) Software*. Open Source Geospatial Foundation, USA, http://grass.osgeo.org. 47, 74, 119, 224, 225

Grings, F., Salvia, M., Karszenbaum, H., Ferrazzoli, P., Kandus, P. & Perna, P. (2009). Exploring the capacity of radar remote sensing to estimate wetland marshes water storage. *Journal of Environmental Management*, **90**, 2189–2198. 28, 34, 149, 156, 157, 158

Groten, E. (2004). Fundamental parameters and current (2004) best estimates of the parameters of common relevance to astronomy, geodesy, and geodynamics. *Journal of Geodesy*, **77**, 724–797. 79

Hamilton, S., Sippel, S. & Melack, J. (2002). Comparison of inundation patterns among major south american floodplains. *J. Geophys. Res. Atmos.*, **107**, 8038. 144

Henderson, F.M. & Lewis, A.J. (2008). Radar detection of wetland ecosystems: a review. *International Journal of Remote Sensing*, **29**, 5809–5835. 2, 21, 22, 24, 25, 26, 27, 28, 32, 35, 39, 90, 156

Hess, L.L., Melack, J.M., Novo, E.M., Barbosa, C.C. & Gastil, M. (2003). Dual-season mapping of wetland inundation and vegetation for the central amazon basin. *Remote Sensing of the Environment*, **87**, 404–428. 122, 144, 156

Hostache, R., Matgen, P., Schumann, G., Puech, C., Hoffmann, L. & Pfister, L. (2009a). Water level estimation and reduction of hydraulic model calibration uncertainties using satellite sar images of floods. *IEEE Transactions on Geoscience and Remote Sensing*, **47**, 431–441. 25, 28, 35, 45

Hostache, R., Matgen, P., Schumann, G., Puech, C., Hoffmann, L. & Pfister, L. (2009b). Water level estimation and reduction of hydraulic model calibration uncertainties using satellite sar images of floods. *IEEE Transactions on Geoscience and Remote Sensing*, **47**, 431–441. 141

Huang, F., Liu, D., Tan, X., Wang, J., Chen, Y. & He, B. (2011). Explorations of the implementation of a parallel idw interpolation algorithm in a linux cluster-based parallel gis. *Computers and Geosciences*, **37**, 426–434. 74

HUNT, E., GILLHAM, J. & DAUGHTRY, C. (2010). Improving potential geographic distribution models for invasive plants by remote sensing. *RANGELAND ECOLOGY & MANAGEMENT*, **63**, 505–513. 121, 159

HUNT, E.R. & MIYAKE, B.A. (2006). Comparison of stocking rates from remote sensing and geospatial data. *Rangeland Ecol. Manage.*, **59**, 11–18. 146

ISRO (2012). RISAT-1. In *Earth Observation Satellites*, Indian Space Research Organisation, http://www.isro.org/satellites/risat-1.aspx, viewed 29 May 12. 179

JARLAN, L., MOUGIN, E., MAZZEGA, P., SCHOENAUER, M., TRACOL, Y. & HIERNAUX, P. (2005). Using coarse remote sensing radar observations to control the trajectory of a simple sahelian land surface model. *Remote Sensing of Environment*, **94**, 269–285. 146

JARVIS, A., REUTER, H., NELSON, A. & GUEVARA, E. (2008). *Hole-filled seamless SRTM data V4*. International Centre for Tropical Agriculture (CIAT), available from http://srtm.csi.cgiar.org. 62, 116

JASIEWICZ, J. (2010). A new grass gis fuzzy inference system for massive data analysis. *Computers and Geosciences*, doi:10.1016/j.cageo.2010.09.008. 74

JONES, K., LANTHIER, Y., VAN DER VOET, P., VAN VALKENGOED, E., TAYLOR, D. & FERNANDEZ-PRIETO, D. (2009). Monitoring and assessment of wetlands using earth observation: The globwetland project. *Journal of Environmental Management*, **90**, 2154–2169. 145

KANDUS, P., KARSZENBAUM, H., PULTZ, T., PARMUCHI, G. & BAVA, J. (2001). Influence of flood conditions and vegetation status on the radar backscatter of wetland ecosystems. *Canadian Journal of Remote Sensing*, **27**, 651–662. 27

KASISCHKE, E.S., SMITH, K.B., BOURGEAU-CHAVEZ, L.L., ROMANOWICZ, E.A., BRUNZELL, S. & RICHARDSON, C.J. (2003). Effects of seasonal hydrologic patterns in south Florida wetlands on radar backscatter measured from ERS-2 SAR imagery. *Remote Sensing of Environment*, **88**, 423–441. 149, 158, 162

KERNIGHAN, B.W. & PIKE, R. (1984). *The Unix Programming Environment*. Prentice Hall, Inc. 74

KUGLER, Z., DE GROEVE, T., BRAKENRIDGE, G.R. & ANDERSON, E. (2007). *Towards a Near-Real Time Global Flood Detection System (GFDS)*. European Commission / Dartmouth Flood Observatory, Joint Research Centre, Ispra Site, European Commission, Ispra 21020, Via Fermi 1, Italy. 1

LANDIS, J.R. & KOCH, G.G. (1977). The measurement of observer agreement for categorical data. *Biometrics*, **33**, 159–174. 166

LANDSBERG, J., GILLIESON, D. & SALT, D. (2011). *Trees in Savanna Landscapes*. David Gillieson, http://www.skyviewsolutions.com.au. 182

LAW, R. & GARNETT, S.T. (2011). Mapping carbon in tropical Australia: Estimates of carbon stocks and fluxes in the Northern Territory using the national carbon accounting toolbox. *Ecological Management and Restoration*, **12**, 61–68. 179

Leblanc, M., Razack, M., Dagorne, D., Mofor, L. & Jones, C. (2003). Application of Meteosat thermal data to map soil infiltrability in the central part of the Lake Chad basin, Africa. *Geophys. Res. Lett.*, **30**. 145

Leblanc, M., Lemoalle, J., Bader, J.C., Tweed, S. & Mofor, L. (2011). Thermal remote sensing of water under flooded vegetation: new observations of inundation patterns for the 'Small' Lake Chad. *Journal of Hydrology*. 60, 145

Leblon, B. (2005). Monitoring forest fire danger with remote sensing. *Natural Hazards*, **35**, 343–359. 184

Li, R.R., Kaufman, Y., Gao, B.C. & Davis, C. (2003). Remote sensing of suspended sediments and shallow coastal waters. *IEEE Trans. Geosci. Remote Sens.*, **41**, 559–566. 144

Liebe, J.R., van de Giesen, N., Andreini, M.S., Steenhuis, T.S. & Walter, M.T. (2009). Suitability and limitations of envisat asar for monitoring small reservoirs in a semiarid area. *IEEE Transactions on Geoscience and Remote Sensing*, **47**, 1536–1547. 112, 149, 157

Lillesand, T.M. & Kiefer, R.W. (2004). *Remote Sensing and Image Interpretation*. John Wiley & Sons, Inc., New York, 5th edn. 14, 16, 17, 18, 19, 20

Liu, Q., Wang, M. & Zhao, Y. (2010). Assimilation of asar data with a hydrologic and semi-empirical backscattering coupled model to estimate soil moisture. *Chinese Geographical Science*, **20**, 218–225. 141

Low, A. & Mauser, W. (2003). Generation of geometrically and radiometrically terrain corrected scansar images. In *Geoscience and Remote Sensing Symposium, 2003. IGARSS apos;03. Proceedings.*, vol. 6, 3995–3997, IEEE International. 40

Ludwig, R. & Schneider, P. (2006). Validation of digital elevation models from srtm x-sar for applications in hydrologic modeling. *ISPRS Journal OF Photogrammetry AND Remote Sensing*, **60**, 339–358. 141

M.-Muslim, A., Foody, G.M. & Atkinson, P.M. (2007). Shoreline mapping from coarsespatial resolution remote sensing imagery of seberang takir, malaysia. *Journal of Coastal Research*, **23**, 1399–1408. 146

Martinez, J., Karzenbaum, H., Le Toan, T., Kandus, P., Tiffenberg, J., Pratolongo, P. & Parmuchi, G. (2001). Detecting anthropogenic and natural disturbances in wetland ecosystems with multitemporal ers 2 data. In *Proc. 3rd International Symposium, 'Retrieval of bio- and geophysical parameters from SAR data for land applications'*, 11–115, Sheffield, UK. 35

Martinez, J.M. & Le Toan, T. (2007). Mapping of flood dynamics and spatial distribution of vegetation in the amazon floodplain using multitemporal sar data. *Remote Sensing of Environment*, 209–223. 144

Matgen, P., Hostache, R., Schumann, G., Pfister, L., Hoffmann, L. & Savenije, H. (2011). Towards an automated sar-based flood monitoring system: Lessons learned from two case studies. *Physics and Chemistry of the Earth, Parts A/B/C*, **36**, 241–252. 143, 144

M.B., R.N. & Pivello, V. (2000). Lightning fires in a Brazilian savanna national park: Rethinking management strategies. *Environment Management*, **26**, 675–684. 183

Milzow, C., Kgotlhang, L., Bauer-Gottwein, P., Meier, P. & Kinzelbach, W. (2009a). Regional review: the hydrology of the okavango delta, botswana-processes, data and modelling. *Hydrogeology Journal*, **17**, 1297–1328. 141

Milzow, C., Kgotlhang, L., Kinzelbach, W., Meier, P. & Bauer-Gottwein, P. (2009b). The role of remote sensing in hydrological modelling of the Okavango Delta, Botswana. *Journal of Environmental Management*, **90**, 2252–2260. 141

Monsiváis, A., Chênerie, I., Baup, F., Mougin, E. & Sarabandi, K. (2006). Angular normalization of envisat asar data over sahelian-grassland using a coherent scattering model. In *Progress In Electromagnetics Research Symposium*, Cambridge, USA. 112

Montanari, M., Hostache, R., Matgen, P., Schumann, G., Pfister, L. & Hoffmann, L. (2009). Calibration and sequential updating of a coupled hydrologic-hydraulic model using remote sensing-derived water stages. *Hydrology and Earth System Sciences*, **13**, 367–380. 141

Moore, R. & Fung, A. (1979). Radar determination of winds at sea. In *IEEE*, vol. 67, 1504–1521. 92

NASA (2011). Mod 09 - surface reflectance; atmospheric correction algorithm products. In *MODIS Web*, National Aeronautics and Space Administration, http://modis.gsfc.nasa.gov/. 90

NDMA (2011). *Pakistan floods relief, recovery and rehabilitation*. National Disaster Management Authority, Prime Minister's Secretariat, Government of Pakistan, http://www.pakistanfloods.pk/, 11-Feb-2011 Accessed online. 107

Neilson, R. (1995). A model for predicting continental scale vegetation distribution and water balance. *Acological Applications*, **5**, 362–385. 183

Neteler, M. & Mitasova, H. (2008). *Open Source GIS a GRASS GIS Approach*. Springer, New York, USA, 3rd edn. 74

Noernberg, M.A., Novo, E.M. & Krug, T. (1999). The use of biophysical indices and coefficient of variation derived from airborne synthetic aperture radar for monitoring the spread of aquatic vegetation in tropical reservoirs. *International Journal of Remote Sensing*, **20**, 67–82. 2, 24, 26, 50, 90, 156

Oberstadler, R., Hönsch, H. & Huth, D. (1997). Assessment of the mapping capabilities of ers-1 sar data for flood mapping: a case study in germany. *Hydrological Processes*, **11**, 1415–1425. 13, 32, 50

O'Grady, D., Leblanc, M. & Gillieson, D. (2011). Use of Envisat ASAR global monitoring mode to complement optical data in the mapping of rapid broad-scale flooding in Pakistan. *Hydrology and Earth System Sciences*, **15**, 3475–3794. 61, 81, 149, 159, 163

Onoda, M. (2008). Satellite observation of greenhouse gases: Monitoring the climate change regime. *Space Policy*, **24**, 190–198. 179

Ordoyne, C. & Friedl, M.A. (2008). Using modis data to characterize seasonal inundation patterns in the florida everglades. *Remote Sensing of Environment*, **112**, 4107–4119. 120

Park, S.E., Bartsch, A., Sabel, D., Wagner, W., Naeimi, V. & Yamaguchi, Y. (2011). Monitoring freeze/thaw cycles using envisat asar global mode. *Remote Sensing of Environment*. 146

Parmuchi, M.G., Karszenbaum, H. & Kandus, P. (2002). Mapping wetlands using multi-temporal radarsat-1 data and a decision-based classifier. *Can. J. Remote Sensing*, **28**, 175–186. 23, 24, 32, 35, 43, 46, 48, 49, 50, 52, 90, 157, 158

Pathe, C., Wagner, W., Sabel, D., Doubkova, M. & Basara, J.B. (2009). Using envisat asar global mode data for surface soil moisture retrieval over oklahoma, usa. *IEEE Transactions on Geoscience and Remote Sensing*, **47**, 468–480. 22, 29, 32, 36, 37, 39, 44, 52, 61, 89, 122, 146

Pauwels, V.R.N., Balenzano, A., Satalino, G., Skriver, H., Verhoest, N.E.C. & Mattia, F. (2009). Optimization of soil hydraulic model parameters using synthetic aperture radar data: An integrated multidisciplinary approach. *IEEE Transactions on Geoscience and Remote Sensing*, **47**, 455–467. 142

Pope, K., Sheffner, E., Linthicum, K., Bailey, C., Logan, T., Kasischke, E., Birney, K., Njogu, A. & Roberts, C. (1992). Identification of central Kenyan Rift Valley fever virus vector habitats with Landsat TM and evaluation of their flooding status with airborne radar. *Remote Sensing of Environment*, **40**, 185–196. 157

Pope, K.O., Rejmankova, E., Paris, J.F., & Woodruff, R. (1997). Detecting seasonal flooding cycles in marshes of the yucatan peninsula with sir-c polarimetric radar imagery. *Remote Sens. Environ.*, **59**, 157–166. 24, 25, 33, 35, 157, 158, 159

Powell, S., Letcher, R. & Croke, B. (2008). Modelling floodplain inundation for environmental flows: Gwydir wetlands, australia. *Ecological Modelling*, **211**, 350–362, `http://www.sciencedirect.com/science/article/B6VBS-4R34F7P-1/2/565bf4509d20760f47ba799477a5b849`. 1

Prigent, C., Papa, F., Aires, F., Rossow, W.B. & Matthews, E. (2007). Global inundation dynamics inferred from multiple satellite observations, 1993–2000. *Journal of Geophysical Research*, **112**, 1–13. 144, 146

Quan, J.J., Wen, X.B. & Xu, X.Q. (2008). Multiscale probabilistic neural network method for sar image segmentation. *Applied Mathematics and Computation*, **205**, 578–583. 48, 50, 51

Quegan, S., Le Toan, T., Yu, J.J., Ribbes, F. & Floury, N. (2000). Multitemporal ERS SAR analysis applied to forest mapping. *IEEE Transactions on Geoscience and Remote Sensing*, **38**. 61

Quincey, D. & Luckman, A. (2009). Progress in satellite remote sensing of ice sheets. *Progress in Physical Geography*, **33**, 547–567. 146

Ramsey, E.I. (1998). Radar remote sensing of wetlands. In R. Lunetta & C. Elvidge, eds., *Remote Sensing Change Detection: Environmental Monitoring Methods and Applications*, chap. 13, 211–243, Ann Arbor Press, Chelsea, MI. 25, 26, 158

Raney, R.K., Freeman, T., Hawkins, R.W. & Bamler, R. (1994). Plea for radar brightness. In *International Geoscience and Remote Sensing Symposium (IGARSS)*, vol. 2, 1090–1092. 41, 43, 45

Rees, W.G. & Steel, A.M. (2001). Simplified radar mapping equations for terrain correction of space-borne sar images. *International Journal of Remote Sensing*, **22**, 3643–3649. 62, 63

Reuter, H., Nelson, A. & Jarvis, A. (2007). An evaluation of void filling interpolation methods for SRTM data. *International Journal of Geographic Information Science*, **21**, 983–1008. 116

Robinson, C., El-Baz, F., Al-Saud, T. & Jeon, S. (2006). Use of radar data to delineate palaeodrainage leading to the kufra oasis in the eastern sahara. *Journal of African Earth Sciences*, **44**, 229–240. 19, 113, 115, 123

Rojas, O., Vrieling, A. & Rembold, F. (2011). Assessing drought probability for agricultural areas in africa with coarse resolution remote sensing imagery. *Remote Sensing of Environment*, **115**, 343–352. 146

Rosenqvist, A., Forsberg, B.R., Pimentel, T., Rauste, Y.A. & Richey, J.E. (2002). The use of spaceborne radar data to model inundation patterns and trace gas emissions in the central amazon floodplain. *International Journal of Remote Sensing*, **23**, 1303–1328. 2, 23, 24, 32, 45, 52, 54

Rosenqvist, A., Finlayson, C.M., Lowry, J. & Taylor, D. (2007). The potential of long-wavelength satellite-borne radar to support implementation of the ramsar wetlands convention. *Aquatic Conserv: Mar. Freshw. Ecosyst.*, **17**, 229–244. 1, 108, 144, 157

Sabel, D., Bartalis, Z., Bartsch, A., Doubkova, M., Hasenauer, S., Naeimi, V., Pathe, C. & Wagner, W. (2008). Synergistic use of scatterometer and scansar data for extraction of surface soil moisture information in australia. In *Soil moisture for hydrometeorologic applications in the SADC region (SHARE)*, ESA Tiger, Viewed online 1-Jun-09 `http://www.ukzn.ac.za/sahg/share/index.php?go=literature`. 29, 36, 52, 89

Sakamoto, T., Van Nguyen, N., Kotera, A., Ohno, H., Ishitsuka, N. & Yokozawa, M. (2007). Detecting temporal changes in the extent of annual flooding within the cambodia and the vietnamese mekong delta from modis time-series imagery. *Remote Sensing of Environment*, **109**, 259–313. 146

Sanyal, J. & Lu, X.X. (2004). Application of remote sensing in flood management with special reference to monsoon asia: A review. *Natural Hazards*, **33**, 283–301. 13, 26, 32, 35, 142, 149

Saux-Picart, S., Ottlé, C., Decharme, B., André, C., Zribi, M., Perrier, A., Coudert, B., Boulain, N., Cappelaere, B., Descroix, L. & Ramier, D. (2009). Water and energy budgets simulation over the amma-niger super-site spatially constrained with remote sensing data. *Journal of Hydrology*, **375**, 287–295. 141

Schaber, G.G. (1999). Sar studies in the yuma desert, arizona: Sand penetration, geology, and the detection of military ordnance debris. *Remote Sensing of Environment*, **67**, 320–347. 18

Schaber, G.G., McCauley, J.F., & Breed, C.S. (1997). The use of multifrequency and polarimetric sir-c/x-sar data in geologic studies of bir safsaf, egypt. *Remote Sensing of Environment*, **59**, 336–363. 20, 21, 22, 93, 112, 113, 115, 123, 149

Schiermeier, Q. (2011). Increased flood risk linked to global warming. *Nature*, **470**, 316. 140

Schroeder, R., Rawlins, M.A., McDonald, K.C., Podest, E., Zimmermann, R. & Kueppers, M. (2010). Satellite microwave remote sensing of north eurasian inundation dynamics: development of coarse-resolution products and comparison with high-resolution synthetic aperture radar data. *Environmental Research Letters*, **5**. 146

Schumann, G., Matgen, P., Hoffmann, L., Hostache, R., Pappenburger, F. & Pfister, L. (2007). Deriving distributed roughness values from satellite radar data for flood inundation modelling. *Journal of Hydrology*, **344**, 96–111. 141

Scipal, K., Scheffler, C. & Wagner, W. (2005). Soil moisture-runoff relation at the catchment scale as observed with coarse resolution microwave remote sensing. *Hydrology and Earth System Sciences*, **9**, 173–183. 146

Seiler, R., Schmidt, J., Diallo, O. & Csaplovics, E. (2009). Flood monitoring in a semi-arid environment using spatially high resolution radar and optical data. *Journal of Environmental Management*, **90**, 2121–2129. 29, 46, 47

Shimada, M. (2010a). Generating large-scale high-quality SAR mosaic datasets: Application to PALSAR data for global monitoring. *IEEE Journal of Selected Topics in Applied Earth Observations and Remote Sensing*, **3**, 637–656. 43, 88

Shimada, M. (2010b). Ortho-rectification and slope correction of sar data using dem and its accuracy evaluation. *IEEE Journal of Selected Topics in Applied Earth Observations and Remote Sensing*, **3**, 657–671. 73

Silva, T.S.F., Costa, M.P.F., Melack, J.M. & Novo, E.M.L.M. (2008). Remote sensing of aquatic vegetation: theory and applications. *Environmental Monitoring and Assessment*, **140**, 131–145. 157

Silveira, M. & Heleno, S. (2009). Separation between water and land in sar images using region-based level sets. *IEEE Geoscience and Remote Sensing Letters*, **6**, 471–475. 143

Sippel, S., Hamilton, S., Melack, J. & Novo, E. (1998). Passive microwave observations of inundation area and the area/stage relation in the amazon river floodplain. *Int. J. Remote Sens.*, **19**, 3055–3074. 144

Spessa, A., McBeth, B. & Prentice, C. (2005). Relationships among fire frequency, rainfall and vegetation patterns in the wet-dry tropics of northern Australia: An analysis based on NOAA-AVHRR data. *Global Ecology and Biogeography*, **14**, 439–454. 151, 182, 183

Stisen, S., Jensen, K.H., Sandholt, I. & Grimes, D.I.F. (2008). A remote sensing driven distributed hydrological model of the senegal river basin. *Journal of Hydrology*, **354**, 131–148. 141

Sullivan, A.L. (2010). Grassland fire management in future climate. *Advances in Agronomy*, **106**, 173–208. 183

Tolpekin, V.A. & Stein, A. (2009). Quantification of the effects of land-cover-class spectral separability on the accuracy of markov-random-field-based superresolution mapping. vol. 47, 3283–3297, IEEE, PISCATAWAY. 121, 159

Tortosa, D. (2008). Topic 13: Radar imagery. In *Geoforum*, http://hosting.soonet.ca/eliris/remotesensing/bl130lec13.html. 15, 16, 17

Töyrä, J. & Pietroniro, A. (2005). Towards operational monitoring of a northern wetland using geomatics-based techniques. *Remote Sensing of Environment*, **97**, 174–191. 23, 26, 27, 28, 29, 35, 37, 46, 48, 157, 159

Töyrä, J., Pietroniro, A. & Martz, L.W. (2001). Multisensor hydrologic assessment of a freshwater wetland. *Remote Sensing of Environment*, **75**, 162–173. 26, 35, 54, 157, 159

Töyrä, J., Pietroniro, A., Martz, L.W. & Prowse, T.D. (2002). A multi-sensor approach to wetland flood monitoring. *Hydrological Processes*, **16**, 1569–1581. 157

Trouvé, E., Chambenoit, Y., Classeau, N. & Bolon, P. (2003). Statistical and operational performance assessment of multitemporal SAR image filtering. *IEEE Transactions on Geoscience and Remote Sensing*, **41**, 2519–2530. 60

Ulaby, F.T., Moore, R.K. & Fung, A.K. (1982). *Radar Remote Sensing and Surface Scattering and Emission Theory*, vol. 2. Addison-Wesley, New York. 21, 44, 89, 90, 92, 113, 123

Ulander, L. (1996). Radiometric slope correction of synthetic-aperture radar images. *IEEE Transactions on Geoscience and Remote Sensing*, **34**. 175

van der Werff, H.M.A. & van der Meer, F.D. (2007). Shape-based classification of spectrally identical objects. *ISPRS Journal of Phoyogrammetry and Remote Sensing*, **63**, 251–258. 143

van Zyl, J., Chapman, B., Dubois, P. & Shi, J. (1993). The effect of topography on SAR calibration. *IEEE Transactions on Geoscience and Remote Sensing*, **31**, 1036–1043. 175

Vidal, A., Pinglo, F., Durand, H., Devaux-Ros, C. & Maillet, A. (1994). Evaluation of a temporal fire risk index in Mediterranean forests from NOAA thermal IR. *Remote Sensing of Environment*, **49**, 296–303. 184

Vining, B.R. & Wiseman, J. (2006). Multispectraland synthetic aperture radar remote-sensing-based models for holocene coastline development in the ambracian gulf, epirus, greece. *Archaeological Prospection*, **13**, 258–268, dOI: 10.1002/arp.292. 22

WAISURASINGHA, C., ANIYA, M., HIRANO, A., KAMUSOKO, C. & SOMMUT, W. (2007). Application of c-band synthetic aperture radar data and digital elevation model to evaluate the conditions of flood-affected paddies: Chi river basin, thailand. In *Asian Association on Remote Sensing, Proceedings ACRS 2007*, http://www.a-a-r-s.org/acrs/proceeding/ACRS2007/Papers/PS1.G5.4.pdf. 23, 28, 54, 87, 108

WANG, Y., HESS, L.L., FILOSO, S. & MELACK, J.M. (1995). Understanding the radar backscattering from flooded and nonflooded amazonian forests: Results from canopy backscatter modeling. *Remote Sensing of the Environment*, **54**, 324–332. 157, 162

WBG (2011). Pakistan floods 2010: Preliminary damage and needs assessment. In *Pakistan*, The World Bank. 108

WILSON, B.A. & RASHID, H. (2005). Monitoring the 1997 flood in the red river valley. *Canadian Geographer*, **49**, 100–109. 23, 35, 54, 87, 108

WOODHOUSE, I.H. (2006). *Introduction to Microwave Remote Sensing*. Taylor & Francis, Boca Raton, FL, USA. 21, 42, 43

YU, Q. & CLAUSI, D. (2007). Sar sea-ice image analysis based on iterative region growing using semantics. *IEEE Transactions on Geoscience and Remote Sensing*, **45**, 3919–3931. 143

ZHOU, C., LUO, J., YANG, C., LI, B. & WANG, S. (2000). Flood monitoring using multi-temporal avhrr and radarsat imagery. *Photogrammetric Engineering & Remote Sensing*, **66**, 633–638. 29, 48

ZINK, M., BUCK, C., SUCHAIL, J.L., TORRES, R., BELLINI, A., CLOSA, J., DESNOS, Y.L. & ROSICH, B. (2001). The radar imaging instrument and its applications: ASAR. In *ESA Bulletin 106*, European Space Agency. 61